ADAM MICKIEWICZ UNIVERSITY IN POZNAŃ

Structural features and tribo-mechanical properties of TiAlBSiN nanocomposite coatings

by

Oleksandr Pshyk

Supervisor: Prof. dr hab Stefan Jurga

NanoBioMedical Centre

Faculty of Physics

Adam Mickiewicz University in Poznań

Co-supervisor: Prof. dr. sci. Alexander Pogrebnjak

Department of Nanoelectronics

Faculty of Electronics and Information Technology

Sumy State University

Ph.D. Thesis

Poznan 2016

To my Family

Mojej Rodzinie

Моїй Сім'ї

Acknowledgements

This thesis would not has been possible without continuous support of many people. First of all, I would like to thank my supervisor Prof. Stefan Jurga for giving me the opportunity to join the Nanobiomedical centre. I would like to thank you for your confidence and endless support during the implementation of the thesis. My special thanks to a scientist who has opened the world of science for me and provided me with continuous motivation and inspiration during my first steps in this field. I am highly thankful to you Prof. Alexander Pogrebjak for everything you have done for my professional and personal development and for the realization of my research work.

The most of the results of the thesis obtained by means of various experimental techniques would not have been possible without my skilled colleagues and co-authors from the Nanobiomedical centre. Thank you all for performing the measurements and valuable input into the results. My very special thanks to Dr Emerson Coy from whom I have learned so much about science-related issues, I thank you for sharing knowledge, useful discussions and excellent time spent starting from our first days in the Nanobiomedical centre. My sincere gratitude to Dr Karol Załęski for his patience and help in experiments on FIB. Many thanks to Dr Igor Iatsunskyi for all long discussions about experiments.

I am very proud and happy to have a family that always inspires me and supports in all my beginnings. Дякую Вам мої любі тато і мама за моє життя.

Table of contents

List of author's papers and contributions

Articles incuded in this thesis:

[1] A.D. Pogrebnjak, A.A. Bagdasaryan, **A. Pshyk**, K. Dyadyura, Adaptive multicomponent nanocomposite coatings in surface engineering, Physics-Uspekhi. 60 (2017). doi:10.3367/UFNe.2016.12.038018.

[2] **A. Pshyk**, E. Coy, A. Pogrebnjak, High temperature behavior of functional TiAlBSiN nanocomposite coatings, Surf. Coat. Technol. 305 (2016) 49–61. doi:10.1016/j.surfcoat.2016.07.075.

[3] **A.V. Pshyk**, L.E. Coy, L. Yate, K. Załęski, G. Nowaczyk, A.D. Pogrebnjak, et al., Combined reactive/non-reactive DC magnetron sputtering of high temperature composite AlN–TiB_2–$TiSi_2$, Mater. Des. 94 (2016) 230–239. doi:10.1016/j.matdes.2015.12.174.

[4] A.D. Pogrebnjak, **A. V. Pshyk,** V.M. Beresnev, B.R. Zhollybekov, Protection of specimens against friction and wear using titanium-based multicomponent nanocomposite coatings: A review, J. Frict. Wear. 35 (2014) 55–66. doi:10.3103/S1068366614010073.

[5] A.D. Pogrebnjak, G. Abadias, O.V. Bondar, O.V. Sobol, V.M. Beresnev, **A.V. Pshyk**, et al., High Temperature Annealing of Ion-Plasma Nanostructured Coatings Based on AlN-TiB_2($TiSi_2$), Acta Phys. Pol. A. 125 (2014) 1284–1287. doi:10.12693/APhysPolA.125.1284.

[6] N.A. Azarenkov, **A.V. Pshyk**, O.V. Sobol, V.M. Beresnev, P.V. Turbin, S.V. Lytovchenko, et al., Properties of AlN-TiB_2 -$TiSi_2$ coating system obtained by magnetron sputtering, in: 23rd Int. Crime. Conf. "Microwave Telecommun. Technol. (CriMiCo'2013)., 2013: pp. 824–825.

Other publications:

[1] A. Shypylenko, **A. V Pshyk**, B. Grześkowiak, K. Medjanik, B. Peplinska, K. Oyoshi, et al., Effect of ion implantation on the physical and mechanical properties of Ti-Si-N multifunctional coatings for biomedical applications, Mater. Des. 110 (2016) 821–829. doi:10.1016/j.matdes.2016.08.050.

[2] K.V. Smyrnova, A.A. Demianenko, A.S. Radko, **A.V. Pshyk**, O.V. Kuzovlev, H. Amekura, et al., The Influence of the Ion Implantation of Au– to the Microstructure

of the Amorphous-nanocrystaline AlN-TiB_2-$TiSi_2$, J. Nano- Electron. Phys. 7 (2015) 1–5.

[3] A. D. Pogrebnyak, Y. A. Kravchenko, A. A. Dem'yanenko, O. V. Sobol', V.M. Beresnev, **A. V. Pshik**, Peculiarities of the formation of multicomponent AlN-TiB_2-$TiSi_2$ composite ceramics coatings during heat treatment, Phys. Met. Metallogr. 116 (2015) 576–585. doi:10.1134/S0031918X15040122.

[4] A. D. Pogrebnjak, A. A. Demianenko, **A. V. Pshik**, Y. A. Kravchenko, O. V. Sobol', V.M. Beresnev, et al., Structural features and physico-mechanical properties of AlN-TiB_2-$TiSi_2$ amorphous-like coatings, J. Superhard Mater. 37 (2015) 310–321. doi:10.3103/S1063457615050032.

[5] S.N. Bratushka, O.V. Kolisnichenko, A.D. Mikhalev, A.I. Kupchishin, B.A. Mukushev, **A.V. Pshyk**, et al., Formation of ultradispersed state of surface layers of the steel alloyed with metal ions in the mode of melting by plasma jet, Metallofiz. I Noveishie Tekhnologii. 35 (2013) 1251–1270.

[6] S.N. Bratushka, Y.N. Tyurin, O. V. Kolisnichenko, A. D. Mikhalev, R.Y. Tkachenko, N. A. Makhmudov, **A.V. Pshik** et al., Structure and tribological characteristics of steel under melting by plasma flow and simultaneous Mo and W alloying, J. Frict. Wear. 33 (2012) 22–33. doi:10.3103/S1068366612010047.

[7] D.L. Alontseva, S.N. Bratushka, M. V. Il'yashenko, N.A. Makhmudov, N. V. Prokhorenkova, E.L. Onanchenko, **A.V. Pshik** et al., Formation of stable nanostructured phases in plasma-jet-treated Ni-Cr powder coatings, Phys. Met. Metallogr. 113 (2012) 785–794. doi:10.1134/S0031918X12080029.

[8] D.L. Alontseva, S.N. Bratushka, A.A. Borysenko, A.A. Drobyshevska, I.A. Kulik, N.V. Prokhorenkova, **A.V. Pshyk** et al., Formation of micro- and nanostructured phases in coatings based on Ni-Cr and Co-Cr, their structure and properties, Metallofiz. I Noveishie Tekhnologii. 33 (2011) 721–745.

[9] A.D. Pogrebnyak, S.N. Bratushka, M. V. Il'yashenko, N.A. Makhmudov, O. V. Kolisnichenko, Y.N. Tyurin, **A.V. Pshik** et al., Tribological and physical-mechanical properties of protective coatings from Ni-Cr-B-Si-Fe/WC-Co-Cr before and after fission with a plasma jet, J. Frict. Wear. 32 (2011) 84–90. doi:10.3103/S1068366611020085.

[10] A.D. Pogrebnjak, O.V. Sobol, V.M. Beresnev, P.V. Turbin, G.V. Kirik, N.A. Makhmudov, et al., Phase composition, thermal stability, physical and mechanical properties of superhard on base Zr-Ti-Si-N nanocomposite coatings, Ceram. Eng. Sci. Proc. 31 (2010) 127–138.

[11] A.D. Pogrebnjak, M.V. Il'yashenko, M.V. Kaverin, A.P. Shypylenko, **A.V. Pshyk**, V.M. Beresnev, et al., Physical and mechanical properties of the nanocomposite and combined coatings Ti-Si-N/WC-Co-Cr/and Ti-Si-N/$(Cr_3C_2)_{75}$-$(NiCr)_{25}$, J. Nano-Electron. Phys. 1 (2009) 101–110.

[12] A. Shypylenko, **A.V. Pshyk**, B. Grześkowiak, K. Medjanik, B. Peplinska, K. Oyoshi, et al., Influence of Ion Implantation on the Physical and Mechanical Properties of Multifunc-tional Coatings Based on Ti-Si-N, in: Int. Conf. Nanomater. Appl. Prop., 2016: p. 01NTF18-1. doi:10.1016/j.matdes.2016.08.050.

Streszczenie

Wieloskładnikowe nanokompozytowe pokrycia, składające się z co najmniej dwóch faz, stały się w ostatnich latach obiektem zainteresowania naukowców i technologów, głównie z uwagi na bardzo dobre właściwości fizyczne tych materiałów. Szczególną uwagę poświęca się pokryciom TiAlN, które posiadają bardzo dobre właściwości mechaniczne i trybologiczne, są odporne na utlenianie i korozję, a także charakteryzują się stabilnością termiczną w zakresie wysokich temperatur. Dzięki tym funkcjonalnym cechom nanokompozytowe warstwy TiAlN znalazły już zastosowanie w wielu dziedzinach przemysłu jako powłoki zabezpieczające. Ciągle rosnące wymogi przemysłu w zakresie zaawansowanych powłok zabezpieczających w połączeniu z rozwojem technik wytwarzania cienkich warstw stały się podstawą do opracowania metody wytwarzania nanokompozytów TiAlN w formie stopów. Metoda ta pozwala na wytworzenie układu wielofunkcyjnego, łączącego w sobie zalety poszczególnych składników stopu. Unikatowe właściwości stopów TiAlN wynikają głównie z powstawania w ich obrębie bogatej w Al kubicznej fazy krystalicznej. Z uwagi na to, ważne jest opracowanie metody wytwarzania materiału w tej właśnie fazie, przy jednoczesnym zapobieganiu dekompozycji układu do heksagonalnej fazy AlN. Obecnie stosowane są dwa główne podejścia gwarantujące spełnienie powyższych kryteriów: tworzenie stopów oraz osadzaniu wielowarstwowych powłok. Jak zaobserwowano, tworzenie stopów TiAlN z B i Si wykazuje korzystny wpływ na właściwości mechaniczne oraz odporność na utlenianie powstałych nanokompozytów. Niewiele jest natomiast doniesień na temat stopu bogatej w Al kubicznej fazy TiAlN z B i Si, co stanowi motywację do podjęcia badań w tym obszarze. Otrzymywanie stopu TiAlN w warunkach, w których rozpoczyna się dekompozycja TiAlN i tworzenie heksagonalnej fazy AlN, również nie zostało w pełni zbadane. Podobnie ma się sprawa wpływu stapiania dużej ilości B i Si z bogatą w glin fazą TiAlN na mikrostrukturę i mechaniczne właściwości powstałych nanokompozytów. Jest to związane głównie z tym, iż optymalizacja metod wytwarzania powłok ochronnych o gradientowej mikrostrukturze poprzez zastosowanie szerokiej gamy technik nanotechnologicznych nadal pozostaje obszarem niezbyt intensywnie eksplorowanym.

Amorficzne wieloskładnikowe pokrycia typu TiAlBSiN są interesujące z puntu widzenia ich wysokiej stabilności termicznej i odporności na utlenianie. Pomimo wielu prowadzonych badań nad pokryciami nanokrystalicznymi, niewiele jest tych dotyczące amorficznych warstw oraz stopów opartych na TiAlN, przez co potencjał tego typu układów nie został w pełni odkryty. Jednym z istotnych wyzwań w kontekście tych materiałów jest optymalizacja stabilności termicznej i opracowanie metod zapobiegania

dyfuzji materiału podłoża do warstwy wskutek działania wysokich temperatur. Innym ważnym aspektem pod kątem przyszłego zastosowania układów TiAlN jest z kolei opracowanie metody wytwarzania pokryć amorficznych odpornych na utlenianie.

W niniejszej pracy doktorskiej przedstawiono wyniki badań dotyczące struktury i właściwości fizycznych pokryć opartych na TiAlSiBN o strukturze amorficznej i nanokompozytowej mikrostrukturze gradientowej.

Gradientowe pokrycia TiAlBSiN były wytwarzane poprzez użycie reaktywnego/niereaktywnego magnetronowego rozpylania z targetu kompozytowego AlN-TiB_2-$TiSi_2$. Target został zsyntetyzowany poprzez izostatyczne ściskanie na gorąco, w temperaturze 1860-1880 °C w atmosferze powietrza mieszaniny AlN (50 wt.%), TiB_2 (35 wt.%) i $TiSi_2$ (15 wt.%). Głównymi fazami obecnymi w targecie po syntezie były AlN, TiB_2 i $TiSi_2$ oraz mała ilość Al_2O_3, TiN i Si_3N_4 wywołana spiekającymi reakcjami zachodzącymi podczas syntezy. W celu wytworzenia pokryć z mikrostrukturą gradientową, sekwencyjnie stosowano mody reaktywnego i niereaktywnego rozpylania, z wstrzykiwaniem N_2 do gazu roboczego podczas osadzania reaktywnego. Dzięki zastosowaniu tej metody wytworzono nieopisaną wcześnie w literaturze bogatą w Al warstwę TiAlN o względnie wysokich koncentracjach B i Si. Ocena chropowatości powierzchni powłoki gradientowej za pomocą AFM pozwoliła na ujawnienie nanowymiarowej chropowatości w różnych skalach, R_a = 0.38 nm dla 1.297 μm i R_{rms} = 0.51 nm mierzonej na powierzchni 1×1 μm. Powstała nanochropowatość byłą prawdopodobnie konsekwencją kilku czynników wpływających na wzrost powłoki podczas depozycji. Powłoka gradientowa miała gęstą i płaską strukturę widoczną na zdjęciu SEM przełamu poprzecznego. Ponadto, nie stwierdzono jej porowatości ani delaminacji. Badania wykazały, iż wytworzona gradientowa powłoka złożona byłą z dwóch warstw o różnej mikrostrukturze i składzie pierwiastkowym. Górna warstwa składała się głównie z lekkich pierwiastków: N, B, C i O, podczas gdy warstwa dolna zbudowana byłą z cięższych pierwiastków: Al, Ti, Si. Obie warstwy składały się głównie z krystalicznych faz fcc-(Ti,Al)(N,O,B) i hcp-(Al,Ti)(N,O) otoczonych amorficzną fazą. Górna warstwa o grubości około 220 nm złożona była z drobnych krystalitów o wymiarach w przedziale 15-40 nm. Dolna warstwa została uformowana przez niejednorodnie rozłożone nanokryształy o wymiarach około 5-40 nm. Faza krystaliczna była oparta na metastabilnym roztworze stałym Ti i O wewnątrz sieci hcp-AlN, gdzie atomy Ti zastępują atomy Al w metalicznych węzłach podsieci, podczas gdy atomy O są włączone w niemetalicznych węzłach podsieci lub a przerwach międzywęzłowych sieci. Druga faza krystaliczna to metastabilny stały roztwór Al, O i B wewnątrz sieci fcc-TiN, gdzie atomy

Al zastępują atomy Ti w metalicznych węzłach pod-sieci, podczas gdy atomy O i B zastępują N w niemetalicznych węzłach podsieci. Jak ujawniły pomiary XPS, faza krystaliczna została zawarta w amorficznej fazie mieszaniny a-TiB_2/a-BN(O)/a-SiB/a-AlO_x/a-TiO_x/a-Si_3N_4. Powstanie takiej wielofazowej struktury wytłumaczono występowaniem termodynamicznych i kinetycznych ograniczeń podczas wzrostu powłoki. Po pierwsze, ze względu na bardzo wysoką i ujemną entalpię formacji, AlN i TiN mają największa siłę napędową do formowania spośród możliwych faz, które mogą być uformowane z pierwiastków składowych powłoki. Fazy stałych roztworów pojawiają się w powłoce z powodu niedużej różnicy w energii swobodnej Gibbsa i równowagowej entalpii formacji trójskładnikowych zmieszanych faz $Ti_{1-x}Al_xN$ w strukturach fcc i hcp. Ponadto, powstanie faz roztworów stałych było podyktowane stosunkowo małym rozmiarem niedobranych atomów, małą różnicą elektroujemności i wartościowości pomiędzy atomami Al i Ti. Niewielkie odchylenie od prawa Vegarda wytłumaczono inkorporacją atomów B do sieci fcc-TiN. Głównymi powodami inkorporacji atomów B jest izostrukturalność siei TiN i TiB, odobna konfiguracja elektronowa, rozmiar atomów i chemiczna natura atomów B i N. Po drugie, formowanie stałych roztworów w powłoce było promowane przez małą mobilność dodatkowych atomów podczas wzrostu, wywołaną nierównowagowymi warunkami depozycji. W rezultacie, duża liczba atomów na jednostkę powierzchni została inkorporowana w pozycjach nierównowagowych ze względu na brak energii potrzebnej do dyfuzji na duże odległości. Ponieważ powstawanie roztworów stałych było ograniczone przez limit rozpuszczalności pierwiastków w sieciach fcc-TiN i hcp-AlN, nadmiarowe B, O i Si miały tendencję do osadzania się wzdłuż granic ziaren. W wyniku tego zmienił się mechanizm wzrostu. Wydzielone B, O i Si uformowały fazę amorficzną dalej ograniczając mobilność na granicy ziaren i stymulując ich renukleację. W konsekwencji wzrost ziaren był ograniczony, co doprowadziło do przekształcenia struktury powłoki do stanu nanokrystalicznego. Faworyzowanie formacji fazy bazującej na hcp-AlN w powłoce zostało wyjaśnione faktem, że faza hcp-AlN jest bardziej stabilna niż fcc-TiN gdy stosunek Al/(Al+Ti) jest rzędu 0.7. Ponadto, faza amorficzna pełni rolę ograniczenia kinetycznego dla dyfuzji Ti bardziej efektywnie niż dla dyfuzji Al, ograniczając przez to nukleację fazy bazującej na TiN. Wykazano, iż wstrzykiwanie N_2 podczas osadzania reaktywnego skutkuje preferencyjnym powstawaniem fazy BN w mieszanej fazie amorficznej oraz nieznacznym zwiększeniem wielkości ziaren.

Badania mechaniczne i trybologiczne wskazały na dobre właściwości elastyczne oraz względnie wysoką odporność na ścieranie wytworzonych materiałów. Twardość i zredukowany moduł sprężystości miały wartość odpowiednio 17.55 GPa oraz 216.71 GPa.

Zasugerowano, że za stosunkowo niską zaobserwowaną wartość twardości odpowiada kilka czynników. Duże odstępy pomiędzy cząsteczkami nanokrystalicznych ziaren i duża objętość frakcji stanowiącej amorficzną matrycę zmniejsza energię spójności granic interfejsu pomiędzy fazą nanokrystaliczną i amorficzną, sprzyjając przez to przesuwaniu się granic ziaren. Dodatkowo założono, że zwiększenie twardości spowodowane twardnieniem stałego roztworu nie jest znaczące, ponieważ powłoka jest oparta na stosunkowo miękkiej fazie hcp-(Al,Ti)(N,O), dla której twardnienie roztworu stałego jest mniej efektywne niż w przypadku jej kubicznego odpowiednika. Jednocześnie silne wiązania B-N, Ti-B i Si-N w fazie amorficznej mogą mieć wkład w twardość powłoki. Powłoka wykała doskonałą sprężystość i wiązkość, nawrót sprężysty o wartości 60%, odkształcenie sprężyste poprzedzające deformację plastyczną około ~0.08 i odporność na deformację plastyczną ~ 0.12 GPa. Oznacza to, że powłoka może wytrzymać duże obciążenia z niewielkim prawdopodobieństwem powstania i propagacji pęknięć, a także zachowaniem sprężystym w szorstkim kontakcie podczas ścierania pod dużym obciążeniem i ciśnieniem kontaktowym. Zaproponowano, że osiągnięta wiązkość wynika głównie z uwalniania rozładowania odkształcenia w pewnym stopniu przez poślizg nanokryształów w amorficznej matrycy i relaksację naprężenia przez odkształcenie plastyczne fazy amorficznej. Pomiary nanościerania pozwalają na ujawnienie stosunkowo małej objętości ścieranej w porównaniu ze stalą nierdzewną i Si (100) podczas przesuwania nanoindentera pod obciążeniem 1000 μN na powierzchni 5 μm × 5 μm powłoki i głębokości penetracji ~ 15 nm.

Amorficzne pokrycia TiAlBSiN były wytwarzane z wykorzystaniem metody niereaktywnego rozpylania magnetronowego z kompozytowego targetu AlN–TiB_2–$TiSi_2$. Po raz pierwszy przeprowadzono wzrost amorficznej bogatej w Al powłoki TiAlBSiN za pomocą napylania magnetronowego z kompozytowego targetu. Powłoka po depozycji miała bardzo gładką powierzchnię o R_{rms} równym 0.38 nm (mierzonym na powierzchni 1×1 μm) i R_a wynoszącym 0.47 nm (mierzonym wzdłuż 1.2 μm), podczas gdy wygrzewanie w wysokiej temperaturze spowodowało niewielki wzrost chropowatości, R_{rms} = 2.16 nm i R_a = 1.76 nm. Głównym powodem tego wzrostu okazało się być formowanie tlenków Me-Met-O_x (Me- metal, Met-półmetal) podczas wygrzewania w temperaturze 900 ºC w środowisku utleniającym, wzrost wyspowy i gęstnienie materiału powłoki. Wykazano, że amorficzna powłoka charakteryzuje się w przekroju poprzecznym gęstszą i mniej wyrazistą strukturą o wyraźnym interfejsie powłoka/substrat. Wygrzewanie spowodowało wzrost powierzchniowych okrągłych tlenkowych zgrubień i makroziaren o rozmiarach ok. 400 nm na powierzchni powłoki. W przekroju poprzecznym powłoki

zaobserwowano formację powierzchniowej warstwy tlenku i rozpraszanie interfejsu z substratem. Amorficzna powłoka wykazywała gęstą i pozbawioną luk mikrostrukturę, powstałą w wyniku dostarczenia wystarczająco dużej energii rosnącej powłoce na skutek stosunkowo wolnego tempa depozycji w połączeniu z optymalnymi wartościami biasu substratu i gęstości prądu jonowego substratu. Duży strumień jonów i ich wysoka energia wywołały powstanie dużej gęstości defektów wzrostu, co po przekroczeniu granicy amorfizacji sprzyjało wzrostowi fazy amorficznej. Duża różnica w rozmiarach atomów pierwiastków składowych dodatkowo sprzyjała wzrostowi powłoki w stanie amorficznym. Wygrzewanie powłoki w temperaturze 900 °C w środowisku utleniającym spowodowała dyfuzję Al, Ti i N na zewnątrz, w kierunku powierzchni swobodnej powłoki, co wywołało ubytek N w powierzchniowej warstwie i niejednorodną dystrybucję Ti i Al w głąb powłoki. Zaobserwowano wzrost powierzchniowej warstwy tlenkowej do ~35 nm z mała zawartością Al i Ti. Badania wykazały, iż naniesienie warstwy buforowej znacząco obniża dyfuzję atomów krzemu z podłoża do warstwy. Jednak po wygrzewaniu miała miejsce znacząca redystrybucja pierwiastków w objętości warstwy granicznej, co było kinetycznie wywołane zainicjowaną temperaturą dyfuzją pierwiastków warstwy granicznej i prawdopodobnie skierowaną do wewnątrz dyfuzją pierwiastków powłoki i substratu. W wyniku wygrzewania w powietrzu w temperaturze 900 °C naniesiona amorficzna warstwa ulegała transformacji strukturalnej, co objawiało się zmianą parametrów topologicznych i chemicznych w obrębie krótkozasięgowego uporządkowania. Jest to związane z powstawaniem w układzie trójwymiarowych nanokompozytowych struktur nc-$TiAl_3$/a-SiBN(O). Stąd powierzchniowa warstwa tlenkowa pozostała w czystym amorficznym stanie po utlenieniu w otaczającym powietrzu w 900 °C. Mikrostruktura powłoki pozostała gęsta i pozbawiona luk po wygrzewaniu. Widok warstwy granicznej w przekroju poprzecznym ukazał jej krystalizację po wygrzewaniu oraz powstawanie gęstego amorficznego interfejsu z substratem. Rozmiary nanokryształów SiO_2, Al_2O_3 i TiO_2 określono na 8–15 nm. Wykazano, że powłoka jest złożona z małych nanokryształów $TiAl_3$ o rozmiarach od 2 do 3 nm otoczonych przez nieuporządkowane obszary. Ułamki objętości fazy krystalicznej i amorficznej określono odpowiednio na ~30% i ~70%. Amorficzna matryca złożona jest z różnego rodzaju nanoklastrów lokalnie uporządkowanych i rozdzielonych granicami międzyklastrowymi składającymi się z nieregularnie ułożonych atomów. Faza amorficzna osadzonej powłoki będąc w początkowym metastabilnym stadium, ma tendencje do transformacji do stanu stabilnego pod wpływem podgrzewania z lokalnym minimum wolnej energii. Obserwowana separacja na dwie amorficzne fazy o różnym uporządkowaniu krótkiego zasięgu jest

prawdopodobnie związana ze złożonym składem powłoki i obecnością kilu faz w tym przedziale koncentracji na diagramie równowagi fazowej systemu Ti-Al-N i Ti-Al-O które są baza dla powłoki TiAlBSiN. Wysokotemperaturowe wygrzewanie pokryć amorficznych w warunkach atmosferycznych skutkuje z kolei powstawaniem gęsto upakowanej powierzchniowej warstwy tlenków metali, które w głównej mierze odpowiadają za zapewnienie odporności nanokompozytu na objętościowe utlenianie i zapobiegają dyfuzji tlenu w głąb materiału. Warstwa tlenku była złożona głównie z mieszaniny amorficznych faz TiO_2, Al_2O_3, B_2O_3, i SiO_2 (Al_2O_3 i SiO_2 są znane jako dobre bariery przeciwko dyfuzji tlenu). Grubość warstwy tlenu wynosząca ~35 nm była mniejsza od krytycznej wartości potrzebnej dla transformacji do stanu krystalicznego. Zaproponowano, że warstwa powierzchniowa może pełnić funkcję bariery przeciwko skierowanej do wewnątrz dyfuzji O w wysokiej temperaturze głównie ze względu na brak szybkich ścieżek dyfuzji O spowodowany wydajnym lokalnym upakowaniem atomów i brakiem granic międzyziarnowych i luk atomowych, przez co odpowiedzialna jest za utrzymywanie stabilności powłoki w wysokich temperaturach w środowisku utleniającym. Badana amorficzna powłoka TiAlBSiN bogata w Al wykazała lepszą stabilność termiczną w środowisku utleniającym niż powłoki oparte na TiAlBSiN opisane wcześnie w literaturze. Stabilność amorficznej fazy powłoki TiAlBSiN może być związana z zawartością atomów Si i B, co ze względu na zmniejszoną mobilność dyzfuzyjną może ograniczać wzrost ziaren tlenku i zmniejszać zmianę masy powłoki podczas utleniania. Właściwości mechaniczne amorficznych pokryć ulegają znaczącej poprawie na skutek tworzenia się struktury nanokompozytowej. Twardość miała największą wartość, wynoszącą H = 24.41 GPa, dla powłoki po wygrzewaniu, natomiast twardość świeżo osadzonej powłoki wynosiła H = 15.20 GP. Redukowany moduł sprężystości wykazywał ten sam trend, mając najwyższą wartość E^* = 212.46 GPa dla powłoki po wygrzewaniu, a nieco niższą E^* = 177.6 GPa bezpośrednio po osadzeniu. Nawrót sprężysty powłok, W_e, wyznaczony z krzywych obciążenie-odciążenie, wynosił 61% dla powłoki TiAlBSiN zaraz po osadzeniu i 68% dla połoki wygrzanej w 900 °C. Stosunkowo niska twardość amorficznej powłoki może być związana z występowaniem lokalnych obszarów o wysokim stosunku wolnej objętości, co z kolei prowadzi do zmniejszenia gęstości fazy amorficznej. Inną możliwą przyczyną może być mała gęstość uporządkowanych w bliskim zasięgu cząstek (wiązań) o dużej sile. Większa gęstość słabszych wiązań może sprzyjać łatwiejszemu przearanżowaniu obszarów nasilonej transformacji po wpływem przyłożonego naprężenia, co prowadzi do odkształcenia plastycznego. Transformacja fazy amorficznej i powstawanie struktury nanokompozytowej dramatycznie zmienia mechaniczne

zachowanie systemu. Oddziaływanie pomiędzy ziarnami ogranicza generację dyslokacji (rozmiar ziaren jest mniejszy niż długość dyslokacji) oraz przeciwdziała propagacji pęknięć, na skutek uwydatnienia granic miedzy ziarnami i wstrzymania po ślizgu na granicy ziaren w powłokach nanokompozytowych o małym rozmiarze ziaren. W naszym przypadku, wzrost twardości może być powiązany z połączonym efektem kompozytowej struktury oraz anihilacji wolnej objętości (anihilacji defektów) w wyniku transformacji struktury po wygrzewaniu. Wiązkość (odporność na deformację plastyczną, stosunek H^3/E^{*2}) i odkształcenie sprężyste poprzedzające deformację plastyczną (H/E^*) obliczono otrzymując wartości H^3/E^{*2} = 0.322 GPa i H/E^* = 0.115 dla powłoki po wygrzaniu oraz H^3/E^{*2} = 0.111 GPa i H/E^* = 0.0856 dla powłoki bezpośrednio po depozycji. Stąd, wyższy stosunek H^3/E^{*2} dla powłoki po wygrzewaniu wskazuje na zdolność powłoki do opierania się mechanicznej degradacji i zniszczeniu w zdarzeniach trybo-kontaktowych, ponieważ kontakt może pozostawać sprężysty dla dużych naprężeń podczas przykładania zewnętrznego nacisku. Amorficzne pokrycia TiAlBSiN wykazują również obiecujące właściwości trybologiczne w mikroskali. Analiza ścieranej objętości po testach nanościerania wykazała większą ścieraną objętość 0.3818 μm^3 w przypadku wygrzewanej powłoki, niż 0.046 μm^3 dla powłoki świeżo osadzonej, co najprawdopodobniej wiąże się z przyrostem Al_2O_3 po wygrzewaniu. Średnia wartość współczynnika tarcia dla amorficznej powłoki wynosiła 0.871, a tempo ścierania 0.2946 $\mu m^3/Nm$. Biorąc pod uwagę istnienie przynajmniej dwóch pierwiastków, które mają tendencję do formowania związków zdolnych do samolubrykacji można się spodziewać że amorficzny TiAlBSiN może potencjalnie wykazywać własność samolubrykacji w środowisku wewnętrznym po wpływem wysokiej temperatury. Jednocześnie, wykazane własności sprężyste powłoki TiAlBSiN oraz ich polepszenie po wygrzaniu pozwolą na opór przez tarciem i ścieraniem przez zmianę mikrostruktury w odpowiedzi na zmiany otoczenia i nacisku.

Abstract

Over the last few years, multicomponent nanocomposite coatings, composed of at least two different phases, have become of great scientific and technological interest because of their outstanding physical and chemical properties. Special interest has been recently devoted to TiAlN coatings due to their attractive mechanical and tribological properties, oxidation and corrosion resistance, high thermal stability and self-adaptation at high temperatures. Therefore, they are widely used as protective coatings. Further development toward the quaternary and multinary TiAlN-based coating systems through the alloying concept gave rise to more sophisticated coating systems with outstanding multifunctional properties. In particular, the alloying of TiAlN with either elemental B or Si has allowed improving of both tribo-mechanical properties and oxidation resistance. However, in case of the alloying of Al-rich TiAlN composites with both B and Si, such nanocomposites were poorly studied and there are the concerns needed for a solution such as stabilization of the cubic phase and the alloying with high amount of both B and Si. At the same time, the amorphous TiAlBSiN multielement coatings are promising due to their potential high-temperature stability and oxidation resistance. Despite many advantages, the studies devoted to the amorphous TiAlSiBN based coatings are rare and their potential has not been fully explored.

The deposition of the amorphous and gradient nanocomposite coating based on TiAlBSiN, their structural and physical properties are studied in this thesis.

The gradient TiAlBSiN coating is deposited by means of reactive/non-reactive magnetron sputtering of the composite target AlN–TiB_2–$TiSi_2$. The gradient microstructure is formed by sequential reactive/non-reactive mode of the sputtering process with the injection of N_2 into the working gas during the reactive stage of the deposition. For the first time, the Al-rich TiAlN coating alloyed with the relatively high concentration of B and Si is synthesized. The studies presented in this thesis reveal that the gradient coating is composed of two layers with the different microstructure and elemental composition. Both layers are based on the crystalline fcc-(Ti,Al)(N,O,B) and hcp-(Al,Ti)(N,O) phases which are encapsulated into the mixed amorphous a-TiB_2/a-BN(O)/a-SiB/a-AlO_x/a-TiO_x/a-Si_3N_4 phase. It is shown that the injection of N_2 causes the preferred formation of BN in the mixture of the amorphous phase and slightly increased the growth of the crystalline phase. The study of the mechanical and tribological properties reveals the promising elastic properties and relatively high wear resistance of the coating due to the separation of the randomly oriented nanocrystals by the thick amorphous matrix, which facilitates grain

boundary sliding and thus hindering of initiation and propagation of dislocations in the coating.

The amorphous TiAlBSiN coating is deposited by means of non-reactive magnetron sputtering of the composite target AlN–TiB_2–$TiSi_2$. For the first time, the dense, void-free and featureless amorphous Al-rich TiAlBSiN coating was grown by means of magnetron sputtering from a composite target. Moreover, a sacrificial barrier layer is applied between the substrate and the coating in order to qualitatively investigate its efficiency in avoiding of the diffusion of the substrate material to the coating. The study shows that the barrier layer suppresses the Si diffusion from the substrate to the coating. The changes of structural parameters of the amorphous phase, such as topological and chemical short-range order, are revealed in the amorphous TiAlBSiN coating after the post-deposition annealing at 900 °C in air. The observed structural transformation results in the formation of a three-dimensional nc-$TiAl_3$/a-SiBN(O) nanocomposite structure. The high temperature annealing promotes the formation of the densely mixed metal oxide layers on the coating surface. This layer retards the inward oxygen diffusion into the coating and therefore is responsible for oxidation resistance and thermal stability of the coating. The mechanical properties of the amorphous coating are significantly improved due to the formation of the nanocomposite structure. At the same time, the micro-scale tribological measurements of TiAlBSiN amorphous coating showed very promising tribological characteristics of the coating.

Outline of the thesis

Chapter 1 highlights state-of-the-art and accomplishments in the field of protective multicomponent nanocomposite coatings. In this chapter, the basic concepts of the protective nanocomposite coatings design are described and summarized. The recent development of the most widespread nanocomposite coatings such as TiAlN, TiAlSiN, TiAlBN and TiAlBSiN are presented for the reader. The objectives of the thesis are set at the end of this chapter.

Chapter 2 reviews the experimental methods and techniques used for implementation of the thesis objectives. First, a brief theoretical basis of the each of the techniques is given, and then the experimental set-up and quipment specification is presented. Finally, the protocols usted for each method are described.

Chapter 3 is devoted to the characterization of TiAlBSiN-based coatings and discussion of the obtained results. First, section 3.1 reports on the elemental and phase composition of the target used for deposition of TiAlBSiN coatings. Then, in Section 3.2 the structural features and tribo-mechanical properties of TiAlBSiN coating with gradient microstructure are characterized by various experimental techniques. Section 3.3 contains results on the investigation of the amorphous TiAlBSiN coating which is concentrated on a structural transformation in the amorphous phase after high temperature annealing at 900 °C in ambient air. Further, the effect of structural transformation in the coating on its mechanical and tribological properties is examined. The obtained results are discussed and correlated with the previous results given in literature references.

The results of the thesis are summarized by the conclusions and details on the contribution of the work to the research field.

Chapter 1

Protective nanocomposite coatings and thin films

The knowledge acquired by material scientists and material engineers over the years has allowed to develop the advanced principles of protective coating design. The most established and widely used concept for the design of protective coatings is based on the introduction of multifunctional nanostructured coatings. Recent achievements of research community in this field have given rise to the development of a wide range of different types of protective coatings. The state-of-the-art concepts and approaches for the creation of different types of protective coatings are summarized and described in the following section of the thesis.

1.1 Design concept of nanocomposite coatings and thin films

The surface of bulk materials of working tools is usually the most important engineering part during operation. While it is in operation, it is often the surface of a workpiece that undergoes different kinds of external impact which is accompanied by a damage of the material, and as a result of wear, corrosion, and oxidation etc. Therefore, the search of scientific community is focused on surface modification techniques, which can increase the resistance of materials to any kind of the damage induced by the external impact **[1,2]**. The choice of a surface treatment has to be such that does not impair too much the properties of the substrate for which it was originally chosen. Equally important, the chosen surface treatment should be suitably related to the application.

Coatings and thin films, i.e. material layers that range from a couple of nanometres to several micrometres in thickness, are applied to bulk materials in order to improve the desired properties of the surface, such as wear resistance, friction, oxidation resistance, thermal stability, corrosion resistance and others, yet keeping the bulk properties of the material unchanged **[3,4]**. The breakthrough in the development of the protective coatings and thin films was the deposition of TiN and other transition metal (TM) nitride coatings on machining tools in 1980s that has allowed to improve the life time of working tools and also the quality of the surface of the parts being machined **[5,6]**. The bond structure of TM nitrides consists of a mixture of covalent, metallic and ionic components, and is responsible for the relatively high hardness, excellent wear resistance, chemical inertness, good electrical conductivity and superconducting properties **[7]**. Nevertheless, the main drawback of TiN is that it begins to oxidize in air already at 550 ºC **[8]**. It is important to note, that besides the high hardness of protective coatings, it is also required to achieve a

high oxidation resistance. Since the temperature of the cutting edge during a machining in ambient atmosphere can exceed 1000 ºC, the chemical wear due to the formation of soft oxides with poor adherence dominates over the abrasive wear that is important at lower temperature. Later, the incorporation of Al into TiN allowed to improve the oxidation resistance from 550 ºC to 800 ºC, as well as the hardness, wear resistance and the thermal stability of the obtained Ti-Al-N coatings **[9,10]**. Addition of Y and Cr into Ti-Al-N further improved the oxidation resistance up to 900 ºC **[11]**. Ternary Ti-Zr-N and Ti-V-N coatings demonstrate higher microhardness, corrosion resistance and better wear resistance than corresponding binary compounds TiN, VN and ZrN **[12–14]**. The alloying of TiN with Si has resulted in the improvement of the oxidation resistance and led to the superhardness of coatings of the Ti-Si-N system **[15]**. Such an approach was extended to a large number of element combinations (Hf, V, Nb, Cr, Mo, W, Al, Si, B, C, Ta etc.) that have led to the development of multielement coatings **[16–18]**.

Moreover, the increasing industrial demand for advanced coating systems with tailored protective properties has motivated the continuous development toward quaternary and multinary TM nitride-based thin films and coatings. Ternary, quaternary and multicomponent coatings with different metallic and non-metallic alloying elements combine the benefit of individual components leading to further refinement of the protective properties of coatings **[16,19–22]**. Hence, intensive efforts during last decades have been made to develop high-performance multicomponent (multiphase) materials **[23–25]**.

The contribution of bonding components is responsible for a particular specific property of a material which then, together, give a unique and unusual combination of properties of multicomponent coatings. Fig. 1.1 gives an overview on the classification of hard materials according to their chemical bonding and the associated change in properties **[26]**. The distinct metallic contribution causes electrical conductivity, as well as a good adhesion and considerable ductility (as compared to ionic hard materials), while the high hardness and phase stability caused by covalent and ionic bonding components. The charge transfer from metal to non-metal species associated with ionic bonding is, however, relatively small in TM nitrides, as compared to ionic hard materials such as alumina or zirconia.

Besides chemical advances, microstructural engineering has also yielded significant improvements of protective coatings properties **[27–29]**. One of the very basic findings of the physics of solids is the insight that most properties of solids depend on their microstructure. The key structural factor determining functional properties of materials is

the size of building blocks (grains) of which a material is consisted of, these can be of one-, two- and three-dimensional nature. It has been found that the reduction of grain sizes of materials down to the nanometre scale improves their functional properties that significantly distinguishes this materials from conventional coarse-grained polycrystalline materials which have grains of several micrometers in size **[30–33]**.

Materials with nanometre-scale microstructure where the atomic arrangement, crystallographic orientation, chemical composition, and the size of grains vary on a length scale of a few nanometres throughout the bulk are known as nanocrystalline materials **[34,35]**. The very fine size of grains of nanocrystalline materials is known to have outstanding effect on their mechanical properties. It is also reason for reduced density, lower diffusivity, higher electrical resistivity, increased specific heat, higher thermal expansion coefficient, lower thermal conductivity and specific magnetic properties of nanocrystalline materials in comparison with traditional coarse grained materials **[36]**.

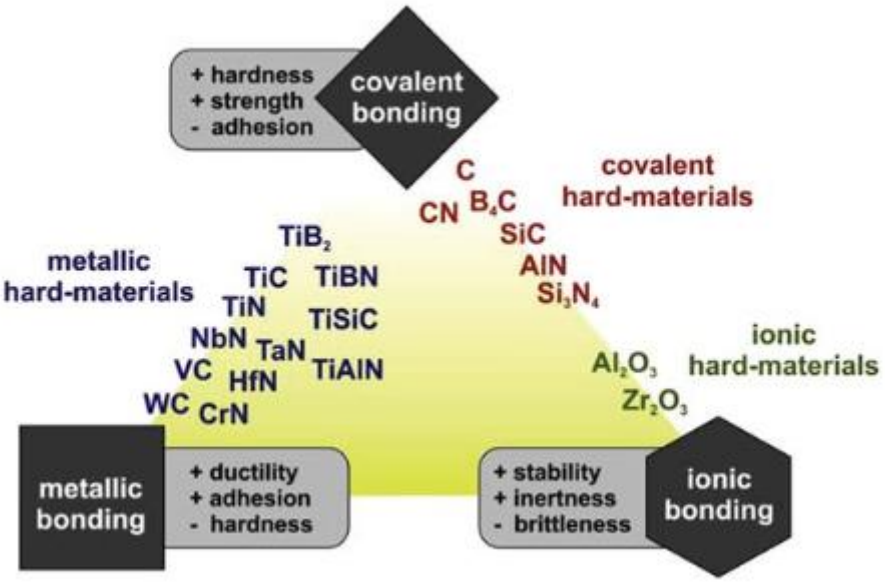

Figure 1.1. Classification of hard materials according to their chemical bonding and the corresponding change in properties **[26]**.

The design of protective coatings by applying nanocomposite approach when a material composed of at least two separated phases with nanocrystalline and/or amorphous structure or their combination represents a novel way for improvement of functional properties of the coatings **[37]**. The main feature of these nanocomposites is an enhanced hardness. It was found that there are at least four types of nanostructures that result in the enhanced hardness of nanocomposite coatings **[27]** (Fig. 1.2): (a)

bilayers of different phases with nanosize period $\lambda=h_1+h_2$ (here h_1 and h_2 is the thickness of first and second layer of bilayer, respectively), (b) the columnar nanostructure composed of the grains assembled in nanocolumns (there is insufficient amount of the second (tissue) phase to cover all grains), (c) a dense globular nanostructure composed of nanograins fully surrounded by very thin (~1 to 2 ML) amorphous tissue phase, (d) the mixture of nanograins with different crystallographic orientations or different phases.

The nanostructure of every individual material forms under different conditions using either a sequential deposition of individual layers in the nanosized bilayers or in transition regions where the coating structure changes from crystalline to amorphous. There are three groups of transition regions: (1) transition from the crystalline phase to the amorphous, (2) transition between two crystalline phases of different materials and (3) transition between two crystallographic orientations of grains of the same material (Fig. 1.3).

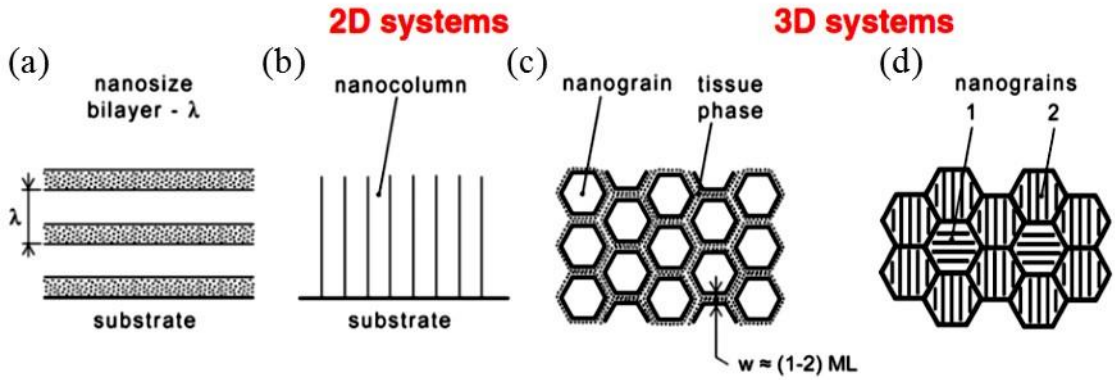

Figure 1.2. Schematic illustration of four nanostructures of the nanocomposite coating with enhanced hardness: (a) nanosize bilayers, (b) columnar nanostructure, (c) nanograins surrounded by a tissue phase and (d) mixture of nanograins with different crystallographic orientation **[27]**.

The transition from a crystalline phase to an amorphous occurs in the case when the second element B added to the AN compound forms the amorphous phase B_xN_y in the $A_{1-x}B_xN$ film. The $A_{1-x}B_xN$ films with a preferred crystallographic orientation of grains mostly form when the concentration of B ≈ B1 in the crystalline region in the front of the transition from the crystalline region to the amorphous phase. These films have mostly a columnar microstructure and the columns perpendicular to the film/substrate interface are composed of small grains oriented in one crystallographic direction **[37]**.

The films composed of grains mixture with two preferred crystallographic orientations or two crystalline phases $A(B)N_x$ and $B(A)N_y$ (Fig. 1.3b and Fig.1.3c, respectively) are another microstructures which commonly demonstrate enhanced hardness. The transition region between two preferred crystallographic orientations of grains (Fig.1.3b) usually exhibit X-ray amorphous structure (characterized by no X-ray reflection on XRD spectrum). This is the main difference between the structure of the nanocomposites based on the transition region between two preferred crystallographic orientations of grains or two crystalline phases and that of the nanocomposite films produced inside the transition from crystalline to amorphous phase.

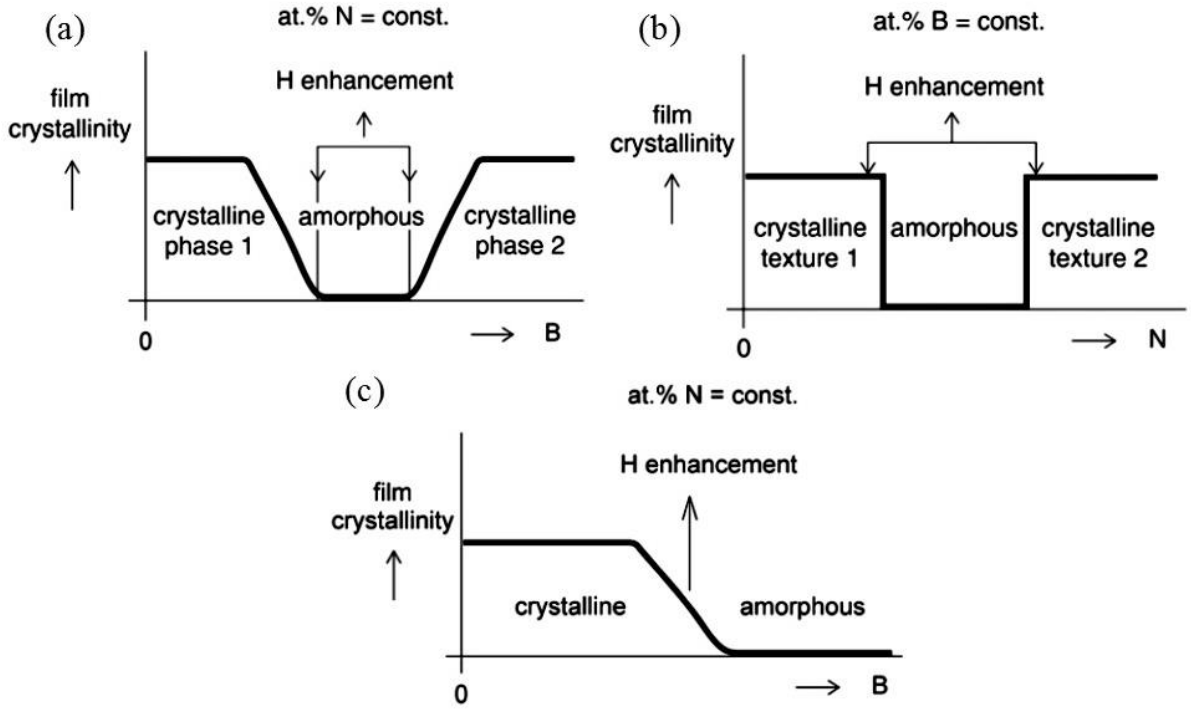

Figure 1.3. Schematic illustration of three transition regions of $A_{1-x}B_xN$ compounds. (a) Transition region from crystalline to amorphous phase and (b) transition between grains of the same material with two different preferred crystallographic orientations and (c) transition between crystalline phases of two different materials **[37,38]**.

While the concentration of B element increases in the $A_{1-x}B_xN$ compound the amount of amorphous phase B_xN_y also increases. Subsequently, this lead to the converting of the nanocomposite columnar microstructure (Fig. 1.4a) into an $A_{1-x}B_xN$ nanocomposite in which every $A_{1-x}N_{1-y}$ nanograin is covered by a thin (~1-2 ML) tissue of amorphous B_xN_y phase (Fig. 1.4b). A further increase of B element and therefore of the content of a-B_xN_y phase results in the increase of the separation distance between the nanograins.

Moreover, the number of the nanograins decreases with the formation of a nanocomposite with the nanograins embedded in the amorphous B_xN_y matrix (Fig. 1.4c). The even higher content of B element stimulates formation of a pure amorphous BN-based phase (Fig. 1.4d).

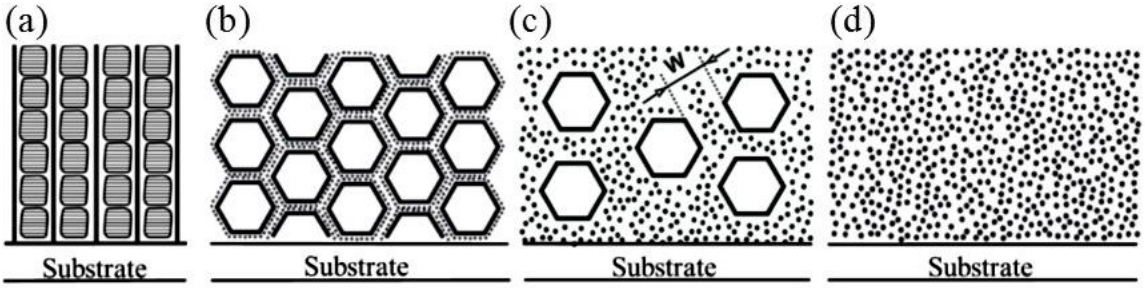

Figure 1.4. Schematic illustration of the development of microstructure of nanocomposite films produced in the transition from crystalline to amorphous phase with increasing amount of B element in $A_{1-x}B_xN$ film **[37]**.

From the Fig. 1.3 is seen that to every transition region corresponds an optimal elemental composition at which nanocrystalline/amorphous or nanocrystalline/nanocrystalline nanocomposite coatings can be formed. The addition of one or more selected elements into the base material is a very effective way to tailor the microstructure of materials and as a result to produce nanocomposite coatings with enhanced functional properties **[39–41]**. Thus, a variety of boride, nitride, carbide, or oxide (and their combinations) materials forming nanocomposite structure with ceramic, metal, or carbon amorphous matrix with a desirable set of physical and chemical properties for structural applications have been developed **[17,42,43]**.

Nanocomposite coatings composed of structural elements with a characteristic size of a few nanometres are related to thermodynamically non-equilibrium materials. These materials are inherently heterogeneous on a nanometre scale consisting of nanometre-sized building blocks separated by boundary regions. The various types of nanocomposite coatings differ by the characteristic features of their building blocks (e.g. different or identical chemical composition of crystallites, atomic structure, shape, size, etc.).

Despite the considerable research work carried out in the field of TM nitride-based nanocrystalline nanocomposites, almost no studies are directed to nitride-based amorphous nanocomposite thin films **[44–46]**. Yet, they are potentially attractive due to the lack of long range order, that is characteristic for crystalline materials, and the homogeneous structure composed of different kinds of bonds and their density states. The combination of TM nitrides (Ti, Zr, Hf, V, Nb, Ta, or Cr) with metalloids (Si, C, B, O) which can form

diversity of bond combinations is a well-known route for the formation of nanocomposite amorphous coatings and thin films with an interesting group of functional properties. For example, nanocomposite amorphous nitride coatings demonstrate superior oxidation resistance, which was reported to be much more higher than that of nanocrystalline/amorphous nanocomposites **[27]**. The absence of grain boundaries reduces the diffusion of permeating molecules which occurs along them, minimizing chemical and physical interactions of the underlying material with environmental gas molecules. Additionally, from a practical point of view, amorphous coatings, in general, allow more scalable and less stringent deposition processes to be implemented **[27,45]**. Moreover, when their chemical bonds are saturated, their high covalence provides a resistance to corrosion **[47]**.

It is commonly known that it is impossible to combine a set of enhanced properties, such as high hardness and wear resistance, low coefficient of friction, high temperature stability and high oxidation and corrosion resistance, only by using a particular coating structure and its element composition. Therefore, the structure of a protective coating and its composition must be chosen depending on the specific application it will be used in. In spite of a variety of coatings with high hardness, the choice of possible candidates which would meet the most of the requirements is extremely limited **[48]**. Consequently, coatings must be tailored to a defined range of applications, and therefore, currently there are no "universal" protective coating. Nowadays, a huge effort is devoted by many researchers to synthesize multifunctional coatings with exceptional protective properties through new unique structures for operation under wide range of conditions **[49–51]**.

The outlined above nanocomposite coatings are mostly developed based on the approach of traditional reductionism. This approach based on the development of one or two properties (e.g. hardness and wear resistance) for a protective coating while other properties are neglected that considerably restricts their application. Following this approach, the coating is considered as a completely artificial system that has to sustain the specific external impact with minimal changes by limited number of advanced properties. Nevertheless, a variety of characteristics are needed to maintain good performance in a wide range of environments, temperatures, and contact loads. This could be realized by applying the second approach, which is based on the concept that both natural and synthetic processes should be considered during performance of protective coatings. The most promising approach to the design of protective coatings, which is based on an integrative concept of emergence, is smart nanocomposite coatings. This approach refers to creation of novel structures and properties during self-organization in complex systems.

This integrative approach where characteristics of the system are combined as a whole would be a new strategy in nanostructured materials design to achieve multifunctionality and adaptive behaviour. The objective of smart nanocomposite coating design is to provide a reversible self-adjustment of surface chemistry, structure, and mechanical behaviour depending on applied loads and operational environment to maintain protective properties. In some publications, an analogy with the protective skin of a chameleon was used to highlight the intention of a reversible surface adaptation to follow environment changes or temperature cycles **[52–55]**.

The whole family of smart nanocomposite coatings according to G. Fox-Rabinovich **[55]** can be divided into three main groups:

- Adaptive nanocomposite coatings which change their structure and properties in response to various operational conditions. This adaptation mostly achieved by combination of different compounds such as hard phases and/or lubricating compounds in coating structure;
- Smart coating based on functionally graded systems. These coatings can change its properties depending on the stages of wear process due to the variation in composition and structure gradually over the volume;
- Adaptive coatings that characterized by the formation of surface tribo-film as a result of the engineered surface dynamic response to the environmental impact thus leading to changes in their structure and properties.

The difference in the design of these coatings is that in the first two groups adaptive behaviour is provided in the initial design of the coating while in the third group, the adaptability dynamically develops during operation of the coating.

In order to achieve reversible adaptation, two design concepts were suggested by A. Voevodin **[52]** to the outlined above concept of nanocomposite coatings:

- In order to minimize reduction in composite hardness and elastic modulus, solid lubricant (they are typically very soft) reservoirs need to be introduced to the protective coating in form of amorphous of quasi-crystalline inclusions;
- Sufficient conditions for the generation of a lubricious transfer film or “skin” with the required chemistry and structure for reduction of friction at the tribological contact must be created by friction forces and surface reactions with the environment.

The main mechanisms responsible for adaptive behaviour of the coatings include, but is not limited to, metal diffusion and formation of lubricant phases at worn surfaces, thermally- and mechanically-induced phase transitions in solids, contact surface tribo-

chemical evolutions to form phases with low melting point, the formation of easy to shear solid oxides, and others **[56,57]**.

1.2 Functional properties of protective coatings and thin films

Protective coatings are subjected to severe operation conditions during exploitation, such as high temperature, plastic deformation, severe friction and high local stresses. Therefore, a powerful protective coating must meet a set of mandatory demands as dedicated by individual applications, including good toughness, excellent wear resistance, and high elastic strain prior to plastic deformation (H/E^*), high resistance to plastic deformation (H^3/E^{*2}), thermal and chemical stability, oxidation resistance and corrosion resistance. An adequate material selection in combination with intelligent microstructural design is obligatory for protective coatings with mentioned above multiple functionalities **[58]**. In this regard, multielement nanostructured coatings are becoming the materials which can meet the outlined set of demands. Being composed of mixtures of various phases, metastable solid solutions, or composite structures with nanometre dimensions and due to the complementarity of individual components, they can demonstrate new unique functional properties.

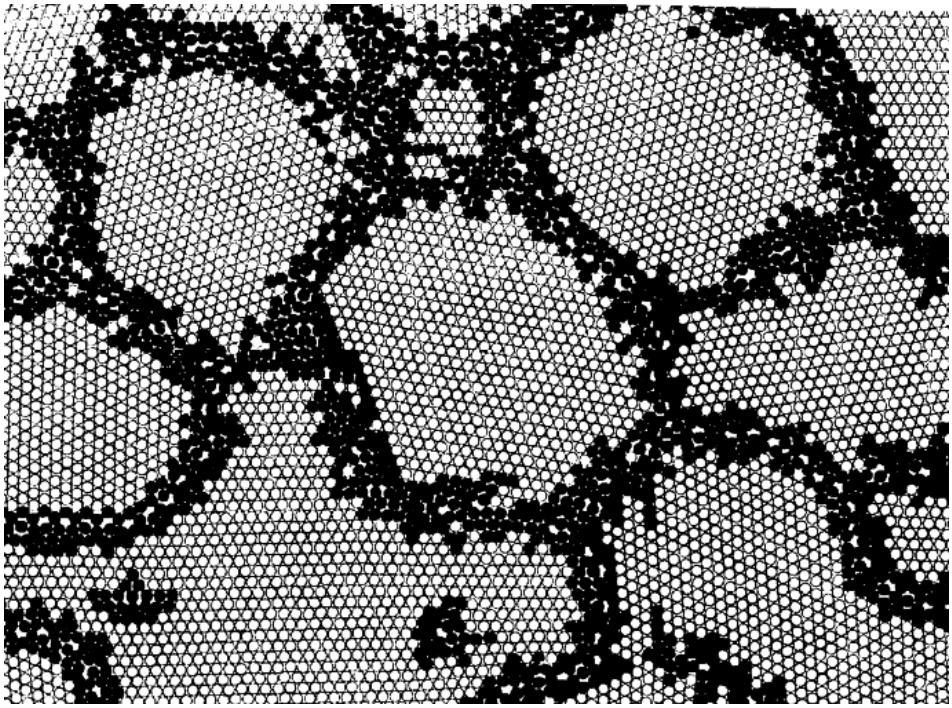

Figure 1.5. Two-dimensional model of a typical nanostructured material. Crystal atoms corresponding to the lattice represented by open circles and atoms in boundary regions with variety of interatomic spacing (dark circles)**[59]**.

It is well known that the key factor which determines functional properties of materials is their microstructure and element composition. The properties of nanostructured materials are mostly defined by the chemical composition and the distribution of nanometer-sized (below 100 nm) building blocks (nanograins) in one-, two-, or three- dimensions (Fig. 1.5) **[59]**. The reduction of grain size of nanocrystalline materials, down to certain physical point, is known to have an outstanding effect on mechanical behaviour, density, diffusivity, electrical resistivity, specific heat, thermal expansion coefficient, thermal conductivity, and specific magnetic properties of the materials **[31,60,61]**. The atomic structure of nanocrystalline materials (e.g. the average atomic density, the nearest-neighbor coordination etc.) undergo considerable changes at the misfit between adjacent nanocrystalls in relation to the perfect crystal. The nanocrystalline structure consists of two types of atoms: crystal atoms with neighbour configuration corresponding to the lattice and boundary atoms with a variety of interatomic spacing. The fraction of the atoms at the grain boundaries increases together with deviation of the coordination between nearest neighbour atoms as the grain size is decreased (Fig. 1.6).

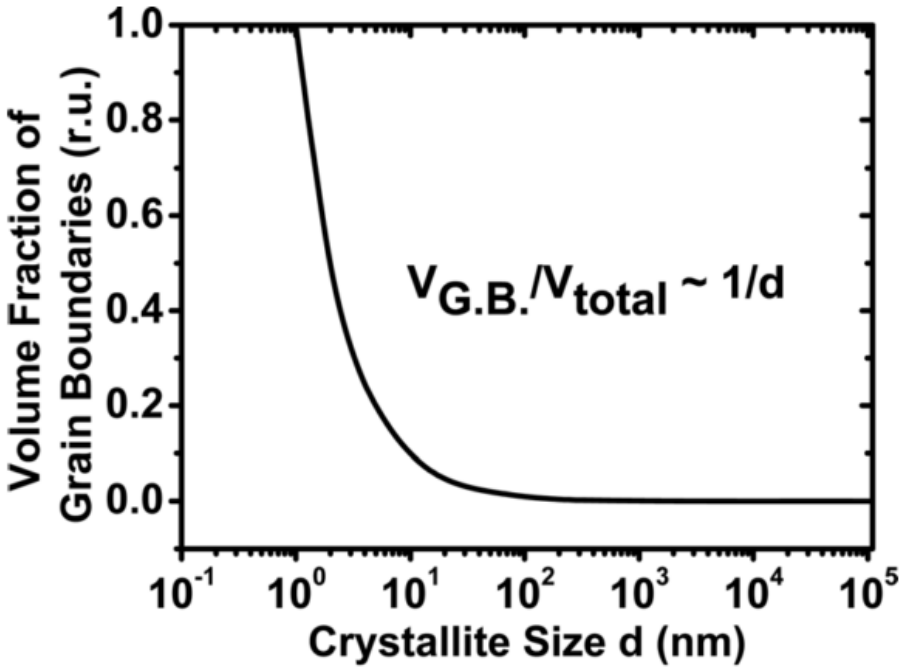

Figure 1.6. Dependence of the volume fraction of the material within the grain boundaries on crystallite size (notice that the actual volume fraction will depend on the thickness of the grain boundaries) [62].

The volume fraction of interfaces in the nanocrystalline materials may be estimated as $3\Delta/d$ (where Δ is the average interface thickness and d is the average grain diameter).

Thus, depending on the shape of the grains (spheres or cubes), the volume fraction of interfaces is about 30 % for 10 nm grains and increases up to 50 % for 5 nm grains, and, correspondingly, a contribution of atoms in the grain boundaries in a small volume region to the material properties becomes enormous. Consequently, the unique properties of nanocrystalline materials are strongly influenced by the atomic structure, thickness, and chemical composition of incoherent or coherent interfaces where the individual nanograins are joined together **[63]**.

The combination of grains with different chemical composition, different or identical atomic structure together with the diversity of their shapes and sizes as well as the nature and morphology of grain boundaries and interfaces are equally decisive for the extraordinary properties of nanocrystalline materials.

1.2.1 Hardness

Obviously, of special importance from both fundamental and applied viewpoint are mechanical and tribological properties of protective coatings. In most applications, a protective coating is exposed to external loads, and the eventual failure of its structure can take place at certain point of a load through the mechanism of the creation, multiplication and movement of dislocations. The development of defects such as dislocations, twinning, micro cracks upon plastic deformation in an ordinary perfect crystal limit its real strength and hardness. A measure describing the resistance of a material against plastic deformation is it hardness. Moreover, a protective material must demonstrate the resistance against crack nucleation and propagation, i.e. high toughness. The strengthening of a protective material can be realized by introducing special obstacles which impede the plastic deformation by a hindering of dislocation multiplication and motion. These obstacles can be created by the formation of a multiphase nanocrystalline structure, and therefore, the enhancement of the hardness and toughness of a protective material can be achieved **[64]**.

In general, the enhanced mechanical properties of nanocomposite coatings may originate from two basic hardening mechanisms: intrinsic hardening and extrinsic hardening. The intrinsic hardening depends on the response of well-localized atomic bonds to shear **[65,66]**. Whereas the extrinsic hardening comes from microstructure of a material and includes solid solution hardening, precipitate hardening, grain boundary hardening, compressive stress hardening and work hardening.

The enhanced mechanical properties of nanocrystalline materials is explained mainly by Hall-Petch effect. Since the slip systems for dislocation are different for the neighbouring grains, dislocations are hindered to cross from one grain to another **[67]**.

Also, the dislocations movement is impeded because the grain boundary is much more disordered than inside the grain. To overcome these obstacles, a dislocation requires more energy to change the direction of movement and to penetrate into the neighbouring grain. As a consequence, dislocation "pile up" occurs at the grain boundary. The repulsive stress fields generated by dislocations will apply a repulsive force to the dislocation incident with the grain boundary that causes the dislocation diffusion across the grain boundary. These reduce the energetic barrier for the dislocation diffusion across the grain boundary allowing deformation in the material. A critical shear stress τ_c to move a dislocation in adjacent grains with different slip systems can be calculated by

$$\tau_c = \tau_0 + \sqrt{\frac{k'}{d_c}}, \qquad (1.1)$$

where τ_0 is the shear stress to move a dislocation through single crystalline material, k' is the constant, d_c – grain size **[68]**. It is clearly seen, that the amount of pile ups at the grain boundary decreases with decreasing grain size, increasing the amount of applied stress necessary to move a dislocation across the grain boundary, and thus, the hardness of the material increases.

Fig. 1.7 shows schematically the dependence of the hardness as a function of grain size of coating material **[27]**. It is seen that deformation of microcrystalline materials driven by the intragranular processes in accordance with Hall-Petch law.

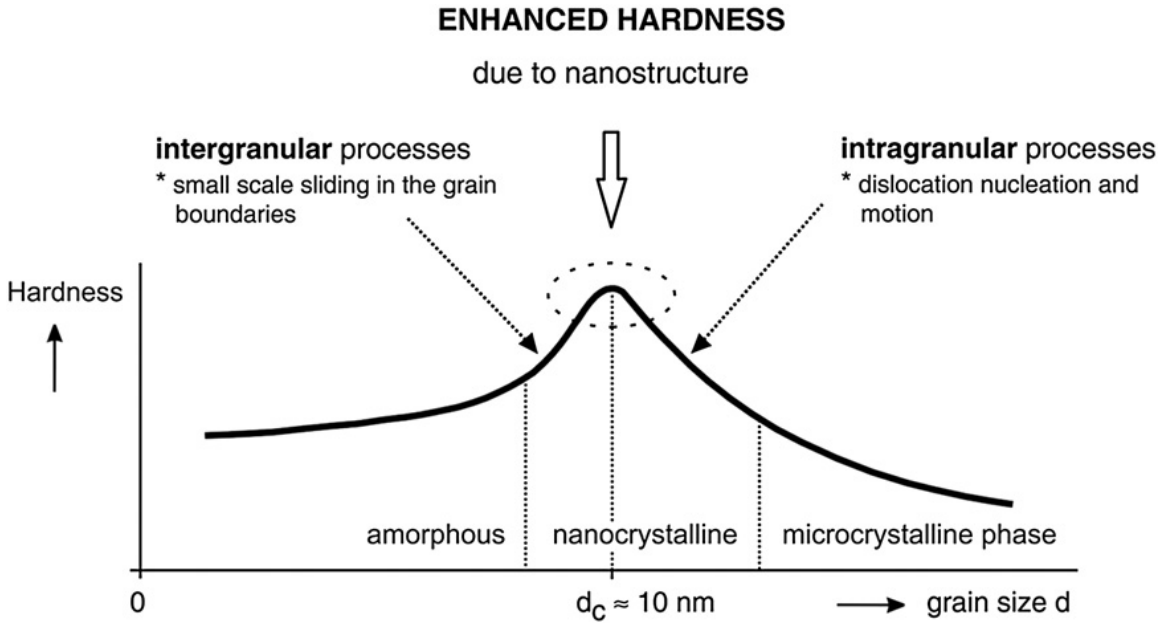

Figure 1.7. Schematic dependence of the hardness as a function of the grain size d of coating material **[37]**.

With reduction of grain size down to less than 10 nm, the intergranular processes, such as the interactions between atoms of neighbouring grains and/or the small scale sliding in grain boundaries, start to dominate and the dislocation activity is effectively prevented by the grain boundaries whose volume fraction increases with reduction of grain size (Fig. 1.6). After reaching a critical value of the grain size d_c, a maximum value of hardness H of the coating is achieved. This region corresponds to a continuous transition from the intragranular processes to the intergranular processes. Below d_c a softening effect is typically observed because the Hall-Petch relationship break down at this point due to a large amount of defects at the grain boundaries, so pile up of the dislocations against grain boundaries would not occur and small-scale boundary sliding becomes dominating deformation mechanism **[69]**.

The hardness of nanocomposite coatings is related to specific deformation mechanisms operating in nanocrystalline materials having grain sizes less than critical value. Since the volume fraction of grain boundaries becomes dominant at nanoscale, deformation behavior controlled by active roles of grain boundaries dominate, and involves the following deformation mechanisms:

- lattice dislocation slip;
- grain boundary sliding;
- grain boundary diffusional creep;
- triple junction diffusional creep;
- rotational deformation occurring via movement of grain boundary dislocations;
- twin deformation conducted by partial dislocations emitted from grain boundaries.

The hardness can be enhanced even more in two-phase nanocomposite coatings, which can be explained by the following inequality:

$$H_n > \left(1/V_n\right)\left(H_1V_1 + H_2V_2\right) \tag{1.2}$$

where H_1, H_2 and V_1, V_2 are the hardness and the volume fraction of the first and second phase, respectively, V_n is the total volume of the nanocomposite coating. So that the hardness of nanocomposite coating can be more than two times greater than that of the hardest component **[33]**.

Thus, the new concept of microstructural design, where a combination of different phases with complex boundary interfaces of nanosized grains provides the enhanced hardness, can be used for producing of protective coatings with the superior mechanical properties.

1.2.2 Elastic recovery, H/E^* and H^2/E^{*3} ratio

The relative motion of contacting surfaces in tribological processes are considerably influenced by a normal load and tangential load. This results in the wear of a material from contacting solid surfaces. The most important material parameters controlling the tribological behaviour of materials are the elastic modulus (describing elastic deformation), the strength (describing plastic deformation), and the toughness and fracture toughness (describing fracture behaviour) **[70]**. Over the years, hardness has been regarded as the prime property which defines wear resistance of a material. It was revealed that the hard protective materials are often very brittle that limits their practical utilization. For the practical engineering applications of protective coatings, their hardness should be accompanied by toughness. According to the definition, toughness is the ability of a material to absorb energy during deformation up to fracture, while fracture toughness is the ability of a material to resist the growth of a preexisting crack. Therefore, toughness encompasses the energy required for the crack creation and further propagation until fracture, whereas fracture toughness accounts the energy required to facilitate the crack propagation to fracture **[71]**. There have been some theoretical and experimental studies **[3,72–74]** suggesting that the elastic strain to failure, which is related to the ratio of hardness and elastic modulus (*H/E*), can be a more suitable parameter for the prediction of a material ability to resist mechanical degradation and failure during wear. It has been imperative for many years to achieve ultra-high hardness of protective coatings, however, coating elasticity and toughness are equally important factors, particularly in abrasion, impact, and erosive wear.

A. Leyland and A. Mattews **[72]** have suggested that fracture toughness (i.e. resistance to crack propagation, leading to failure) can be described by the following equation:

$$G_c = \sigma_c^2 \frac{\pi a}{E}, \tag{1.3}$$

where σ_c^2 – the critical stress for fast fracture, a – the critical crack size, E – the elastic modulus. Thus, fracture toughness would appear to be improved by optimizing both a high critical stress for fast fracture (which implies a need for a sufficiently high hardness) and a relatively low elastic modulus. Since a purely elastic contact (low E) is desirable for wear reduction in tribologycal processes, a high H/E ratio, which is related to a high elastic strain prior to plastic deformation, is preferred for better wear performance of protective coatings.

If the system protective coating/substrate deforms under the load, the coating needs to be simultaneously hard and flexible, and additionally must exhibit an enhanced resistance to cracking during the substrate bending and without failure by debonding. J. Musil has recently proposed the general rules enabling to design flexible hard nanocomposite coatings **[39,75]**:

1. The low effective Young's modulus E^* resulting in a high $H/E^* \geq 0.1$ ratio and the high elastic recovery $W_e \geq 60\%$.
2. The dense and voids-free microstructure.
3. The compressive macrostress ($\sigma<0$).

E^* is related to E and the Poisson's ratio ν by $E^* = E/(1-\nu^2)$.

The yield pressure (i.e. resistance to plastic deformation) P_y in a rigid-ball on elastic/plastic plate contact can be determined by the equation **[76]**:

$$P_y = 0.78 r^2 \left(\frac{H^3}{E^2} \right) \tag{1.4}$$

where r is the contacting sphere radius.This equation shows that the contact loads needed to induce plastic deformation are higher in materials with larger values of the H^3/E^{*2} ratio, i.e., the H^3/E^{*2} ratio should be a sufficient indicator of a coating's resistance to plastic deformation. Therefore, the likelihood of plastic deformation will be low in materials with high hardness and low elastic modulus.

Experiments indicate **[72,74]** that the higher is the toughness of the system coating/substrate as the higher is the H^3/E^{*2} ratio (resistance to plastic deformation). It means that the H^3/E^{*2} ratio is proportional to the elastic deformation of the coating. It is shown **[74]** that the resistance of coating to the formation of cracks increases with increasing ratio H^3/E^{*2} ratio, i.e. with increasing resistance of the coating to plastic deformation. Therefore, the ratio H^3/E^{*2}, should be maximized to improve the coating elastic recovery W_e and its toughness. It means that instead of the coating toughness, the ratio H^3/E^{*2} should be used to assess the protective efficiency of the thin film exposed to the external load.

It is evident from all the above arguments, that high hardness is not necessarily the prime requirement for protective coatings, while for many applications the toughness and the elasticity are more important. Therefore, it is important to develop the flexible protective coatings which are simultaneously hard, tough and resistant to cracking. This class of protective coatings exhibiting novel combinations of properties can be produced and optimized by the careful selection of structural and compositional constituents of multicomponent nanostructured coatings.

1.2.3 Wear resistance and friction

There is an increasing demand to reduce or control wear on engineering surfaces and machining tools in most industrial applications **[20,77]**. The decrease of wear allows to prolongate the lifetime of tools, and thereby to save energy and recourses **[4,78]**.

Both friction and wear are simultaneously the results of the same tribological process that takes place between two moving surfaces. The interrelation between friction and wear is not well understood. Commonly, the low friction corresponds to low wear and vice versa, however, there are several exceptions of contradictory behaviour.

Friction is the resistance to motion during sliding when one solid body moves tangentially over another remaining in contact. The resistive tangential force acting in a direction directly opposite to the direction of motion is called the friction force. Friction can be described by a dimensionless scalar parameter called the coefficient of friction, which defined as the ratio of tangential friction force to the normal load force:

$$\mu = \frac{F_t}{F_n}, \tag{1.5}$$

where F_t is the tangential force, and F_n is the applied normal force.

According to Bowden and Tabor's theory of friction **[79]**, friction is based on two independent components, namely, adhesive component (μ_a) and plowing component (μ_p):

$$\mu = \mu_a + \mu_p, \tag{1.6}$$

where μ_a defined by the material pair, lubrication and the real area of contact, while μ_p depends on the degree of plastic deformation taking place at the asperity level **[80]**.

During sliding of solid bodies agains each other, most of energy input is generally used up in plastic deformation which directly converted to heat in the material close to the interface **[81]**. The contact temperature that generated at the tip of asperities of both the sliding surfaces, so called "flash temperature", is given as **[82]**:

$$T_f = T_b + \frac{\mu \vartheta r}{2K_e}\left(\frac{H_0 F}{NA_n}\right)^{\frac{1}{2}} \tag{1.7}$$

where T_b is the bulk temperature during sliding, μ is the friction coefficient, ϑ is the sliding velocity, r is the radius of the contacting area, K_e is the equivalent thermal conductivity, H_0 is the hardness of the oxide scale, F is the applied load, N is the total number of the

asperities, A_n is the nominal area of the contact. The heat thus generated is conducted into the bulk, T_b, and is given by **[82]**:

$$T_b = T_0 + \frac{\alpha \mu F \vartheta l_b}{A_n K_n} \tag{1.8}$$

where T_0 is the room temperature, α is the heat distribution coefficient, l_b is the mean heat diffusion distance, K_n is the thermal conductivity of a material. It is evident from the equation (1.7) and (1.8) that for a given tribologycal condition, the bulk temperature and the flash temperature depend on friction coefficient, i.e. the increment of coefficient of friction cause the increment of these remperatures. Flash temperatures are much higher than the bulk temperature. The interface temperature plays an imporatant role in the tribologycal performance of a material. Thus its rise can cause microstructural changes and tribo-chemical reactions, which in turn induce the changes in the operatin wear mechanisms and wear transitions **[81]**. The increment of the flash temperature above some limit can induce change of the wear mechanism from plasticity-dominated wear to mild oxidation wear, whereas a relatively high bulk temperature can cause a degradation of the hardness of a material leading to increased wear rate in plasticity dominated wear. Therefore, it is vitally important to reduce the friction coefficient of protective coatings.

The coefficient of friction for an elastic sphere sliding on a hard plate with a soft coating can be expressed by the equation **[70]**:

$$\mu = \frac{\pi S}{w^{1/3}} \left(\frac{3R}{4E'} \right)^{2/3} \tag{1.9}$$

where S is the shear strength of the coating, w the normal load, R the radius of the sphere and $E`$ the reduced modulus of elasticity of the contact materials. It is clear that there are two ways for achieving low friction: the coating must possess the property of low shear strength and it must be applied onto surfaces of high hardness or high elastic modulus. The most common way of reducing friction and wear is to introduce a lubricant between the two moving surfaces, which promotes the development of a surface with low resistance to shearing during sliding.

Wear is the surface damage or progressive loss of material from one or both of two solid surfaces in a sliding, rolling, or impact motion relative to one another brought about by mechanical action **[81]**. The wear process is very complex phenomenon, which depends on materials, contact conditions and evironmetal parameters in a number of different combinations. Therefore, it has not been possible to formulate a universal equation of wear. However, the common feature for the different wear modes is that the worn volume

is directly proportional to the normal load and the distance of movement and inversely proportional to the hardness of the material. This relationship was introduced by Archard **[83]**:

$$V = K' \frac{w \cdot s}{H}, \tag{1.10}$$

where V is the worn volume, w is the normal load, s is the distance moved, H is the hardness and $K`$ is a constant, frequently called coefficient of wear. However, there are several examples oftribological contacts where this relationship is invalid.

The main tribological contact conditions taking place between two moving surfaces are sliding, abrasion, fatigue, impact, fretting, chemical dissolution and corrosion. Usually, in a real contact more than one condition is acting at the same time and results in a specific type of wear at different scale levels. It was identified **[84]** that the elastic modulus, shear strength and fracture toughness are the key mechanical properties of contacting materials by which the wear velocity differences can be accommodated. Since, the nanocomposite coating approach provides an effective way for tailoring of mentioned above mechanical properties independently, and over a wide range of values, through the control of the grain size as well as a proper selection of the constituting phases, it allows to control and optimize the wear and friction phenomena in typical engineering applications.

The chemical reactions taking place at the surfaces during sliding contact have a considerable influence on both friction and wear because the outermost surface layer undergoes structural and chemical changes that, in turn, promote changes of tribologivcal behaviour of the surface **[85]**. Contact surface tribo-chemical evolutions and high temperature in tribo-contact, which can be over 1000 °C, can cause thermally- and mechanically-induced phase transformations with formation at worn surfaces of easy to shear solid phases which act as a lubricant and provide ultra-low friction and superior wear resistance over broad operating temperatures, environments, and contact loads **[56]**. These mechanisms can be realized by means of nanocomposite coatings whose structural design and element composition allow a controlled supply of lubricious elements leading to self-adaptation of surface structure and chemistry during operation **[53,86]**.

The advanced microstructural design of multielement nanocomposite coatings with combined functional properties hold the potential to fulfil any desired operating requirements, and this will lead to the adoption of these multifunctional materials in an increasingly diverse range of demanding applications.

1.2.4 Thermal stability and oxidation resistance

The process of machining of metals and alloys is commonly accompanied by the increacement of the temperature at the cutting edge up to 1000 °C. In this regard, thermal stability of coating materials is a key parameter to ensure the efficient operation and long lifetime of a metal cutting tool insert during machining, while a low thermal stability of protective coatings strongly limits their industrial utilization. Therefore, it is required to produce thermally stable films that keep their functional properties constant up to temperatures, which are higher than the service temperature in a given application. Moreover, oxidation is one of the most commonly proceeding reaction at elevated temperatures in many applications which considerably decreases thermal stability of the protective material and leads to a loss of adherence and a rapid degradation of the tribological effectiveness of the protective coating at elevated temperatures. Even segregation of small amount of oxygen at the grain boundaries and interphase interfaces can drastically change the response of the material to the loading and can eventually lead to brittle failure **[87]**.

High-temperature oxidation resistance and high thermal stability of protective nanocomposite coatings strongly depend on the structure, phase composition and thermal stability of individual phases of which the coating is composed. Nanostructured nanocomposite coatings due to their metastable state start to crystallize if the operation temperature achieves or exceeds the crystallization temperature T_{cr} of the coating material. The grain growth, phase transformations and temperature-induced variations of the atomic structure affect the coating nanostructure and results in the formation of new crystalline phases **[88]**. These lead to a destruction of nanostructure with converting to the conventional crystalline material. These are the main reasons of losing of unique properties of nanocomposite coating at elevated temperatures. Moreover, the grain boundaries in polycrystalline materials provide fast diffusion paths for oxygen that allows connecting of an oxidation atmosphere with the substrate and, thus, decreases oxidation resistance of the protective coating at high temperatures (Fig. 1.8a). The thermal stability of the nanocomposite coatings so far produced is lower than 1000 °C **[89,90]**, that is not sufficient for their utilization in some applications, and therefore, they are required to be temperature stable and oxidation resistant up to 2000 °C.

Recent research have shown that the doping of the nanocomposite coating with suitable elements can shift the onset of the phase transformation to higher temperatures **[91]**. The improvement of the oxidation resistance was achieved by impurity segregation at the grain boundaries during oxidation of the nanocomposite coating that blocks grain

boundary out-diffusion of metal and in-diffusion of oxygen ions **[92]**. Additionally, oxidation resistance of the coating material can be improved by alloying elements which, when the coating exposed to oxidizing environment at elevated temperatures, form dense oxide scale with low ion mobility and thereby acts as an effective oxygen diffusion barrier **[93,94]**.

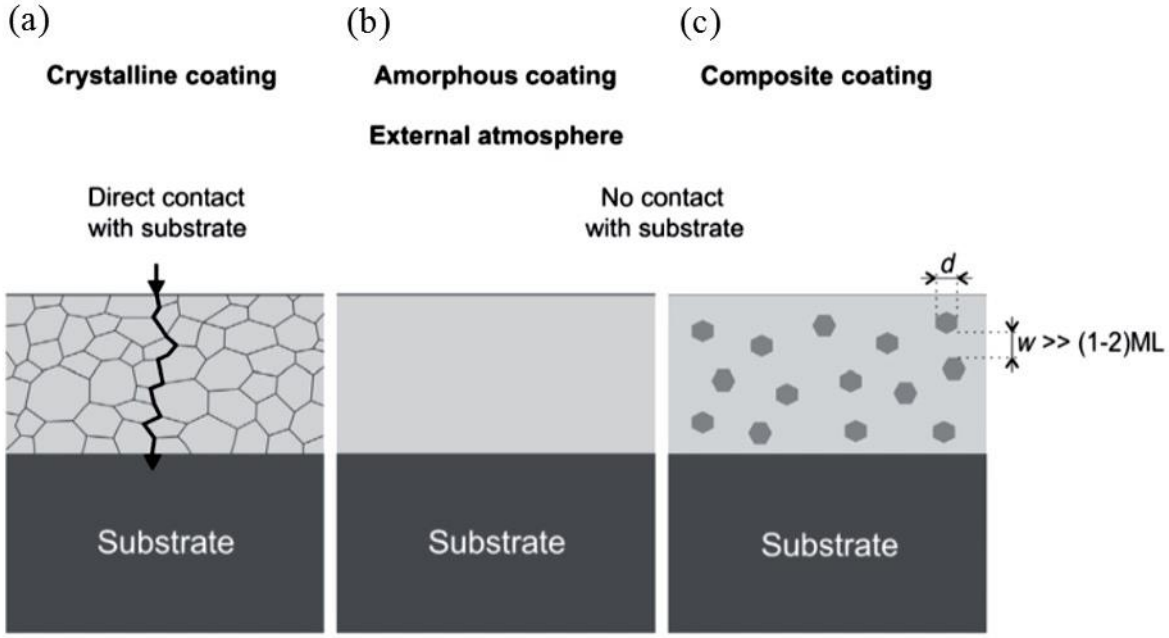

Figure 1.8. Principle of substrate protection against oxidation from the external atmosphere by means of the coating with crystalline structure (a), the coating with amorphous structure (b) and the composite coating composed of well-separated grains in an amorphous matrix (c). d is the grain size, w is the distance between grains, ML denotes the monolayer **[27]**.

Recently, J. Musil has suggested an efficient way to increase the oxidation resistance of protective coatings at high temperatures $T > 1000$ °C by using amorphous nanocomposite coatings **[27,45,95,96]**. A direct connection of the external atmosphere with the substrate surface can be completely avoided only by means of protective coating with amorphous structure (Fig. 1.8b) and those in which well-separated grains are embedded in an amorphous matrix (Fig. 1.8c). In the absence of grains and grain boundaries, there is no direct contact of external atmosphere with the substrate through them like in the case of crystalline materials **[89]**.

The thermal stability and oxidation resistance of protective coatings with amorphous nanocomposite structure is determined by three main factors **[97]**:

- Thermal stability of individual phases from which the amorphous coating is composed;

- The elemental composition of the annealing atmosphere;
- Interdiffusion of substrate elements into the coating during thermal annealing, because diffused elements can decrease T_{cr} of the amorphous phase.

The protective coatings with amorphous nanocomposite structure investigated so far exhibit high hardness ranging from ~20 to 40 GPa and remain stable at temperatures considerably exceeding 1000 °C **[46,98–101]**. The improvement of the oxidation resistance of the amorphous nanocomposite coatings was reported due to the effective doping with B and Si which are able to delay phase transformation of the amorphous structure by inhibiting of the formation of unfavourable oxide phases **[99,102]**. Additionally, the elements of an amorphous coating can form barrier layer against oxygen diffusion at the coating surface at high temperatures in ambient air; at the same time this barrier layer can act as a lubricant layer improving tribological performance of the protective coating at elevated temperatures **[103]**.

It was shown that the crystallization of the protective coatings starts directly at the coating/substrate interface due to the diffusion of substrate elements into the coating layer **[104,105]**. The action of this factor can be avoided if a barrier interlayer is inserted between the substrate and the coating. In the present work, a sacrificial barrier layer is applyed between the substrate and the coating in order to investigate its applicability. The material of the sacrificial barrier can react with both, the elements of a coating and the substrate, which could lead to its adaptation and resistance to the interdiffusion at high annealing temperatures. In the approach presented in this thesis, the Oxygen-based multielement barrier layer was deposited in order to create a highly reactive layer, thanks to the high electronegativity of Oxygen and the amorphous material.

The achievement of the high thermal stability and oxidation resistance of protective coatings with amorphous structure is, however, a difficult problem and therefore not only new coating materials are need to be developed, but also it is vitally important to investigate in details the causes of structural changes in amorphous coatings during thermal annealing.

1.3 Methods for protective coatings and thin films synthesis

Protective thin films and coatings have been prepared by a variety of deposition techniques developed recently **[106]**. Microstructure and resulting film properties can

be controlled by the deposition process, so the optimum properties for each application may depend on the deposition process used **[60]**. Since, not all deposition technologies yield the same microstructures and associated properties, the deposition process must be chosen to fit the required properties and applications.

The main deposition techniques for thin films and coatings fabrication may be conventionally divided into two groups depending on principles of material synthesis – a technology based on a physical vapour deposition (PVD) and that based on a chemical vapour deposition (CVD) **[107,108]**.

1.3.1 Physical vapour deposition methods

Physical vapour deposition (PVD) is referred to deposition processes of thin films and nanostructures through the evaporation of solid precursors into their vapour phase by physical approaches followed by the condensation of the vapour phase on substrates. Every PVD process starts with physical transformation by evaporation, sputtering, or chemical vapours and gases of a target material (a material, which is intended to be a coating) from solid or liquid to vapour state. Then, a vapour is transported from the source to the substrate under line-of-sight thermal scattering, or molecular flow conditions (i.e. without collisions between atoms and molecules) due to vacuum conditions. At the final step, the condensation and nucleation of vapour atoms by a number of processes onto a substrate take place. PVD processes include the next methods which are most frequently used for synthesis of thin films and coatings **[106]**:

- Thermal evaporation;
- Electron beam evaporation;
- Magnetron sputtering;
- Cathodic arc deposition;
- Ion platting;
- Pulsed laser deposition.
- Molecular beam epitaxy.

Among the available PVD techniques, the two most frequently used for the deposition of different coating and thin film systems suitable for industrial-scale applications are magnetron sputtering and cathodic arc evaporation **[109–111]**. In all these PVD processes, ion bombardment of the growing film is the most important parameter which is used to modify and control the structure and properties of the growing film **[112–114]**.

1.3.1.1 Magnetron sputtering

Magnetron sputtering based on the mechanism of physical sputtering process. In general, the physical sputtering process involves the physical vaporization of atoms from a target surface by momentum transfer from bombarding energetic atomic-sized particles. It is a statistical process that occurs as a result of a collisional cascade process initiated near the target surface by incident energetic projectile particles such us ions of a gaseous material.

The basic sputtering process can be realized in the following way. After a DC voltage is applied between the cathode and anode in a vacuum system that is filled with a homogenous gas (reactive or/and non-reactive), a glow discharge is formed after breakdown at certain voltage by ionization of the working gas. The positively charged ions of a glow discharge plasma bombard the negatively biased cathode (target). The bombardment process causes the removal of target atoms by momentum transfer, which may than condense on a substrate and form a thin film. Secondary electrons, reflected ions and neutrals, and photons are also emitted from the target surface as a result of ion bombardment. These electrons play an important role in maintaining the plasma by ionization of the working gas atoms, which in turn bombard the target and release more secondary electrons in an avalanche process. Some of the sputtered target atoms will be ionized travelling through the plasma and hitting both the vacuum chamber and the substrate holder. Many different materials have been deposited using the basic sputtering process. However, the process is limited by low deposition rates, low ionization efficiencies in the plasma, and high substrate heating effects. These limitations have been overcome by applying a magnetron (Fig.1.9).

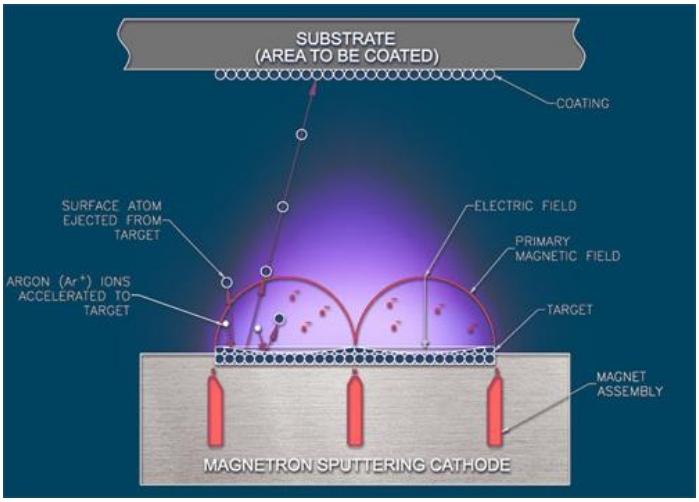

Figure 1.9. Principle of magnetron sputtering.

Magnetrons make use of the fact that a magnetic field configured parallel to the target surface can constrain secondary electron motion to the vicinity of the target **[115]**. It is known, that a Lorentz force affects a charge moving in an electromagnetic field. A direction of this force, according to a force sum rule, depends on a direction of its components, but a fraction of it is affected by the electromagnetic field and is not active, bending only a particle motion trajectory and making a particle move along a circle inside a plane perpendicularly to *E* and *B*. Electrons with a velocity, υ, in an electric field, *E*, and a magnetic field, *B*, will experience a Lorentz force,

$$\overline{F} = q\left(\overline{E} + \overline{\upsilon} \times \overline{B}\right) \tag{1.11}$$

In such a way, the magnetron device changes the electron motion trajectory due to a simultaneous action of the electrical and the magnetic field. Electrons, which are emitted from the cathode, and those, which are formed as a result of ionization, are localized immediately above a sputtered material surface due to an action of closed magnetic field. Trapping the electrons in this way substantially increases the probability of an ionising electron-atom collision occurring. This results in a dense plasma in the target region that, in turn, leads to increased ion bombardment of the target, giving higher sputtering rates and, therefore, higher deposition rates on the substrate.

A film growths on the substrate which can be positioned depending on configuration of sputtering system within a region with dense plasma (typically 60 mm from the target) or can lie in an area of low plasma density. Thus, depending on substrate position the growing film will be subjected to ion bombardment that can strongly influence the structure and properties of the growing film. The ion current drawn at the substrate in an area of low plasma density (typically, <1 mA/cm^2) is generally not sufficient to modify the structure of the film. An application of the negative bias voltages to the substrate stimulates positive ion bombardment of the growing film. When the substrate is biased U_s<0 positive ions are extracted from the plasma to the substrate and the difference between the plasma potential U_p and U_s determines the energy E_{bi} if the ion acquired in a collisionless voltage sheath in front of the substrate. The nergy E_{bi} of singly charged ions, in collisionless, fully ionized plasma, can be expressed as follows **[116]**:

$$E_{bi} = e\left(U_p - U_s\right)\nu_i / \nu_m \propto i_s U_s / a_D \tag{1.12}$$

where *e* is the elementary charge, and ν_i and ν_m are the fluxes of ions and condensing atoms, respectively, a_D is the deposition rate of the film, and i_s is the substrate ion current density.

In such a way, it is possible to control and vary the energy of the bombarding ions and, thus, effectively tailor properties of the growing coating by adjusting U_s, i_s and a_D according to equation (1.12). Relatively low-energy (E<100 eV) ion bombardment has been shown to be suitable for controlling the growth kinetics and the physical properties of thin films **[114,115,117,118]**.

At sputtering pressures $p_T \geq 1$ Pa the energy E_{bi} is lower than that defined by equation (1.12) in a result of collisions between particles and can be deremined as:

$$E_{bi} = i_s U_s \exp(-L/\lambda_i)/a_D \qquad (1.13)$$

where L is the sheath thickness and λ_i is the ion mean free path for collisions leading to losses of the ion energy in the sheath.

The energy of the sputtered atoms incident on the substrate surface, E_{ca}, can be estimated by the Meyer equation as follows **[116]**:

$$E_{ca} = (E_0 - k_B T_g)\exp(N \ln(E_f / E_i)) + k_B T_g \qquad (1.14)$$

where E_0 is the initial energy of sputtered atoms, T_g is the temperature of gas molecule, E_f/E_i is the ration of energies before and after a collision, N is the number of collisions between sputtred and gas atoms, and k_B is the Boltzman constant. The N and E_f/E_i are determined using following expressions:

$$N = dp_T \sigma_{col} / k_B T_g \qquad (1.15)$$

$$E_f / E_i = 1 - 2\gamma/(1+\gamma)^2 \qquad (1.16)$$

where d is the distance travelled, σ_{col} is the collision cross section assuming hard core interaction, and γ is the atomic mass ratio of colliding particles. It is clearly seen that the contribution of E_{ca} will decrease with increasing p_T, and at $p_T \geq 0.5$ Pa the E_{bi} will dominate over E_{ca}.

Target-generated secondary electrons do not bombard substrates because they are trapped in cycloidal trajectories near the target, and thus do not contribute to increased substrate temperature and radiation damage. This allows the use of substrates that are temperature-sensitive (for example, plastic materials) and surface sensitive (for example, metal-oxides-semiconductor devices) with minimal adverse effects.

Reactive magnetron sputtering refers to the process where a reactive gas is introduced in the chamber **[119]**. The reactive gas, e.g. nitrogen, oxygen, or hydrogen sulphide, can react with the sputtered material to form a compound on the substrate. However, the addition of the reactive gas to the discharge influences the deposition process in several ways increasing the complexity of the overall deposition process **[119,120]**.

Magnetrons can be powered by a variety of methods such as radio frequency (RF), direct current (DC), pulsed DC and, recently developed, high-power impulse magnetron sputtering (HIPIMS) **[118,121–123]**.

The main advantages of magnetron sputtering are the following **[115]**:

- low plasma impedance and thus high discharge currents from 1 A to 100 A (depending on cathode length) at typical voltages around 500 V;
- deposition rates in the range from 1 nm/s to 10 nm/s;
- low thermal load to the substrate;
- coating uniformity in the range of a few percent even for several meters long cathodes;
- easy to scale up;
- dense and well adherent coatings;
- large variety of film materials available (nearly all metals and compounds);
- broadly tunable film properties.

Magnetron sputtering is the most widely used method for industrial purposes since this method can be scaled easily for industrial applications. Moreover, any kind of material can be used as target for sputtering.

Among all available PVD methods, magnetron sputtering is a deposition technique with the advantage of producing unique fine grained and metastable structures with exceptional properties by the optimization the energy and flux of impinging sputtered atoms and bombarding ions.

1.4 Growth of nanocomposite coatings and thin films

Thin film growth is described as a kinetic adsorption of vaporized target atoms or ions and their diffusion on the substrate. First, the process starts with the condensation and nucleation of adsorded atoms, i.e. adatoms, on the substrate surface. The condensation of an atom occur through a sequence of steps in which kinetic energy is transferred to the substrate and dissipated into lattice vibrations. The atom has to dissipate a sufficient fraction of its total energy during the collision in order to stick at the substrate surface. This energy has to be below the adsorption energy, which is some fraction of cohesive energy. The adatoms possess enough energy to overcome the activation barrier E_D for surface diffusion (a few tens of an eV) that promotes their ballistical movement over the surface. The surface diffusion of an adatom regarded as a two-dimensional random walk on the lattice of preferential adsorption sites of different stability defined by the atomic

structure and chemistry of the substrate surface. The mean square displacement for this random walk **r**(*t*) grows linearly in time according to **[124]**:

$$\left\langle \left(\mathbf{r}(t)-\mathbf{r}(0)\right)^2 \right\rangle = \upsilon l^2 t = 4Dt \qquad (1.17)$$

where l^2 is the mean square distance covered in a single jump, υ is the jump rate and D denotes the surface diffusion coefficient. The jump rate is expected to follow the universal Arrehenius law for thermally activated processes:

$$\upsilon = \nu_0 e^{-\frac{E_D}{k_B T}} \qquad (1.18)$$

Here, v_0 is the attempt frequency, while k_B denotes Boltzman's constant. The surface diffusion coefficient of diffusivity can be calculated taking into account that the diffusion barrier is the same in all directions and that the adsorption sites are separated by a distance, a **[125]**:

$$D = \frac{1}{4} a^2 \upsilon = \frac{1}{4} a^2 \nu_0 e^{-\frac{E_D}{k_B T}} = D_0 e^{-\frac{E_D}{k_B T}} \qquad (1.19)$$

where the factor 1/4 is a convention reflecting the two-dimentional nature of surface diffusion. D_0 and E_D are parameters which can beobtained by experimental investigations of surface diffusion. Accordingly, the diffusion of adatoms is a thermally activated process, which plays a decisive factor in all stages of film growth because it defines the mechanism of atoms arrangement onto the incorporation sites that in turn decisive for the resultant structure of the film.

The continuous random diffusion of adatoms on the substrate surface results in the formation of small clusters or islands, which grow in size by the addition of another adatom or cluster. The next stage, called coalescence, is the growth of islands due to their merging. The growth and coalescence of the islands decreases their density creating areas for new nucleation sites that finally lead to the formation of compact film. Depending on the interaction of substrate atoms and film atoms, three characteristic modes of growth have been stated **[126]**.

The way an atom moves during deposition can be estimated using the simple equation **[127]**:

$$\overline{X} = \left(2D \frac{a}{R} \right)^{1/2} \qquad (1.20)$$

where $\overline{X}$ is the distance (cm) an atom can move on the surface during deposition, D is the surface diffusion coefficient ($cm^2\ s^{-1}$), a is the atomic spacing (nm) and R is the deposition rate ($nm\ s^{-1}$). It is obvious that only surface diffusion can contribute to considerable atomic

mobility during the deposition of a coating from the vapour phase. The probability of the occurrence of metastable phases increases with the distance the atoms have to move to find their equilibrium state because the diffusion coefficients of 10^{-15} cm^2 s^{-1} are correlated with distances in the nanometre region for realistic deposition conditions. Therefore, two-phase and multiphase systems are most favourable for the formation of metastable phases. During the atomistic deposition of a multicomponent coating from the vapour phase, the intermixed condensed atoms try to rearrange to stable configurations characterized by a low energy of formation. In order to reach this the most energetically favourable position, the atoms have to cover considerable distances which depend on the composition of the stable configuration. Adatoms have to cover short distances to form amorphous, nanocrystalline or unordered mixed coating, whereas the atoms have to travel for long distances for the formation of ordered or two phase structures **[127]**. As consequence, a competitive fashion and the kinetic limitations induced by low-temperature growth allows the controlled synthesis of metastable phases and artificial structures showing completely new properties.

The microstructure evolution and the resulting film properties are generally highly dependent on atomic-scale diffusional processes taking place during thin film growth. Therefore, the microstructure of the deposited coatings can be tailored by optimizing the growth conditions.

1.4.1 Role of energy in growth of films

One of the main advantages of plasma based methods is a highly non-equilibrium state of the deposition process of coatings because the growth is often proceed at temperatures T_s which are less than 0.2–0.3 of the melting point T_m. The using of plasma in combination with low deposition temperature and high deposition rates enables the formation of metastable phases as the atoms may not have time and energy to rearrange in the most energetically favourable positions.

The determining atomic process that control structure evolution of thin film during its growth is surface diffusion. Although surface diffusion is normally a thermally activated process, it can be promoted by the ion bombardment during PVD process because non-penetrating ions may transfer their kinetic energy to the adatoms of the growing film and thus heat it at an atomic level. The diffusion processes are highly affected by energy delivered to the growing film. The energy delivered to the growing film E is a key parameter, which determines the mechanism of its growth, element and phase composition, microstructure and structure and so its final functional properties **[113]**. The

different kind of energy can be delivered by substrate heating (E_s), conversion of the kinetic energy of bombarding ions (E_{bi}, see equation (1.12)) and fast condensing atoms (E_{ca}, see equation 1.14) incident on the surface of growing film, i.e. by $E_p=E_{bi}+E_{ca}$ (known as non-equilibrium atomic scale heating), the heat evolved during formation of the compound E_{ch} (energy released in exothermic chemical reactions), heating from the sputtered target E_t which is always not sufficiently cooled, and heat radiation from plasma E_{rad}. The total energy E_T delivered to the growing film can be expressed by the formula **[33,39,116]**:

$$E_T = E_S(T_S, t_d) + E_p(U_S, i_S, a_D, p_T, t_d) + \\ + E_{ch}(T_S, t_d) + E_t(W_d, t_d, d_{s-t}) + E_{rad}(t_d) \quad (1.21)$$

where, T_s is the substrate temperature, t_d is the time of film deposition, U_s is the substrate bias, i_s is the substrate ion current density, a_D is the film deposition rate, $p_T=p_{Ar}+p_{RG}$ is the total pressure of sputtering gas mixture, p_{Ar} and p_{RG} are the partial pressure of argon and reactive gas (RG), respectively, $W_d=U_dI_d/S$ is the magnetron target power density, I_d and U_d are the magnetron current and voltage, respectively, S is the whole area of the magnetron target and d_{s-t} is the substrate to target distance.

The equation (1.21) clearly shows that the conditions of thin film growth can be controlled by simply varying the basic deposition parameters, such as the discharge current, substrate temperature, bias voltage, substrate ion current density, and partial pressure of reactive gas. This gives the ability of selective and controllable growth of films at the atomic scale with different microstructures in terms of grain size, crystallographic orientation, lattice defects, phase compositions, and surface morphology.

1.4.2 Structure zone diagram

Extensive studies of the correlation between film structure and deposition parameters have led to the development and refinement of structure zone diagrams (SZD) which systematically categorize self-organized structural evolution of a film during PVD as a function of deposition parameters **[128–131]**. SZD depicts the morphology and microstructure of a film, independently of its material, as a function of the adatom mobility. SZD for PVD describes the evolution of the microstructure as function of the generalized temperature T^*, the normalized energy E^*, and the net film thickness t^*, see Figure 1.10 **[131]**. The generalizing temperature T^* includes the homologous temperature ($T_h = T_s/T_m$, where T_s is the substrate temperature, T_m is the melting temperature of a material), which is related to sublimation energy and activation energies for surface and

bulk diffusion for most materials, plus a temperature shift caused by the potential energy of particles arriving on the surface, and can be defined by the following expression **[131]**:

$$T^* = T_h + T_{pot} = T_h + \frac{1}{k_B}\sum_\alpha \frac{E_{pot,\alpha} J_\alpha}{N_{moved,\alpha}} \Big/ \sum_\alpha J_\alpha \qquad (1.22)$$

Here, $T_{pot}=E_{pot}/(k_B N_{moved})$ is the characteristic temperature of a heated region affecting the rearrangement of N_{moved} atoms, J_α is the flux of arriving species (ions and atoms). The potential energy includes the heat of sublimation, or cohesive energy, E_c, as well as the ionization energy, E_i, reduced by the work funcrion of the electron needed for neutralization; hence $E_{pot}=E_c+(E_i-\phi)$.

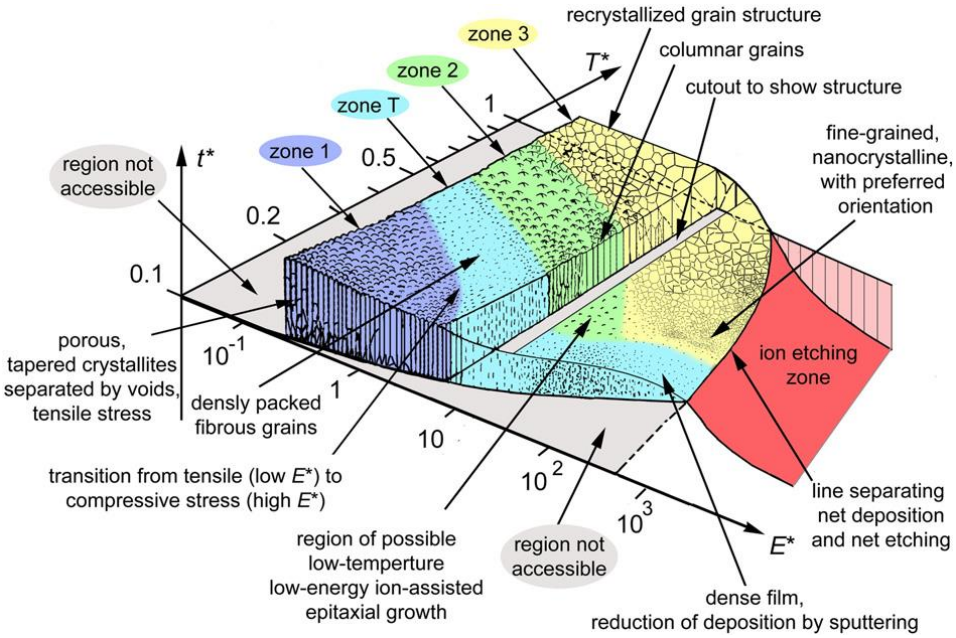

Figure 1.10. Structure zone diagram for film growth by PVD **[131]**.

The normalized energy E^* describes displacement and heating effects caused by the kinetic energy of bombarding particles **[131]**:

$$E^* = \sum_\alpha \frac{E_{kin,\alpha}}{E_c}\frac{m_\alpha}{m_s} \Big/ \sum_\alpha J_\alpha \qquad (1.23)$$

where m_α/m_s is the mass ratio of arriving ions and atoms on the surface. Here, the kinetic energy is defined as a sum of an initial component from the plasma, E_0, and a change due to acceleration in the sheath, $E_{kin}=E_0+QeV_{sheath}$, where Q is the ion charge state number, e is the elementary charge, and V_{sheath} is the voltage drope between plasma and substrate. The energy flux is normalized by a characteristic energy of the material, E_c, such as cohesive energy (other energies related to bond strength can be considered too). The net film thickness t^* is a qualitative illustration of film structure while indicating thickness

reduction by densification and sputtering; it also allows to include "negative thickness", i.e. ion etching.

Zone 1 is characterized by low substrate temperature (T_s/T_m<0.2-0.3) and low energy that cause the extremely low surface mobility on the substrate surface. These conditions favour a fine-grained structure consisting of textured and fibrous grains. The formation of the film structure is mainly driven by adatom surface diffusion in zone 2 ($0.3 \leq T_s/T_m < 0.5$), thus leading to uniform columnar grain growth which proceed from the substrate to the free surface of the film. A transition zone between zone 1 and zone 2 (zone T) where the film growth is affected by the energetic bombardment by high energetic ions and/or neutrals. Zone T exhibits the competitive growth which is given by transition from the film growth of immobile grain boundaries to the growth driven by surface diffusion which makes the migration of adatoms possible between neighbouring grains. This lead to V-shaped grain growth with a dense voids-free fibrous microstructure and smooth film surface. In zone 3 ($T_s/T_m \leq 0.5$), bulk diffusion is dominant and leads to recrystallization, grain growth, and densification.

Importantly, the zone T expands to low values of the ratio T_s/T_m .This means that dense and voids-free coatings can be formed without the substrate heating. Instead of the substrate heating, the energy can be delivered in the growing film by the non-equilibrium atomic scale heating, E_p, (either by combined action of bombarding ions and fast neutrals or by the fast neutrals only). Therefore, there are two decisive parameters which are responsible for the formation of such films: the energy E_p and the melting temperature T_m of created film. Since the melting temperature T_m depends on the amount of elements added in the base material of the film, the ratio T_s/T_m can be increased by the addition of selected elements in the film because the melting temperature T_m of such films can be decreased compared to the pure films. This allows to deposit the films with microstructure corresponding to zone T at low substrate temperature or even at unheated substrates **[75]**.

Nevertheless, films with amorphous structure are not presented in the SZD. The growth of amorphous films requires high deposition rates and low substrate temperatures ($T_s/T_m \leq 0.3$). At these conditions, the adatom are hindered from finding their equilibrium position and have not time to diffuse on the substrate to find favoured positions before yet another adatom arrives at the surface. Thus, the atoms are placed in unfavourable positions and are covered in the growing film. Moreover, ion bombardment of the growing film can restrict grain growth and permit the formation of crystalline structure by the generation of defects which act as preferential nucleation sites or/and by stimulation of a preferential resputtering of adatoms that decreases adatom mobility **[6,132]**.

In general, the formability of nanocomposite films with amorphous structure can be enhanced by following three empirical rules **[133]**:

- Heat of mixing among the elements is strongly negative;
- There is a large difference (>12%) in atomic size;
- The phase diagram contains deep eutectic points.

1.4.3 Formation of nanostructure by phase segregation

The formation of multiphase films with nanocomposite nanostructure requires conditions for the development of the segregating phases. A solid solution is formed in the initial stage of the deposition of the multicomponent coatings, because the fluxes of different atoms toward the surface of growing film are random. The solid solution will decompose during the growth of the film with the formation of strong nanocomposite nanostructure if the de-mixing driving force will be sufficiently high and the diffusion fast.

There are two possible mechanisms of the decomposition of such thermodynamically unstable solution: by the nucleation and growth, and by the spinodal decomposition **[134]**. The spinodal phase segregation occurs in a mixed binary system $A_{1-x}B_x$ when the second derivative of the Gibbs free energy of the mixed phase G_f^0 with the composition x is negative **[40,135]**:

$$\frac{\delta^2 G_f^0(x)}{\delta^2 x} < 0 \qquad (1.24)$$

Thus, a mixed system that meets condition (1.24) is inherently unstable against any infinitesimally small local fluctuations and the phase segregation occurs spontaneously without any activation **[16]**. This process is diffusion-controlled and therefore a sufficiently high temperature is needed in order to complete the spinodal phase segregation during the film growth. As a result, a fairly regular nanostructure with sharp grain boundaries and fairly uniform crystallite size will be formed by self-organization. This is illustrated in Fig.1.11 for a lower curve within the whole range of the composition and for the upper one for the range between the compositions x_1 and x_2.

The nucleation and growth segregation occurs in a mixed binary system $A_{1-x}B_x$ when the second derivative of the Gibbs free energy of the mixed phase G_f^0 with the composition x is positive:

$$\frac{\delta^2 G_f^0(x)}{\delta^2 x} > 0 \qquad (1.25)$$

Thus, within the range $x`<x<x_1$ and $x_2<x<x``$ of the upper curve (Fig. 1.11), infinitesimal fluctuations results in an increase of free energy. The system there is metastable, and the segregation occurs by nucleation and growth with activation energy of nucleation $E_{act}>0$. A nanostructure formed upon the nucleation and growth consists of nanocrystalls with relatively broad size distribution and not necessarily sharp grain boundaries **[136]**.

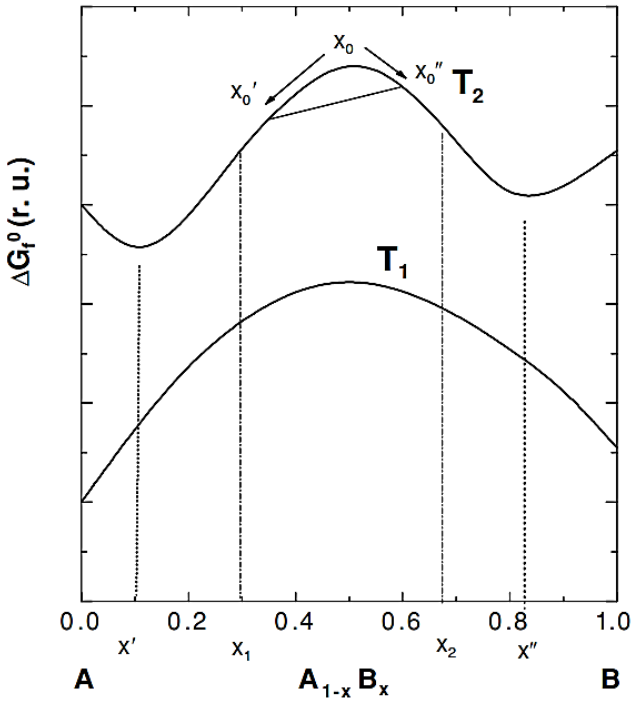

Figure 1.11. Schematic dependence of the free energy of formation of a binary solution $A_{1-x}B_x$ on the composition which show immiscibility between compositions x_1 and x_2 for a low pressure of nitrogen and/or too high temperature T_2 (upper curve) and (lower curve) within the whole composition range at a sufficiently high pressure of nitrogen and a lower temperature T_1 of about 550 °C **[136]**.

The composition modulation as a consequence of spinodal decomposition results in hardening of an alloy due to the coherency internal stresses **[137]**. A nanostructure formed upon spinodal decomposition remains stable against coarsening (Ostwald ripening) while the condition (1.24) holds because any local fluctuations of the composition towards mixing increases the free energy of the system. So that, if a system meets this condition at high temperatures, it will not undergo Ostwald ripening and thus retain its nanostructure as well as mechanical properties **[138]**.

Moreover, films with the nanocomposite nanostructure can be formed by crystallization of a completely amorphous film under proper heat treatment conditions (annealing temperature and time, heating rate, etc.). This method is very promising for

producing nanocomposite films composed of small grains whose size continuously varies from approximately 1 to 10 nm **[33]**. In addition, this process avoids the presence of impurities or porosity typical of other methods used for synthesis of the nanostructured films. The nanocrystallization is very simple and well controllable for most alloys and element systems. Moreover, some nanocrystalline intermetallics, supersaturated metallic solid solutions, and nanocomposites with different kinds of interfacial structure can be easily synthesized by this method **[139]**.

1.5 Ti-Al-N based nanocomposite coatings

Among all TM nitrides with high melting point, high hardness, and fairly good oxidation and corrosion resistance, TiN has been found considerable interest in the research community and has been widely used in numerous industrial applications as the wear protective coating because of its excellent performance characteristics **[6]**. In order to further improve its functional properties, TiN was doped by metals such as Y **[140]**, Al **[141]**, Hf and Zr **[142]**, Ta **[143]**, Nb **[144]**, V and Cr **[145]**, Mo **[146]**, W **[147]**, Re **[148]** and metalloids such as Si **[15]**, B **[149]** and C **[150]**, or by combination of metal and metalloid. The improvement of properties of all the mentioned above ternary nitrides was achieved due to the realization of one or more of the following mechanisms: changed chemical bonds, solid solution strengthening, mixed crystal strengthening and phase separation with formation of nanocomposite structure.

Currently, a wide range of ternary, quaternary and multinary nanocomposite coatings were designed and developed by utilizing different structural architectures and different chemical compositions (Table 1.1). However, among all the nanocomposite coatings, the most studied systems are “Ti-Si-N”, “Ti-B-N” and “Ti-Al-N”. In this thesis, a detailed overview of the Ti-Al-N based nanocomposite coatings is presented, because the related Ti-Al-N based coatings alloyed with different TMs and/or metalloids have recently found considerable interest of the scientific community and because of recent large-scale industrial applications of Ti-Al-N based coatings.

Highly non-equilibrium deposition conditions of PVD methods allow obtaining the metastable $Ti_{1-x}Al_xN$ solid solution coatings. The atomic reassembly during condensation at temperatures in the range 300-500 °C (typical substrate temperatures for the growth of TiAlN coatings) from the vapour phase is limited, which stimulates the formation of the metastable phase. The combination of high hardness, oxidation resistance and wear resistance of $Ti_{1-x}Al_xN$ coatings is strongly depend on the microstructure of the coating which in turn depends on the amount of Al added to the compound (Table 1.2). Hence,

when Al content is in the range $0<x\leq0.6$, $Ti_{1-x}Al_xN$ coatings exhibit a single face supersaturated face-centred cubic (fcc, NaCl-type lattice, further in the text referred to as "fcc") (Ti, Al)N solid solution with near random orientation which forms by the substitution of Ti atoms by smaller Al atoms in the TiN lattice that causes the decreasing of the lattice parameter of the TiN (see Table 1.2). However, fcc-(Ti, Al)N solid solution was found to be unstable versus decomposition into more thermodynamically stable compounds when Al content in TiN lattice exceeds solubility limit. After increasing of the Al content to around $0.6\leq x\leq0.7$ (depending on the growth conditions) fcc-(Ti, Al)N coatings undergo decomposition to AlN depleted fcc-(Ti, Al)N phase and AlN-rich hcp-(Al, Ti)N phase in the hexagonal close packed (hcp) structure (wurtzite-type lattice, further in the text referred to as "hcp"). Addition of even higher amount of Al $x\geq0.7$ results in the formation of thermodynamically stable AlN-rich (Al, Ti)N single phase with hcp structure. TEM studies of $Ti_{1-x}Al_xN$ coatings have shown the formation of the nanocolumnar microstructure of the metastable single phase Ti-rich fcc structured solid solution (Fig. 1.12a), dual-phase fcc+hcp microstructure (Fig. 1.12b) and Al-rich hcp solid solution (Fig. 1.12c) with several orientations of nanocrystalline domains embedded into more disordered grain boundaries (Fig. 1.12a).

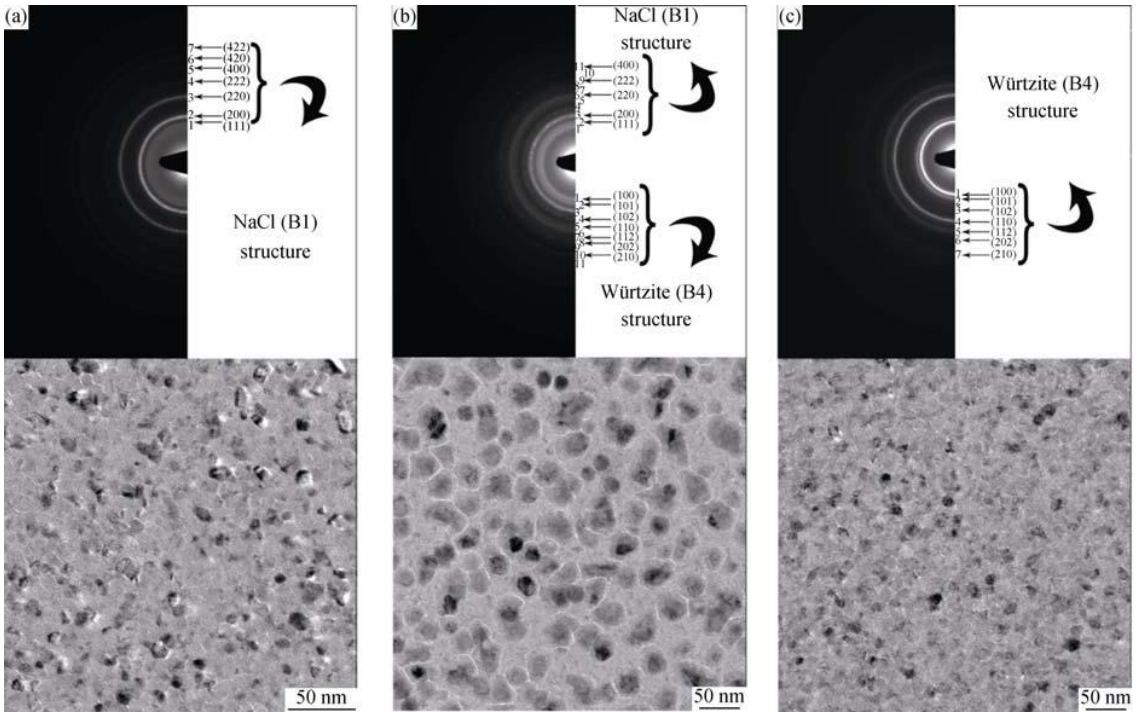

Figure 1.12. Plan-view TEM images and corresponding SAED patterns from $Ti_{1-x}Al_xN$ films with (a) x=0.39, (b) x=0.60, and (c) x=0.75, the SAED pattern in (a) being indexed with the fcc structure; (b) being a mixture of fcc and hcp structures; and (c) being würtzite structure **[151]**.

Table 1.1. Comparison of single layer crystalline (c-), nanocrystalline (nc-), amorphous (a) and nanocomposite (nc-/a-) coatings.

Coating structure	H, GPa	E^*, GPa	Oxidation resistance, ºC	Reference
c-TiN	18-21	~245	550ºC	**[152]**
nc-TiN	32-52	370-480	–	**[153]**
nc-$Ti_{1-x}Al_xN$	23-32	405	~850	**[154]**
nc- $Ti_{1-x}Al_xN$/a-AlN	46.8	402	–	**[141]**
a- $Ti_{1-x}Al_xN$	31-41	–	~700	**[155]**
nc-TiN/a-Si_3N_4	50	500	800	**[156]**
a-Ti-Si-N	25	~200	1480	**[96]**
nc-(Ti, Al)N/a-BN/a-TiB_2	17-37	210-320	–	**[157,158]**
nc-TiN/a-BN	45-55	–	770	**[159]**
nc-TiN/a-BN/a-TiB_2	50	–		**[160]**
nc-TiN/nc-TiB_2/a-BN	37	332		**[161]**
nc-(Ti, Al)N/a-Si_3N_4	42.4	–	900	**[162,163]**
nc-(Ti, Al, Si)N/a-Si_3N_4	55	650	–	**[164]**
nc-(Ti, Al, Si)N	34	–	–	**[165]**
nc-(Cr, Al)N/a-Si_3N_4	40	–	–	**[166]**
nc-TiN/a-Si_3N_4/a-$TiSi_2$/nc-$TiSi_2$	100	–	800	**[167,168]**
nc-TiN/a-Si_3N_4/a-$TiSi_2$	70-80	479	800	**[168,169]**
nc-W_2N/a-Si_3N_4	40-50	≥500	–	**[170]**
nc-VN/a-Si_3N_4	52	≥500	–	**[171]**

– Denotes data are not given in the references or not determined

Table 1.2. Structure-property relationship of $Ti_{1-x}Al_xN$ nanocomposite coatings deposited by different PVD methods.

Al atomic ratio	Coating structure	Lattice constant, Å	Grain size, nm	Hardness, GPa	Elastic modulus, GPa	Oxidation resistance, ºC	Deposition method	Ref.
x≤0.6	fcc-(Ti, Al)N	4.2448	–	~38	650	~800	RF magnetron sputtering	**[172]**
0.6≤x≤0.7	fcc-(Ti, Al)N +hcp-(Al,Ti) N	4.2448≤a≤4.1462	–	~34	540	~900		
x≥0.7	hcp-(Al,Ti) N	4.1462	–	~22	415	~900		
x=0.25	fcc-(Ti, Al)N	–		31.9	605	–	Cathodic Arc Evaporation	**[173]**
x=0.33				32	608			
x=0.5				33.4	627			
x=0.66				33.1	595			
x=0.74	fcc-(Ti, Al)N +hcp-(Al,Ti) N		–	–	–			
x=0.5	fcc-(Ti, Al)N	–		33	350	–	DC magnetron sputtering	**[174]**
x=0.6				30	330			
x=0.67				25	320			
x=0.69	fcc-(Ti, Al)N +hcp-(Al,Ti) N			20	240			
x=0.75	hcp-AlN			19	220			
x=0.54	fcc-TiAlN/a-AlN	–	29	47	402	–	DC magnetron sputtering	**[141]**
x=31.7	XRD amorphous	–	–	31		–	DC magnetron sputtering	**[155]**
x=31.4				41				
x=0.54	XRD amorphous	–	–	17.7	–	700	DC magnetron sp.	**[141]**
x=0.57				9.5				

Table 1.2. Continuation.

x=0.52	fcc-(Ti, Al)N	–	–	~31.9	400	850 for 20 h	Unbalanced magnetron sputtering	**[154]**
x=0.62				~31.3	380	850 for 20 h		
x=0.67	fcc-(Ti, Al)N +hcp-(Al,Ti) N			~27.2	315	850 for 20 h		
x=0.75	hcp-(Al,Ti) N			22.9	260	850 for 4 h		
x=0.09	fcc-(Ti, Al)N	4.238	25.4	25.4	262.9	–	Unbalanced close-field magnetron sputtering	**[175]**
x=0.17		4.235	18.9	26.1	276.7			
x=0.25		4.233	18.6	27.3	288.3			
x=0.33		4.224	17.7	27.4	295.6			
x=0.41		4.209	16.8	31.4	312.2			
x=0.46	fcc-(Ti, Al)N	–		41	–	–	RF magnetron sputtering	**[176]**
x=0.50				29				
x=0.62	fcc-(Ti, Al)N +hcp-(Al,Ti) N			23				
x=0.68				21.5				

– Denotes data are not given in the references or not determined

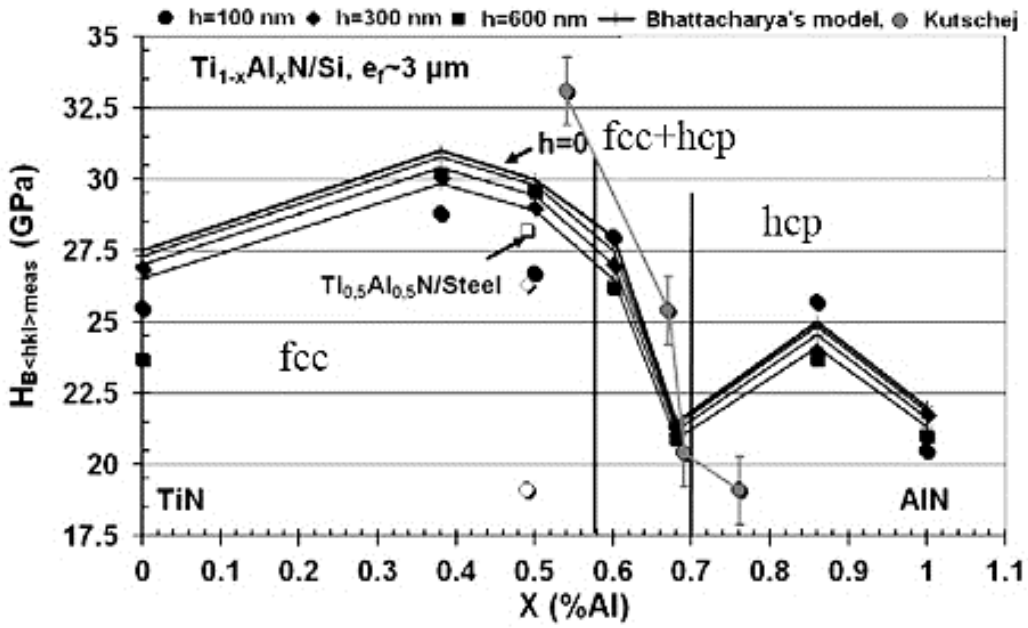

Figure 1.13. Hardness of $Ti_{1-x}Al_xN$ coatings as a function of the Al content for three indentation depths **[177]**. The results obtained with a steel substrate and those of Kutschej et al. **[174]** are presented.

The combination of high hardness, wear resistance and oxidation resistance of $Ti_{1-x}Al_xN$ coatings can be achieved when x increases to the maximum Al content substituted for Ti in the fcc lattice of TiN that is close to solubility limit at around x = 0.6 (Fig. 1.13 and Table 1.2). After the Al content exceeds $x \geq 0.6$ the hardness and oxidation resistance decrease rapidly that is because of the structural decomposition and formation of the mixed structure fcc + hcp. Therefore, the stabilization of Al-rich fcc structured (Ti, Al)N based coatings is of special interest. However, hcp structured (Al, Ti)N coatings (x = 0.75) have shown the best oxidation resistance at 850 ºC during 40 h in comparison to the coatings with x < 0.75, but having the worst hardness **[154]**.

The oxidation behaviour of $Ti_{1-x}Al_xN$ coatings is attributed to the formation of Al-rich oxide surface layer which protects the underlying nitride coating from further inward diffusion of O due to its very good oxygen barrier properties **[178–180]**. At relatively low Al content x<0.2, the Al-rich oxide layer formed at the surface is not thick enough to protect the coating from further O diffusion at high temperatures and the coating oxidizes after short period of time. When $0.2 \leq x \leq 0.5$, the topmost Al_2O_3 layer forms rapidly that prevents inward diffusion of O during longer oxidation time and retards the growth of TiO_2 which can lead to the cracking of protective Al_2O_3 because of the generation of compressive stresses **[181]**. In contrast, at higher Al content $x \geq 0.5$, a mixed oxide layer Al_2O_3+TiO_2 forms at the surface, which allows gradual inward diffusion of O. The low oxidation resistance of the Al-rich (Al,

Ti)N coatings can be associated with the segregation of Ti between hexagonal (Al, Ti)N domains **[182]** that makes outward diffusion of Ti and subsequent growth of TiO_2 at high temperatures more favourable than that of Al.

The hardening mechanism of $Ti_{1-x}Al_xN$ coatings with relatively low Al ($x \leq 0.4$) content originates from the effect of solid solution hardening due to the created compressive stresses by incorporation of Al which react with the elastic field of a dislocation. At the same time, the change of the nature of atomic bonding due to the incorporation of Al atoms into fcc lattice and the grain boundary hardening have showed a negligible contribution to the hardening phenomena. Whereas the enhanced effect of grain boundary hardening, caused by the segregation of solutes on the grain boundaries and the increasing of grain boundary density (the decreasing of the grain size, see Table 1.2), becomes predominant when the amount of incorporated Al to fcc solid solution is higher than 0.4 **[175]**.

The major reason of the considerable interest to $Ti_{1-x}Al_xN$ coatings based on their ability to increase the hardness by the formation of a coherent nanostructure by self-organization upon spinodal phase segregation at high temperature, i.e. age hardening **[183–185]** (Fig. 1.14).

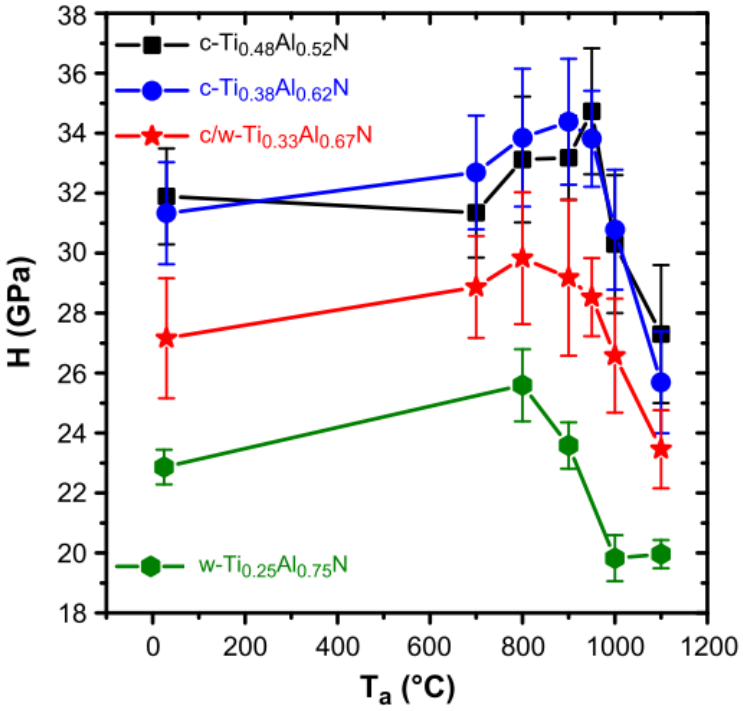

Figure 1.14. Hardness of $Ti_{1-x}Al_xN$ coatings on MgO (001) after annealing in vacuum for 20 min at T_a.[154].

Annealing up to 900 °C of single phase cubic (Ti, Al)N coatings with Al content close to the metastable solubility limit (around x=0.6) was found to result in the formation of an

interconnected 3D network of fcc-Ti(Al)N and fcc-Al(Ti)N domains which are separated by diffusive boundaries. The decomposition of metastable solid solution $Ti_{1-x}Al_xN$ upon spinodal phase segregation toward the cubic lattice is due to existence of miscibility gap in the pseudo-binary TiN-AlN system **[186]**. A higher Al content within the cubic phase favors spinodal decomposition at lower T_a (hence earlier increase in hardness with T_a) due to an increase in driving force (mixing enthalpy), Fig. 1.14 [154]. The observed age hardening in $Ti_{1-x}Al_xN$ coatings is due to hindering of dislocations movement by strain fields originating from the 2.8 % lattice mismatch between coherent c-Ti(Al)N and c-Al(Ti)N domains ($a_{c\text{-}TiN}$ = 4.24 Å , $a_{c\text{-}AlN}$ = 4.12 Å), and also due to hardening from a difference in shear modulus. A further increase in the annealing temperature results in a phase transformation of fcc-Ti(Al)N and fcc-Al(Ti)N domains to interconnected stable fcc-TiN and hcp-AlN domains by nucleation and growth that in turn results in a loss of coherency and a significant strain and hardness decrease **[187]**. This loss of hardness at higher temperatures is the main drawback of these coatings that limits their utilization on tools for high-temperature operation.

The differences of $Ti_{1-x}Al_xN$ coatings structure play a major role in their wear behaviour. The hcp structured (Al, Ti)N coatings demonstrate a low wear resistance because of a low resistance to crack initiation that causes brittleness and crack formation. As a result, the generation of a large amount of wear debris during the wear is promoted. The fcc structured (Ti, Al)N coatings which contains enough Al atoms to limit the surface oxidation shows very low wear due to a high resistance to crack initiation **[188,189]**. Moreover, the better tribological behaviour of fcc-(Ti, Al)N coatings can be attributed to growth of high volume of [100] domains and the lesser volume of [111] domains **[188]**. The texturization which is based on small crystallized domains randomly in-plane distributed and the presence of a sufficiently high amount of Ti atoms in the cubic environment play a significant role in the improvement of tribological properties of Ti rich (Ti, Al)N coatings **[189]**.

The self-organization of $Ti_{1-x}Al_xN$ coatings during thermal annealing with the formation of the nanostructured domains and their superior oxidation resistance enable a self-adaptation process of the coatings to the thermal load applied generated during tribological testing or cutting operations.

1.5.1 Ti-Al-Si-N nanocomposite coatings

Continuous industrial demands for protective coatings and cutting tool coatings with higher hardness, better high-temperature oxidation resistance above 1000 °C, and better wear resistance have led to the further active research with aim to overcome certain deficiencies of $Ti_{1-x}Al_xN$ coatings. In order to achieve an improvement of the functional

properties, $Ti_{1-x}Al_xN$ coatings were alloyed by wide range of metals or/and metalloids, among which the alloying by Si is regarded as the most promising approach to improve hardness, oxidation resistance and wear resistance.

The incorporation of Si into the $Ti_{1-x}Al_xN$ coating promotes considerable changes in the growth mechanism. The solubility of Si in the $Ti_{1-x}Al_xN$ is very low and was reported to be approximately in the range 6-9 at.% **[164]**. The incorporation of less than 6-9 at. % of Si causes the substitution of aluminium and titanium atoms in the fcc-$Ti_{1-x}Al_xN$ lattice by smaller Si atoms that results in nanocolumnar growth of the metastable fcc-(Ti, Al, Si) N solid solution (see Table 3 and references therein). Si incorporation beyond solubility limit around 9-17 at.% leads to co-precipitation of Si with $Ti_{1-x}Al_xN$ crystallites that accompanied by the formation of amorphous silicon nitride phase. The formed amorphous silicon nitride draws Si atoms from the surrounding fcc-(Ti, Al, Si) N crystals in order to grow itself. This non-metallic nitride due to a pronounced immiscibility with and low diffusivity in the $Ti_{1-x}Al_xN$ concentrates at the grain boundaries of $Ti_{1-x}Al_xN$ and reduces their mobility **[190]**. As a result, the amorphous silicon nitride decreases the mobility of other atoms and thus limits the growth of the $Ti_{1-x}Al_xN$ grains and stimulates their re-nucleation. As a consequence, a columnar growth is suppressed that results in the development of a 3D nanocomposite structure where fine nanocrystallites of fcc-(Ti, Al)N are embedded in very thin amorphous matrix of Si_3N_4. The highest hardness was achieved when (Ti, Al)N nanocrystallites of about 10-40 nm were covered by about 1 ML (less than 1 nm) of a-Si_3N_4 (Fig. 1.15a and Table 1.3). When the thickness of a-Si_3N_4 increases up to 1 ML the hardness increases to a maximum value, whereas the average crystalline size reaches a minimum. The minimization of crystalline size corresponds to maximum surface area of the interfaces between the nanocrystalls and amorphous matrix thus the interfaces start to play the determinative role in the mechanical behaviour of the system. It was suggested that the large increase in the hardness of fcc-(Ti, Al)N/ a-Si_3N_4 is due the grain boundary hardening both by strong cohesive energy of the interface boundaries and by Hall-Petch relation derived from crystal size refinement **[16]**. Additionally, dislocations that can occur in the crystallites can not move through the amorphous matrix. The strong cohesive energy of the interface boundaries is due to strengthening of the covalent Si-N bond across the interface by valence charge transfer from the Ti(Al)-N that has high density of delocalized electrons at the Fermi level and, therefore, is of metallic nature **[191]**. This valance charge transfer decreases the interface grain boundary energy thus stabilizing it against grain boundary sliding and hence increases the strength and hardness.

Table 1.3. Structure-property relationship of Ti-Al-Si-N based nanocomposite coatings deposited by different PVD methods.

Composition, at %			Structure	Hardness, GPa	Elastic modulus, GPa	Grain size, nm	Oxidation temperature, °C	Deposition method	Ref.
Ti	Al	Si							
0.69	0.25	0.06	nc-(Ti, Al)N/a-Si_3N_4	33.6	–	~30	800 for 1000 h	Arc ion plating	**[183, 184]**
0.48	0.46	0.06	nc-(Ti, Al)N/a-Si_3N_4	42.4	–	~3.8	–	Cathodic arc evaporation	**[162]**
0.49	0.44	0.07	nc-(Ti, Al)N/a-Si_3N_4	–	–	8	900		**[194]**
0.28	0.51	0.21	a-TiAlSiN	32.36	–	–	–	Ion enhanced magnetron sputtering	**[195]**
0.97	0.01	0.02	nc-(Ti, Al)N/a-Si_3N_4	31	–	90	750	Plasma immersion ion implantation and deposition	**[94]**
0.82	0.06	0.12		40		40	790		
0.62	0.1	0.28		27		4	830		
0.34	0.66	0.08	nc-(Ti, Al)N/a-Si_3N_4	28.7	–	–	950	Cathodic arc evaporation	**[196]**
0.62	0.32	0.06	nc-(Ti, Al)N/a-Si_3N_4	38.6	–	8	–		**[197]**
0.48	0.46	0.06		42.4		3.6			
0.59	0.28	0.13	nc-(Ti, Al)N/a-Si_3N_4	31	317	7.5	850	Reactive DC Magnetron sputtering	**[198]**
0.55	0.28	0.17		38	303	–			
0.53	0.27	0.2		33	273	5			
0.29	0.59	0.12	nc-(Ti, Al)N/ nc-AlN/a-Si_3N_4	20	–	4.5	–	Reactive unbalanced pulsed DC magnetron sputtering	**[199]**
0.42	0.48	0.1	nc-(Ti, Al)N/a-Si_3N_4	38		5.5			
0.57	0.35	0.08		43		6.1			
0.63	0.3	0.07		66		7.5			
0.65	0.29	0.06		56		6.9			

– Denotes data are not given in the references or not determined

Table 1.3. Continuation.

0.61	0.20	0.19	a- TiAlSiN	37	–	–	–	Arc ion plating	**[200]**
0.325	0.67	0.05	nc-TiN+nc-AlN	–	–	–	900 for 300 min	Cathodic arc evaporation	**[201]**
0.31	0.67	0.2							
0.6	0.24	0.16	nc-(Ti, Al,Si)N	45	–	17	–	Reactive RF magnetron sputtering	**[202]**
0.49	0.43	0.08	nc-(Ti, Al, Si)N	31	340	–	900 for 2 h	Arc ion platting + magnetron sputtering	**[203]**
0.48	0.38	0.14	nc-(Ti, Al, Si)N/a-Si_3N_4	35	380				
0.45	0.39	0.17		29	340				
0.4	0.35	0.25	a- TiAlSiN	19	236				
0.26	0.46	0.28	a- TiAlSiN	19.4	252-263	–	–	Cathodic arc evaporation	**[98]**
0.31	0.41	0.28							
0.34	0.39	0.27							
0.56	0.18	0.26	nc-(Ti, Al, Si)N	40	–	30	–	RF and DC magnetron sputtering	**[204]**
0.62	0.18	0.2	nc-(Ti, Al)N/a-SiN_x/a-AlN	54	452	1-10			
0.74	0.18	0.04		38	–	–			
0.42	0.55	0.03	nc-(Ti, Al, Si)N	34	–	50-250	1100	Arc ion platting	**[165]**
0.72	0.24	0.04	nc-(Ti, Al, Si)N	40	470	–	–	Arc ion plating+Magnetron sputtering	**[164]**
0.70	0.24	0.06		42	530	–			
0.68	0.23	0.09	nc-(Ti, Al, Si)N/a-Si_3N_4	55	650	8			
0.61	0.20	0.19	a- TiAlSiN	32	400	–			
0.86	0.11	0.03	nc-(Ti, Al, Si)N/a-Si_3N_4	37.1	402	10-20	–	Arc ion plating+Magnetron sputtering	**[205]**
0.78	0.17	0.05		42	455	8.3			
0.73	0.28	0.08		32.4	394	7.5			
0.63	0.28	0.09		30.4	370	7.3			

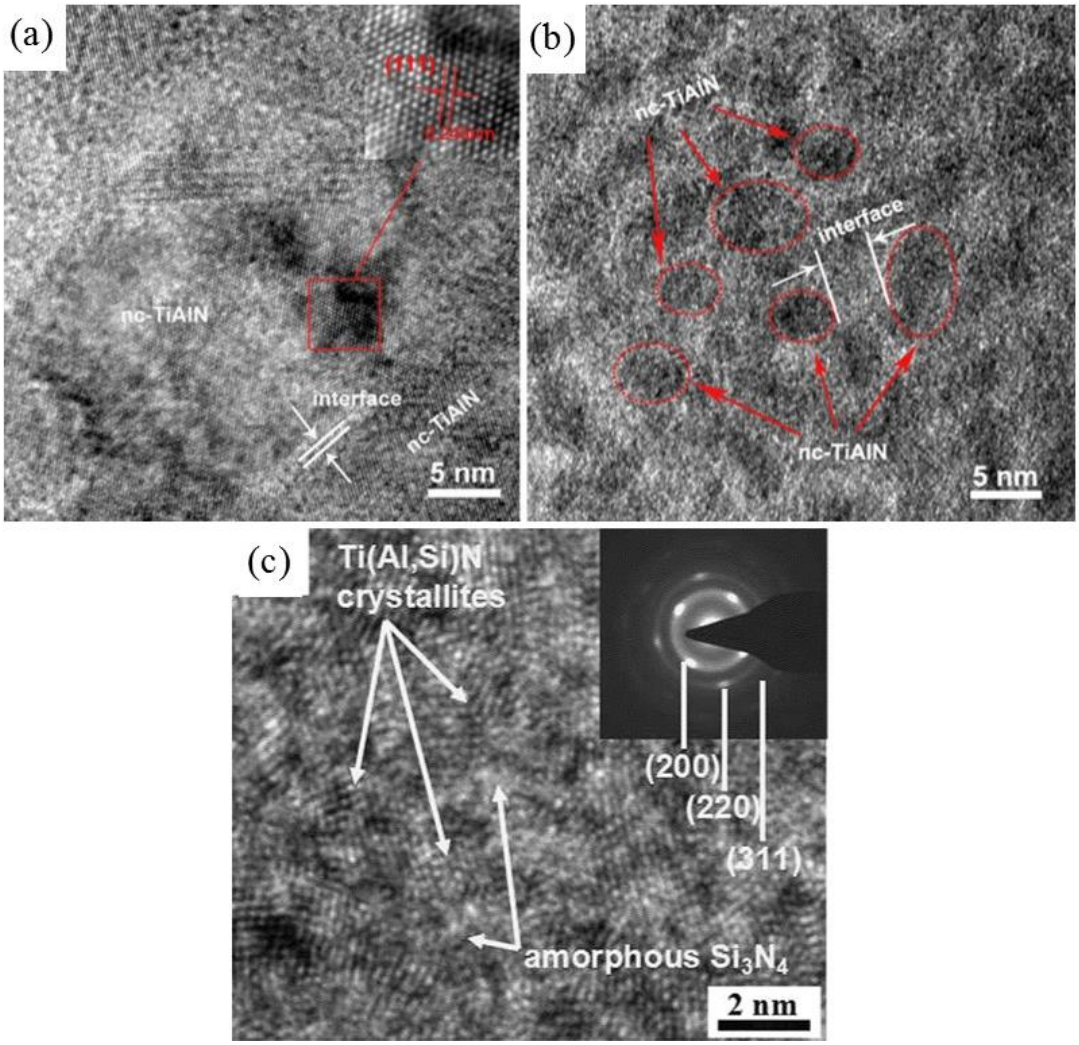

Figure 1.15. HRTEM images, showing a nanocomposite structure of nc-(Ti, Al)N/a-Si_3N_4 coatings with 6 at. % (*H*=44 GPa) (a) and 15.7 at. % (*H*=27 GPa) (b) of Si **[94]**, and nc-(Ti, Al, Si)N/a-Si_3N_4 coating (*H*=37.1 GPa) (c) **[205]**

Nevertheless, the further incorporation of the higher amount of Si≥17 at.% stimulates growth of a-Si_3N_4 and larger coverage of (Ti, Al)N nanocrystallites promoting the decrease of their size that accompanied by decrease in the hardness of nc-(Ti, Al)N/a-Si_3N_4 coatings (Fig. 1.15b, Table 1.3). The observed softening is mainly due to the increasing weakening of the Ti(Al)-N bonds attached to a-Si_3N_4 interfacial layer, as a result of the increase in the amplitude of oscillations of valence charge density next to that interface which is the result of a larger electronegativity of Si as compared with Ti and Al **[191]**. The optimum Si content for achieving the maximum hardness value can vary in wide range from 9 at.% to 17 at.% depending on deposition condition and Al/Ti ratio (see Table 1.3).

However, the low energy deposition conditions (high deposition rate, low nitrogen activity and low growth temperature) can cause the low adatom mobilities, which are not sufficient for full segregation of a-Si_3N_4 and as result some amount of Si atoms could

remain dissolved in fcc-(Ti, Al)N lattice, where they partially replace the Al and Ti atoms **[165,203,205]**. The coatings formed under such conditions had nc-(Ti, Al, Si)N/a-Si_3N_4 nanocomposite structure (Fig. 1.15c).

It was reported that the growth of (Ti, Al)N nanocrystallites can be inhibited completely by high Si content (more than 17 at.%) and/or low deposition temperature **[195,206,207]**. Since the mobility of the surface atoms is decreased, the coating tend to grow with a high volume of the amorphous phase or completely amorphous that results in a drop of the hardness. When the Ti-Al-Si-N coating contains a high volume fraction of the amorphous phase, the interaction between the nanocrystalline phase and the amorphous phase becomes negligible and thus the hardness of the coating becomes strongly dependent on the properties of the amorphous phase.

The microstructure of Ti-Al-Si-N coatings is determined not only by Si content but also by the concentration of Ti and Al (N concentration is mainly fixed at around 50 at.% according to the publications considered in this thesis). However, the addition of one element leads to a decrease of another one, therefore the determination of the influence of a concentration of the each element on the evolution of the microstructure of Ti-Al-Si-N coatings is not a simple task. According to Q. Ma **[199]**, except for Si, the Ti concentration has a significant influence on the Ti-Al-Si-N coatings' hardness. The maximum hardness was reached at 63 at.% of Ti and 7 at.% of Si due to the formation of nc-(Ti, Al)N/a-Si_3N_4 nanocomposite structure. Whereas, when Ti content was 29 at.% the amorphous phase was wrapped in the crystalline phase, which is in contrast to the traditional nc-/a- microstructure (see Fig. 1.5). At 42 and 57 at.% of Ti the hardness decreased because of the columnar microstructure of the coatings. Following the results of L. Chen **[197]**, it is concluded that the Al content plays an essential role in the microstructure and hardness of Ti-Al-Si-N coatings. L. Chen showed that the increase of Al content from 0.32 at.% to 0.46 at.% (the decrease of Ti content from 0.62 to 0.49 at.%, Si content was kept constant at 6 at.%) induced a decrease of the (Ti,Al)N grain size and concomitant increase of hardness up to 42.4 GPa due to the formation of nc-(Ti, Al)N/a-Si_3N_4 nanocomposite structure.

Ti-Al-Si-N nanocomposite coatings demonstrate the superior oxidation resistance due to their unique microstructure and elemental composition (Table 3). Due to high chemical inertness to air and excellent anti-diffusion properties at high temperatures of amorphous Si_3N_4, the oxidation and coarsening of nc-(Ti, Al)N/a-Si_3N_4 nanocomposite coatings are avoided, since the grain boundary in-diffusion of oxygen ions and out-diffusion of metal elements through a-Si_3N_4 are inhibited **[208]**. This allows to sustain the properties of the Ti-Al-Si-N coatings up to 1100 °C, since the interface phase a-Si_3N_4

retards the grain growth and decomposition process during thermal annealing **[190]**. Additionally, the inward diffusion of oxygen can be suppressed due to the formation of the dense and protective layer SiO_2 and/or Al_2O_3 on the coating surface during oxidation at high temperatures (Fig. 1.16 **[196]**) **[94]**.

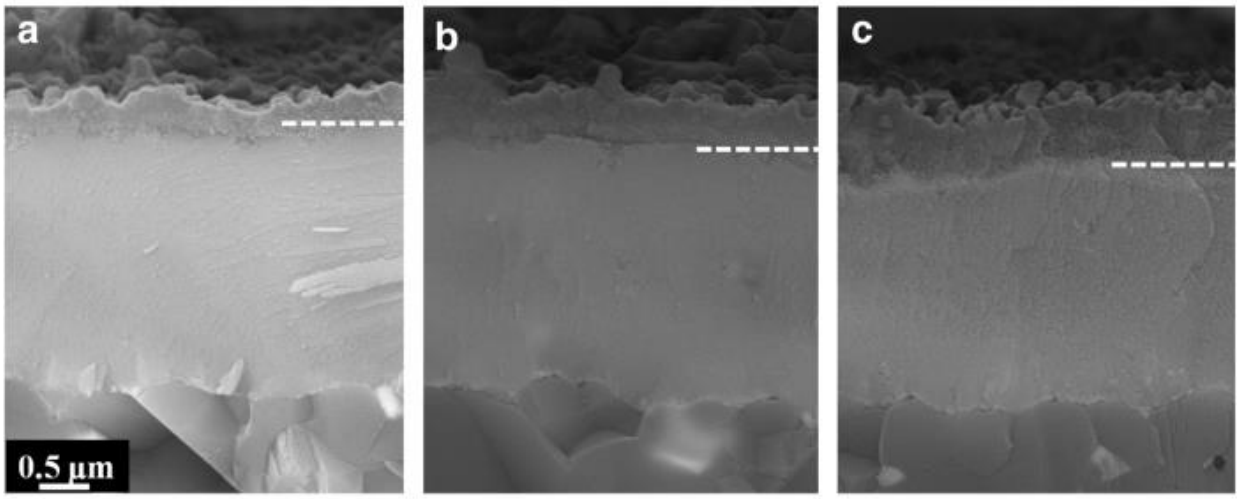

Figure 1.16. SEM facture cross sections of nc-(Ti, Al)N/a-Si_3N_4 coating after oxidation in synthetic air for 15 h: at 1000 °C (a), the second thermal exposure of oxidized (T_a= 1000 °C) coating at 950 (b), and 1100 °C (c) **[196]**.

The ability of an amorphous Si-based phase to inhibit the growth of TiO_2 grains was suggested to be responsible for the improved oxidation resistance of Ti-Al-Si-N based coatings **[196,201]**. Mostly, the increasing of Al and Si content in the Ti-Al-Si-N coatings is known to be responsible for the improvement of the oxidation resistance **[209]**, but, at the same time, this can lead to the decreasing of the hardness as was mentioned above. So it is vitally important to control the elemental composition of Ti-Al-Si-N coatings in order to obtain the optimal combination of the desired protective properties.

The wear resistance of Ti-Al-Si-N coatings do not fit to Archard model and, as was reported **[164,204,210,211]**, the high hardness of the coatings does not always mean high wear resistance. The average friction coefficient of both nc-(Ti, Al)N/a-Si_3N_4 and nc-(Ti, Al, Si)N/a-Si_3N_4 nanocomposite coatings was reported in the range 0.5-0.9. Many studies report **[164,200,205]** that when the tribo-contacts favour the nucleation of tribochemical reactions the average friction coefficient of Ti-Al-Si-N coatings largely decrease with an increase of Si content. The decreasing of the friction coefficient is mainly associated with the formation of self-lubricating SiO_2 or $Si(OH)_2$ tribo-layer as a result of the tribocemical reaction between Si and ambient humidity (Fig.1.17a). Thus, the lowest friction coefficient was reported for Ti-Al-Si-N coatings with a high volume fraction of the amorphous phase

or even for fully amorphous coatings. However, the lowering of the friction coefficient due to the self-lubricious tribo-layer at high Si content is not the only reason of high wear resistance of the coatings. It is showed in the literature **[94,210,212]** that the improvement of wear resistance with the increasing of Si content is due to the formation of a high volume fraction of the amorphous phase which promotes increase of the coatings' toughness (high values of *H/E* ratio). Additionally, a high amount of the amorphous phase was reported to compensate the negative influence of residual stress (due to energetic ion bombardment) in the coatings on their wear resistance.

Some researchers reported on the better wear resistance of amorphous Si-rich Ti-Al-Si-N coatings in comparison to the harder coatings with nanocomposite structure **[164,200]**. This could be due to considerable age hardening by 40 % **[213]** which is caused by a transformation from a mainly amorphous to a nanocrystalline state promoted by high temperature in tribo-contact. However, the wear resistance of such multicomponent amorphous coatings is not fully understood and further studies are needed.

Recently, many researchers have reported on different wear mechanisms of Ti-Al-Si-N coatings depending on the coatings composition, test temperature and environment **[94,205,214,215]**. N. He **[205]** showed that the wear rate of the coatings with relatively high Si content is higher at 400 °C than that at room temperature (Fig. 1.18). This behaviour is explained by absence of $Si(OH)_2$ tribo-layer, since the moisture in the air can be neglected at 400 °C and there is no oxide generated. When the temperature rises to 600 °C, the wear rates of all the coatings decrease that assigned to the formation of the compact surface layer of Al_2O_3 and SiO_2 mixed phases due to outward diffusion of Al and Si (Fig.1.17b and c, and Fig. 1.18). The increase of the temperature up to 800 °C caused the largest variation of the friction coefficient and the friction coefficients of the coatings at 800 °C are lower than that obtained at 600 °C. Interestingly, for the coating $Ti_{0.73}Al_{0.28}Si_{0.08}N$ the friction coefficient was even lower than that at room temperature and the wear rate decreased significantly. This phenomenon explained by the higher diffusion of Al and Si atoms toward the surface with subsequent oxidation as well as the oxidation of TiN to rutile TiO_2 at 800 °C, which could significantly reduce the shear strength in the process of sliding and thus plays the role of a lubricating material.

Z. Xie at el have confirmed **[215]** that nc-TiO_2/a-SiO_2 nanocomposite formed on the surface of Ti-Al-Si-N retains high hardness and relatively low coefficient of friction of the coating at 800 °C. However, the worst wear resistance of other coatings at 800 °C was assigned to the decrease of the oxidation resistance and peeling phenomena. Indeed, T. Chen showed **[94]** that Ti-Al-Si-N coatings with highest Al and Si content exhibit

excellent wear resistance at room temperature and 800 °C due to better oxidation resistance and thermal stability originated from high volume fraction of amorphous Si_3N_4 interphase which effectively stabilize nc-TiAlN grains against the interface reaction and recrystallization during the annealing.

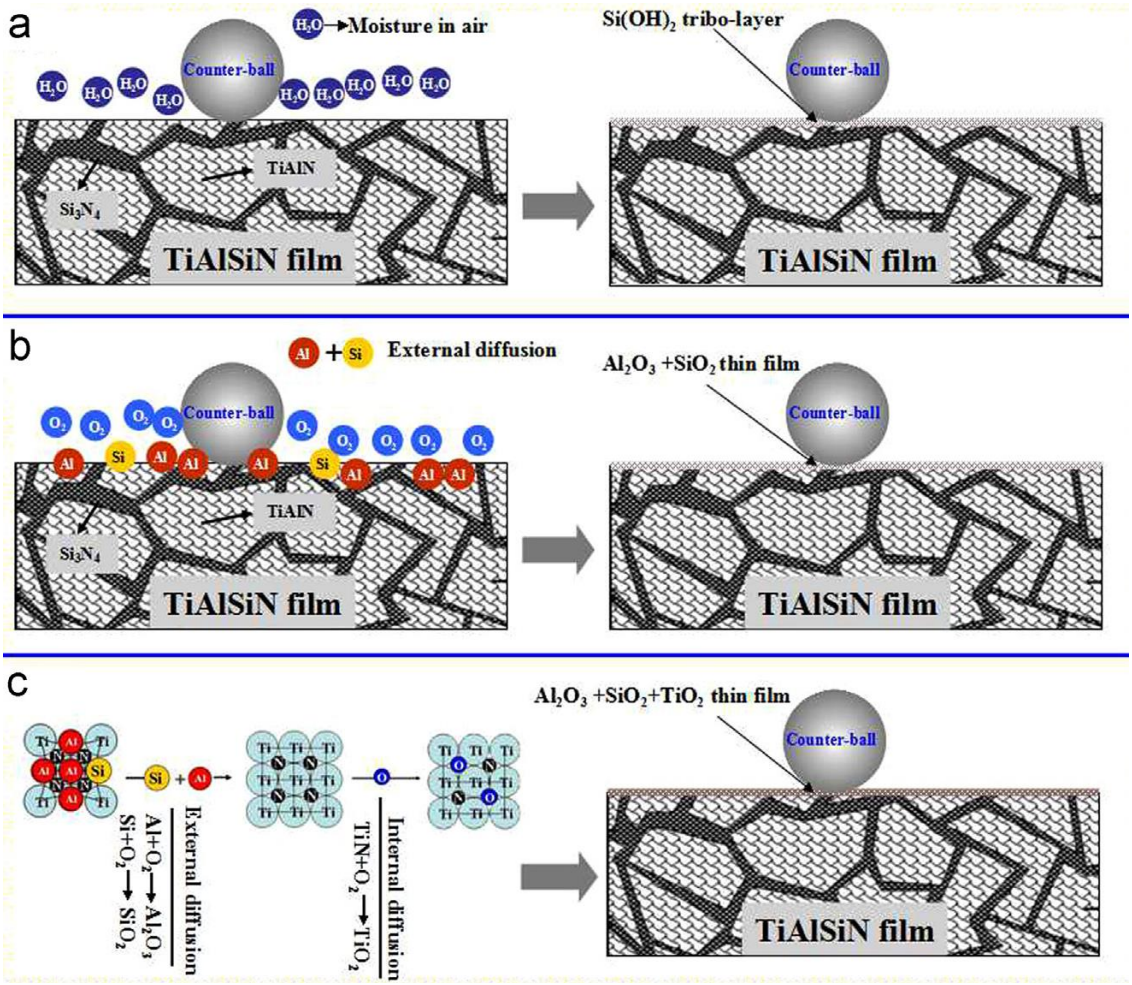

Figure 1.17. Schematic of tribo-layer formation in the process of ball-on-disc test of nc-(Ti, Al, Si)N/a-Si_3N_4 nanocomposite coatings at room temperature with formation of $Si(OH)_2$ (a), at 600 °C with formation Al_2O_3 and SiO_2 mixed oxide film (b), at 800 °C with formation of Al_2O_3, TiO_2 and SiO_2 mixed oxide film (c) **[205]**.

At the same time, G. Fuentes reported **[214]** that high Al content in Ti-Al-Si-N coatings can cause an injurious effect on high temperature wear resistance of the coatings due to the formation of wurtzite-like microstructure which results in low hardness and low adhesion strength. This ability of Ti-Al-Si-N coatings to adapt to high-temperature impact and a high load during friction is responsible for the prolongation of the life time of cutting tools coated by Ti-Al-Si-N coatings **[200]**.

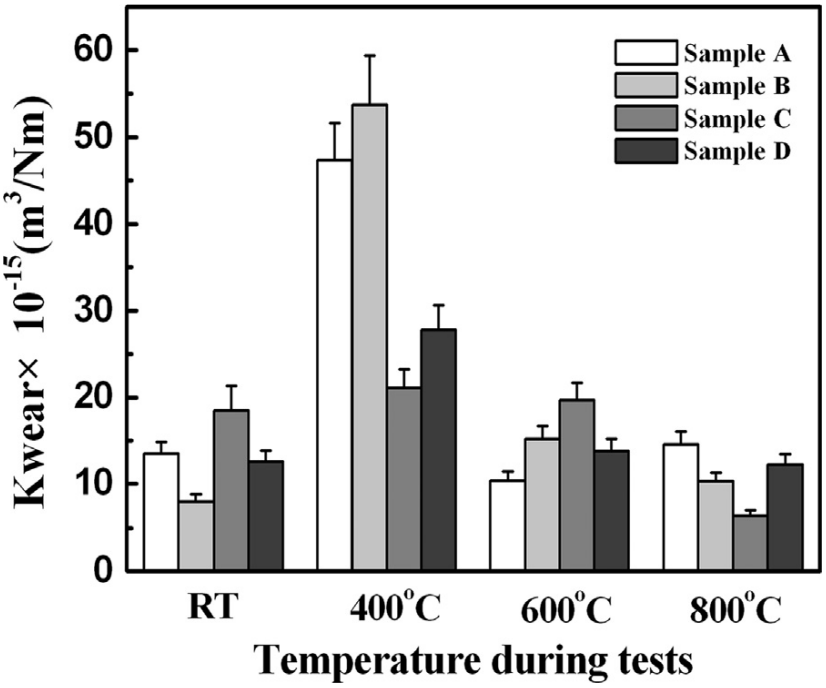

Figure 1.18. Wear rates of the coatings $Ti_{0.86}Al_{0.11}Si_{0.03}N$ (sample A), $Ti_{0.78}Al_{0.17}Si_{0.05}N$ (sample B), $Ti_{0.73}Al_{0.28}Si_{0.08}N$ (sample C) and $Ti_{0.63}Al_{0.28}Si_{0.09}N$ after ball-on-disc tests carried out at RT, 400 °C, 600 °C, 800 °C **[205]**.

The enhancement of the performance of the Ti-Al-Si-N coated drills **[198]**, style inserts **[197]**, end-mills **[200,216]** in comparison to the performance of tools coated by Ti-Al-N and Ti-Si-N is an addition representation of the superior functional properties of Ti-Al-Si-N nanocomposite coatings. Nowadays, Ti-Al-Si-N coatings are available on industrial scale as cutting tool coatings for high speed machining as well as protective coatings on tools for forming and stamping **[4,217]**.

1.5.2 Ti-Al-B-N nanocomposite coatings

Firstly, the incorporation of B into Ti-Al-N with aim to combine the good properties of TiB_2 and Ti-Al-N in one coating system and incorporation of Al and Ti into BN with aim to stabilize cubic BN were unsuccessful because the hardness of the obtained coatings was worse than that of TiB_2, AlB_2 and Ti-Al-N coatings **[218,219]**.

Since B can also form amorphous phases, it was added to Ti-Al-N coatings in order to improve its functional properties in analogy to Si. Boron due to its very low solubility in TiN under equilibrium conditions was found to retard the growth of TiN grains during deposition under proper conditions. There is no clear evidence of whether B substitutes N forming fcc-(Ti, Al)(N, B) solid solution when is being incorporated in low amount (around 0.1 at.%) into $Ti_{1-x}Al_xN$ coatings with $x \leq 0.6$, i.e. in the range of the fcc-(Ti, Al)N

existence, or segregates at the grain boundaries of (Ti, Al)N nanocrystalls forming Ti-B bonds **[220–222]**. However, as has been recently showed by M. Baker **[220]** the both scenario could take place at relatively high B content (around 0.3 at.%) and the growth of amorphous BN phase covering fcc-(Ti, Al)(N, B) grains was observed. Whereas the decrease of N content in the Ti-Al-B-N coatings at B/Al≈5 stimulated the growth of TiB_2 amorphous phase or co-precipitation of very small nanocrystalls of hexagonal TiB_2 **[223]**. The preferable formation of TiB_2 amorphous tissue phase with encapsulated (Ti, Al)(N, B) grains at relatively low N content was also reported in **[220]** (Fig. 1.19). It was showed **[220]** that the increase of B concentration in the Ti-Al-B-N coatings to more than 0.3 at.% leads to competitive grain growth of borides (at low N content) or/and nitrides (at high N content) and was accompanied by reduction of grain size down to full amorphization of the coating.

In general, the highest hardness was reported for coatings with nanocomposite structure where nanocrystalline grains of (Ti, Al)N or (Ti, Al)(N, B) were covered by amorphous tissue phase of BN or/and TiB_2 (see Table 1.4). Among the works on Ti-Al-B-N coatings (Table 1.4), authors do not report on sufficient evidence of the formation of 1 ML thick amorphous phase. However, in the latest work of M. Baker **[220]**, the coverage of the (Ti, Al)(N, B) grains by 1ML a-TiB/a-TiB_2 in the coating with the highest hardness has been clearly showed by means of XRD, XPS and HRTEM (Fig. 1.19). The studies on Ti-Al-B-N coatings listed in Table 1.4 revealed that the enhancement of the coatings hardness is due to Hall-Petch strengthening and the nanocomposite structure with optimal grain sizes and sufficient amount of amorphous phase. According to the studies, the nanocomposite structure with the highest hardness and elastic modulus forms when the coatings contain B in the range of 0.1-0.3 at.% and the volume fraction of fcc-(Ti, Al)N grains is maximally high. The relatively lower hardness values were reported for the amorphous Ti-Al-B-N coatings or for the coatings with a high volume fraction of the amorphous phase and a very small grain size. The highest hardness among the amorphous coatings was reported for the coatings with high density and high volume fraction of TiB_2 phase **[220,223]**. Additionally, it was showed that the incorporation of low amount 0.05 at.% of either B or Si into fcc-(Ti, Al)N can enhance the hardness to the same extent due to solid solution strengthening **[222,224]**.

In spite of a considerable research work which have been carried out on the characterization of the structure and mechanical properties of Ti-Al-B-N coatings, their thermal stability and oxidation resistance have been less studied. However, it was reported that the doping of hcp-(Al, Ti)N with low amount of B results in the increase of the

Table 1.4. Structure-property relationship of Ti-Al-B-N based nanocomposite coatings deposited by means of different PVD methods.

Composition, at %				Structure	Hardness, GPa	Elastic modulus, GPa	Grain size, nm	Oxidation temperature, °C	Deposition method	Ref.
Ti	Al	B	N							
0.15*		2.7*	1.15*	$B_{48}B_2N_2$+hcp-TiBN	16.18	–	–	–	RF magnetron sputtering	**[219]**
0.55*		3.9*	3.3*	fcc-TiBN+hcp-BN	10.79					
–	–	–		–	17.24	–	–	–	DC magnetron sputtering	**[218]**
0.63	0.37	2.32	1.47	nc-Ti(Al)N/nc-TiB_2/nc-BN	26	300	–	–	Electron beam plasma assisted PVD	**[225]**
0.73	0.27	0.65	0.85		30	350				
0.80	0.2	1.08	1.92		18	300				
0.28	0.31	0.31	0.10	a-TiAlBN	15	200	–	–	DC sputtering	**[214, 219]**
0.21	0.29	0.29	0.21	nc-AlN/nc-TiN	16.5	220				
0.19	0.20	0.22	0.39	a-TiAlBN	15	195				
0.28	0.10	0.52	0.10	nc-TiB_2/a-AlN	24	285	2-3			
0.24	0.09	0.5	0.17	a-TiAlBN	23	260				
0.2	0.08	0.4	0.32	a-TiAlBN	15	170				
0.12	0.14	0.34	0.40	a-TiAlBN	17	210	–	–	Electron beam plasma assisted PVD	**[227]**
0.21	0.12	0.27	0.41		18	220				
0.23	0.10	0.25	0.42	nc-Ti(Al)N/nc-TiB_2/a-BN	20	250				
0.30	0.12	0.17	0.41		30	310				
0.34	0.11	0.15	0.40		37	320				
0.3	0.1	0.22	0.38	nc-(Ti, Al)(N, B)/a-BN	–	–	0.6-3	–	Magnetron sputtering	**[221]**
0.38	0.08	0.27	0.27	nc-TiAlN/nc-TiB_2/a-BN			0.3-0.1			

Table 1.4. Continuation.

0.10	0.11	0.3	0.49	nc-(Ti, Al)N/a-BN	21	240	3	–	Electron beam PVD	**[148, 149, 217]**
0.17	0.09	0.26	0.48		22	250	5			
0.25	0.1	0.16	0.49		40	340	5-6			
0.36	0.08	0.06	0.5		40	340	5-6			
0.39	0.07	0.04	0.5		26	300	4			
0.32	0.62	0.06	–	hcp-AlTi(B)N	39	–	5-15	–	DC sputtering	**[229]**
0.44	0.44	0.12	–	nc-$TiAl_3$/nc-TiN	25		8-12	800	RF magnetron sputtering	**[230]**
0.48	0.47	0.05	–	fcc-(Ti, Al, B) N	32	–	90	900	Cathodic arc ion plating	**[222]**
0.31	0.68	0.0003		fcc-(TiAl)N+hcp-(AlTi)N	–	–	–	900 for 1 h	Cathodic arc evaporation	**[201]**
0.31	0.68	0.014								
0.15	0.06	0.39	0.39	fcc-TiAlN/a-BN/ a-Ti(Al)B_2	22	225	2	–	Electron beam PVD	**[220]**
0.12	0.07	0.33	0.48		22	240	2			
0.21	0.05	0.24	0.48		32	277	5.2			
0.47	0.04	0.34	0.13	a-TiAlBN	26	260	3			
0.52	0.04	0.17	0.26	fcc-(Ti, Al)(B, N) / a-TiB_2/a-TiB	32	280	1.8			
0.21	0.24	0.03	0.51	fcc-TiAlN/nc-TiB_2	36	–	–	–	Magnetron sputtering	**[224]**
–	–	–	–	a-TiAlBN	35-37	–	–	–	Magnetron sputtering	**[231]**
0.16	0.28	0.03	0.53	a-TiAlBN	20	213	–	–	Cathodic arc evaporation	**[97]**

– Denotes data are not given in the references or not determined

* – only molar fractions are given in the reference

hardness values at 500 °C which remained unchanged up to 700 °C **[229]**. C. Rebholz has showed **[228]** that nc-(Ti,Al)N/a-BN coatings with relatively low B content demonstrate age hardening from 39.5 GPa to 45 GPa at 700 °C which occurs due to completion of phase segregation. Whereas, the B rich coatings with high volume fraction of amorphous phase demonstrated stability of the hardness even at 900 °C.

I. Zukeram has reported **[230]** on an onset of oxidation of Ti-Al-B-N coatings with 12 at.% of B at 850 °C. V. Derflinger **[222]** and later M. Pfeiler **[201]** have showed that the alloying of fcc-(Ti, Al)N and hcp-(Al, Ti)N with 5 and 0.5 at. % of B, respectively, improves the oxidation resistance of the fcc-(Ti, Al)N based coatings at 900 ºC during 30 minutes and of the hcp-(Al, Ti)N at 900 °C during 60 minutes, while the addition of the same amount of Si to the coatings improves the oxidation resistance of the coatings much better. This was assigned by M. Pfeiler to the ability of B to modify the oxidation sequence of Ti by delaying the transformation of anatase to rutile. However, at longer oxidation time, B sublimates from the coating that deteriorates the performance of B doped coatings, while Si containing coatings remain stable during longer oxidation time.

In the work of J. Morales-Hernandez **[232]**, the reported elemental composition of the TiAlBN coatings is not in an agreement through the text, and therefore the results reported in their paper are not included into Table 1.4.

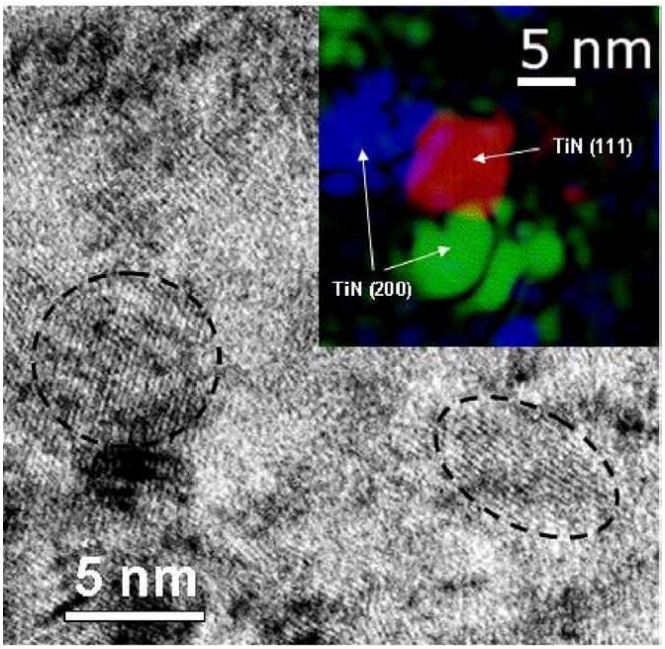

Figure 1.19. HRTEM image of nc-(Ti, Al)(N, B)/a-TiB_2/a-TiB nanocomposite coating (H=32 GPa) with an inverse Fourier Transformed filtered image as an inset, highlighting the (Ti,Al)(N, B) nanocrystals **[220]**.

In contrast to hardness, the tribological properties of Ti-Al-B-N coatings tend to the improvement when the content of amorphous BN increases. Thus, no failure in the wear path after 15000 passes and low wear rate were observed for amorphous Ti-Al-B-N coatings with B/Al~5, which contained a large amount of amorphous BN **[226]**. Furthermore, the Ti-Al-B-N coatings showed a reduction of the friction coefficient from 0.8 to 0.7 and the enhancement of the wear resistance with the increasing of amount of lubricious hexagonal BN **[225]**. D. Jung reported **[224]** that low B content in the coatings favours the decrease of the friction coefficient more considerably compared to approximately the same amount of Si. Frequently, Ti-Al-B-N coatings with high volume fraction of (Ti,Al)N grains exhibited high *H/E* ratio values, i.e. high fracture toughness, and, thus, had an excellent wear resistance and wet-cutting performance, demonstrating a 150 % increase in lifetime compared to standard TiAlN and TiN **[158,225,227,228]**.

1.5.3 Ti-Al-B-Si-N nanocomposite coatings

Currently, a systematic study on doping of Ti-Al-N by both Si and B is lacking. Only two research groups have recently reported on structure-property relationships of Ti-Al-B-Si-N nanocomposite coatings **[97,104,233,234]**. The group of D. Shtansky **[233–235]** reported on the oxidation resistance of amorphous Ti-Al-B-Si-N coatings with high Ti/Al ratio (~4.8) and high B content. The onset of oxidation of the coatings was observed beginning from 800 °C that resulted in inward diffusion of Oxygen to the depth of more than 500 nm and nucleation of TiO_2. The oxidation at 800 °C for 1 hour caused the formation of a very thin oxide layer of TiO_2 and $TiBO_3$ on the surface and the enrichment of the subsurface region in TiN_xO_y and $Ti_xAl_ySiO_z$. However, the increase of oxidation temperature to 900 °C led to the full oxidation of the coating. The coating showed high temperature stability that was demonstrated by the increase in hardness from 15 to 20 GPa after annealing at 800 °C in vacuum and subsequent decreasing at 1000 °C. Moreover, the wear rate and friction coefficient of the Ti-Al-B-Si-N coatings were found to increase after annealing at 600 °C, but decreased after annealing at 800 °C. At the same time, C. Paternoster et al **[236]** reported that the formation of several oxide layers of mixed rutile-TiO_2+Al_2O_3 and TiN phase and decrease in hardness from 21 to 15 GPa were observed after oxidation at 900 ºC for 4 hours of amorphous Ti-Al-B-Si-N coatings with lower Ti/Al ratio (~2.8).

H. Fager et al showed **[97]** that the annealing of amorphous Ti-rich Ti-Al-B-Si-N coatings in vacuum results in the coatings crystallization by clustering of hexagonal TiB_2

at 700 °C which further disappears at higher temperature while TiN grains start to nucleate only at 900 °C and continue to grow at higher temperature up to 1100 °C. These phase transformations were accompanied by increase of hardness of the coatings from 17-18 GPa to 21 GPa.

It is important to note, that all the authors have reported in their works on amorphous Ti-Al-B-Si-N coatings on the fact that the diffusion of substrate material to the coatings during high temperature annealing promoted a decrease of crystallization temperature and nucleation of unfavorable phases. This fact points on the necessity of the suppression of the substrate material diffusion to the coating by applying diffusion barrier layer. So far investigated Ti-Al-B-Si-N coatings were fabricated with high Ti/Al ratio that highly favors to the growth of non-protective TiO_2 at the coating surface while the formation of topmost protective layer of Al_2O_3 or SiO_2 was less probable. In my opinion, this may be the decisive factor which is responsible for the poor oxidation resistance of these coatings at high temperatures. Moreover, the slight increase of the hardness of Ti-Al-B-Si-N coatings at high temperatures was not clearly explained in those works. Thus, there is still a need for a deeper and thorough characterization of structure-property relationships of amorphous Ti-Al-B-Si-N coatings at high temperatures. As a result, the better understanding of their structural features and corresponding properties will open a way for their possible applications.

Moreover, the works on Ti-Al-N based coating have been devoted to that with high Ti content that apparently favours the formation of fcc phase. However, the stabilization of fcc phase with high Al content is of technological interest because such coatings demonstrate much better functional properties. However, in the most studies on the alloying of Ti-Al-N this fact was mainly ignored, and the most of Ti-Al-N-based coatings were studied with relatively high Ti content. The different ways for the stabilization of the Al-rich fcc-(Ti, Al)N phase were proposed, among which the alloying by other TM or metalloinds. The latter assumes the formation of either the amorphous tissue or a solid solution. The alloying of Ti-Al-N with metals and metalloids is one of the ways for stabilization of fcc phase with high Al content. Indeed, recent ab initio studies of H.W. Hugosson **[237]** suggest that the alloying of Ti-Al-N with B, Si, O and C is a promising way for stabilization of fcc-(Ti, Al)N with high Al-content. The recent studies were focused on doping by B, Si, O or C of TiAlN coatings with high Ti content in the range of fcc phase. While the studies on the alloying of Al-based Ti-Al-N coatings with low amount of B **[201,222,229]** or Si **[201,222]** are insufficient to understand the effect of alloying on the structure-property relationship of this coatings.

1.5.4 Gradient nanocomposite coatings

Up to date, a wide range of structural architectures have been employed for the designing of protective coatings with the aim to enhance their performance such as nanomultilayer coatings, single-layer nanocomposite coatings, smart adaptive coatings and more recently functionally gradient coatings. Functionally gradient coatings are an integrative approach in the engineering of protective coatings which creates a midway link between single-layer nanocomposite coatings and nanomultilayer coatings that allows to combine the benefits of both coatings in one.

Functionally gradient coatings are either composite or single phase coatings in which their functional properties change uniformly or unevenly at least in one direction by smoothly varying distribution of phases and/or elemental composition. It is possible to easily regulate the wide spectrum of functional properties of gradient coatings by changing during deposition process the proportions of reactive gases and/or sputtering intensity of materials, chamber pressure, substrate temperature and substrate bias voltage.

Thus, better mechanical properties and adhesion were achieved when using gradient (Ti, Al)N coating than in the corresponding single-layer coating. It was realized by a linear change of chemical composition of the gradient coating in the direction from the substrate to the coating surface, in particular, the distribution of stresses on the coating surface and at the substrate/coating interface has determined such behaviour **[238]**. Moreover, the gradient (Ti, Al)N coating has improved the durability of the cutting tool in comparison with the single-layer coating. The gradient (Ti, Al)N coatings deposited by varying substrate bias voltage exhibited better adhesion and lower friction coefficient as compared to the corresponding single-layer coatings **[239]**. This was attributed to the improved stress–strain distribution within and around the interface of the gradient coating and the substrate. The (Ti, Al)N coatings with gradient of N concentration demonstrated better hardness than that of the single-layer coatings due to gradual increase of N concentration that caused growth of hard ceramic phases. Additionally, thermal shock resistance of these coatings was reported to increase too due to a small difference of thermal stress and thermal strain between any two conterminous layers and presence of soft metal phase which relaxes a part of thermal stress **[240]**. There is no a pile-up of stress and the stress maxima is much smaller in the laminate with a graded interlayer due to smoothly changing composition as compared to the laminate with homogeneous layers and sharp interfaces. This smooth stress distribution is responsible for an increased lifetime **[241]**. Additionally, gradient coatings may be kinetically stabilized against the recrystallization at elevated

temperature due to microstresses and concentration gradients which can influence the diffusion coefficient and also change the melting point of the coating material **[242,243]**.

Nowadays, this concept was applied for nanocomposite coatings with different elemental composition. Thus, gradient nanocomposite coatings Ti-Al-Si-N and Ti-Al-Cr-N with increasing Al content toward the surface **[232–235]**, Ti-Al-Cr-N and Ti-Al-Nb-N with increasing N content toward the surface **[248,249]** were successfully developed. All this gradient nanocomposite coatings had much better functional properties in comparison to conventional nanocomposite or nanomultilayer coatings. Therefore, gradient nanocomposite coatings can markedly outperform single layer nanocomposite coatings and nanomultilayer coatings in machining tests, especially those carried out at high speeds, where high temperatures of 800 °C – 900 °C are reached (Fig. 1.20).

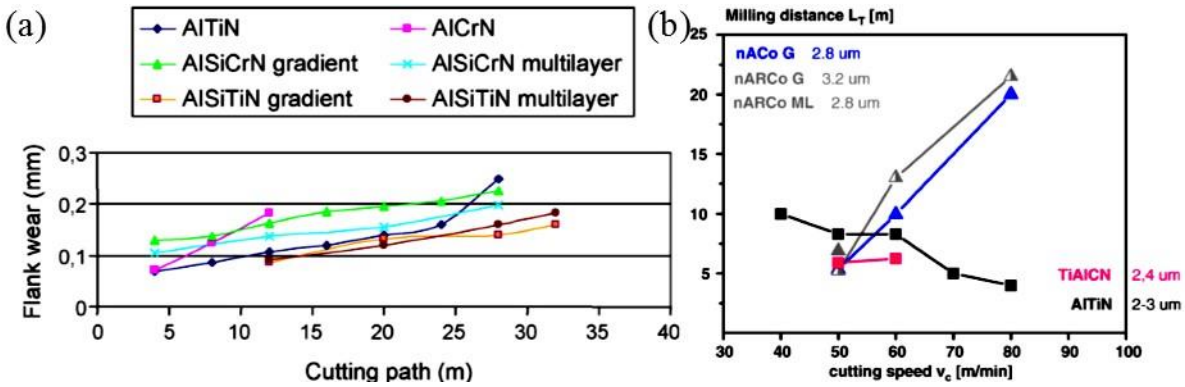

Figure 1.20. (a) Cutting test results in terms of flank wear vs. cutting path for conventional AlTiN, AlCrN, and AlSiCrN and AlSiTiN with both gradient and multilayer structure **[245]**. (b) Dependence of the lifetime of mills made of HSSCo8 and coated with nACo G (AlTiSiN-based nanocomposite gradient coating with increasing Al-content toward the surface), nACRo G (AlCrSiN-based nanocomposite either with Al gradient or a multilayer (ML)), TiAlCN and AlTiN **[4]**.

The concept of nanocomposite coatings with gradient elemental composition offers excellent potential for further enhancement of the properties of protective coatings. Different operation conditions influence on protective coating's structure and its properties in different way during the performance. Therefore, it is vitally important to design corresponding protective coatings that will be able to withstand a destructive influence at a certain stage of exploitation. In this regard, the concept of gradient nanocomposite coatings is still need to be studied using different elemental combinations and various types of structural architectures that may allow obtaining efficient protective coatings. Moreover, the realization of this approach by applying to multielement nanocomposite coatings, such

as Ti-Al-B-Si-N, can significantly contribute to the development of more advanced protective coatings and will serve for the development of the protective coatings field.

Hence, despite the extensive study of the TiAlN based coatings over the last years, there are still many open questions and challenges that call for solution. In this regard, in an attempt to contribute to the understanding of some of the open questions in this field of material science, as well as to comprehend the mechanism behind these issues, the following objectives of the thesis are determined.

Objectives of the thesis

The main aim of this thesis is a thorough and meticulous characterization of TiAlSiBN based coatings obtained by means of magnetron sputtering. In order to further understand the complex structural features and tribomechanical properties of TiAlSiBN based coatings, the following objectives were established:

- **Synthesis and characterization of gradient nanocomposite coatings based on TiAlSiBN.**

– to grow TiAlBSiN coatings with gradient microstrusture and composition by means of combined reactive/non-reactive DC magnetron sputtering of composite target AlN–TiB_2–$TiSi_2$;

– to investigate the effect of N injection during the growth of TiAlBSiN coatings on their structure and properties;

– to qualitatively evaluate the alloying of Al-rich TiAlN coatings with high amount of B and Si;

– to determine and investigate tribological and mechanical properties of TiAlBSiN coatings.

- **Synthesis and characterization of amorphous nanocomposite coatings based on TiAlSiBN.**

– to deposit amorphous TiAlBSiN based coatings by means of DC magnetron sputtering of composite target AlN–TiB_2–$TiSi_2$;

– to investigate the effect of high temperature annealing at 900 °C in ambient air on structural-phase composition of amorphous TiAlBSiN coatings;

– to evaluate and discuss the oxidation resistance and thermal stability of amorphous TiAlBSiN coatings;

– to investigate the effectiveness of the sacrificial barrier layer between amorphous TiAlBSiN coatings and Si substrate during high temperature annealing at 900 °C;

– to study and discuss the effect of structural-phase transformation in amorphous TiAlBSiN coatings after high temperature annealing at 900 °C in ambient air on their tribo-mechanical characteristics.

Chapter 2

Overview of experimental methods and techniques

This chapter rewiev experimental methods and techniques used throughout the thesis. The chapter starts with a detailed description of the deposition technique and the target synthesis method used in this work. Then, a description of the each of the techniques used for the structural, microstructural, morphological and chemical characterization is presented. Additionally, the methods used for characterization of the mechanical and tribological properties of the coatings are introduced in this chapter.

2.1 Growth technique

Coatings in this thesis were grown by means of DC magnetron sputtering operating in reactive and non-reactive modes. The coatings were deposited in V.N. Karazin Kharkiv National University (Ukraine) under the direction of Prof. V.M. Beresnev. The schematical representation of DC magnetron sputtering system is shown in Figure 2.1. The coatings were deposited on steel 45 and Si (001) substrates. The substrates were cleaned in Ar plasma discharge using a bias voltage of – 600 V during 15 min prior to deposition. The discharge power was supplied from a stabilized DC power unit (400 V, 7.7 A) working in the voltage-regulated mode. High-temperature ceramic AlN–TiB_2–$TiSi_2$ was used as a target.

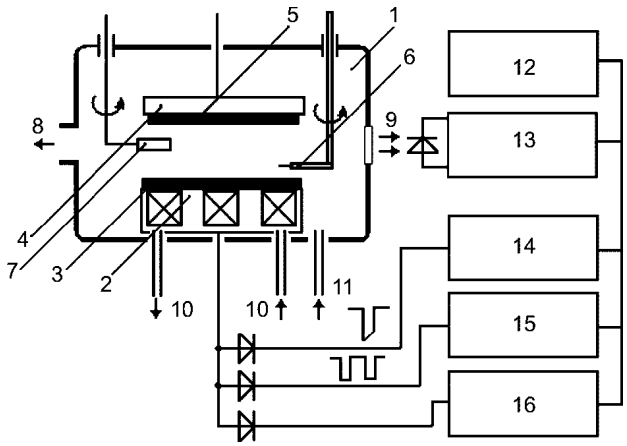

Figure 2.1. Schematic representation of magnetron sputtering system: 1 – vacuum chamber, 2 – planar magnetron, 3 – sputtering target, 4 – substrate holder, 5 – substrate, 6 – Langmuir probe, 7 – quartz thickness and the deposition rate measuring instrument, 8 – pumping, 9 – observation window, 10 – water cooling, 11 – operational gas buffing, 12 – system of control and data acquisition, 13 – photometer, 14 – ignition block, 15 – impulse power supply unit, 16 – constant power supply unit.

2.1.1 Target synthesis

High-temperature ceramic AlN–TiB_2–$TiSi_2$ target 70 mm in diameter and 40 mm thickness was synthesized from a powder mixture of AlN (50 wt.%), TiB_2 (35 wt.%) and $TiSi_2$ (15 wt.%) by hot isostatic pressing at 1860–1880 °C in air. The residual porosity of the target was less than 2%. Due to corrosion resistance of AlN up to 1000 °C **[250,251]**, electric conductance and superior physical and mechanical properties of both TiB_2 and $TiSi_2$, the high temperature composite ceramic AlN-TiB_2-$TiSi_2$ is a promising candidate for the production of protective coatings for high temperature applications **[252,253]**. Bulk ceramics AlN-TiB_2-$TiSi_2$ display superior physical, mechanical and tribological properties up to 1450 °C **[254]**. Moreover, such metalloids as Si and B can very effectively stabilize an amorphous phase. The addition of a relatively low Si amount to the coating can effectively suppress grain growth and promote the re-nucleation of grains. Furthermore, the addition of Si in a very small concentration can significantly improve the thermal stability and oxidation resistance of the coating. Boron is known to be both three- and fourfold coordinated and thus can stimulate the growth of an amorphous phase and additionally, it was reported that the incorporation of B into the coating significantly decreases the mass changes during oxidation processes at high temperatures **[221,255]**.

The target synthesis was carried out in the Frantsevich Institute for Problems of Materials Science, National Academy of Sciences of Ukraine by I.A. Podcherniaieva.

2.1.2 Deposition of the gradient coating

The deposition parameters were chosen from the previous publications on TiAlBSiN coatings. These parameters were further used for the test deposition of TiAlBSiN coating in order to optimize the parameters in our set-up **[256]**.

The deposition of the gradient nanocomposite coatings was performed using the following parameters of DC magnetron: discharge current ~200 mA, cathode–substrate distance was 65 mm. A negative DC bias of –100 V was applied to the unheated substrates during whole deposition process. In order to produce gradient composition of the coating the deposition started in non-reactive mode with Ar gas partial pressure 0.078 Pa for 60 min. Then the target was sputtered in gas mixture of argon and nitrogen in amount 5%N_2/Ar. The nitrogen-to-argon ratio and working gas pressure at ~0.078 Pa were kept constant during next 35 min of deposition. The obtained thickness of the gradient coatings was approximately 1 μm.

2.1.3 Deposition of the amorphous coating

The deposition of the amorphous coatings was performed using the following parameters of DC magnetron: discharge current ~200 mA, argon pressure 0.078 Pa, bias potential on the unheated substrate – 200 V, substrate ion current density ~ 1 mA/cm^2, cathode-substrate distance was 65 mm. Deposition time was 90 min with a deposition rate of ~11nm/min. The barrier layer was deposited by means of reactive DC magnetron sputtering with the use of 5% O_2/Ar mixture. The obtained thickness of the amorphous TiAlSiBN coatings was approximately 1 μm.

The as-deposited amorphous coatings were annealed in air at 900 °C in ordet to investigate their thermal stability and oxidation resistance. The annealing cycle consisted of 4 stages: heating up to 200 °C for 15 min, heating up to 900 °C for 60 min, annealing at 900 °C for 60 min, cooling to RT for 30 min.

2.2. Characterization Techniques

2.2.1 Atomic Force Microscopy (AFM)

Atomic force microscopy is a standard tool in nano- and microtechnology for the characterization of surfaces **[257]**. The AFM is capable of producing very high resolution, three-dimensional images of a sample surface and is widely used for surface height imaging and roughness characterization at the nanoscale **[35]**. The characterization of the surface roughness is important for the field of protective coatings because the deformation of asperities influences the contact and subsurface stresses in a loaded contact during the friction and wear.

Surface roughness basically refers to the variations in the height of the surface relative to a reference plane. Among all surface roughness parameters, the vertical characteristics of the surface deviations can be expressed by the following most important amplitude parameters:

- Average roughness (R_a). Ra is defined as the arithmetic mean of the absolute value of vertical deviation from the mean line through the profile and can bedefined by:

$$R_a = \frac{1}{n}\sum_{i=1}^{n}\left|z_i - \bar{z}\right| \qquad (2.1)$$

  where n is the number of data points on the profile, and z and $\bar{z}$ are the data points on the profile and the average, respectively.

- Root-mean-square roughness (R_{rms}). R_{rms} is the standart deviation of the distribution of surface heights and defined as the square root of the arithmetic mean of square of the vertical deviation from the mean line:

$$R_{rms} = \sqrt{\frac{1}{n}\sum_{i=1}^{n}\left(z_i - \bar{z}\right)^2} \qquad (2.2)$$

The operation of an AFM based on the registration of the interaction of a mechanical probe (a sharp tip) with the sample surface (Fig. 2.2a). A tip is attached to the free end of spring-like cantilever whose vertical and lateral deflections, caused by the reaction of the probe to the forces that the sample imposes on it, are monitored by an optical detection system (a split photodiode register the laser signal reflected by the back side of the cantilever). The sample is mounted on the sample stage which permits a displacement in x, y, and z directions with respect to the tip apex. The detection system measures the deflections of the cantilever and further converts them into an electric signal which then processed by a computer providing a topographical image of the surface. The imaging of the sample surface can be performed by two main operation modes of the AFM. In a contact mode (Fig. 2.2b, upper), the probe tip is scanning the sample in the x-y plane remaining in constant contact with the sample surface. A feedback loop keeps the probe-sample force constant and uses the feedback response, which is caused by the sample topography, to generate a topographic image.

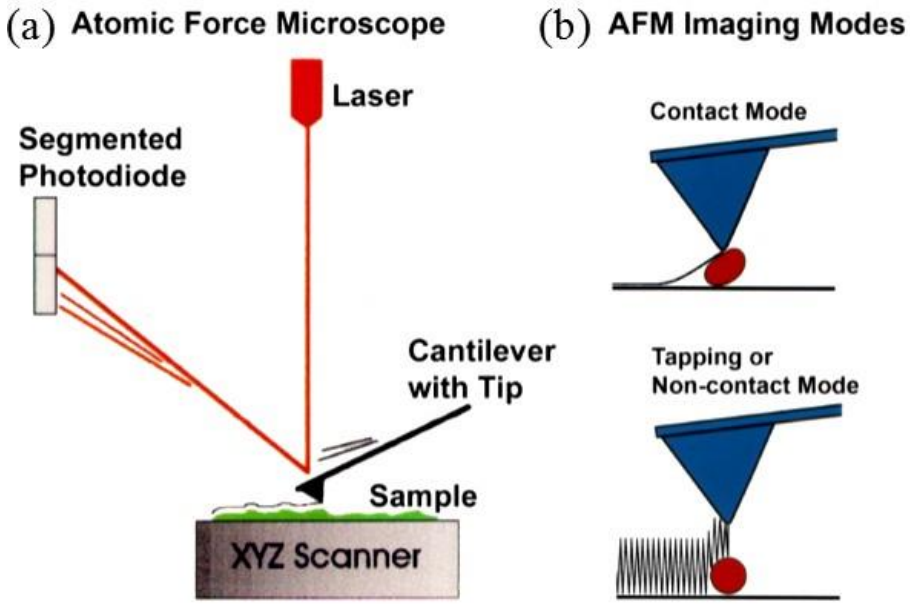

Figure 2.2. Principle of the Atomic Force Microscopy technique (a) and representation of the contact mode (upper image) and tapping mode (lower image) (b).

In a tapping mode (or a noncontact mode) (Fig. 2.2, lower image), the sample topography is scanned by an oscillating probe tip which is lightly tapping the sample surface. An amplitude of the cantilever oscillation changes when the tip approaches sufficiently close to the sample surface. The amplitude changes at each data point due to electrostatic forces and Van der Walls interaction between the tip and the surface. The surface topography image is obtained by monitoring these changes when the tip encounters features of different height.

2.2.1.1 AFM apparatus description

The topography and structure of coatings' surface were studied by means of AFM at the Nanobiomedical Center of Adam Mickiewicz University under the supervision of Dr. hab. Maciej Wiesner. Measurements were performed using atomic force microscope Bruker Dimension Icon operating in contact mode and by using Si_3N_4 cantilever with Si probe (SNL-10) with radius of curvature 2 nm. The AFM images were analysed by means of Gwiddion scanning probe microscopy software **[258]**.

2.2.2 Scanning electron microscopy (SEM) and energy-dispersive X-ray spectroscopy (EDS)

A scanning electron microscope (SEM) is the most popular type of electron microscope that allows to analyse the sample surface topography, morphology and element composition. In SEM, a solid sample is placed in a vacuum chamber and scanned by an electron beam. Electrons of the incident electron beam interact with atoms of the solid sample penetrating to a depth of a few microns depending on the accelerating voltage and the density of the sample. Due to elastic and inelastic electron scattering by the sample atoms, the generation a variety of useful signals occurs from the sample such as secondary electrons (SE), Auger electrons, backscattered electrons (BSEs), fluorescent X-ray and characteristic X-Rays (Fig. 2.3). Each of these signals carries an information on the structure and elemental composition of the sample and can be detected by specialized detectors of SEM. In general, SE are generated within small depth (<5 nm for metals) below the surface and escape into the vacuum toward the detector. The secondary electron yield depends on the angle between the incoming electron beam and the sample surface. Thus, the SE signal intensity registered by the detector represents the variations of the surface structure (topography) of the sample. As a result of the synchronization of the beam position on the sample with an image pixel, and the modulation of the pixel

brightness by the signal from the SE detector, the resulting image displays topological contrast of the sample surface. Since the fraction of BSEs increases with atomic number of the sample material, the registration of BSEs is used in SEM to produce images with atomic number contrast **[259]**.

The incident electron beam may excite inner-shell electrons of the sample atom that can cause the ejection of electrons from the shell and the creation of an electron vacancy (hole). An electron from outer-shell fills the hole with subsequent emission of the energy difference between the high energy outer-shell and low energy inner-shell in the form of an X-ray photon. The energy of this photon is unique ("characteristic") for each element. The measurement of the number and energy of X-ray photons emitted from the sample by means of energy-dispersive spectrometer (EDS) allows to determine the elemental composition and concentration ratios of elements of the sample. The coupling of SEM with EDS allows to obtain spatial distribution of elements over the sample surface or in depth distribution on the cross-sections of a sample.

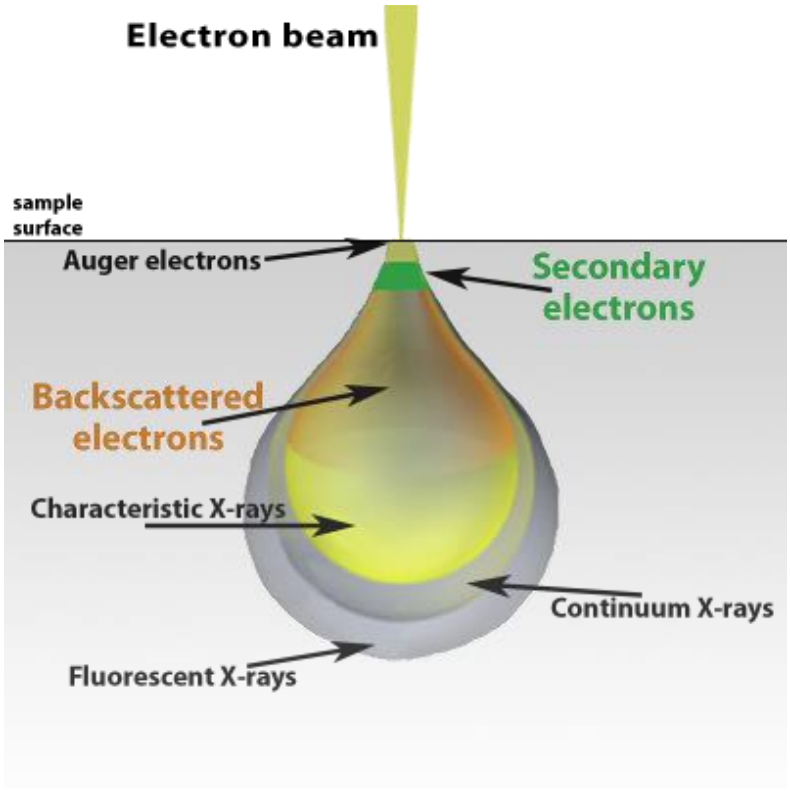

Figure 2.3. Schematic of electron beam interaction with a solid sample.

The modern SEMs provides an image resolution typically between 1 nm and 10 nm, which depends on multiple factors such as the electron spot size, penetration depth of the electron beam and the sample preparation.

2.2.2.1 SEM apparatus description

The surface microstructure and elemental composition of coatings were examined by scanning electron microscope (SEM) JEM-7001TTLS, JEOL at the Nanobiomedical Center of Adam Mickiewicz University under the supervision of Dr. Barbara Peplińska. The imaging of the coatings surface and their cross-sections was carried out in SE regime by applying accelerating voltage of 15 kV. The investigation of the coatings after wear tests was carried out by means of SEM with EDS. The preparation of cross-sectional samples was performed using focused ion beam system (see section 2.2.4).

2.2.3 Transmission electron microscopy (TEM)

A transmission electron microscope (TEM) is a very powerful type of electron microscope which is capable of imaging structural features of a material such as the crystal structure, grain boundaries, defects, density variations, etc. **[260]**. In TEM an electron beam is accelerated at a voltage of around 120-200 kV and focused toward a very thin sample (typically less than 200 nm) by means of electromagnetic lenses. Electrons of the beam have energy in the range 100-1000 keV and are partially transmitted through the sample undergoing elastic and inelastic scattering by the specimen atoms. The differential scattering of electrons results in intensity variations at the exit surface of the sample that reflects information about the internal structure of the sample. Further, these intensity variations are magnified by the system of electromagnetic lenses and the resultant image is projected on the fluorescent screen or recorded by charge-couple device camera which can be displayed on a computer monitor. The image resolution of the microscope can be described in terms of Rayleigh criterion which states that the smallest distance that can be resolved, δ, is given approximately by **[260]**:

$$\delta = \frac{0.61\lambda}{k \sin \beta} \tag{2.3}$$

Here, λ is the wavelength of the radiation, k is the refractive index of the viewing medium, and β is the semi-angle of collection of the magnifying lens. Louis de Broglie's equation shows that the wavelength of electrons is releted to their energy, E_e, ignoring relativistic effects and the inconsistency in units, as follows:

$$\lambda = \frac{1.22}{E_e^{1/2}} \tag{2.4}$$

For simplicity $k \sin\beta$ (which is called the numerical aperture) can be approximated to unity and so resolution is equial to about half the wavelength of electrons. So from equation (2.4) it is clear that for an electron microscope operating at acceleration voltage of 200 kV, $\lambda \sim 3$ pm (0.003 nm), which is much smaller than the diameter of an atom.

The selection of direct electron beam (transmitted) while excluding scattered beam by the objective diaphragm allows to obtain bright-field image of the sample, whereas the registration of only scattered beam results in dark-field image. The contrast in these imaging modes occurs due to variations in sample's thickness or mass (atomic number) or a combination of the two. The each atom in the sample acts as a scattering centre for electron wave and cause the generation of new wavelets at the exit surface of the sample. The secondary wavelets will interfere creating a diffraction pattern as regular array of scattered intensities (spots) which carry information about the distribution, number and types of atoms in the sample, while the relative positions of the diffraction spots are determined by the size and shape of the unit cell.

As it was mentioned before, the sample for TEM studies must be very thin in order to be electron transparent (typically less than 100 nm for TEM with accelerating voltage 200 kV). Thus, the preparation of samples for TEM requires a very precise and careful preparation process. Among all the preparation techniques, focused ion beam system (FIB) is the most frequently used technique for the preparation of specimens for TEM studies due to its advantages over such methods as broad ion beam milling, electro-polishing, or mechanical polishing (see section 2.2.4). Nanocomposite coatings have many small structural features which affect their properties and performance, and thereby, the structural, chemical and geometrical high resolution analysis of their cross-sections through the depth is required. The precise preparation of such cross-sections can be carried out by means of FIB.

Chemical analysis can also be performed in TEM by the registration of characteristic X-rays (EDS) and electron energy loses (EELS) **[261]**.

2.2.3.1 High-resolution transmission electron microscopy (HRTEM)

Thus, the structural characterization of materials by means of TEM is possible using two basic methods: image analysis (bright field and dark field imaging modes, and high resolution TEM) and electron diffraction analysis. However, electron diffraction analysis has a drawback of dynamic scattering phenomenon because

electron diffraction data is acquired from large sample area. This problem can be overcame by utilizing a high resolution imaging of a small area of the sample with subsequent Fast Fourier Transform (FFT) of the image **[262]**. Moreover, FFT data of HRTEM images contains structural information which is similar to that obtained using electron diffraction.

High-resolution transmission electron microscopy is a phase contrast imaging mode of the conventional TEM, which allows to resolve the crystallographic properties of materials with atomic resolution. For the imaging in this mode the combination of both transmitted and scattered electron beams is used. A contrast arises due to the phase difference of electron waves leaving the sample because of scattering of incident electron wave by the sample atoms. Nowadays, the highest resolution achived in HRTEM imaging is around 0.5 Å that allows to resolve individual atoms a crystal and its defects.

2.2.3.2 TEM apparatus description

The microstructure and elemental composition of the coatings were characterized by means of transmission electron microscope JEOL ARM-200F at the Nanobiomedical Center of Adam Mickiewicz University under the supervision of Dr. Grzegorz Nowaczyk and Dr. Emerson Coy. The microscope was operated at accelerating voltage of 200 kV and equipped with electron energy dispersive spectrometer (EDS). The preparation of the coatings' cross-section specimens was performed by means of focused ion beam system (see section 2.2.4). The results were analyzed using Gatan DigitalMicrograph and ImageJ computer software.

2.2.4 Focused ion beam system (FIB)

Focused ion beam system is a multifunctional technique used for direct micro and nano-scale deposition of materials or material removal from a solid surface **[263]**.

In FIB system, ions (usually Ga^+) are produced in a liquid-metal ion source and focused into a beam by an electric field. The ion beam is accelerated toward the sample and strikes the sample causing ion-atom collisions (elastic or inelastic). Due to elastic collisions of high-energy and massive ions with the sample atoms, the surface atoms of the sample are disturbed from their aligned positions and leave the sample. The focusing of the ion beam on one area of the sample for an extended period of time leads to sputtering or milling of the sample. A modern FIB can focus the ion beam to a spot size in the order of nanometres that allows to sputter the sample in a very precise and

controlled manner. Due to inelastic collisions, the energy of incident ions transfers to either the surface atoms or electrons causing emission of secondary electrons, which are collected by the detector to form an image (on the analogy to SEM). At relatively low ion beam currents the sputtering of the sample is negligible and 5 nm image resolution can be achieved. Moreover, FIB can be combined with SEM in order to mutually compensate the limitations of each other: FIB (the sample damage and implantation during imaging) and SEM (no milling option).

FIB can be used to deposit materials by an injection of organometallic gas in the path of the ion beam above the sample surface. As a result of precursor decomposition, the non-volatile component deposits on the sample surface.

The nanometre scale imaging and the precise milling conditions of the FIB allow to prepare site-specific cross-sections and lamellae for TEM to within 50 nm of a region of interest as well as to prepare cross-sections for SEM to within 500 nm of a region of interest. Such positional accuracy is very difficult to achieve using other preparation methods **[264]**.

2.2.4.1 FIB apparatus description

The preparation of samples for TEM and SEM studies was performed by means of focused ion beam system JIB 4000 (JEOL) with Ga^+ ions under the supervision of Dr. Karol Załęski.

2.2.4.2 Sample preparation protocol

The lamellae of the coatings for TEM studies were prepared using the standard H-bar technique. The preparation steps are given below:

- Deposition of thin carbon film (15 μm long and 3 μm wide) on the site of interest on the coating surface in order to prevent sample damage during further milling operations.
- Milling of two staircase-shaped tranches (12 μm×15μm) at a distance of 1.5 μm from each side of the site of interest using a high power ion beam (10 nA ion current with accelerating voltage of 30 kV) of normal incidence. The ion beam scans the tranches in a serpentine pattern.
- The remained material between the tranches is then thinned to approximately 300 nm by stepwise reducing ion beam power (ion beam current reduced from 10 nA to 0.32 nA) (Fig. 2.4). The beam current was decreased in order to decrease the spot size that gives better control of the milling procedure and

causes less sample damage. Additionally, the ion beam was scanned the sample in line during the milling and was moved toward the site of interest in steps of a half of the beam diameter in order to avoid re-deposition of the coating material onto the lamella and to avoid the sample damage.

- The bottom and right side of the lamella are cut off from the base specimen, while the left side is partially cut off on 80 % of its length.
- Next, the spacemen is rotated to +/-2º from its normal position and the lamella is further polished at the right side by low-energy beam (0.023 nA ion current and accelerated at 30 kV). This procedure was made in order to obtain V-shaped right edge of the lamella with the aim to obtain electron transparent thickness on the edge of the lamella.
- The spacemen is additionally tilted by +/-2º and polished with ultralow-energy beam (0.023 nA ion current and accelerated at 5 kV) in order to remove the damaged material generated during high energy ion milling.
- The next step is lifting the lamella away from the FIB cuts by means of a micromanipulator equipped with a thin electrostatic glass needle. This operation was monitored using an optical microscope. The lamella is then placed from the needle edge onto a TEM grid.

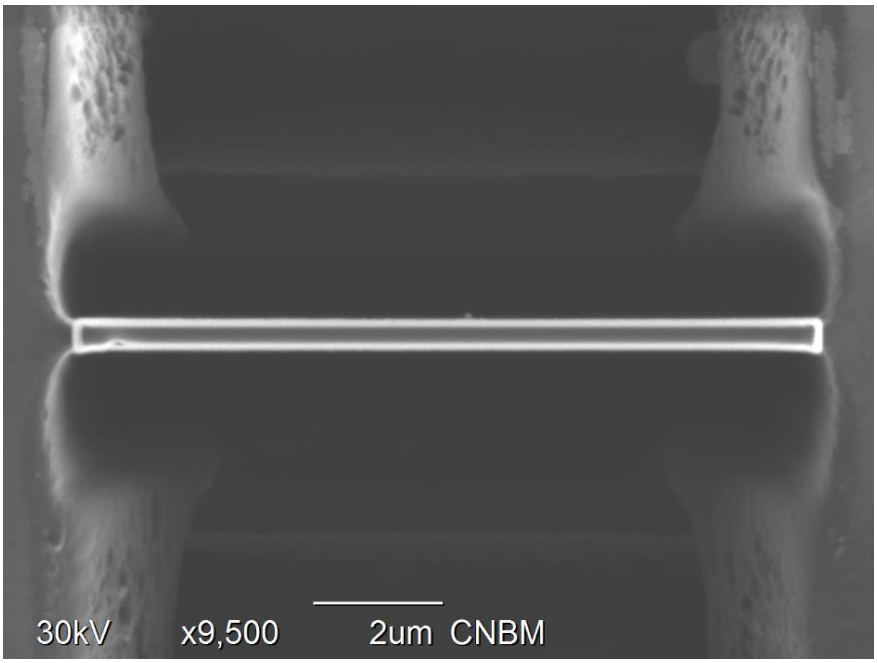

Figure 2.4. FIB top-view image of the lamella after the milling by ion beam of 0.32 nA ion current and accelerated with 30 kV.

The preparation of the coatings' cross-sections for SEM studies was performed by milling of one staircase-shaped tranche using a high-energy ion beam. The area of interest in the staircase-shaped tranche was subsequently polished by stepwise reduction of the ion beam power.

2.2.5 Raman spectroscopy

Raman spectroscopy is a standard non-destructive spectroscopic technique for the characterization of crystalline, nanocrystalline, and amorphous materials **[265]**.

Raman spectroscopy is based on the effect of inelastic scattering of monochromatic light (usually from a laser source) on atoms or molecules of matter which is commonly known as the Raman effect (Fig. 2.5). Inelastic scattering process is a two-photon event of simultaneous annihilation of an incident photon and the emission of scattered photon through an intermediate quantum state of a material (virtual level). It is well-known that each molecule of a material has a defined vibrational energy. Most of the sample molecules are in the lowest energy vibrational state at room temperature conditions, while only a few molecules in a higher energy vibrational state. The former condition is known as the ground vibrational state and the latter is known as excited vibrational state. The incident photons of the laser beam, which can be considered as oscillating electromagnetic wave, induce an oscillating polarization in the molecules of the sample, exciting them to virtual energy states.

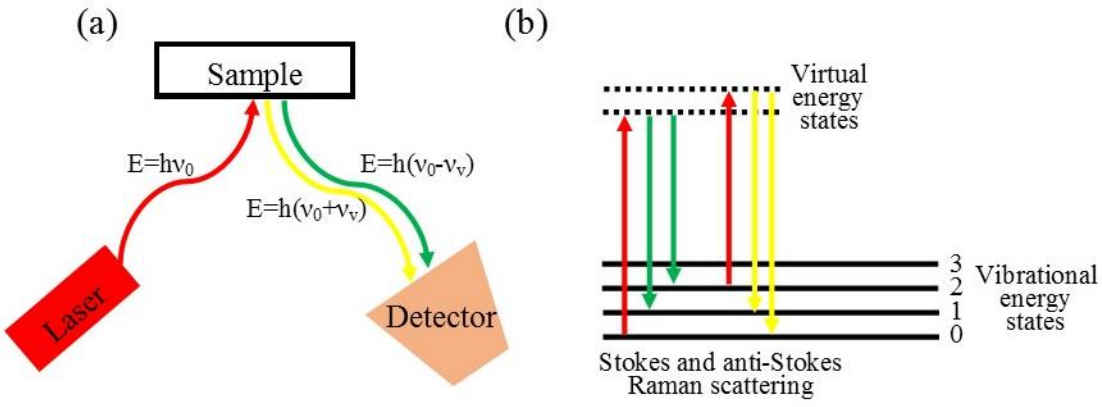

Figure 2.5 Schematic representation of Raman spectroscopy (a) and energy level diagram of Raman scattering (b).

When the polarization in the molecule leads to a different vibration state than before polarization, then the energy difference between annihilated photon and the emitted photon

is the amount of energy required to vibrationally excite the molecule. If the Raman active molecule is in ground state at the time of interaction than the molecule will set to a higher vibration level after interaction and the scattered photon will have less energy than the incident photon $E=h(\nu_0-\nu_v)$ (the material absorbs energy). This outcome is known as Stokes Raman scattering (Fig. 2.5b). When the molecule is already in the excited vibration state at the time of interaction, than after excitation the molecule will set down to its ground vibration state or to the vibration state which is lower than the state it had started in (Fig. 2.5b). The resulting energy of the scattered photon will be higher than that of incident photon, $E=h(\nu_0+\nu_v)$ (the material loses energy). This type of Raman scattering is known as anti-Stokes scattering (Fig. 2.5b). The Raman scattering is measured as light collected by the detector and the maximum amount of light detected will correspond to the highest point on the spectrum. Thus, the Raman spectrum shows the intensity of the scattered light as a function of its energy difference to the incident photons, known as Raman shift. The Raman shift is reported in wavenumbers, which have units of inverse length, cm^{-1}. The Raman shift is characteristic for a specific molecule and contain information about chemical composition and structure of a material. This energy shift can be affected by atomic mass, bond strength or the system geometry (interatomic distances, atomic substitutions). Accordin to Hooke's law, the mass of the atoms involved in the vibration and bond strength for a diatomic molecule are related to the vibrational frequency, ω, as follows **[266]**:

$$\omega = \frac{1}{2\pi c}\sqrt{\frac{K}{\mathrm{M}}} \tag{2.5}$$

where c is the speed of light, K is the force constant of the bond between A and B, and $M=M_AM_B/M_A+M_B$ is the reduced mass of atoms A and B of masses M_A and M_B. While such parameters as iono-covalency, band structure, electronic insertion set intensity as a result of the vibration-induced charge variations occurring at the very bond scale.

The intensity of the Raman scattered radiation I_R is given by **[265]**:

$$I_R \propto \omega_0^4 I_0 N\left(\frac{\partial\alpha}{\partial Q}\right)^2 \tag{2.6}$$

where I_0 is the incident laser intensity, N is the number of scattering molecules in a given state, ω_0 is the frequency of the exiting laser, α is the polarizability of the molecules, and Q is the vibrational amplitude. The expression (2.5) indicates that the signal is concentration dependent, and thus quantitation is possible. Moreover, only molecular vibrations which cause a change in polarizability are Raman active:

$$\left(\frac{\partial \alpha}{\partial Q}\right) \neq 0 \tag{2.7}$$

2.2.5.1 Raman spectroscopy apparatus description

The Raman spectroscopy experiments were carried out using Renishaw inVia confocal Raman microscope with 633 nm laser wavelength. The spectra were recorded with 50% laser power with 8–9 accumulations and exposition was set to 10 s. The spectra were collected with resolution of 0.5 cm^{-1}. The experiments on Raman spectroscopy were performed under the supervision of Dr. Błazej Scheibe and Dr. hab. Maciej Wiesner at the Nanobiomedical Center of Adam Mickiewicz University.

2.2.6 X-ray diffraction analysis (XRD)

X-ray diffraction analysis is a non-destructive technique used for determining chemical and structural features of materials by means of X-rays (usually $Cu_{K\alpha}$ radiation) **[267]**.

The X-rays are produced by a cathode ray tube, filtered to obtain a monochromatic X-ray beam which is further projected onto a material. The incoming plane wave is elastically scattered by electron cloud of material atoms that results in the generation of new waves. The re-emitted waves cancel one another out through destructive interference. However, when the distance travelled by the waves in a material is equal to an integer multiple of the wavelength of the incident radiation, the scattered waves interfere constructively in a few specific directions. This effect of constructive interference of X-ray waves in a crystalline solid is determined by Bragg's law (see Fig. 2.6):

$$d \sin\theta = n\lambda \tag{2.8}$$

where d is the lattice planes distance, θ is the angle of incident X-ray beam, n is an integer and λ is the wavelength of X-rays.

In the case of constructive interference, the intensities of overlapped waves are added up together. Thus, when measuring intensities of scattered waves as a function of angle of incident X-ray beam, the points where Bragg's conditions are satisfied will appear as strong intense peaks. If different crystallographic parallel planes are present in a material, the corresponding diffraction pattern will contain intense peaks at different angles. X-ray diffraction analysis can be used for characterization of crystalline materials in terms of the lattice constant, crystal orientation and crystal size of different phases in a material **[267]**.

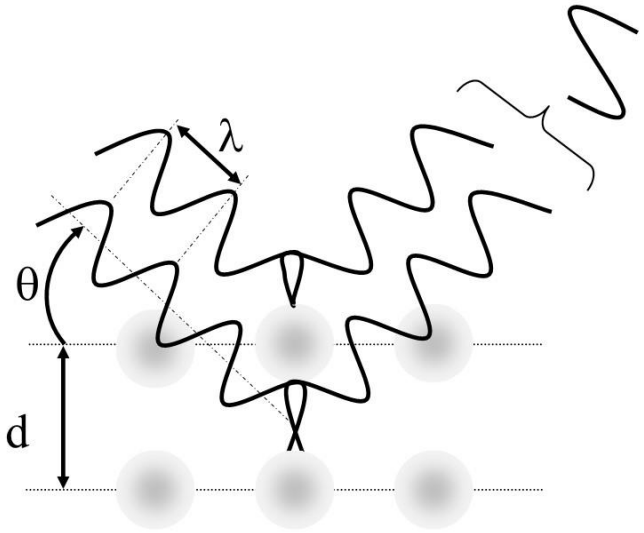

Figure 2.6. Schematic illustration of X-rays diffraction according to Bragg's law on a crystalline material.

2.2.6.1 XRD apparatus description

XRD measurements were performed on X-ray diffractometer PANalytical working with filtered $Cu_{K\alpha}$ radiation (λ = 1.5418 Å) and equipped with PIXcel 3D detector in Bragg-Brentano geometry. The diffraction patterns were recorded in continuous scan mode at room temperature conditions. The obtained diffraction patterns were processed in the PANalytical X'Pert software. Measurements and analysis of the results were performed at the Nanobiomedical Center of Adam Mickiewicz University under the supervision of Dr. Emerson Coy and Dr. Marcin Jarek.

2.2.7 X-ray photoelectron spectroscopy (XPS)

X-ray photoelectron spectroscopy is a non-destructive surface-sensitive technique used to analyse both the elemental composition and the chemical state of a material. XPS permits precise identification and quantification of elements, measurement of empirical formula, chemical state and electronic state of the elements within a material.

In XPS measurements, the sample under investigation is irradiated with X-ray beam (usually radiation of Al Kα at 1486.7 eV or Mg Kα at 1253.6 eV). The incident X-ray photons interact with core electrons of an atom transferring its energy to electrons of the atom. When energy of the incident photon ($h\nu$) is higher than the electron core level binding energy (E_B), the electron can be ejected from the atom with kinetic energy E_K.

(Fig. 2.7) This process is known as the photoelectric effect and is described by the Einstein equation **[268]**:

$$E_B = h\nu - E_K - \phi_S, \tag{2.9}$$

where ϕ_S is the work function of the spectrometer (typically 4-5 eV). Further, the amount of the emitted photoelectrons and their kinetic energies can be detected by a coaxial cylindrical analyser or hemispheric concentric. Thus, E_B can be calculated for each element in the sample, except for Hydrogen and Helium.

After the core electron is emitted, an outer shell electron fills the core hole and an excess energy can be transferred to another electron which then emits from the atom. This second emitted electron is called Auger electron. The kinetic energy of the Auger electron is defined as follows:

$$E_k = E_b(A) - E_b(B) - E_b(C), \tag{2.10}$$

where $E_b(A)$ is the binding energy of the emitted photoelectron from the core level, $E_b(B)$ is the binding energy of electron that fills the core hole and $E_b(C)$ is the binding energy of the level from which the Auger electron is emitted. It is evident that the kinetic energy of Auger electron depends only from the atomic energy levels and the chemical environment of the atom and independent of the excitation energy.

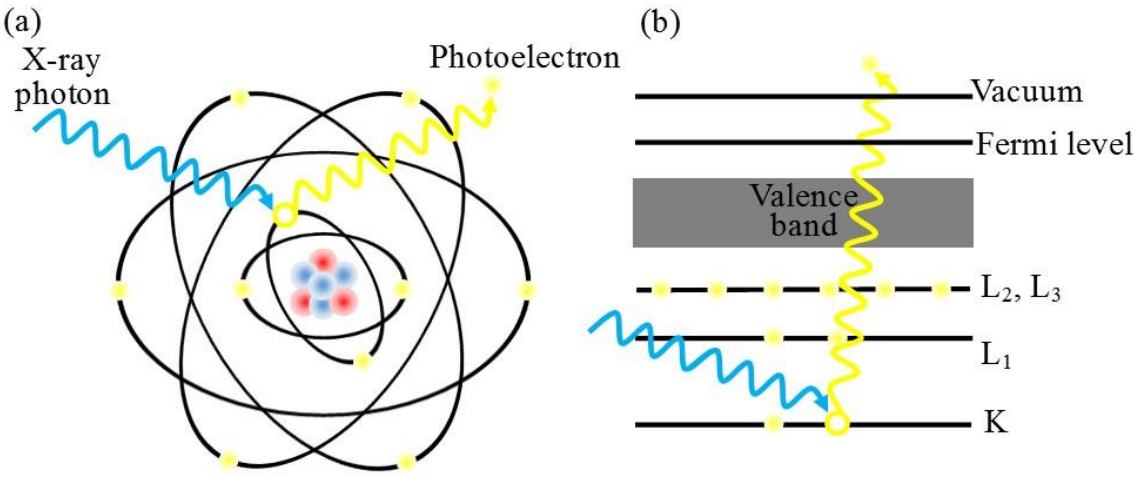

Figure 2.7. Schematic illustration of photoemission process of core electron from an isolated atom (a) and the corresponding schematic diagram of the electron energy levels (b).

Therefore, the additionally measured Auger peaks in the XPS survey spectrum can be useful for both elemental and chemical state analysis. For a given element and its chemical state, there is a well-defined and fixed energy difference of the Auger electron and photoelectron lines which is known as the Auger parameter **[269]**:

$$\alpha = E_k(ABC) - E_k(A), \tag{2.11}$$

where $E_k(ABC)$ is the kinetic energy of the Auger transition involving electrons from A, B, C atomic levels and $E_k(A)$ is the kinetic energy of the photoelectron from core level A. In this form the Auger parameter depends on the excitation energy and can possess negative values. Therefore, the Auger parameter was modified by addition of the photon excitation energy. This modified Auger parameter (α') is independent of the excitation energy and is calculated by **[269]**:

$$\alpha' = E_k(ABC) + E_b(A), \tag{2.12}$$

where $E_b(A)$ is the binding energy of the core electron A. Moreover, α' is independent of charging effects since any charging shifts are be of the same magnitude but of opposite direction in both Auger and photoelectron transitions.

Since the E_B is unique for each element, it is possible to determine the composition of the sample. Moreover, by counting the number of photoelectrons corresponding to the characteristic E_B, it is possible to measure the relative amount of the elements. Thus, measured XPS spectrum contains peaks, whose position is dependent on the element from which the photoelectron originates, and its intensity is a measure of the elemental concentration. Additionally, electron binding energy is influenced by the chemical surrounding of the atom because the energy levels of the core electrons depends on the redistribution of valence electron charges that in turn can be affected by the oxidation state of the atom, by its nearest-neighbour atoms, by difference in lattice site etc. Therefore, when the atom of interest is bounded to the strongly electron withdrawing atom (e.g. atoms with higher electronegativity), a charge transfer to the latter will cause increasing of core electron binding energy of the former, and vice versa. These changes in chemical environment of atoms give rise to "chemical shift" of E_B values of the pure element to E_B values of a specific chemical state which are tabulated for many compounds in a variety of databases. Thereby, chemical state information can be extracted from XPS spectrum. The chemical shift of core electron binding energy in turn results in the analogical shift of the subsequent Auger transition. Moreover, any change of Auger electron energy is a result of the net effect of chemical shift of the three levels A, B and C, therefore the Auger lines show a larger chemical shift than photoelectron lines that makes the procedure of identification of multiple chemical states in the sample more accurate. Hence, the binding energy and modified Auger parameter complement each other and thereby both can provide a meaningful and correct information on chemical state of a given compound **[268]**.

Due to many obstacles on the way of photoelectrons from the sample such as inelastic collisions within the sample's atomic structure, recombination, recapture or trapping in excited states, the depth of photoelectrons emission is limited to few atomic layers, thus, only outer 5-10 nm of a sample surface can be analysed by XPS. In order to perform a depth profile XPS analysis, the sample is sputtered step-by-step by using argon ion beam and exposed to XPS analysis after the each step of sputtering.

2.2.7.1 XPS apparatus description

XPS measurements were carried out on two different systems: (1) SPECS Sage HR 100 system working with a non-monochromatic X-ray source (Al Kα line of 1486.6 eV energy) at CIC biomaGUNE in San Sebastian under the supervision of Dr. Luis Yate. The selected resolution for the high-resolution spectra was 15 eV of Pass Energy and 0.15 eV/step. The measurements were performed in an ultra-high vacuum (UHV) chamber at a pressure around 8×10^{-8} mbar. The depth profiling of the samples was done with an Ar^+ beam with energy of 3 kV. (2) Omicron Nanotechnology multiprobe UHV system at NanoBioMedical Centre at Adam Mickiewicz University under the supervision of Dr. Mateusz Kempiński. The measurements were performed under ultrahigh vacuum (10^{-10} mbar) using a monochromatized Al Kα X-ray as the excitation source. CasaXPS software was used to process and analyse the obtained XPS data. The peak fitting was done by subtracting the background using a Shirley-type function and Gaussian/Lorentzian mixed function was used for the peak fit.

2.2.8 Nanoindentation

Indentation is a standard method for probing the mechanical properties of materials at the micro- and nanoscale. Among the mechanical properties of interest, indentation can be used to measure hardness, elastic modulus, continuous stiffness, scratch resistance, residual stresses, film-substrate adhesion, fracture toughness, time dependent creep, relaxation properties, and fatigue **[270,271]**.

In a conventional indentation test, a sharp tip with a well-defined geometry and very high hardness is pressed into a material whose mechanical properties are unknown. The tip is indented into a material by applying load that is stepwise increased up to the maximum user-defined value (P_{max}) leading to maximum penetration depth of the indenter (h_{max}). At the point of the maximum penetration depth, the load is hold constant for a defined period of time. After the end of the holding stage, the load is removed while the response of a material is recorded due to pushing out of the indenter by a material as a result of elastic

recovery. When the indenter is fully withdrawn, the residual impression in a material have a depth h_f. By continuously monitoring the load applied to the indenter and its penetration into a material relative to the surface (i.e. evaluation of the deformed area), the load-displacement data is derived and further used for determination of hardness and elastic modulus of a material by using the well-known method developed by W. C. Oliver and G. M. Pharr **[272]**. Figure 2.8 shows schematic illustration of loading and unloading stages of an indentation process and corresponding load-displacement curve (often known as the P-h curve). Figure 2.9 shows schematic representation of a cross-section of an indent during and after indentation. The variations of a load-displacement curve shape reflect mechanical properties of materials under investigation. Mechanical characterization of small volumes of material is realized by means of nanoindentation that relies on a very precise control of the indenter penetration in the range of nanometres by applying very small loads in the range of μN. Nanoindentation is efficient for mechanical characterization of thin films and coatings on harder or softer substrates, since it allows to avoid the influence of the substrate on the measured mechanical properties of a film or coating **[273]**. Additionally, the indenter can be utilized for raster scanning across the surface of the sample (scanning probe microscopy, SPM) that provides topographic imaging of the surface prior and after nanoindentation. In-situ SPM imaging allows to choose precisely the desired testing location and analyse the residual impressions regarding material deformation behaviour.

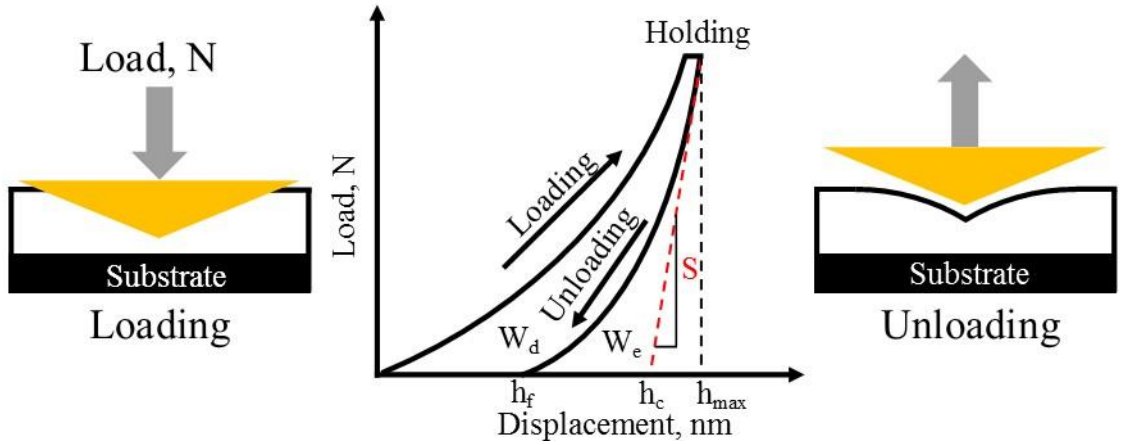

Figure 2.8. Schematics of loading and unloading stages of an indentation process and corresponding load-displacement curve.

The indenter penetration into a material is accompanied by the increase of the mean contact pressure (load divided by contact area). At a certain point, any increase in indenter load will lead to an increase in the contact area while the mean contact pressure will be remaining the same. This value of mean contact pressure is called “hardness”. Thus, the

hardness of a material is defined as the mean pressure the material sustains under load and thus can be evaluated by the equation **[274]**:

$$H = \frac{P_{\max}}{A} \tag{2.13}$$

where A is the projected area of contact. The projected area of contact is determined by the geometry of the indenter and the depth of contact, h_c. The projected area of a three sided pyramid diamond Berkovich tip, which is the most commonly used for nanoindentation testing and was used for measurements in this thesis, is given by **[274]**:

$$A = 3\sqrt{3}h_c^2 \tan^2\Theta = 24.49h_c^2, \tag{2.14}$$

where Θ is the face-half angle of a Berkovich indenter ($\Theta \approx 65.35^\circ$). The contact depth ($h_c$) is defined as the depth of indenter in contact with the sample under load (see Fig. 2.9). Oliver and Pharr **[272]** obtained the equation for h_c of conical indenter at the maximum load:

$$h_c = h_{\max} - \varepsilon\frac{P_{\max}}{S}, \tag{2.15}$$

where maximum penetration depth, h_{max}, can be experimentally measured from the load-displacement data, ε is the geometric constant and is given for conical indenter as $\varepsilon = 0.75$, S is the contact stiffness that defined as the slope of the upper portion of unloading curve (dP/dh) during the initial stages of unloading (see Fig. 2.8).

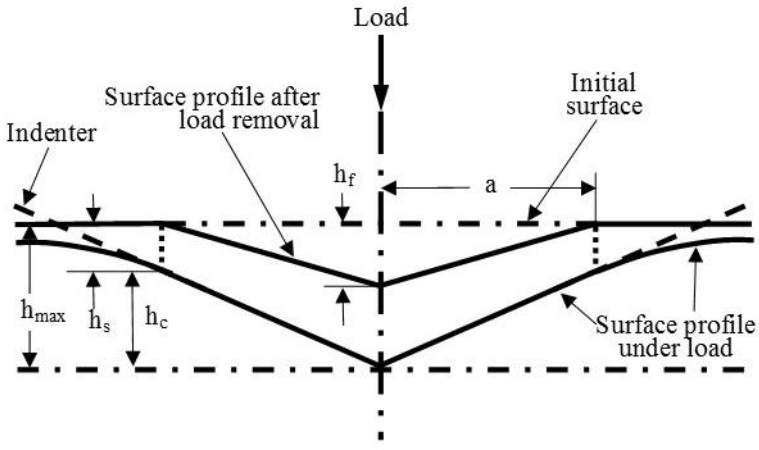

Figure 2.9. A schematic representation of a cross-section of an indentation showing various quantities used for calculation of the hardness and reduced modulus (based on a figure from **[272]**).

Since during the initial stages of unloading the material undergoes an elastic recovery, the elastic modulus of the material can be calculated by measuring the initial unloading stiffness and the projected area of the elastic contact **[272]**:

$$E^* = \frac{1}{2}\sqrt{\frac{\pi}{A}}\left(\frac{dP}{dh}\right), \tag{2.16}$$

where E^* is the combined (reduced) elastic modulus of the contacting bodies that takes into account the fact that elastic displacements occur in both the sample and the indenter. Since the indenter is made from diamond, the elastic properties of the sample mainly contributes to the value of E^*. This realizes for most materials, nevertheless the relationship between the elastic modulus of the indenter and the sample can be found from **[272]**:

$$\frac{1}{E^*} = \frac{\left(1-\nu^2\right)}{E} + \frac{\left(1-\nu_i^2\right)}{E_i}, \tag{2.17}$$

where E and ν, and E_i and ν_i correspond to the elastic modulus and Poisson's ratio of the sample and the indenter (for diamond indenter E_i=1050 GPa and ν_i=0.07), respectively **[275]**.

According to the principle of energy conservation, the total energy expended by the indenter, W_{total}, is transformed into two parts: the elastic recovery energy, W_e, and the energy dissipation, W_d **[276]**. The areas between the loading and unloading curve represents the energy dissipated in the coating due to the plastic deformation, and the area under the unloading curve represents the elastic energy of deformation. In an indentation loading–unloading cycle, the elastic recovery energy can be determined as $W_e=[(h_m-h_f)/h_f] \times 100$ **[73]**, where h_f is the final depth after unloading and h_m is the maximum indentation depth during loading (see Fig. 2.8).

The indentation into a material generates a very complex stress profile in the vicinity of the indenter. In response to the generated stress profile, a wide range of nanoscale physical processes, such as defect nucleation and dynamics, mechanical instabilities or strain localization, and phase transformations etc., taking place in the indented material, which then are reflected in form of specific local features on the corresponding P-h curve. Fig .2.10 demonstrates three exaples of P-h curves that exibit local perturbations as a result of energy-adsorbing or energy-releasing events occurring beneath the indenter **[273]**. These three examples demonstrate three different physical phenomena in three different materials:

- dislocation activity was detected during a shallow nanoindentation into single-crystal Pt at 200 °C, Fig.2.10a **[277]**;
- shear localization into sheat bands was revealed in Pd-Ni-Cu-P amorphous alloy, Fig.2.10b **[278]**;

- a significant volume increase duting unloading as a result of a phase transformation in Si (100), Fig.2.10c **[279]**.

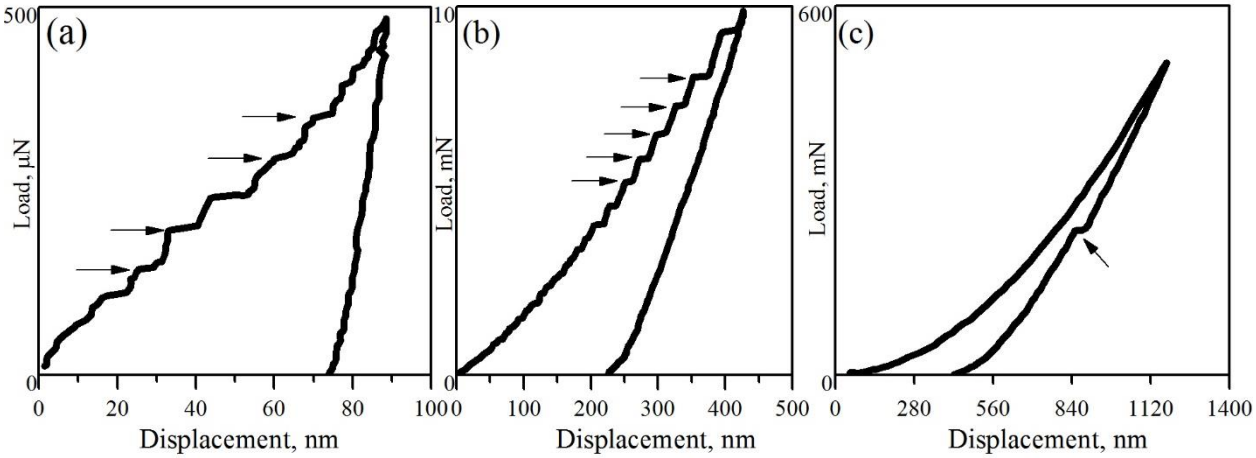

Fig. 2.10. Load-displacement curves from indentation on single-crystal Pt at 200 °C (a) **[277]**, Pd-Ni-Cu-P metallic glass (b) **[278]**, and single-crystal Si (100) **[279]**. Some of the local perturbations are indicated by arrows.

Since hardness is defined as resistance of a material to plastic deformation, it is important to obtain a fully developed plastic zone within a material during indentation. During the probing of thin films and coatings, the plastic zone starts to develop beneath the sample surface and continues to increase in size with increasing the indenter load. At relatively high loads, the plastic zone extends to a depth at which the plastic deformation of the substrate contributes to the measured hardness. In this regard, in order to avoid possible artefacts that may negatively affect the correct value of hardness, it is vitally important to limit the maximum penetration depth to less than 10 % the film's thickness at which an influence from the substrate is generally negligible. Additionally, this difficulty can be circumvented using sequential-nanoindentation approach to obtain "intrinsic" mechanical properties of the coatings by applying a multiple load function to the indenter thus allowing to measure H and E^* at different depth.

2.2.8.1 Nanoindentation apparatus description

The measurements of hardness (H) and reduced elastic modulus (E^*) were carried out by load–depth-sensing nanoindentation method using a Hysitron TriboIndenter 950 equipped with Berkovich diamond pyramid TI-0039 (conical angle 142.3° and 100 nm tip radius) calibrated against fused silica. The measurements were performed using the load function with a 5 second load time, 2 second hold time and a 5 second unloading time (see

Fig. 2.11a). In order to minimize the substrate effect on the measurements, the maximum penetration depth was kept below 10 % of the coatings' thickness. To measure hardness (H) and reduced elastic modulus (E^*) of coatings at different depths a multiple load function (trapezoidal sinus form) was applied to the indenter. The load was changed step-by-step starting from 0.05 μN to 10 mN (a segment of load lasted – 3 s, holding segment – 0.5 s and unloading – 3s) (see Fig. 2.11b). In each cycle, the unloading slope from the force-depth curve was analysed by the Oliver and Pharr method in order to determine coatings hardness.

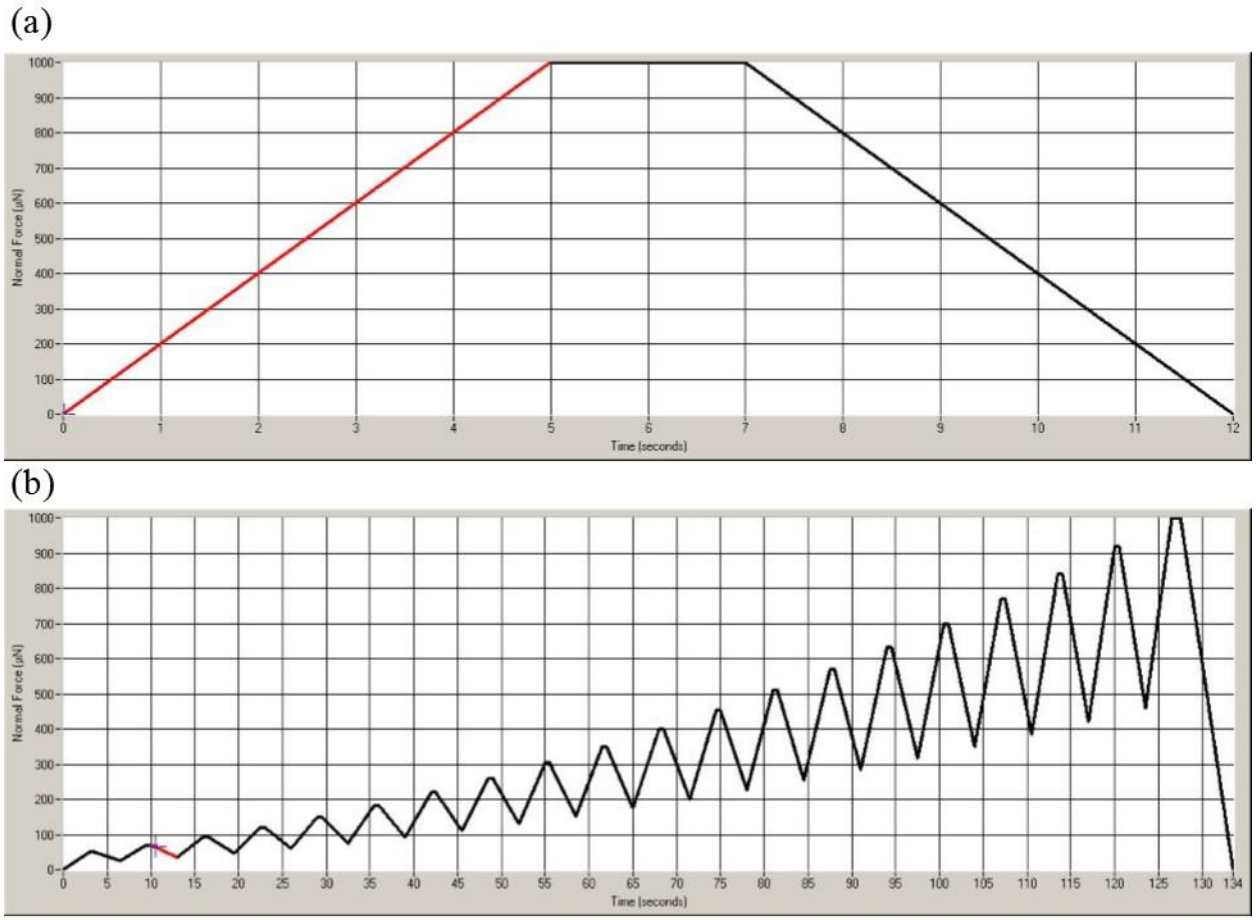

Figure 2.11. The indentation load function for the measurements of H and E^* of coatings (a) and the multiple load function (trapezoidal sinus form) for measurements of H and E^* at different depth of coatings (b).

2.2.9 Nanowear tests

The friction and wear processes in any sliding contact involve deformation and chemical interactions occurring simultaneously at nano- and microscale levels. Moreover, the nano-level tribological mechanisms influence the microlevel effects **[84]**. Thus, in order to optimize the tribological behavior of protective coatings, it is particularly useful to achieve a fundamental understanding of the tribological behaviour at the nano- and micro

scale and to study separately the mechanical and chemical changes as well as material transfer taking place in the contact.

The nanowear test is a nanotribological characterization method for evaluating the wear behaviour of thin films on the nanometre scale by means of in-situ SPM utilizing diamond indenter **[280]**. A typical nanowear test is shown in Fig. 2.12.

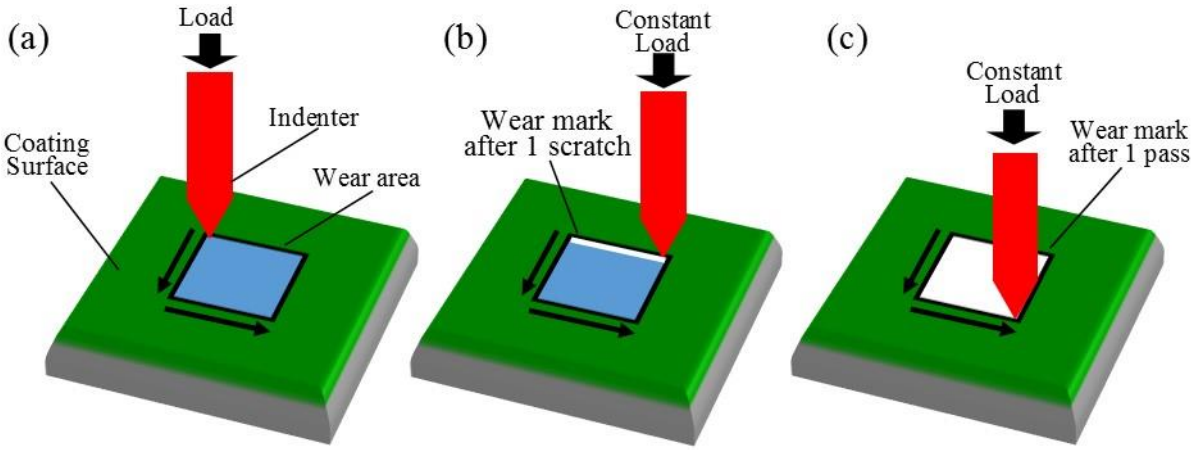

Figure 2.12. Schematic representation of nanowear test procedure: (a) approaching the sample surface and setting the wear scan area, (b) creating constant load scratch, (c) wear mark after 1 pass, nanowear test is completed.

The nanowear test can be provided by scanning an area of interest on the sample surface at an elevated constant load. The indenter approaches the sample and scans the used-defined square area on the sample surface with a high load creating the scratches. The load applied to the indenter is high enough to cause wear or indentation of the surface. The indenter is controlled to scan the defined area by a number of scratches thus causing the wear of the full area. Then the scanning an area of a size twice larger than nanowear region using a small load is performed in order to compare the two surface topographies before and after the wear test.

The change of the two surface topographies is a quantitative indicator of wear resistance of the thin film. The amount of material worn away during high load scanning (the wear volume) is given as the square of the scan size multiplied by the measured wear depth:

$$\text{Wear depth [nm]} = \text{Mean height outside wear region [nm]} - \text{– Mean height inside wear region [nm]}, \quad (2.18)$$

$$\text{Wear volume [}\mu\text{m}^3\text{]} = \text{Square of wear scan size [}\mu\text{m]} \times \text{Wear depth [}\mu\text{m]} \quad (2.19)$$

The wear is different for different materials under the same experimental conditions, and thus the comparison of wear resistance properties of different materials is possible.

2.2.9.1 Nanowear tests apparatus description

The nanowear tests of the coatings were made using a nano-indentation tester Hysitron TriboIndenter 950. Nanowear tests were performed by raster single pass scanning of the sample area of 5 μm×5 μm with a constant force of 1000 μN by means of Berkovich diamond tip. The surface after the scanning wear was imaged by scanning the sample area of 10 μm×10 μm with a constant force of 1 μN. The wear volume was calculated according to the formula (2.19). The latter was measured using the in-situ SPM imaging technique. After the nanowear tests, worn surfaces of the tested samples were investigated with the scanning electron microscopy (SEM) and energy dispersive spectroscopy (EDS) in order to obtain information related to the wear mechanisms.

2.2.10 Ball-on-disc tribological test

Ball-on-disc tribological test is a standard method for the determination of friction and wear characteristics of materials at microscale **[80]**.

In a ball-on-disc test (Fig. 2.13), a sample is mounted onto a rotating disc. The counter ball is placed in contact with the sample via an elastic arm, and a dead weight or load cell is used to apply a normal load to the contact. The test commences with the sample rotation at pre-set speed. A tangential force sensor records the lateral displacements of the elastic arm thus the friction force between counter ball and the sample as a function of distance, time or number of laps is continuously measured. The output signal of the friction force sensor then used for calculation of the friction coefficient based upon the normal load used according to the formula (1.5).

After the test is completed, the amount of material worn away can be measured either as weight loss, volume loss or linear dimension change. The weight loss can be measured by weighting both the sample and the counter ball before and after the test that will give the mass of the material removed. This method is convenient when the worn surface is irregular and unsymmetrical in shape, and in case when the material lost is sufficiently high to be measured by conventional high-resolution mass balance technique.

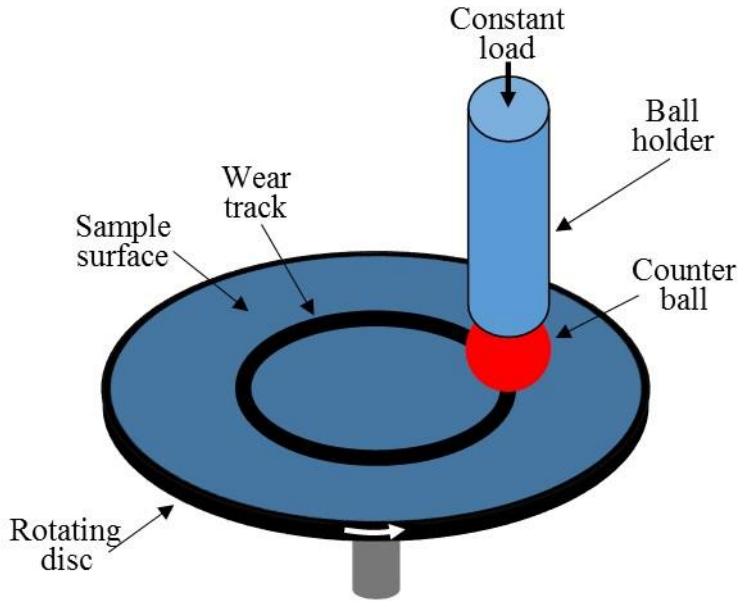

Figure 2.13. The schematic diagram of the ball-on-disc tribometer.

Another the most common option is to calculate the wear volume by measuring a profile across the wear track (depth, length and width) by mean of a profilometer. The volume of the material worn away is then calculated by multiplying the area of wear track by the circumference of the wear track. Further, this value is used for calculation of wear rate of the material that reflects volume loss per unit applied normal force and sliding distance. Thus, the wear resistance of the material can be relatively estimated by comparing its wear loss or wear rate with that of a reference material **[80]**.

2.2.10.1 Ball-on-disc apparatus description

Tribological tests were conducted on a CSM Instruments Tribometer automated friction machine in air by a "ball-on-disc" scheme, at a temperature of 20 °C. A ball of 6mmdiameter made of the Al_2O_3 (certified sintered material) acted as the counter body. The coatings were applied to discs made of steel 45 (55 HRC) of 50mm diameter and 5mm thickness; test load was 3.0 N, the sliding distance was 1200 m and the sliding rate was 10 cm/s. Alumina balls were chosen due to their chemical inertness and high hardness. Thus, only damage due to friction coming from the deposited coatings was observed. The test conditions met the international standards of ASTM G99–959, DIN50324, and ISO 20808. After the wear tests, worn surfaces of the tested samples were investigated with the scanning electron microscopy (SEM) and energy dispersive spectroscopy (EDS) in order to obtain information related to the wear mechanisms.

Chapter 3

Results and discussion

This chapter focuses on the the characterization of TiAlBSiN-based coatings and discussion of the obtained results. First, a description of the elemental and phase composition of the target used for deposition of the coatings is presented. Then, the studies on the structural features and tribo-mechanical properties of the coatings are reported in details.

3.1 Target characterization

In order to deposit TiAlBSiN coatings with amorphous and nanocomposite structure, the target material for magnetron sputtering was synthesized by means of hot isostatic pressing at 1860–1880 °C in air of a powder mixture of AlN (50 wt.%), TiB_2 (35 wt.%) and $TiSi_2$ (15 wt.%). The elemental composition and stoichiometry of sputter-deposited coatings is commonly depend on the elemental and phase composition of the sputtered target. X-ray diffraction pattern of the target used for the deposition of the coatings studied in this thesis is shown in Figure 3.1. The main phases in the target are AlN, TiB_2 and $TiSi_2$ that corresponds to the starting powders. However, it is important to note the formation of low amount of Al_2O_3, TiN and Si_3N_4 due to sintering reactions during synthesis. EDS analysis of the target (Fig. 3.2) revealed a high content of B, Al and N in the target while the relative concentration of O, Ti and Si is significantly lower.

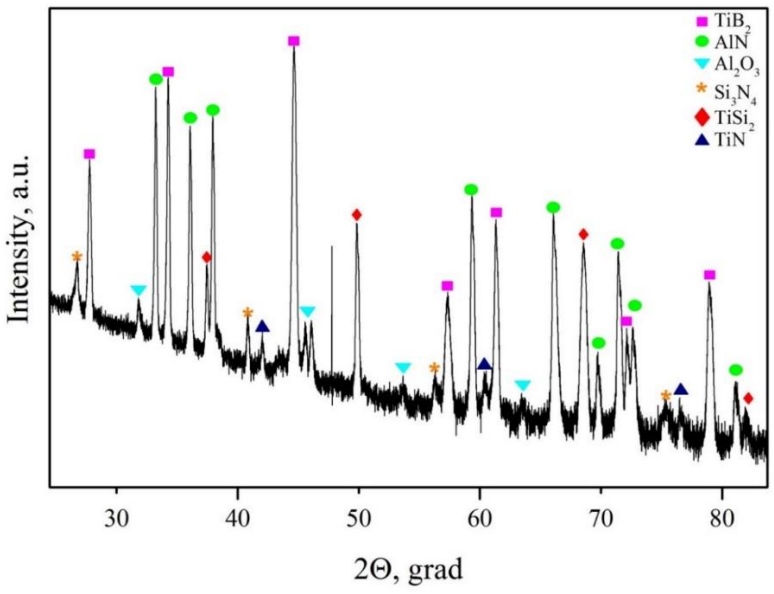

Figure 3.1. X-ray diffraction pattern of the target after sintering.

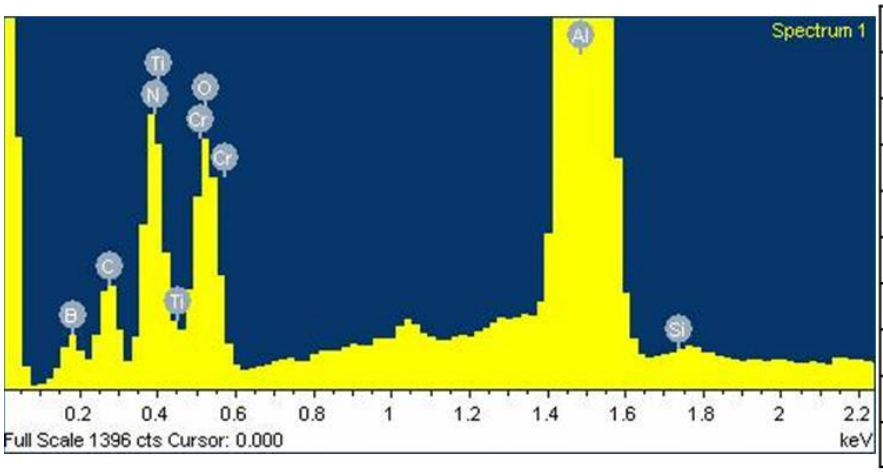

Element	Weight %	Atomic %
B K	24.62	36.60
C K	10.48	14.02
N K	16.32	18.73
O K	10.53	10.58
Al K	28.25	16.83
Si K	0.09	0.05
Ti K	7.14	2.40
Cr K	2.57	0.79
Totals	100	100

Figure 3.2. Energy-dispersive spectra of the target and results of quantitative elemental analysis.

The target is composed of different phases which have very different sputtering yields or masses. This caused a non-uniform sputtering of the target that was revealed after SEM observation of the target surface (Fig. 3.3) which was used in several deposition processes. The target surface has an irregular topography that has developed during the sputtering because of different sputtering yield of individual phases.

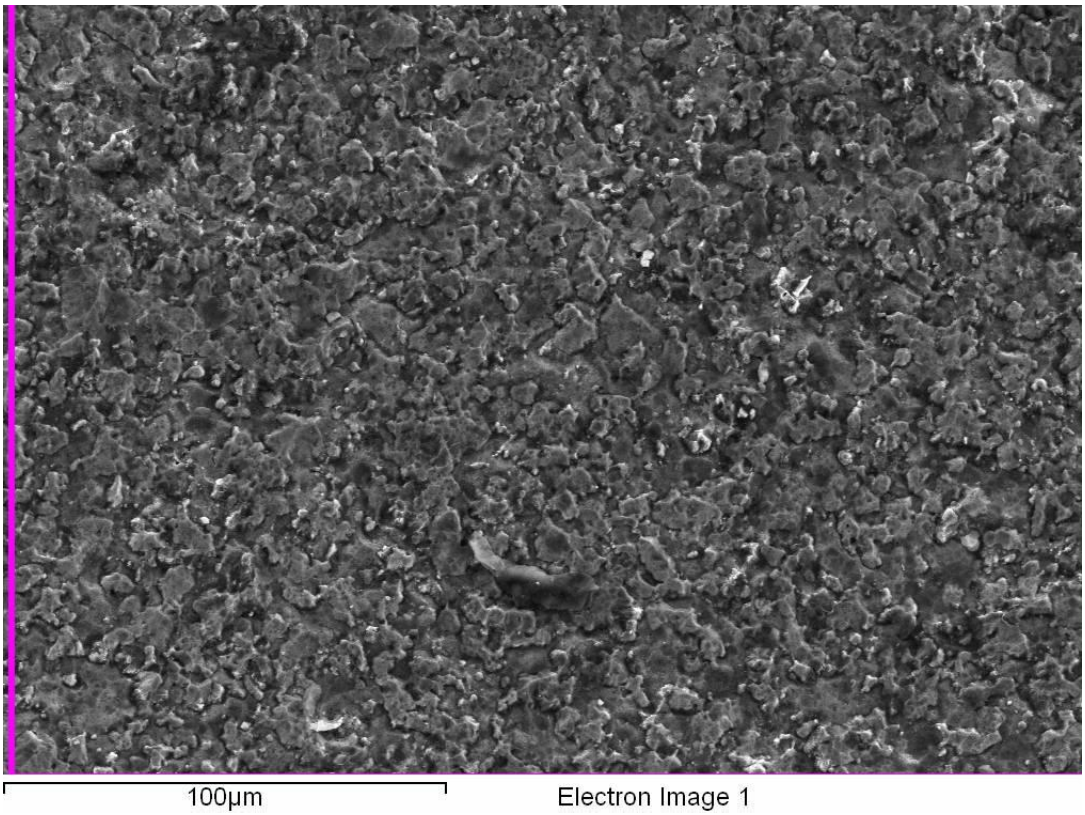

Figure 3.3. SEM image of the target surface after several deposition processes.

3.2. Nanocomposite coating based on TiAlBSiN

This section is devoted to the characterization of the gradient nanocomposite coating based on TiAlBSiN. At the beginning, the structural, microstructural, chemical and morphological chacterization of the coating together with discussion of the growth conditions will be presented. The studies on the mechanical and tribological properties of the coating will be provided and discussed at the end of the section.

3.2.1 AFM studies

A qualitative assessment of the surface roughness of TiAlBSiN coating was carried out using atomic force microscopy (AFM). The AFM images (Fig. 3.4a and b) as well as the cross-section of the surface morphology (Fig. 3.4c) showed that TiAlBSiN coating surface characterized by random distribution of nanodimensional asperities and valleys of varying amplitude and spacing that produces roughness at different scales, R_a = 0.38 nm across 1.297 μm and R_{rms} = 0.51 nm measured over the area of 1×1 μm.

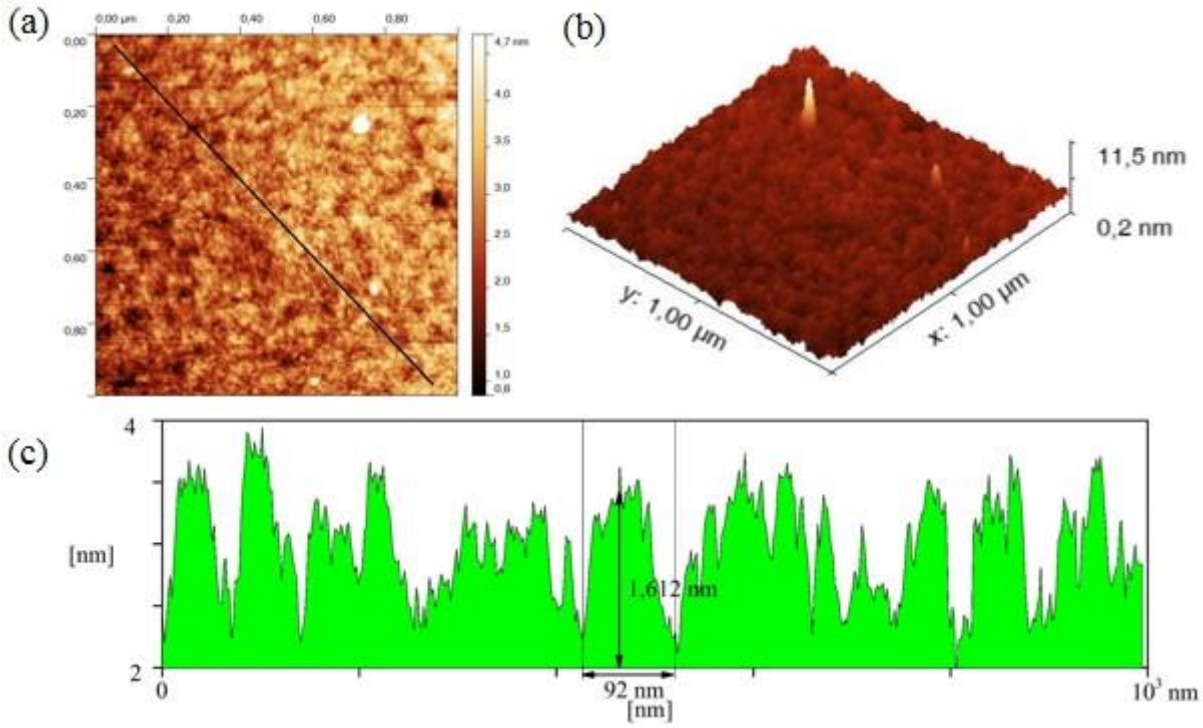

Figure 3.4. AFM 1 × 1 μm 2D (a) and 3D (b) topography images of TiAlBSiN coating surface and cross-sectional profile of the coating surface on 1 μm length (c).

The development of such nanoroughness might be caused by several factors among which we find: low adatom surface diffusion, high ion current density, chemical and topological difference of the forming elements (e.g. difference in atomic size and difference in the valence electron configuration) and competitive nucleation of different phases during the growth of the coating. All these factors can significantly suppress the growth of grains and thus have led to the observed smooth surface of the coating. Indeed, the coating based on the elements with a different atomic size and different configuration of valence electrons which can potentially form different phases. The substrate temperature was not sufficiently high for providing the diffusion of adatoms on long distances and thus the adatoms were hindered from moving to equilibrium lattice positions. Additional effects can be promoted by high ion current density. However, the latter can induce either suppressing the growth of grains by defect generation or increasing the adatom mobility that results in defect relaxation and enhanced grain growth. Thus, the effect of these factors can be either competitive or accommodative during the growth of the coating.

The interaction between two surfaces at the initial stages of sliding friction occurs at the top points of the highest asperities. The asperities undergo deformation, and the frictional behaviour at this stage is independent on material combinations, surface and environmental conditions. The plastic deformation of the asperities lead to their removal in form of wear particles thus causing abrasive wear. Therefore, a smooth surface of the protective coating is beneficial because the abrasive wear is minimized at the initial stages of the sliding. The multiscale roughness (micro- and nanoroughness) formed after DC magnetron sputtering on the surface of the TiAlBSiN coating is its important structural part. Because when being applied as a protective coating on a tool it may be less promted to mechanical damage at initial stages of the exploitation and thus may contribute to the prolongation of the tool's lifetime.

3.2.2. SEM studies

The micrograph (Fig. 3.5) shows a fracture cross-section SEM of the coating, which exhibits a dense and plain structure. The coatings show no porosity or delamination, which suggest good adhesion to a technically important substrate such as steel. The coating was stable in ambient air for several months after deposition with no signs of degradation or delamination at the coating/substrate interface.

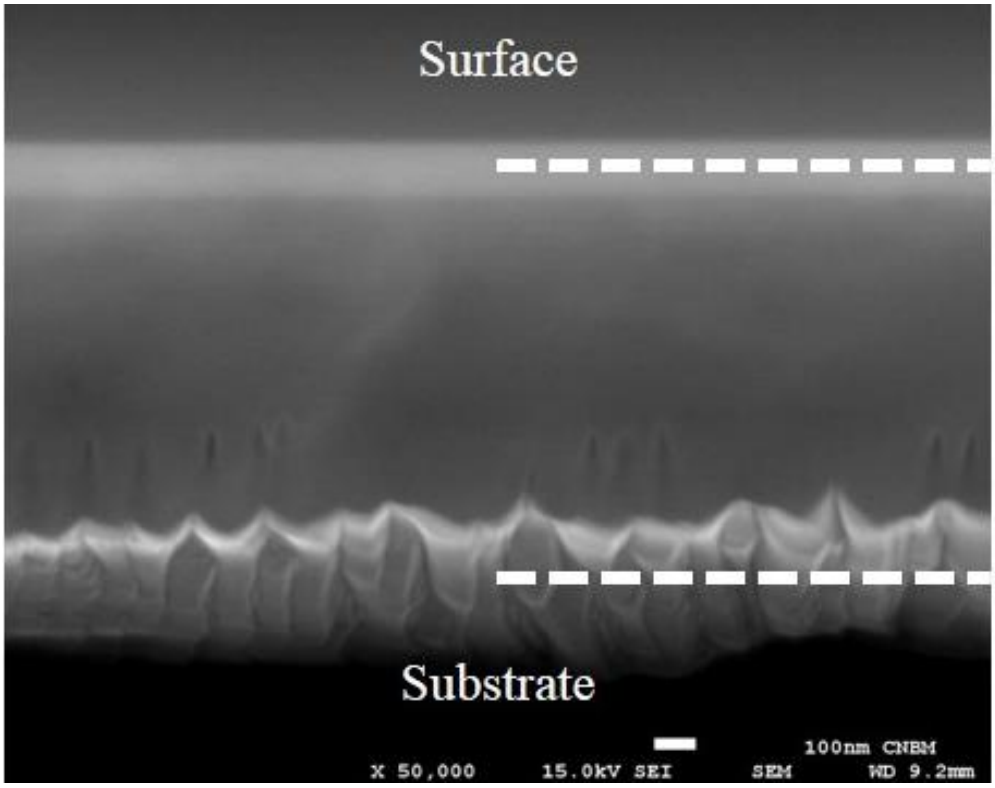

Figure 3.5. Secondary electron cross-section image of TiAlBSiN coating.

3.2.3 Transmission electron microscopy and EDS studies

The microstructure and the qualitative elemental composition of the thin cross-section of the TiAlBSiN coating were investigated via TEM with EDS analysis. According to cross sectional view and EDS mapping (Fig. 3.6) in depth element distribution is not homogenous. It is clearly seen that TiAlBSiN coating consists of two layers with different elemental composition and microstructure. As it is observed in Figure 3.6, the top layer (L1) is mainly composed of light elements N, B, C and O while base composition of the bottom layer (L2) consists of heavier elements Al, Ti and Si. It is important to note a diffusion of Fe from the substrate to the coating that could stimulate additional phase transformations in the coating and making the interpretation of the results more difficult.

Fig. 3.7a and b presents the L1 and L2 structures of the TiAlBSiN coating at a higher magnification. The top layer of about 220 nm in thickness (L1) shows fine crystallites with dimensions in the range of 15–40 nm. L2 is formed by nanocrystals of about 5 to 40 nm, which are almost non-uniformly distributed with a relatively wide size distribution.

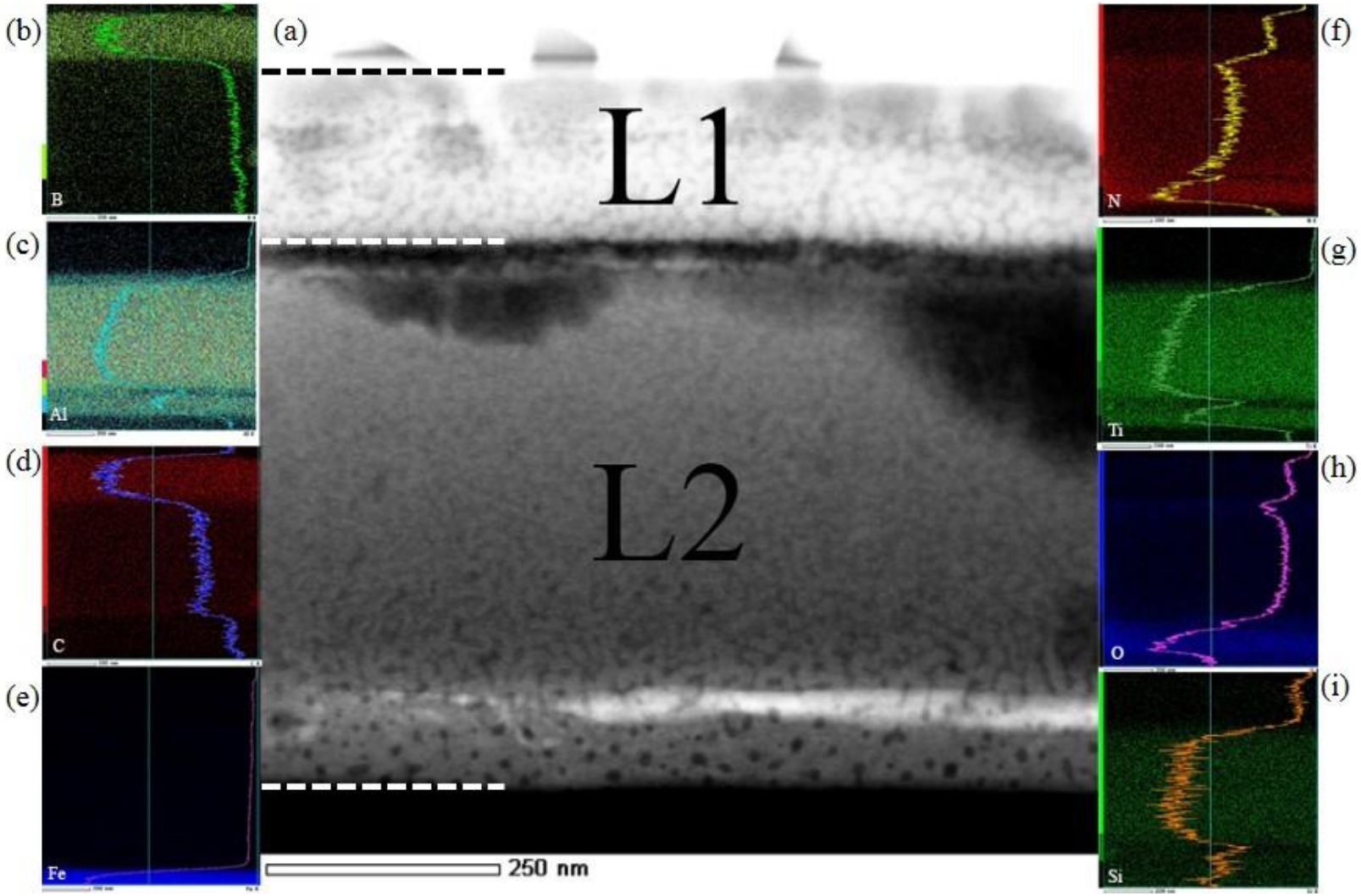

Figure 3.6. BF TEM image of TiAlBSiN coating cross-section (a) and corresponding element mapping images of B (b), Al (c), C (d), Fe (e), N (f), Ti (g), O (h), Si (i).

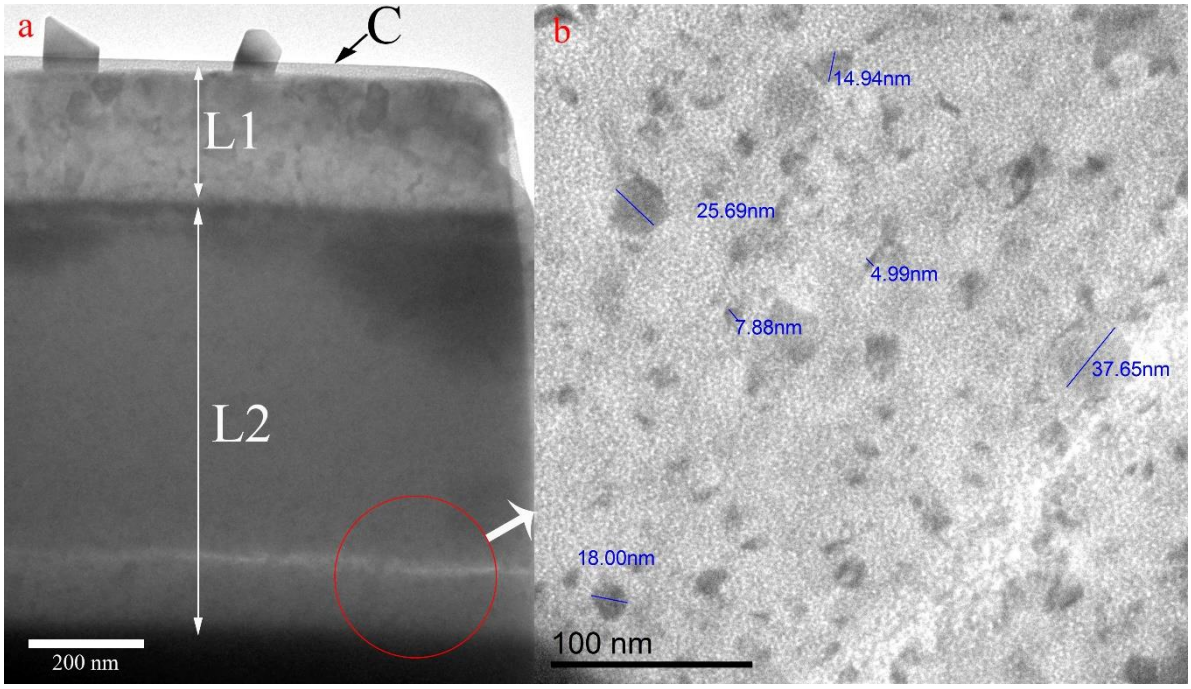

Figure 3.7. Cross-sectional BF TEM micrographs of the TiAlBSiN coating (a). The circle indicates the field shown at higher magnification in (b).

An amorphous matrix in which the randomly oriented nanocrystals in L1 and L2 are embedded is well visible and confirmed by TEM images (Fig. 3.8a and b). A filtered imaged, obtained by using the most intense peaks observed in the fast-Fourier transform (FFT) extracted from the TEM micrographs, allows to clearly visualize the crystalline and amorphous boundaries. It is important to mention that the crystalline indexation of the peaks is used to both comprehend the broad range of possible composition on the coating and give a clear perception of the $(Al_xTi_{1-x})(O_yN_{1-y})$ nanocrystals embedded in the coatings.

These studies clearly show a phase separation between nanocrystalls and amorphous phases with several nanometres in thickness that take place during the coating growth, giving place to the nanocomposite coating structure in both layers. Moreover, the formation of high volume fraction of the amorphous phase and small grains supports the assumption made in Sec. 3.2.1 on the development of smooth surface of the coating.

In order to obtain more detailed and reliable information on structural and phase composition of the coating, HRTEM images of the nanocrystals of the L1 and L2 were acquired and subsequently analysed by means of FFT. HRTEM images of L1 and L2 nanocrystals and their corresponding FFT data are shown in Fig. 3.9 and Fig. 3.10, respectively. It is clearly seen from the HRTEM images and the corresponding inverse-

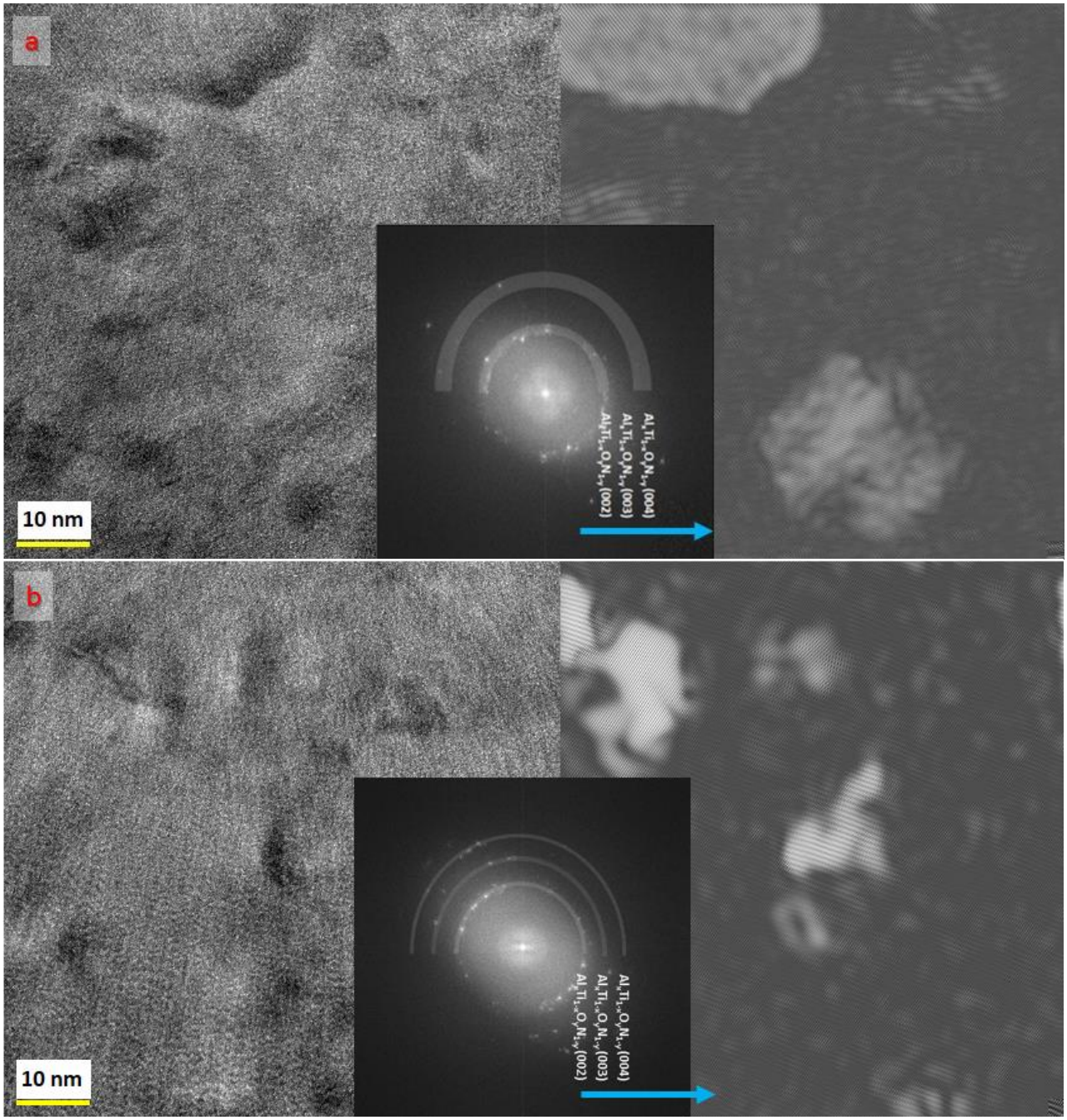

Figure 3.8. Cross-sectional bright field TEM images showing grains of L1 (a) and L2 (b) surrounded by amorphous tissue with corresponding FFT patterns. Right panels show a filtered image of the most intense peaks of in the FFT image, clearly showing the grains within the coating.

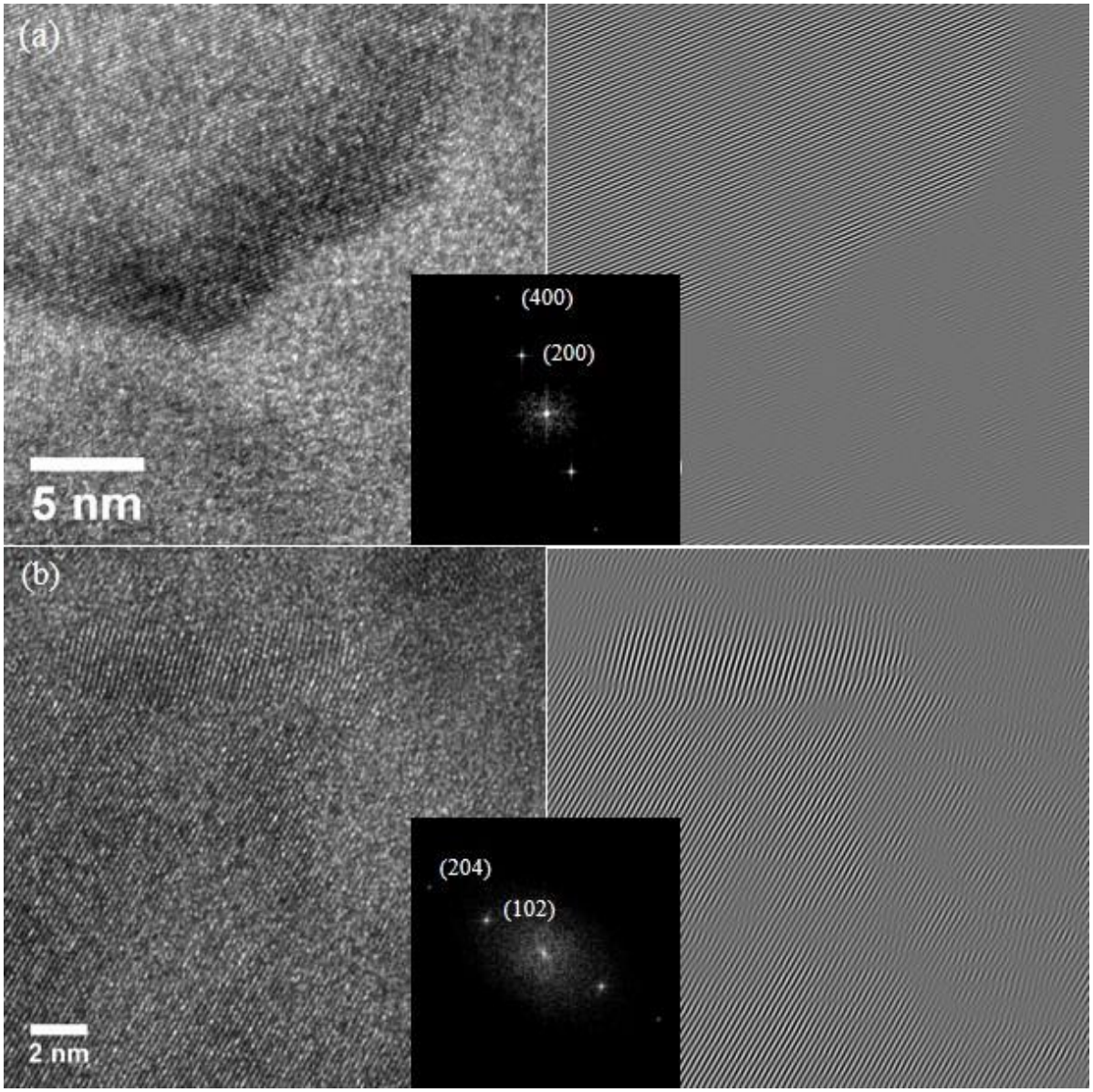

Figure 3.9. High-resolution TEM images of L1 grains (on the left), corresponding FFT pattern as an inset (in the middle) and inverse FFT image (on the right).

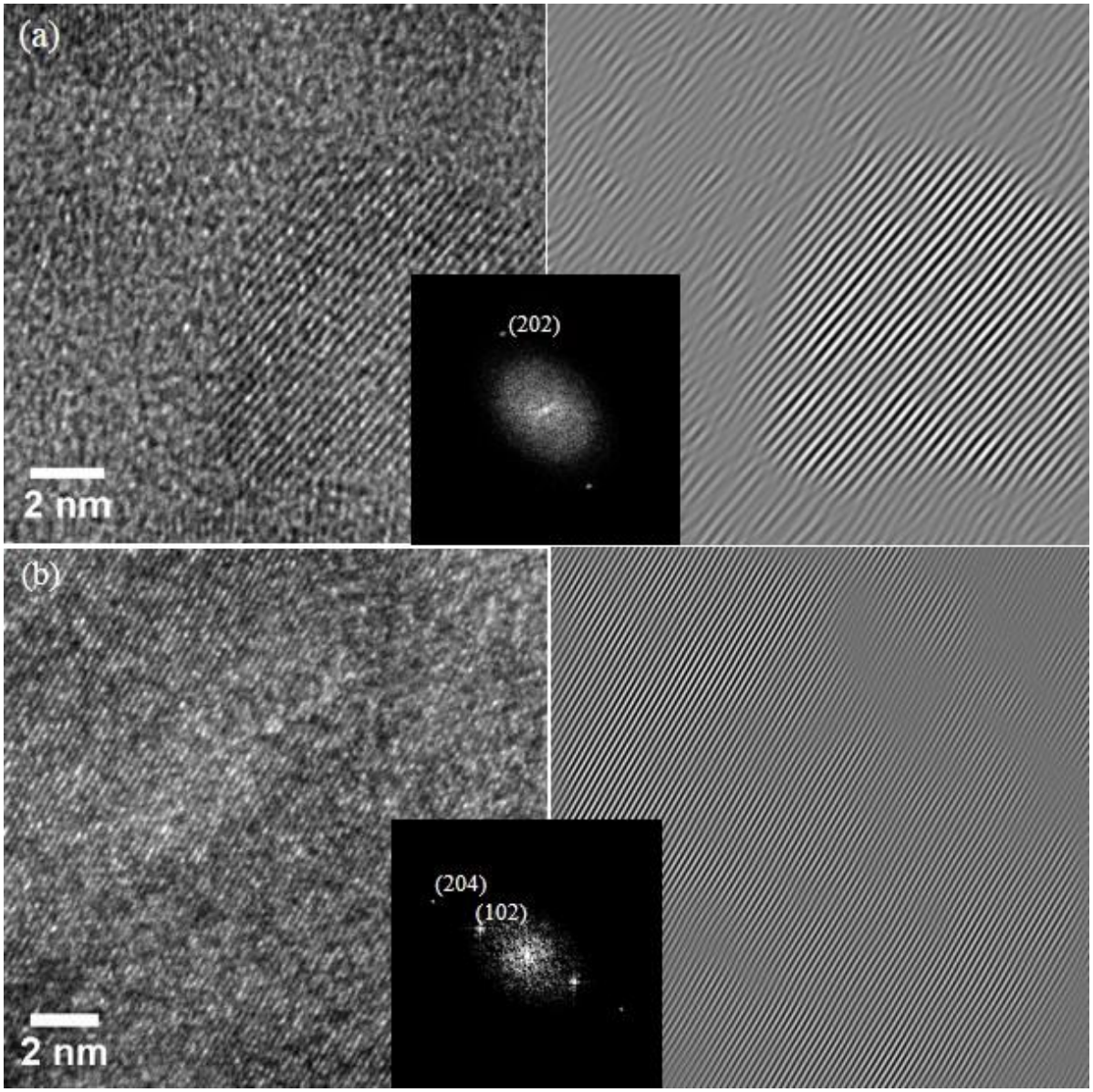

Figure 3.10. High-resolution TEM images of L2 grains (on the left), corresponding FFT pattern as an inset (in the middle) and inverse FFT image (on the right).

FFT images that the crystals of irregular shape were formed in both layers. The crystal showed in Fig.3.9b contains stacking fault and therefore for a clear visualization the area without the stacking fault was used for FFT data generation.

Through FFT analysis of HRTEM images families of first-order and second-order reflections were revealed. Among the possible phases which can be formed by the elements in the coating, these sets of reflections can be assigned with high probability to fcc-NaCl-TiN-based and h-AlN-based nanocrystals. The possible reflection assignations and the lattice parameters of L1 and L2 nanocrystals derived from the FFT data are summarized in Table 3.1. The measured interplanar spacing d_{hkl} of the lattice fringes of the L1 nanocrystal showed in the Fig.3.9a are 2.1505 Å and 0.9413 Å, which can be assigned to the (200) and (400) planes, respectively, of NaCl structured fcc-TiN-based phase. The (200) and (400) lattice parameters were calculated to be a_{200} = 4.301 Å and a_{400} = 4.303 Å. The reflections in FFT data of the L2 nanocrystal showed in Fig.3.10a are assigned to (202) planes of the TiN phase (see Table 3.1). However, the comparison of the obtained interplanar spacings and the corresponding lattice constants of the TiN phase with the corresponding experimental and theoretical structural parameters of stoichiometric fcc-TiN (a_0 = 4.242 Å, d_{200} = 2.1210 Å, d_{400} =1.060 Å, d_{202} = 1.499 Å) allowed to reveal a slight lattice expansion of the TiN nanocrystals. The higher values of the lattice constant can be due to the incorporation of B into fcc-TiN lattice through the substitution of N atoms by the relatively bigger B atoms (r_N = 0.65 Å, r_B = 0.85 Å [281]) in the non-metal sub-lattice. Since the obtained lattice parameters are consistent with the theoretical ($a_{Ti(N,B)}$ = 4.309 Å **[282]**) and experimental ($a_{Ti(N,B)}$ = 4.315 Å **[282]**, $a_{Ti(N,B)}$ = 4.325 Å **[283]**) results of other authors, it seems, there is sufficient evidence to suggest the formation of a metastable fcc-structured Ti(N,B) solid solution phase in the coating.

Moreover, considering that a sub-stoichiometric (Ti, Al)N solid solution phase might be expected in the coating according to the Ti(Al)-B-N equilibrium phase diagram **[220]**, the incorporation of Al into fcc-TiN lattice substituting Ti in the metal sub-lattice can not be excluded completely. This point will be discussed in details in the next sections together with XPS and Raman results.

According to FFT analysis of the HRTEM images in Fig.3.9b and Fig.3.10b, the obtained reflections can be attributed to the (102) and (204) planes of hexagonal AlN. The lattice parameters calculated from the positions of the reflections are up to 2.5% higher then the lattice parameters of pure h-AlN (see Table 3.1). The possible explanation is substitution of Al atoms by bigger Ti atoms (r_{Al} = 1.25 Å, r_{Ti} = 1.40 Å **[281]**) in metal sub-lattice of h-AlN that results in the formation of h-(Al, Ti)N solid solution. Moreover, the

incorporation of B into h-AlN lattice is very probable in this composition range. The latter will be discussed in the next sections.

Table 3.1. Structural parameters of fcc-TiN-based and h-(Al,Ti)N-based nanocrystals of the L1 and L2 calculated from fast Fourier transformed HRTEM images (Fig. 3.9, Fig. 3.10). a – denotes a-lattice constant of face-centered cubic or hexagonal lattice, c – denotes c-axis lattice constant of hexagonal lattice.

Layer	Figure	Reflection	d_{hkl}, Å	Lattice constant, Å	Reference PDF card number	Phase
L1	3.9a	(200)	2.151	4.301_a	04-001-2272	fcc-TiN
		(400)	1.075	4.303_a		
	3.9b	(102)	1.882	3.199_a 5.131_c	04-017-4686	h-(Al,Ti)N
		(204)	0.941	3.201_a 5.129_c		
L2	3.10a	(202)	1.521	4.302_a	04-001-2272	fcc-TiN
	3.10b	(102)	1.879	3.189_a 5.129_c	04-017-4686	h-(Al,Ti)N
		(204)	0.941	3.192_a 5.136_c		

Herein, the coating is assumed to consist of nanocrystals of fcc-TiN-based and h-AlN-based solid solutions encapsulated into amorphous matrix in both layers. It is important to note, the crystalline-amorphous interface is well-pronounced for fcc-TiN-based nanocrystals while diffusive character is observed for h-AlN-based nanocrystals. Furthermore, the injection of N_2 during deposition of L1 promoted growth of the grains, therefore the average grain size in the L1 is relatively larger than in the L2.

3.2.4 X-ray photoelectron spectroscopy studies

XPS was carried out in order to obtain additional information about quantitative elemental composition and chemical binding states of the coating. The element depth profile of TiAlBSiN coating is presented in Fig. 3.9. A two-layer structure is clearly observed for the TiAlBSiN coating which is in agreement with the TEM-EDS studies mentioned above (Fig. 3.6). L1 is characterized by high concentration of light elements and the presence of Al ~20 at.%. It is important to note that N and O have a non-uniform distribution through the depth of the L1. The stepwise changing of elements concentration

is observed close to the interface L1/L2: concentrations of O, C, Al, B are increasing while N and Ti are decreasing. The atomic concentration of Ti, Al, and B increases while concentration of O, N, and C decreases in the L2, demonstrating homogenous distribution with increasing of the sputtering time. The bulk composition of the L1 was determined to be non- stoichiometric $Ti_{0.09}Al_{0.21}B_{0.16}Si_xN_{0.22}C_{0.14}O_{0.18}$ and for L2 – $Ti_{0.11}Al_{0.25}B_{0.23}Si_xN_{0.17}C_{0.11}O_{0.13}$. Although silicon is present in the coating, the total concentration of Si was not determined because of the overlapping of the Si 2p spectrum with the Auger KLL line of Al.

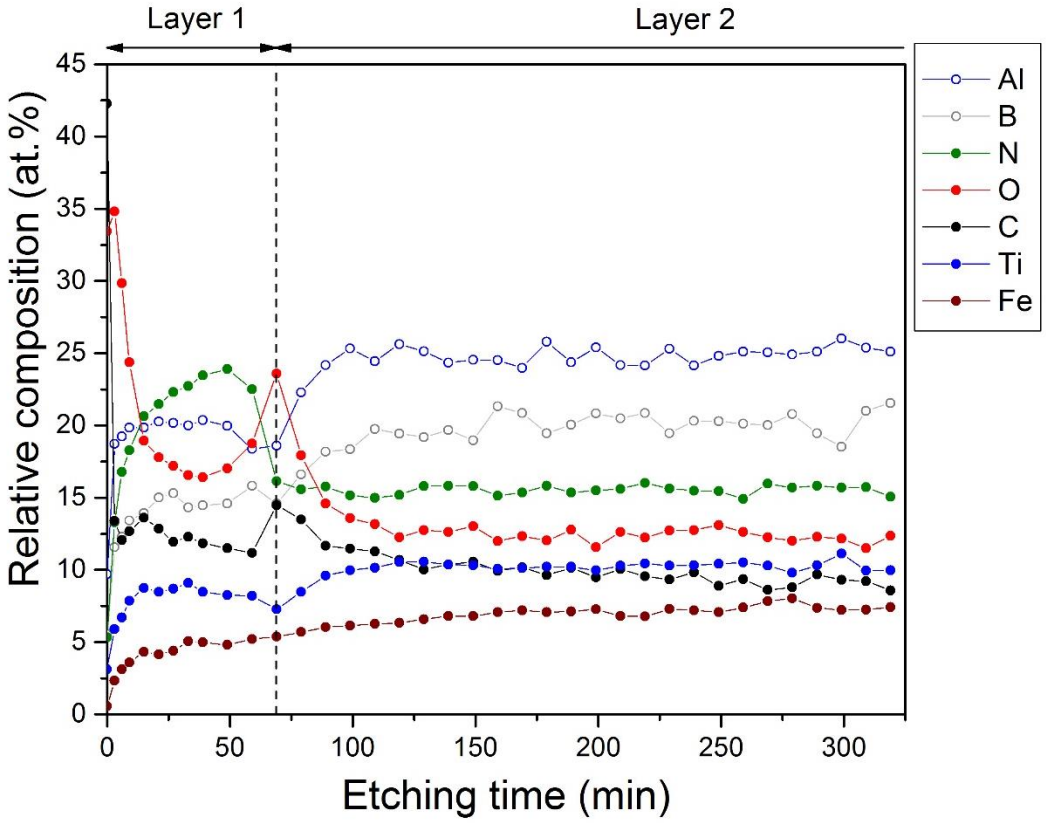

Figure 3.11. XPS depth profile of the TiAlBSiN coating.

Presented distribution of elements over the depth of the TiAlBSiN coating is defined by the characteristic of sputtering processes of a multiphase target, as well as by the specific behaviour of the reactive DC magnetron sputtering [63]. The distribution of elements and phases over the depth in the target is also very important, and it is considerably defined by the fabrication process of the target by the hot isostatic pressing of powders. Thus, the target contained the following phases after sintering: TiB_2, AlN, TiN, $TiSi_2$, Si_3N_4 and Al_2O_3 (see section 3.1) that along with different crystallographic orientation and distribution of these phases over the depth of the target strongly influence

the value of the coefficient of sputtering. This process leads to preferential sputtering of the component with higher yield and the sputtered flux is rich in this constituent. The non-uniform sputtering of the target is confirmed by SEM image of the target surface after several deposition processes (Fig. 3.3). Consequently, the L1 coating is enriched with the material having the highest sputtering yield. Moreover, the difference in composition of L1 and L2 can be explained by the injection of N_2 during deposition of L1. It is well known **[119,120,284]** that the decrease in deposition rate of films sputtered in the reactive mode is due to a reaction of the reactive gas with the surface of the sputtered target and the formation of different additional compounds on its surface. Therefore, the injection of N results in increased target poisoning and thus, a decreased deposition rate and consequently a lower amount of titanium, aluminium and boron in the vapour phase. Consistently, the increasing N content is balanced by a decreasing metal fraction. Moreover, this results in decrease of sputtering yield and magnetron discharge voltage, U_d. Therefore, the contribution of each of these events results in a loss of stoichiometry in the obtained coating compared to the target material.

Because of the irregularity of the target and the injection of N_2 to the working gas, local areas with different elemental concentration are observed and the two layers in the TiAlBSiN coating were formed. The contents of all metal elements in the coating are the same as in the target. Noticeably, the presence of O ~17 at.% in the L1 and ~12 at.% in the L2 layer, which can be explained by to the low deposition rate and presence of O in the target. The O_2 source in the coating is still undefined **[285]**; however, the following sources were suggested in the literature: the residual gas and plasma or heating-induced desorption from the deposition chamber or O containing phases in the target. Because of the very low deposition rate, the O_2 can be incorporated in the growing coating more readily **[286]**.

Figure 3.12 depicts a survey XPS spectrum acquired from the coating surface, a spectrum obtained after 27 minutes of Ar^+ ion etching of the coating which correspond to the middle part of the L1 and a spectrum acquired after 209 minutes of Ar^+ ion etching which corresponds to the middle part of the L2 (see Fig. 3.11). In addition to core-level peaks of Ti, Al, B, Si, C, O, Fe, Ar and N, Auger lines of C, N, Ti and O as well as valence band region can also be observed in the Fig. 3.12. Obviously, the C 1s peaks originate from the surface contaminations. The concentration of Carbon decreases after the etching due to cleaning of the surface. An appearance of the Ar peaks is associated with implantation of Ar^+ ions into the coating after the ion etching. It is important to note that the Fe core-level peaks originate in the spectrum after the etching because of the specific construction of the steel substrate which has uncovered areas on the edges.

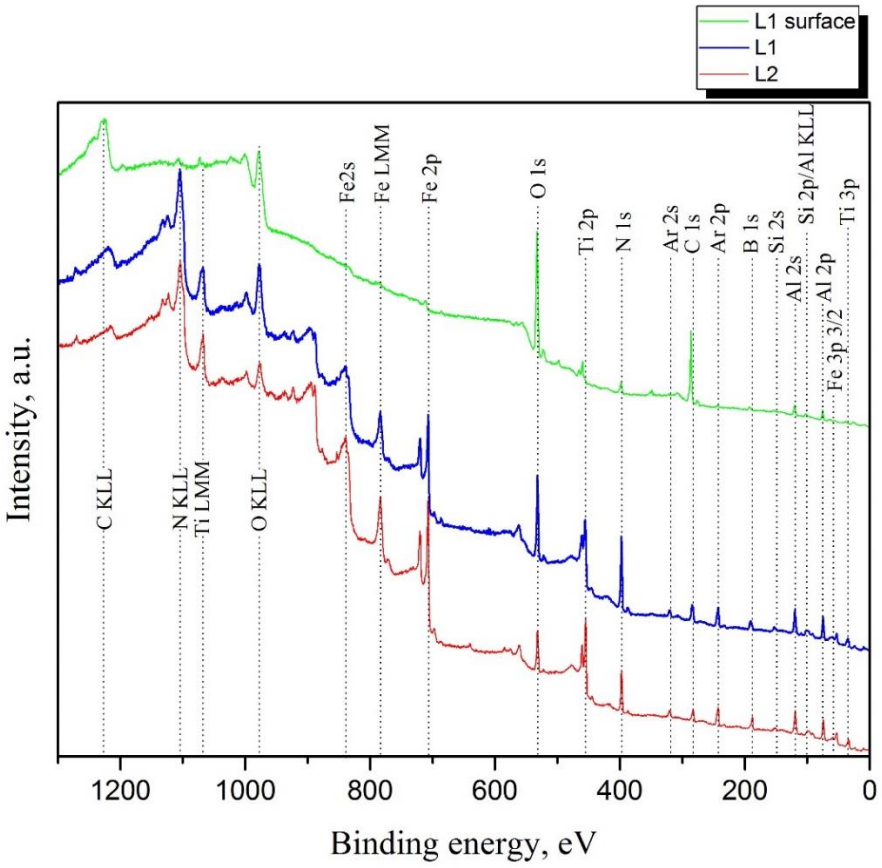

Figure 3.12. Typical XPS survey spectra acquired from the L1 surface of the TiAlBSiN coating (green line), and the spectra corresponding to the L1 (blue line) and L2 (red line) obtained after 27 and 209 minutes of Ar^+ ion etching, respectively.

It is worth noting that in our work on TiAlBSiN coating **[287]** we have reported the high resolution XPS spectra of Ti 2p, N 1s,O 1s, B 1s and Al 2p which were acquired after 5 minutes of Ar^+ ion etching. The short length Ar^+ etching probably caused forward recoil implantation of the surface oxide contamination and therefore the peaks were dominated by oxygen contained components. Herein, the XPS spectra of the TiAlBSiN coating surface without Ar^+ etching and that after long term Ar^+ eatching are reported below, since the longer Ar^+ etching removes the surface oxides completely without causing the recoil surface mixing.

Typical Ti 2p and Al 2p high resolution XPS spectra acquired from the surface, L1 and L2 of the TiAlBSiN coating are presented in Fig. 3.13. The Ti 2p region presents a broad and asymmetrical $Ti2p_{3/2}$ and $Ti2p_{1/2}$ doublets in the binding energy range 454 to 458 eV and in the range 458-467 eV, respectively (Fig. 3.13a). Herein, the stronger $Ti2p_{3/2}$ peaks will be considered since $Ti2p_{1/2}$ peaks do not contain any additional information. The peak of Ti2p is much broader than the expected FWHM of a homogeneous single Ti-based phase. This indicates that Ti presented in the coating as heterogeneous mixture of

different phases. The Ti $2p_{3/2}$ spectrum was fitted into 3 spin–orbit doublets which were assigned to Ti-B, Ti-N-O and Ti-O bonds (see Table 3.2 and references therein). It is important to note that the Ti$2p_{3/2}$ component at around 455.9 eV is shifted towards higher binding energy with respect to stoichiometric oxygen-free Ti-N (455.0 eV [288]) thus indicating a charge transfer from Titanium not only to Nitrogen but also to element with higher electronegativity than of Nitrogen and therefore can be assigned to Ti-N-O bonding. The most intensive peak on the spectrum acquired from the coating surface at around 458.4 eV is assumed to originate from Ti bonded to O as a result of surface oxidation. The intensity of Ti-O component decreases whereas the intensity of Ti-N-O and Ti-B components increases after Ar^+ ion etching due to removing of the surface oxides. The Ti-O component shifts towards the relatively lower binding energy after the etching that can be associated to lower oxidation state of Ti in the bulk of the coating.

The Al 2p spectrum (Fig. 3.13b) can be fitted with three peak components. Considering that the main peak is shifted to a higher binding energy relative to the Al-N peak and corresponds to a binding energy that is intermediate between those reported for Al-N and Al-O, it can be associated with additional charge transfer from Aluminium bonded with Nitrogen to Oxygen thus indicating on the formation of Al-N-O bonds in the coating. This peak component is the dominant peak in both layers of the coating. The peak at the high energy side of the Al 2p spectra can be attributed to a completely oxidized Al phase such as Al_2O_3. The two oxygen-containing components have the highest intensity at the surface due to oxidation of the coating in ambient air.

The O 1s spectra (Fig.3.14a and Table 3.2) were deconvoluted using three peak components. The main peak at around 531.4 eV can be attributed to Oxygen bound to Aluminium with high coordination number, and thus can be assigned to Oxygen bound to Aluminium which is in turn bound to Nitrogen. This Al-N-O bonds can be associated with oxygen defects such as isolated Al-O octahedral complexes within the AlN crystal. Moreover, this assumption is supported by cross-correlation of the Al-N-O peak of O 1s spectra with Al 2p peak at around 74.1 eV. This interpretation is in an agreement with the results of L.Rosenberger and J.Harris **[289,290]**. However, the contribution of the signals from Al-O and Ti-N-O whose binding energies are very close to that of Al-N-O can not be excluded. The high binding energy component centred at around 532.6 is significantly lower than the range of binding energies reported for B-O (533.0-533.2 eV) and thus can be attributed to B-N-O bonds which were formed due to oxygen substitution for nitrogen in B-N. The low binding energy component can be unambiguously associated with Ti-O

bonds, whose peak area decreases in the L1 and L2 due to the removing of contaminants from the coating surface by the etching.

The N 1 spectrum, shown in Fig.3.14b, is dominated by main peak centred at around 396.3 eV which can be associated with the formation of Ti-O bonding within TiN crystal. The formation of Ti-O bonding enhances the ionic character of the Ti-N bonding that in turn, causes the charge transfer from Ti to N (hence lower binding energy of N) **[179]**. An additional evidence for the Ti-N-O formation comes from the observed Ti2p-N1s-O1s cross-peak correlation that at the same time is consistent with binding energies reported in the literature (see Table 3.2 and references therein). The peak centred at around 397.4 eV is assigned to both AlN and TiN since the binding energies of the N 1s core level electrons in TiN and in AlN have been reported to overlap **[291]**. Importantly, the Ti $2p_{3/2}$ binding energies for Ti-N-O component were reported in the range from 455.4 eV to 456.8 eV by many authors and, in addition, was inconsistently assigned to different phases such as NO, over- and under stoichiometric TiN **[292,293]**. However, the latest studies on single-crystalline oxygen containing TiN **[294]** and air-exposed polycrystalline TiN **[288]** showed that the peak at around 456 eV can be unambiguously assigned to Ti in mixed Oxygen and Nitrogen environment and therefore may be assigned to O incorporated into TiN. Indeed, if considering the Ti 2p3/2 peak at around 455.9 eV to be corresponding to the Ti-N component at 397.4 eV of the N 1s, the energy difference between them ΔE(Ti $2p_{3/2}$, N 1s) is 58.7 eV that is 0.75 eV higher than that of stoichiometric oxygen-free TiN. This is in agreement with studies of D. Jaeger, who reported the increase of ΔE(Ti $2p_{3/2}$, N 1s) of Ti-N component with increasing of O content in TiN that is due to lower electronegativity of Ti than that of N that results in a stronger shift of the Ti 2p3/2 binding energy than that of N 1s after Ti-N-O formation. The enhanced charge transfer from Ti to N after O-Ti-N formation causes a shift of the corresponding N 1s component to lower binding energy and due to the existence of Ti-N component results in the broadening of the N 1s line. Since the N 1s and Ti 2p 3/2 peaks are very broad, Ti can be considered in both N-Ti-N and N-Ti-O arrangement. The minor component of the N 1s spectrum at around 398.3 eV is related to N chemically bonded to B. Additionally, the N 1s photoelectron signal of Al-N-O was reported to be in the range of 398.3 eV, therefore it is probably that the B-N component may overlap with Al-N-O signal of the N 1s spectrum. The high binding energy peak is assigned to a C-N-type surface impurities that reinforced by the fact that the C-N contribution decreases after the ion etching.

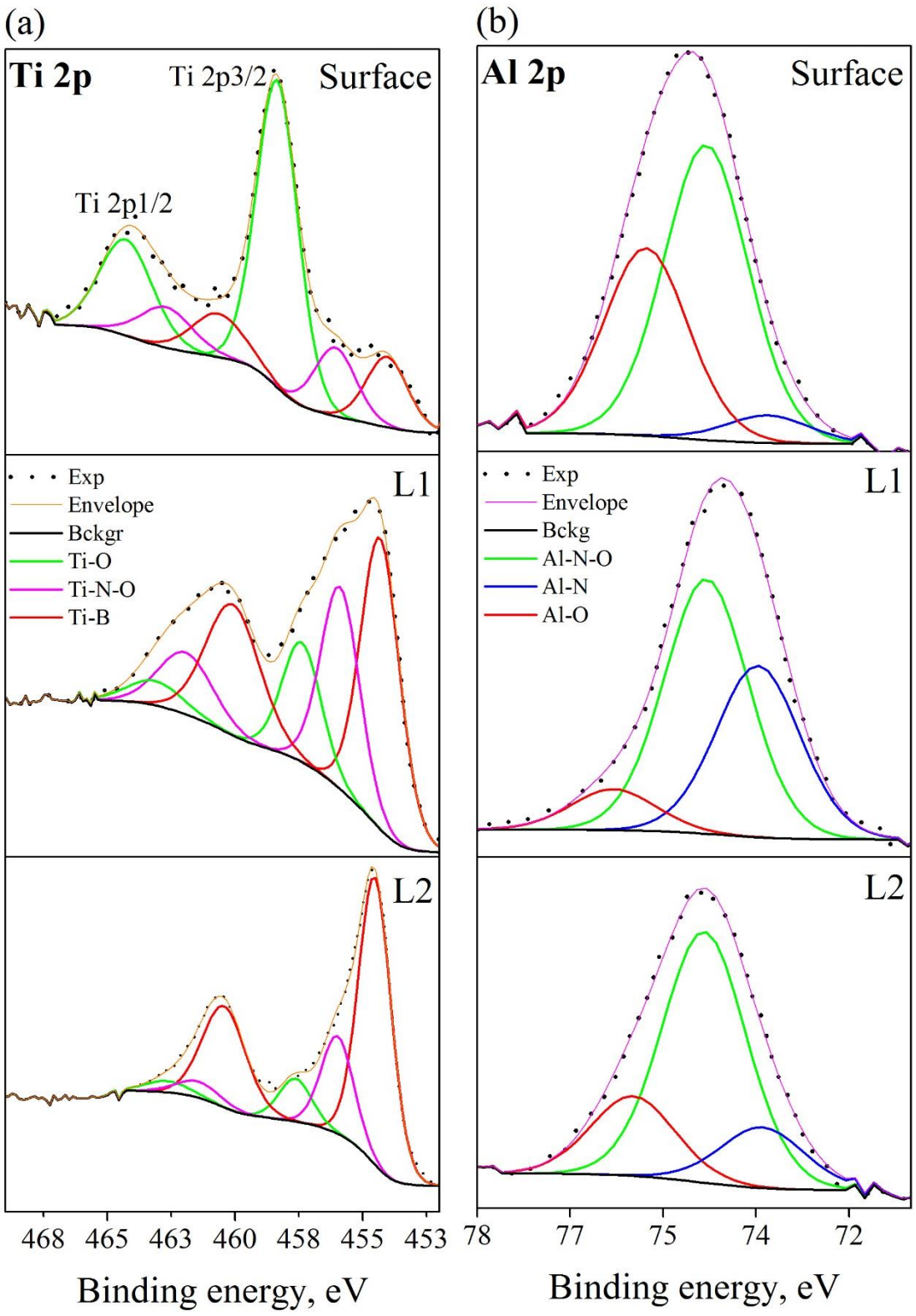

Figure 3.13. High-resolution XPS spectra of the Ti 2p (a) and Al 2p (b) core level signals obtained from the TiAlBSiN coating surface, and from L1 and L2 after Ar^+ ion etching.

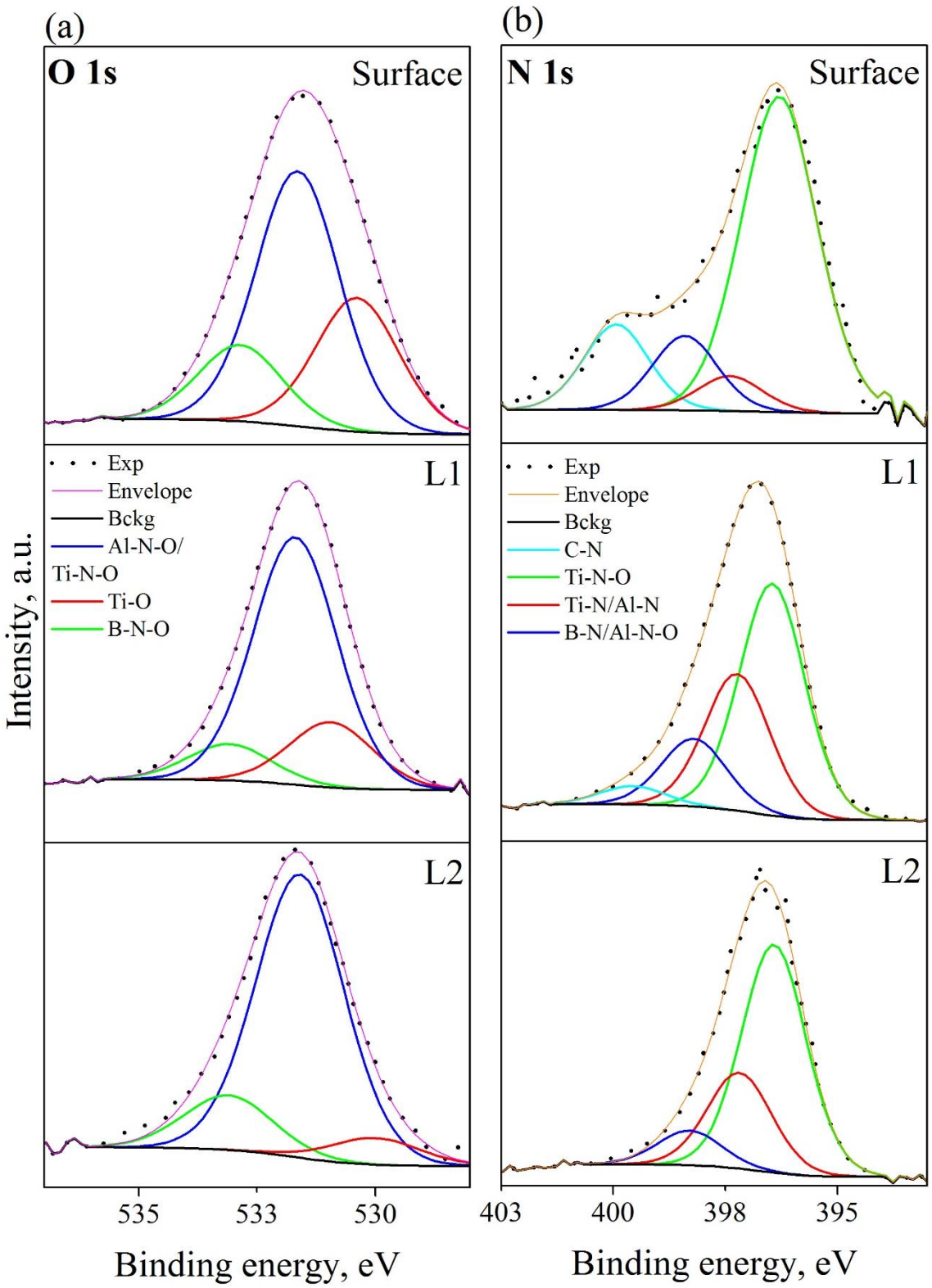

Figure 3.14. High-resolution XPS spectra of the O 1s (a) and N 1s (b) core level signals obtained from the TiAlBSiN coating surface, and from L1 and L2 after Ar^+ ion etching.

The broad B 1s spectrum can be fitted with four components (Fig. 3.15a). The low binding energy component at around 187.6 eV can be assigned to Ti-B bonds (see Table 3.2). The B 1s peak appeared at 190.1 eV is due to B-N bonds. With increasing nitrogen concentration in L1, the intensity of the B-N component becomes relatively higher than that of the Ti-B component. The component at about 191.5 eV is representative of boron atoms in a mixed oxygen-nitrogen surrounding, i.e. to B-N-O bonds, because its binding energy is higher than that of B-N component and lower than that of B-O bonding (193.3 eV). This assumption also agrees with the following electronegativity considerations: the replacement of Nitrogen atom bonded to Boron atom to more electronegative Oxygen atom causes an increase in the binding energies of Boron core electrons thus the B-N-O component of the B 1s shifts to the intermediate position between B-N and B-O. The N 1s component corresponding to B-N-O cannot be determined unequivocally because there are a few publications mentioning the appearance of B-N-O **[295,296]**. The authors report a binding energy of the B-N-O component of the N 1s core-level peak at about 398.1 eV that is mostly reported in other sources as a binding energy corresponding to B-N. In this regard, the N 1s B-N component can also correspond to B-N-O. Moreover, the intensity of the B-N-O component is highest at the surface and decreases after the ion etching. This fact coupled with B 1s-O 1s cross-peak correlation additionally supports the formation of B-N-O bonds in the coating. The B 1 s peak component at 189.0 eV can be assigned to Si-B bonds (see Table 3.2).

The fitting of the Si 2p peak of the spectrum of the surface and L2 cannot be executed properly because of overlapping of Si 2p signal with Al $KL_{23}L_{23}$ Auger line (Fig.3.15b). However, the Si 2p spectrum of the L1 can be distinguished from the Al $KL_{23}L_{23}$ Auger line and the peak at 101.1 eV is assumed to originate from Si bonded to N, and most probably corresponds to stoichiometric Si_3N_4 phase.

The relative concentrations of bonds were calculated using the fitted peak area of the individual components. FWHM of the spectra components in their respective core electron spectra were kept constant during the deconvolution (see Table 3.2) that allows to compare qualitatively the abundance of the individual bonds on the coating surface, in the L1 and L2, Fig.3.16. As can be seen, the oxygen containing components of the Ti 2p, B 1s, N 1s and Al 2p lines dominate at the coating surface due to oxidation of the coating in the ambient air. After the Ar^+ etching the contribution from oxygen containing species is less pronounced due to their removal from the surface.

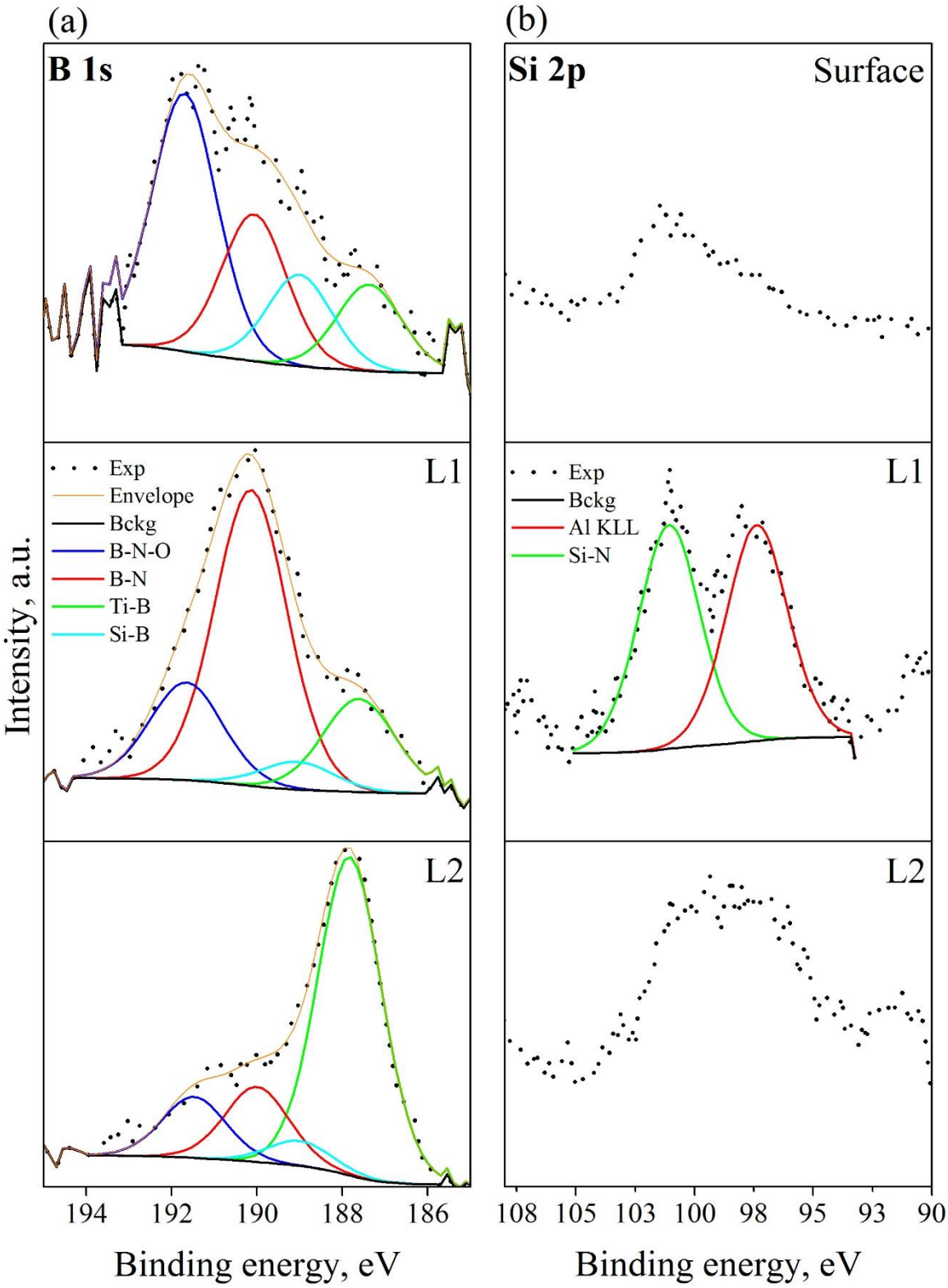

Figure 3.15. High-resolution XPS spectra of the B 1s (a) and Si 2p (b) core level signals obtained from the TiAlBSiN coating surface, and from L1 and L2 after Ar^+ ion etching.

Table 3.2. The interpretation of XPS spectra obtained from the TiAlBSiN coating surface, from the L1 and L2 after the Ar^+ ion etching. FWHF of the spectra components are given in brackets.

Core level	Binding energy, eV			Assignment	Reference
	Surface	L1	L2		
O 1s	530.1 (2.2)	530.5 (2.2)	530.1(2.2)	Ti-O	**[297]**
	531.3 (2.2)	531.4 (2.2)	531.5(2.2)	Al-N-O or Ti-N-O	**[289]**
	532.6 (2.2)	532.9 (2.2)	532.9(2.2)	B-N-O	**[295][298]**
N 1s	396.3 (1.7)	396.4 (1.7)	396.4 (1.7)	Ti-N-O	**[288,293]**
	397.4 (1.7)	397.2 (1.7)	397.2 (1.7)	Al-N or Ti-N in AlN or TiN	**[291]**
	398.4 (1.7)	398.2 (1.7)	398.3 (1.7)	B-N in BN (Al-N-O)	**[289] [299][300]**
	399.9 (1.7)	399.6 (1.7)	–	N-C	**[301]**
Ti 2p 3/2	454.0 (1.9)	454.3 (1.85)	454.5(1.85)	Ti-B	**[302]**
	456.0 (1.9)	455.9 (1.85)	455.9 (1.85)	Ti-N-O	**[288][292]**
	458.4 (1.9)	–	–	Ti-O in TiO_2	**[303]**
	–	457.1 (1.85)	457.6 (1.85)	Ti-O sub-oxides	**[304]**
Al 2p	73.1 (1.73)	73.2 (1.6)	73.3 (1.6)	Al-N	**[289]**
	74.0 (1.73)	74.1 (1.6)	74.3 (1.6)	Al-N-O	
	75.5 (1.73)	75.7 (1.6)	75.5 (1.6)	Al-O in Al_2O_3	**[305]**
B 1s	187.4 (2.0)	187.6 (2.0)	187.8 (2.0)	Ti-B	**[302]**
	189.0 (2.0)	189.0 (2.0)	189.0 (2.0)	Si-B	**[300]**
	190.0 (2.0)	190.1 (2.0)	190.0 (2.0)	B-N	**[300]**
	191.7 (2.0)	191.7 (2.0)	191.5 (2.0)	B-N-O	**[295]**
Si 2p	–	101.1 (3.0)	–	Si-N	**[300]**

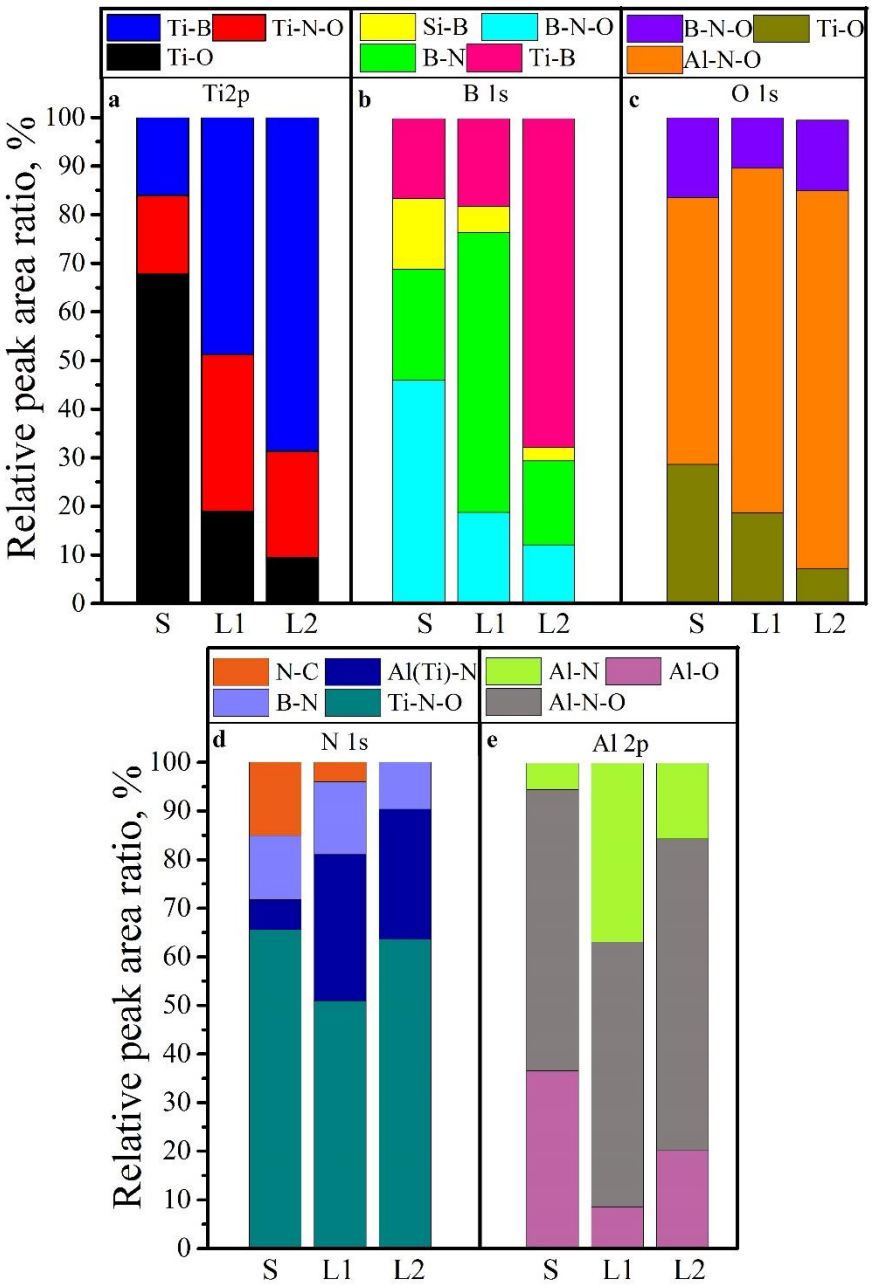

Figure 3.16. Relative peak area ratio of the components of the Ti 2p (a), B 1s (b), O 1s (c), N 1s (d) and Al 2p (e) core level spectra acquired from the surface (S), L1 and L2 of the TiAlBSiN coating.

Moreover, the higher affinity of Oxygen to Aluminium then to Titanium or Boron results in higher concentration of Al-N-O bonds in comparison to other Oxygen-containing compounds. Importantly, the injection of N during the coating growth considerably changed phase composition of the coating. Indeed, the sufficient agreement between the ratio of Ti-B and B-N components of the Ti 2p, B 1s and N 1s core level spectra (Fig. 3.15a, b and d) allows to suggest that during the growth of the L2 in non-reactive mode the Ti-B bonds predominantly form while the amount of nitrogen-based bonds is relatively lower. However, the N injection during growth of the L1 significantly stimulated the growth of nitrogen-based bonds. Although the Ti-B bonding still forms in the L1, the B-N becomes dominant boride phase in the L1. This result is consistent with that published in studies on the Ti-B-N **[283]** and Ti-Al-B-N **[226]** coating systems. The formation of B-N bonds dominates under Ti-B when a sufficient saturation of N is reached. Moreover, B-N starts to form at relatively low N concentration when the ratio of B/Al is around 5 while at lower B/Al~1 a considerably higher N concentration is needed to stimulate BN growth. Additionally, it was shown **[226]** that the both phases can coexists at relatively low N content only when B/Al ratio ~5. The evolution of Ti-N and Al-N bonds can not be evaluated because the binding energy of N 1s electrons in Ti-N and Al-N overlaps and can not be deconvoluted in the N 2s spectrum.

Figure 3.17 and 3.18 show the deconvoluted peaks of Ti $L_3M_{23}M_{45}$, O $KL_{23}L_{23}$, N $KL_{23}L_{23}$, Al $KL_{23}L_{23}$ Auger transitions collected on the coating surface, L1 and L2. Due to the fact that these Auger transitions involve valence band electrons and thus very sensitive to the chemical environment of these atoms, their analysis can give more detailed and meaningful information on the nature of the bonding in the coating. The analysis and interpretation of the Auger peaks are given in Table 3.3 with corresponding references.

The observed broadening of Auger lines of all elements additionally indicates the formation of heterogeneous mixture of different phases in the coating. Indeed, the broad line shape and the measured kinetic energies of the Ti $L_3M_{23}M_{45}$ peak components (Fig. 3.17a and Table .3.3) indicate that Ti is in different chemical environment in the coating. The peak at the high kinetic energy side can be attributed to Ti-B bonds in TiB_2. This is additionally confirmed by the corresponding modified Auger parameter α'. The kinetic energy of the peak at around 416.8 eV is slightly lower than the kinetic energy of TiN given in the literature (see Table 3.3 and references therein). This shift indicates a change in binding state of Ti atoms due to additional

oxidation and therefore this peak can be assigned to Ti-N-O bonds. Indeed, the decrease of O content in the coating (in particular in the L2) give rise to a slight increase of the corresponding modified Auger parameter toward the value of TiN. Analogously, the kinetic energy of Ti-O components decrease from 414.7 in the L2 to 413.5 eV on the surface that occurs due to different coordination number of Ti by nearest-neighbour Oxygen atoms, i.e. due to the difference in oxidation state. This is additionally supported by the relatively higher intensity of Ti-O component on the coating surface which has a lower intensity in the L1 and L2. Importantly, the Auger peak intensities are in good agreement with intensities of the corresponding photoelectron peaks. A peak fitting of O $KL_{23}L_{23}$ Auger transition allowed to reveal that oxygen in the coating is in three different binding states. The simultaneous contributions Ti-O, Al-O and most probably B-O bonds can be resolved in the O $KL_{23}L_{23}$ Auger spectra. The corresponding values of α' are in good agreement with the values reported previously in the literature. However, the kinetic energy of O $KL_{23}L_{23}$ Auger transition corresponding to B-O bond was not found in the literature and therefore the component at the low energy side of O $KL_{23}L_{23}$ Auger line is assigned to B-O according to electronegativity considerations. Importantly, the intensities of the O $KL_{23}L_{23}$ Auger peak components correlate with the intensities of the corresponding O1s photoelectron peaks that additionally confirm the assignments.

N $KL_{23}L_{23}$ Auger line can be deconvoluted by three peak components which correspond to Ti-N, Al-N and B-N (Fig. 3.18a). Although Ti-N and Al-N were not distinguished within N 1s photoelectron peak, Ti-N and Al-N contributions are well resolved in the N $KL_{23}L_{23}$ Auger region. Moreover, it is obvious from the intensity of N $KL_{23}L_{23}$ Auger peak components that among the nitrogen based phases in the coating, AlN is the dominant one.

Fig.3.18b shows the Al $KL_{23}L_{23}$ Auger peak evolution in the coating surface, L1 and L2. As was mentioned previously, the Al $KL_{23}L_{23}$ Auger peaks overlap with Si 2p photoelectron peak. However, the Al $KL_{23}L_{23}$ Auger peak can be resolved from the Si 2p in the spectrum of the L1. The kinetic energy of the Al $KL_{23}L_{23}$ Auger peak in the spectrum of the L1 and the corresponding Auger parameter can be unambiguously assigned to Al-N bonds while the signal at around 1386 eV from the Al-O bonds may overlap with photoelectron signal of Si 2p **[306]**.

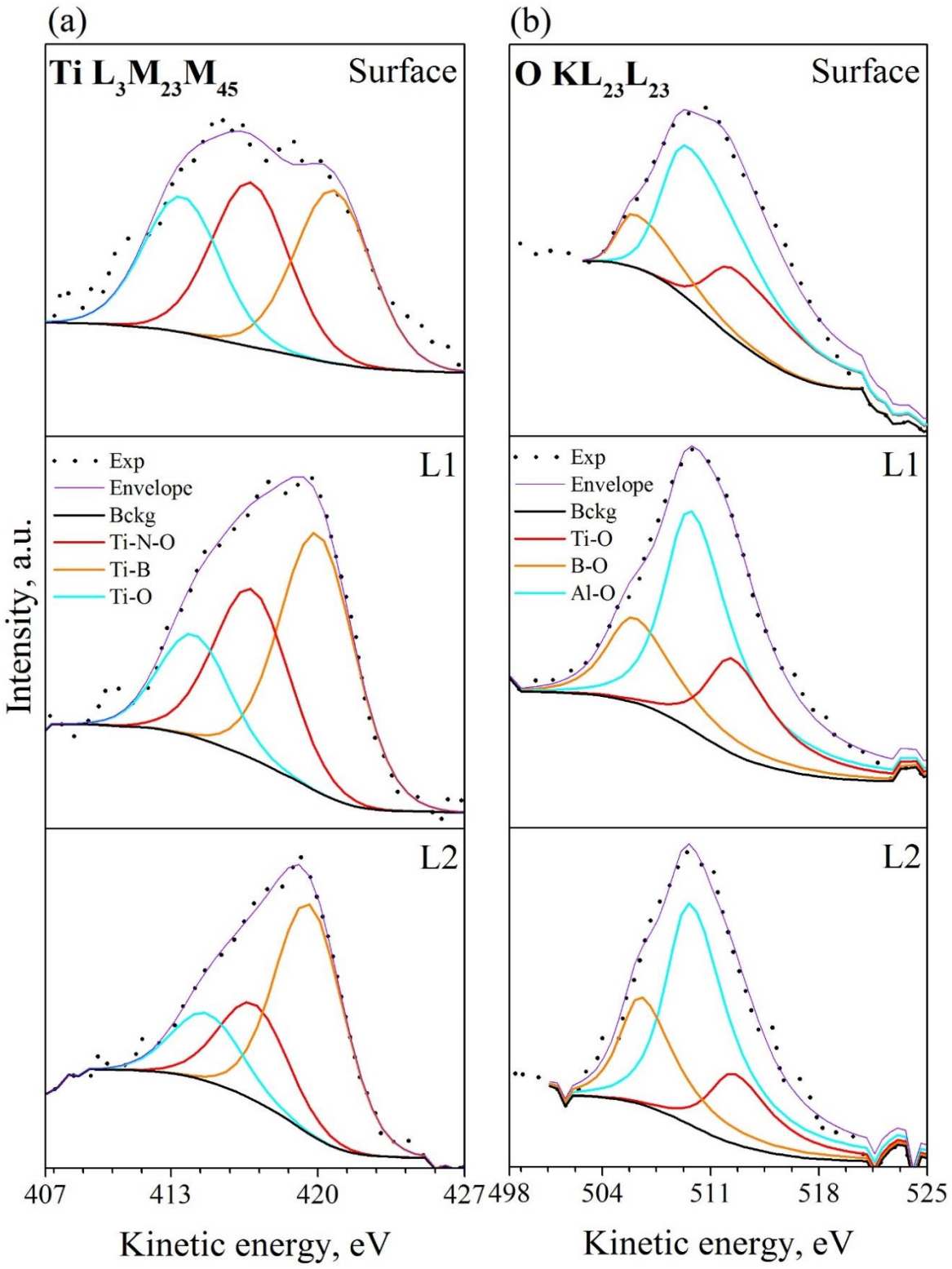

Figure 3.17. The Ti $L_3M_{23}M_{45}$ (a) and O $KL_{23}L_{23}$ (b) Auger lines of XPS spectra taken from the TiAlBSiN surface, from the L1 and L2 after the Ar+ ion etching.

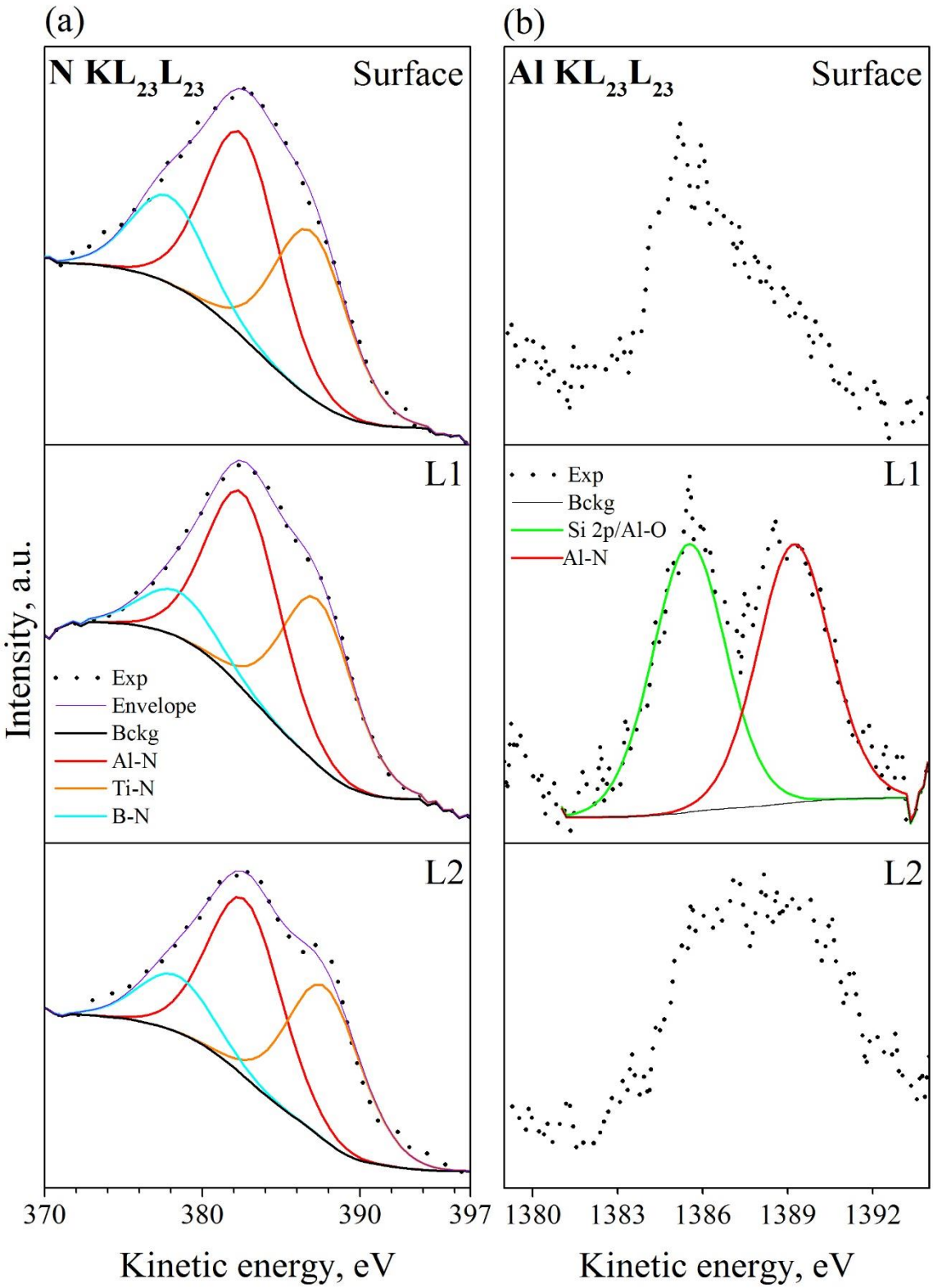

Figure 3.18. The N $KL_{23}L_{23}$ (a) and Al $KL_{23}L_{23}$ (b) Auger lines of XPS spectra taken from the TiAlBSiN surface, from the L1 and L2 after the Ar^+ ion etching.

Table.3.3. The interpretation of Auger lines of the XPS spectra obtained from the TiAlBSiN coating surface, from the L1 and L2 after the Ar^+ ion etching. The corresponding modified Auger parameter (α') of the spectra components are given in brackets (the binding energies of the corresponding components for the calculation of α' were taken from Table 3.2.).

Transition	**Auger peak position (Auger parameter, α'), eV**			**Assignment**	**Reference**
	Surface	**L1**	**L2**		
O $KL_{23}L_{23}$	506 (1038.6)	506 (1038.9)	506.5 (1039.4)	B-O	–
	509.5 (1040.8)	509.7 (1041.1)	509.6 (1041.1)	Al-O	**[307,308]**
	512.5 (1042.6)	512.4 (1042.9)	512.5 (1042.6)	Ti-O	
Ti $L_3M_{23}M_{45}$	420.0 (874)	419.9 (874.2)	419.7 (874.2)	Ti-B	**[309]**
	416.8 (872.8)	416.8 (872.7)	417.1 (873)	Ti-N-O	
	413.5 (871.9)	414.1 (871.2)	414.7 (872.3)	Ti-O	**[307]**
N $KL_{23}L_{23}$	386.8 (784.2)	387.3 (784.5)	387.7 (784.9)	Ti-N	**[310]**
	382.4 (779.8)	382.6 (779.8)	382.7 (779.9)	Al-N	**[311,312]**
	377.8 (776.2)	378.4 (776.6)	378.3 (776.6)	B-N	**[313]**
Al $KL_{23}L_{23}$	–	1389.2 (1462.5)	–	Al-N	**[306]**

XPS valence band spectra in the binding energy range from 0 to 29 eV of the L1 and L2 of the TiAlBSiN coating are presented in Fig.3.19. The lower part of valence band mainly consists of O 2s and N2s states at around 22.9 eV and 16.6 eV below the Fermi level, respectively. The upper valence band is formed mainly by O 2p, B 2p and N 2p states hybridized with Al 3s and Al 3p as well as Ti 3d and Ti 4s. The upper valence band is very broad due to contribution from various hybridization states and it is very difficult to distinguish the separate states. However, there are a well pronounced features of Al 3s-N 2p and N 2p-Ti 3d hybridization states. The states at around 2 eV formed mainly by Ti d-electrons which are localized along the (110) directions of fcc-TiN crystal and form t_{2g} symmetry. The feature at around 6 eV originates due to interaction of N p-orbitals with Ti d-orbitals, forming sp^3d^2 hybridization which results in an e_g symmetry in fcc-TiN (along (100) directions) **[314]**. This component has a higher intensity in the L1 that probably due to higher N concentration in this layer. The feature at 16.6 eV is due to N 2s states in TiN **[294]**.

The substitution of Al to Ti in metal sublattice of fcc-TiN leads to a weakening of sp^3d^2 hybridization since less Ti d-electrons are available to maintain the hybridization. Thus, the broadening of the upper valence band due to additional contribution of Al 3p-N2p and Al 3s-N 2p hybridization is observed, that in turn, stimulates the formation of sp^3 hybridization, which is also apparent for hcp-AlN. Indeed, it was showed (see Fig. 3.19 (red line) and **[315]**) that the substitution of Al to Ti in metal sublattice of TiN give rise to broadening of the band at around 6 eV and the subsequent formation of dual-phase fcc-(Ti, Al)N+hcp-(Al,Ti)N structure results in the contribution from both Al 3s-N 2p and N 2p-Ti 3d hybridization regions. Moreover, the broad feature of N 2s states at around 16.6 eV can be explained, in accordance with the calculated density of states for the system fcc-(Ti,Al)N reported in **[186]**, by substitution of Al to Ti in metal sublattice of TiN. It is obvious, that the higher intensity of Al 3s-N 2p feature in both layers of the coating than that of N 2p-Ti 3d is associated with higher amount of AlN phase in the coating than that of TiN.

Moreover, according to the density functional theory calculations and XPS valence band spectrum of TiAlSiNO system based on fcc-(Ti, Al)(N, O) solid solution reported in the work **[316]**, the presence of Al atoms in Ti-sublattice and O atoms in N-sublattice leads to the broadening of the upper valence band. The broadening is mainly due to the Al 3s-N 2p hybridization states and to the appearance of the O 2s band at around 22.2 eV (see Fig. 3.18 (cyan line)). Moreover, the intensity of O 2s band was reported to increase while the

intensity of N 2s to decrease when the amount of O in N-sublattice was increased **[316,317]**.

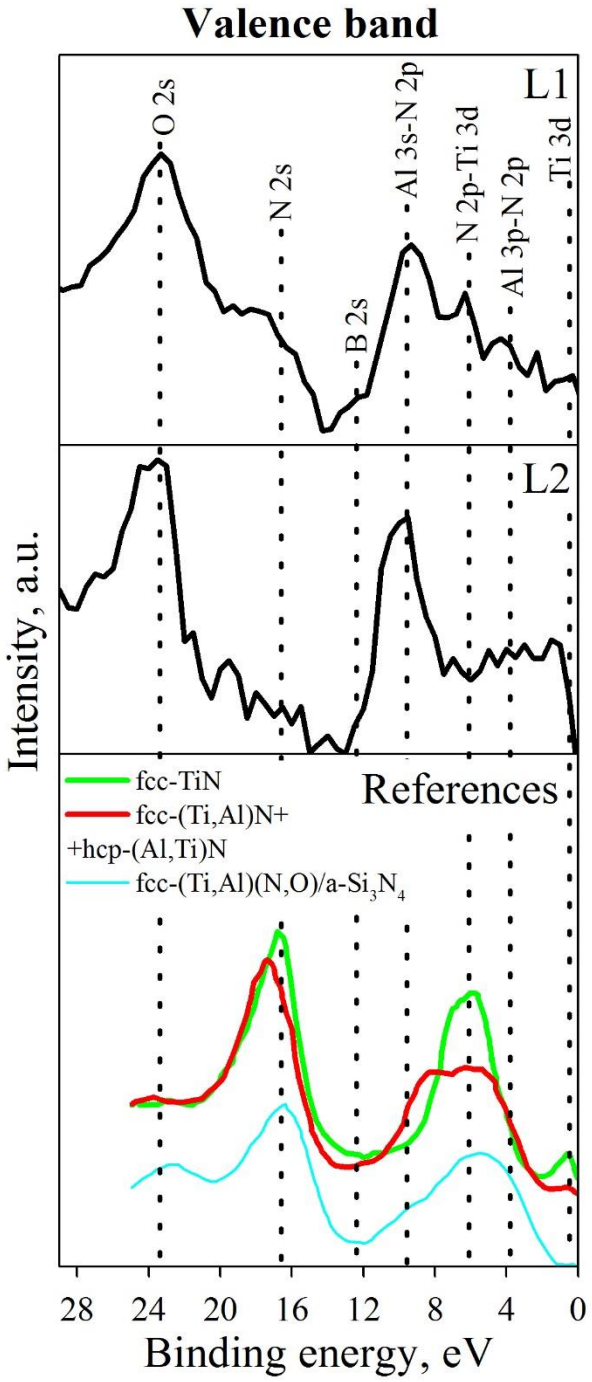

Figure 3.19. Valence band XPS spectra of the L1 and L2 of the TiAlSiBN coating and reference valence band spectra of fcc-TiN, two-phase fcc-(Ti,Al)N+hcp-(Al, Ti)N **[315]** and fcc-(Ti, Al)(N, O)/a-Si_3N_4 **[316]**.

Thus, the higher intensity of the O 2s band than that of N 2s in both layers indicates that the number of oxygen atoms in the non-metal sublattice of TiN is higher than that of N

atoms. However, the injection of N during the growth of the L1 results in the increasing of the intensity of N 2s. Additionally, a low intense peak at around 20.6-19.7 eV appears in the spectrum of the L1 that can be assigned to O 2s states of Ti-O or Al-O [311]. A low intense feature observed at around 12.4 eV can be assigned to B 2s-like states of B-N. Due to significantly lower amount of BN in the L2, this feature is less pronounced in the corresponding valence band. Consequently, these results additionally confirm out interpretation of XPS core-level spectra and give stronger evidence for the solid solution formation in the TiAlBSiN coating.

From the XPS and HRTEM results the following statements can be made. The observed cross-peak correlation of Ti 2p3/2 component at around 456 eV and N 1s component at around 396.3 eV as well as the presence of O 2s state at around 22.2 eV is an undeniable evidence of Ti-N-O bonds formation in the coating and considering that the TiN was observed to be in crystalline state, the mentioned Ti-N-O bonds can be a result of O incorporation into the TiN lattice. From the literature data, these peaks were observed in XPS spectra of air exposed TiN **[288]**, TiN after high temperature oxidation **[293]**, $N_2^+ + O_2^+$ implanted Ti **[292]** and fcc-Ti(O, N) **[318]** and fcc-(Ti, Al)(N, O) **[297,319]** solid solutions. Indeed, the DFT calculations **[320]** showed that the same number of O atoms can be incorporated into fcc-(Ti,Al)N lattice substituting N on non-metal lattice sites and into interstitial tetrahedron gaps of the fcc lattice. Therefore, we can assign the appearance of this peak due to the replacement of N by O in the TiN lattice or/and incorporation of O into interstitial lattice gaps. However, the incorporation of O into TiN lattice leads to the formation of Ti(N,O) solid solution with lattice parameter slightly smaller than that of TiN **[321]**. This is in contrast to our results (see Table 3.1). Among the coating containing elements, the observed lattice expansion can be induced only by the substitution of N to bigger B atoms (r_B=0.85 Å, r_N=0.65 Å **[281]**) in TiN non-metal sub-lattice. Indeed, the formation of solid solution between TiN and TiB is very probable because the fcc-TiN and fcc-TiB are highly isostructural and fcc-TiB is a high temperature boride phase whose formation is highly unfavorable under the deposition conditions used for the coating deposition. Moreover, very similar atomic radii, electronegativity and valence of B and N is the additional driving force to the formation of fcc-Ti (B, N) solid solution. The TiN lattice expansion due to incorporation of B can vary in the range from $a_{Ti\ (B,\ N)}$ = 4.325 Å to $a_{Ti\ (B,\ N)}$ = 4.236 Å depending on the amount of B in the non-metal sub-lattice **[283]**. Thus, the TiN lattice can contain not only O on the N sub-lattice sites but also B. The incorporation of O and B into the TiN can induce either competitive or accommodative effect on the expansion of the TiN lattice. Considering the observed

expansion of the lattice parameter of TiN and presence of characteristic Ti-N-O bonds in the coating, we can speculate, therefore, that the expansion can be partially compensated by incorporation of relatively small O atoms.

The components of Al 2p, N 1s and O 1s core-level spectra which were assigned to Al-N-O bonds in accordance with previous works are attributed to oxygen defects within the AlN crystal. These defects could only slightly contribute to the expansion of the volume of the AlN unit cell **[289,290]**. However, the magnitude of the observed AlN lattice expansion is significantly larger that cab be due only to substitution of Al to larger Ti atoms. Due to low lattice misfit between wurtzite BN and wuztzite AlN, these two phases are isostructural and tend to form solid solution under specific conditions. Moreover, considering that wurtzite BN is not thermodynamically favourable at the used deposition conditions (previously wurtzite BN was only observed under special conditions of very high temperature and pressure **[322]**), B atoms tend to substitute Al atoms in the metal sublattice of the thermodynamically preferable AlN that causes shrinking of the AlN lattice due to lower covalent radius of B atoms **[323]**. This is not observed in our case and therefore B incorporation into AlN lattice can be excluded or amount of the incorporated B in the AlN lattice is very small to cause the shrinking of the lattice.

There is a concern whether the B 1s component at around 187.6 eV is due to the presence of a-TiB_2, isolated Ti-B bonds located at the grain boundaries or B incorporated into (Ti,Al)N lattice. In the work of M. Baker et al **[157]** suggested the assignment of the feature at around 185.9 eV with a relatively small FWHF (0.9 eV) either to isolated Ti-B bonds or to B atoms incorporated in the (Ti, Al)N. However, a photoelectron peak corresponding to an atom with high coordination number and therefore with high electron density (such as in the fcc-lattice) should possess a noticeably broader FWHF **[324]**. Therefore, this peak is most probably due to isolated Ti-B bonds located at the grain boundaries. This is an agreement with results of other authors **[160,325]** where has been showed that higher boron concentration in the Ti-B-N nanocomposites give rise to higher intensity of the B 1s component assigned to a-TiB_2 and lower intensity of Ti-B component. In this regard, the binding energy shift and FWHF of the photoelectron peak of incorporated B atom substituting N in the TiN is expected to be significantly larger and will be comparable with that of TiB_2 due to similar coordination of B in TiB_2 and N in the TiN lattice **[326]**. Moreover, the peak at around 185.9 eV was reported for Ti-B-N coatings where B incorporation into the TiN lattice has not been observed **[327]**. Therefore, it is very difficult to distinguish TiB_2 bonds and B bonds in the TiN lattice in the B 1s core - level spectra.

Hence, the obtained XPS results give much stronger support to the assumption based on FFT/HRTEM results in Sec. 3.2.3 on the formation of nanocrystalline phase based on fcc-TiN and h-AlN. Furthermore, since no other crystalline phases were revealed by means of HRTEM studies, the fcc-TiN and h-AlN nanocrystalls most probably encapsulated into a-TiB_2/a-BN(O)/a-SiB/a-AlO_x/a-TiO_x/a-Si_3N_4 amorphous phase which is based on a-TiB_2 in the L2 and on a-BN in the L1.

3.2.5 Raman studies

In order to complement and support FFT/HRTEM and XPS results, Raman spectroscopy was conducted. The Raman spectrum of the TiAlBSiN coating is shown in Fig.3.20a.

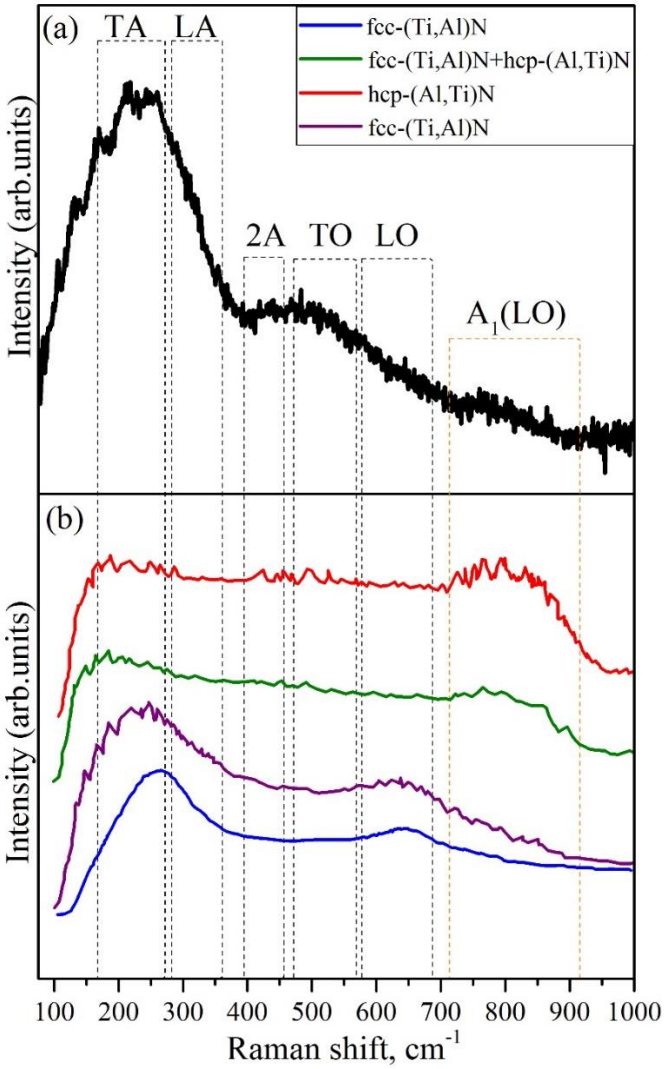

Figure 3.20. Raman spectrum of TiAlBSiN coating (a) and reference Raman spectra of fcc-(Ti, Al)N (blue line) **[328]**, fcc-(Ti, Al)N (purple line), dual-phase fcc-(Ti, Al)N+ hcp-(Al, Ti)N (green line), hcp-(Al, Ti)N (red line) **[174]** (b).

The spectrum of the coating shows the broad bands centred at 240 cm^{-1} and low intense broad band centred at around 482 cm^{-1}. These bands originate due to acoustic transitions in the 150-300 cm^{-1} region (LA and TA) and optic modes in the region 400-500 cm^{-1} (LO and TO) which correlates with the TiAlN phase **[328]**. Primarily the vibration of heavy ions near nonmetallic vacancies determines the scattering in the acoustic range that in the optical range arises from vibration of light atoms adjacent to metallic vacancies. Perfect crystal with fcc structure has O_h symmetry, every ion is at a site of inversion symmetry and consequently first-order allowed Raman active phonon vibrations are forbidden **[329,330]**. However, the effective symmetry of magnetron sputtered coatings is usually reduced, owing to the presence of numerous lattice defects. These defects reduce the effective symmetry, as more aluminium is dissolving in the TiN lattice suggesting the formation of a material with a very different structure. It should be remarked that, although there is a discrepancy in the reported Raman spectra of fcc-(Ti, Al)N based coating of relatively the same stoichiometry and phase composition that is probably caused by different deposition conditions and coating quality, the most pronounced common trend is that the intensity of the bands caused by acoustic transitions in fcc-TiAlN nitrides are more intense compared with that of stoichiometric TiN. This strong first-order scattering, indicate the presence of point defects and/or lattice disorder of the TiN lattice. Moreover, the addition incorporation of O, B or C atoms in the lattice of a fcc-TiAlN phase by substitution of N by O or/and C and B in the nonmetal sub-lattice or by occupying interstitial sites either by substitution of Al and/or Ti by Si, Al or/and Ti in the metal sub-lattice may break the crystal symmetry through the lattice distortion, thus, leading to Raman active vibrations in the range of first-ordered optic and first-ordered acoustic phonon modes, respectively. Thus, the Raman spectrum of a perturbed crystal reflects presence of impurities in the crystal. Indeed, the observed relatively higher intensity of the TA first-ordered phonon modes than that of the LA is a strong indication of the fcc-TiN lattice disorder due to the Al dissolution in the metallic sub-lattice of the TiN. Moreover, the shifts of acoustic vibrations toward higher frequencies compared to TiN is due to the substitution of Ti atoms with lighter Al atoms. Some authors **[331,332]** have assigned the shift of TA mode to higher wave numbers to the increasing of the lattice parameter that also observed in our case. Therefore, the increase of the TA mode intensity and its shift toward higher wave numbers cab be attributed to chemical and topological disordering of the fcc-TiN lattice. These indicate that Al atoms are occupying titanium sites due to the fact that aluminium and titanium have similar atomic radii forming a (Ti, Al)(N, O) solid solution. The broad band in the range of the optical phonon modes has a pronounced maximum at the lower wave number side that, in

accordance to Hook's law, can be caused by the vibration of B atoms at the non-metallic lattice sites of the TiN due to their relatively bigger covalent radius and higher mass than that of O and N atoms **[266,302,331]**.

The broad peak at around 800 cm^{-1} can be attributed to A_1(LO) phonon mode of hcp-AlN based phase. There are only six Raman active phonon modes in the wurtzite AlN. However, depending on AlN crystal orientation certain phonon modes can be forbidden by the polarization configuration of the incident beam according to selection rules **[333]**. This partially explain the discrepancy of the reported Raman spectra of hcp-(Al, Ti)N based coatings **[174,328]**. The observed broadening of the peak can be caused by the Raman processes decay at the grain boundaries or at defect and impurity sites of the AlN as well as due to increasing lattice disorder after incorporation of Ti and/or O into the lattice. Another reason of the broadening can be due to random orientation of AlN nanorcystalls **[333,334]**.

These results are in agreement with the HRTEM results, because the random orientation of the nanodimencional hcp-(Al, Ti)N crystals with presence of defects and the expansion of the lattice due to Ti incorporation were observed, and therefore both mechanism can contribute to the broadening of this line. Note that this observation is in a good agreement with literature reports, according to which, the broad band was observed at around 800 cm^{-1} after the formation of a highly disordered hcp-(Al, Ti)N phase in addition to fcc-(Ti, Al)N (see Fig.3.19b and **[174,335]**). However, the high intense peak at 768 cm^{-1} due to TO phonon mode of Si-C according to previously published data can not be excluded **[336]**. Clearly, there is a high probability of overlap between the optic modes and acoustic modes of different phases formed in the coating and it is extremely difficult to discern different phases, however, using previous data the above described interpretation of the obtained Raman spectra of the TiAlBSiN coating is proposed.

These results additionally confirm and support the interpretation of the HRTEM and XPS results. Therefore, there is a sufficient evidence to conclude that nc-(Ti, Al)(N, O, B) and nc-(Al, Ti)(N, O) nanocrystalls are encapsulated into a-TiB_2/a-BN(O)/a-SiB/a-AlO_x/a-TiO_x/a-Si_3N_4 amorphous phase which is based on a-TiB_2 in the L2 and on a-BN in the L1.

3.2.6 Outcomes of structural characterization

The growth of the coating with the observed nanocomposite structure can be explained by the further considerations. Among the possible phases which can be formed from the constituent elements of the coating, the highest driving force have TiN and AlN (Si_3N_4 is known to grow in an amorphous state at up to 1200 °C **[337]**) (Table 3.4). It is

important to note that the TiAlBSiN coating was deposited with Al/(Al+Ti) atomic ratio ~ 0.71 in both layers. Due to low difference in the Gibbs free energy and equilibrium formation enthalpy of ternary $Ti_{1-x}Al_xN$ mixed phases in fcc and hcp structures in this composition range **[338,339]**, dual phase fcc-TiN and hcp-AlN appear in the coating. Moreover, this composition range characterized by highest probability of forming dual-phase substitution solid solutions of fcc-TiAlN and hcp-(Al,Ti)N by Ti substitution to Al in the TiN metal sublattice and Al substitution to Ti in the AlN metal sublattice. In accordance to Hume-Rothery rules **[340]**, the formation of the solid solutions is most likely a consequence of the relatively low atomic size mismatch (2.72 %), the small electronegativity difference (0.07 units) and the small valence difference between Al and Ti in addition to the mentioned above a low energy difference between the two phases.

Table 3.4. The enthalpy of formation of nitrides, borides and oxides of constituent elements of the TiAlBSiN nitride coating **[342]**.

Nitrides	AlN	TiN	BN	Si_3N_4
ΔH, kJ $mole^{-1}$	-317.9	-337.65	-250.9	-744.74
Oxides	Al_2O_3	TiO_2	B_2O_3	SiO_2
ΔH, kJ $mole^{-1}$	-1662.3	-944.7	-1271.9	-910.86
Borides	AlB_2	TiB_2	TiB	SiB
ΔH, kJ $mole^{-1}$	-161.35	-279.5	-160.2	–

However, the deviation from the Vegard's law is observed for fcc-(Ti,Al)N lattice parameter. According to Vegard's law the Al incorporation might be expected to cause a decrease of the lattice parameter. However, the opposite is observed in our case that indicates on the incorporation of B into the lattice which is having the larges effect on the lattice parameter due to the fact that r_{Al}/r_{Ti}~0.89 while r_B/r_N~1.3. The value of the calculated lattice parameter is in agreement with that obtained by other authors for (Ti, Al)(N, B) **[220]** and Ti(N,B) phases **[282,283]**. Additionally, there is no obvious evidence of the incorporation of Si into the TiN and AlN substituting Ti and Al atoms, respectively, however it might be expected also, and the magnitude of reduction of the lattice parameter after Si incorporation can be very low and negligible in comparison to effect of B in TiN or Ti in AlN **[207,341]**. Moreover, it is clearly seen (Fig. 3.6) that the relative Si

concentration in the L2 is much higher than in the L1. This might be responsible, in addition to the injection of N, for the higher average grain size in the L1 due to probable higher amount of a-Si_3N_4 in the L2, which more effectively hinders the grain growth in this layer.

Due to reasonable degree of matching of fcc-TiN and fcc-TiB lattice parameters and similar electron configuration, atomic size and chemical nature of B and N, the formation of the substitutional solid solution fcc-(Ti, Al)(B,N) is observed. Moreover, due to relatively small atomic size of O atoms in comparison to Ti, Al, B and N and existence of the octahedral and tetrahedral voids in the both lattices, they tend to occupy both the non-metal sublattice sites and interstitial gaps of the fcc-TiN and hcp-AlN lattices. Additionally, the formation of solid solutions is promoted by kinetic constrains caused by non-equilibrium deposition conditions. The used deposition conditions give rise to low adatom mobility, i.e. low growth temperature, which impede atom diffusion on long distances. Because of a lack of energy, atoms cannot reach a low energy lattice sites and therefore remain at non-equlibrium positions and further covered by the next growing layer. Thus, the highest number of atoms per unit area can be incorporated at low energy sites at lower adatom mobility. However, the mechanism of solid solution formation is limited by the solubility limit of the solute elements in the fcc-TiN and hcp-AlN lattices. Limited solubility in the TiN and AlN lattice together with low adatom mobility results in a precipitation of the excessive B, O and Si along the grain boundaries of the growing crystals. These leads to a change in the growth mechanism. The segregation of B, O and Si to the grain boundaries decrease the boundary mobility and stimulates a re-nucleation of grains and therefore hinder their growth and led to the refinement of the coating structure to a nanocrystalline state **[343]**. The segregated B, O and Si form amorphous a-TiB_2, a-BN, a-SiB, a-TiO_x, a-AlOx, and a-Si_3N_4 phase, which prevents crystal growth due to the difficulty of atom mobility in a multi-component amorphous system which has high packing density due to the packing of different-sized atoms **[344]**. Important to note higher amount of AlN in both layers than of TiN. A preferred formation of AlN might be caused by doping with B and Si, as has been also showed by other authors for $Ti_{0.3}Al_{0.7}N$-based dual phase fcc+hcp coatings doped with low amount of B or Si **[201,222,345]**. Due to the insufficient study of a doping of dual phase fcc+hcp TiAlN coatings this phenomenon is not well understood. However, the fcc structure was found to be more unstable when $x>0.7$. The region of coexistence of the hcp and fcc phases is very narrow and fcc+hcp phase is very sensitive to any fluctuations of composition and/or temperature **[127]**. This can partially explain the discrepancy in the reported composition range of the coexistence

of fcc+hcp structured coatings (see Table 1.2). Importantly, Si, B and Ti tend to occupy Al lattice sites in hcp-AlN, while B tends to occupy N lattice sites, and Si and Al tend to occupy Ti lattice sites in the fcc-TiN. Under N deficiency, solubility limit of B in TiN increases **[346]**, while saturation of Al prevents possible incorporation of Si and B into the AlN lattice. DFT calculations of H.W. Hugosson at al **[237]** have demonstrated that Si or B doping of fcc and hcp structured $Ti_{x-1}Al_xN$ in the range x~0.7 results in the formation of corresponding quaternary solid solutions which have stabilities very close to those of the mixture of ternary hcp+fcc $Ti_{x-1}Al_xN$ solid solutions. Moreover, as follows from their study, B preferably tend to substitute N in the TiN lattice than Al in the AlN hcp-lattice and therefore the Ti(N,B) solid solution is even more preferable under nitrogen deficiency. Thus, due higher solubility limit of B in TiN than in AlN, the lattice parameter of TiN increases while possible incorporation of low amount of B into AlN do not effect the lattice parameter significantly. Moreover, since N has a higher affinity to Si than to Al and Ti and thus the a-Si_3N_4 phase may form at first and act as a kinetic constrain to the Ti and N diffusion due to Ti largest atomic radius among the constituent elements. Therefore, the growing a-Si_3N_4 can trap diffusing Ti and N and thus suppress TiN crystal growth much more effectively than the AlN-based crystals (considering that Al mobility is higher than the Ti mobility). This is supported by the fact that injection of N gave rise to the formation of higher amount of a-BN and increases the crystal growth. The appearance the quaternary solid solution phases in the coating is in agreement with the theoretical prediction of H.W. Hugosson at al **[237]** where alloying of Al-rich TiAlN system with B, C, O or Si has been showed to have the stabilization effect on both phases by bringing the energies of the two structures closer. Moreover, the quaternary TiAlBN and AlTiBN are in metastable state and the driving force for decomposition into ternary phases in this composition range is very low thus making possible coexistence of these phases under non-equilibrium conditions **[237]**. However, a much higher amount of hcp-AlN based phase than of fcc-TiN is observed in the coating. This may be due to too high B and Si concentration in the coating that promotes the formation of a dense amorphous phase suppressing Ti diffusion and nucleation of corresponding grains or energetic growth conditions were insufficient to stimulate the growth of TiN-based phase.

The high entropy effect, which comes from the close to equiatomic ratios of the elements of the coating, can equally promote the formation of both the solid solution phase and amorphous phase. In this regard, the decisive role play the mixing enthalpy and the atomic size difference of the constituent elements. In this composition range the mixing enthalpy of dual-phase TiAlN is slightly positive **[347]**, thus the formation of the solid

solution is promoted. However, the atomic size difference between constituent elements, in contrast, stimulates the formation of amorphous phase in the coating. Therefore, as a consequence of competitive growth of solid-solution phase and amorphous phase under low adatom mobility, the nanocomposite structure was formed.

Hence, considering the results of HRTEM, XPS and Raman studies, there is a sufficient evidence to conclude that due to the kinetic and thermodynamic constraints the phase segregation was not completed during growth of the coating and a multi-phase structure where fcc-(Ti, Al)(N, O, B) and hcp-(Al, Ti)(N, O) nanocrystals are encapsulated into a-TiB_2/a-BN(O)/a-SiB/a-AlO_x/a-TiO_x/a-Si_3N_4 amorphous phase which is based on a-TiB_2 in the L2 and on a-BN in the L1 was formed.

3.2.7 Nanoindentation studies

Nanoindentation studies of TiAlBSiN coatings deposited on steel substrate were carried out under depth control mode at indentation depth of 75.5 nm (less than 10% of coating thickness) at the load 2.5mN. Fig. 3.21 shows the P–h (load–depth) plot of the TiAlBSiN coating. The hardness (H) and reduced elastic modulus (E^*) of the TiAlBSiN coating measured from indentation load–displacement data obtained during one cycle of loading and unloading were 17.55 GPa and 216.71 GPa, respectively.

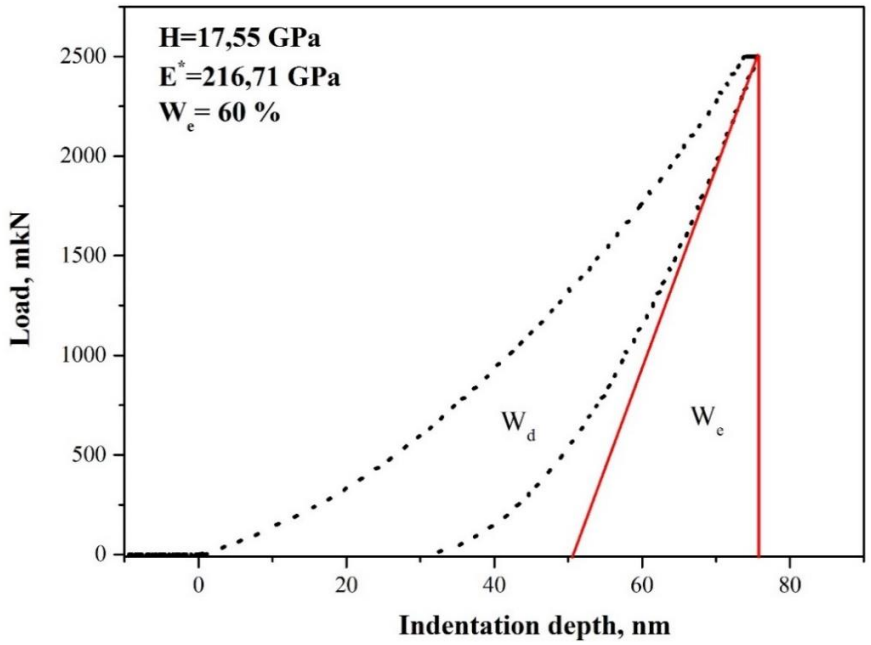

Figure 3.21. P–h plot for the TiAlBSiN coating at an indentation depth of 75.5 nm and maximum load of 2.5 mN.

There are several factors which may be responsible for the observed relatively low hardness. Firstly, the relatively low hardness is probably due to the high inter-particle

spacing of the nanocrystalline grains and the volume fraction of the amorphous matrix that led to decreasing of the cohesive energy of interface boundaries between the nanocrystalline and amorphous phases and thus the decrease of hardness due to grain boundary sliding becomes predominant. Secondly, when the amount of amorphous phase exceed certain limit, the hardness of the nanocomposite becomes dependent on the property of the amorphous phase, which is mainly dependent on the strength and density of bonds forming amorphous phase. Due to high volume fraction of amorphous phase, the strong B-N, Ti-B and Si-N bonds may highly contribute to the hardness of the coating. Thirdly, the gain of hardness due to solid solution hardening is negligible because the coating is based on a relatively soft hcp-(Al,Ti)(N,O) phase in which solid solution hardening is less effective than in cubic counterpart. Hence, these contributions are decisive for the hardness of the TiAlBSiN coating and it is difficult to determine which mechanism has the largest effect.

As can be seen from Fig. 3.21, the TiAlBSiN coating demonstrates excellent elastic properties with an elastic recovery energy value up to 60%.

In situ SPM measurements of the residual impressions after nanoindentation experiments were carried out (Fig. 3.22). The slight pile-up ~10 nm in height can be found in the region around the indent, no shear bands or radial cracks were observed. It has already been noted by Johnson **[348]**, that a large capacity for work hardening drives the plastic zone into the material to greater depths and decreases the amount of pile-up adjacent to the indenter. Moreover, since the pile-up is observed when $h_f/h_m<0.7$, the hardness and elastic modulus were measured without an overestimation.

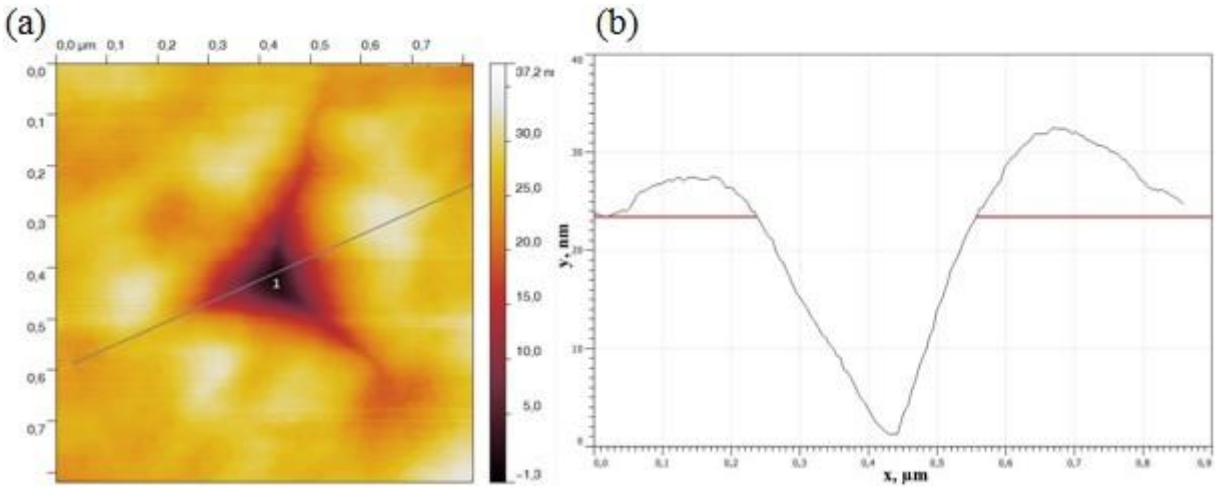

Figure 3.22. SPM top view image of the residual impression (a) and the cross-sectional profile of impression (b) after nanoindentation of the TiAlBSiN coating at the load of 2.5 mN.

Nanoindentation measurements were conducted using a partial load/unload function with maximum loads from 0.05 μN to 10 mN applied to a diamond Berkovich tip in order to measure hardness (H) and reduced elastic modulus (E^*) of the TiAlBSiN coating at different depths. Fig. 3.23a displays a load-depth curve of multiple loading and unloading cycles from which H and E^* were derived using Oliver-Pharr method as a function of indentation depth (Fig.3.23b). The hardness tends to increase with increasing penetration depth and reaches its maximum value H = 18.35 GPa at a depth of 77 nm, Fig. 3.23b. In the range of indentation depths from 77 nm to 130 nm a gradual decrease of the hardness is observed. Importantly, the hardness decreasing starts after reaching 10% of the coating thickness because of the influence of the relatively softer lower layer. The average value of hardness was 17.95 GPa.

It is demonstrated in Sec.1.1.2.2 that not only hardness or elastic modulus but also the ratios H/E^* and H^3/E^{*2} are very important material properties. To predict the wear resistance of the TiAlBSiN coating, the elastic strain prior to plastic deformation (H/E^*) was evaluated from data obtained from multiple indentation test and is depicted in Fig. 3.23c as a function of contact depth. The sharp increase of H/E^* ratio up to 0.088 at a depth of 20 nm is probably caused by nanoroughness, R_a = 0.38 nm, of the coating surface. H/E^* ratio of the TiAlBSiN coating is varying in the range from 0.08 to 0.09 at the contact depth of 20–75 nm. It is clearly seen that the H/E* ratio as well as the hardness start to decrease after a contact depth of 75 nm. Thus elastic strain to failure increases with increasing depth up to 75 nm that can provide elastic behaviour of the coating in rough contact during wear at high load and contact pressure. It is shown that the values of H/E^* ratio of TiAlBSiN coating are close to $H/E^* > 0{,}1$ which satisfy the condition proposed by J. Musil **[39]** for protective nanocomposite coatings resistant to cracking and under certain circumstances, the gain from the H/E^* ratio 0.08–0.09 and W_e~60% in the wear rate reduction could be substantial.

Fig. 3.23c depicts the resistance to plastic deformation (H^3/E^{*2} ratio) of the TiAlBSiN coating, evaluated at the different indentation depth.

H^3/E^{*2} ratio increases from 0.01 to the maximum of 0.12 GPa and stay approximately constant up to the depth of 75 nm. No residual deformation was detected after the indentation tests, confirming that the deformation was mainly elastic. Such values of the resistance to plastic deformation of the coating can play a decisive role for sustaining heavy loads since the minimization of the probability of initiating cracks can be substantial. Moreover, the observed values of H^3/E^{*2} ratio of the coating can provide an effective protection against solid particle erosion **[349]**.

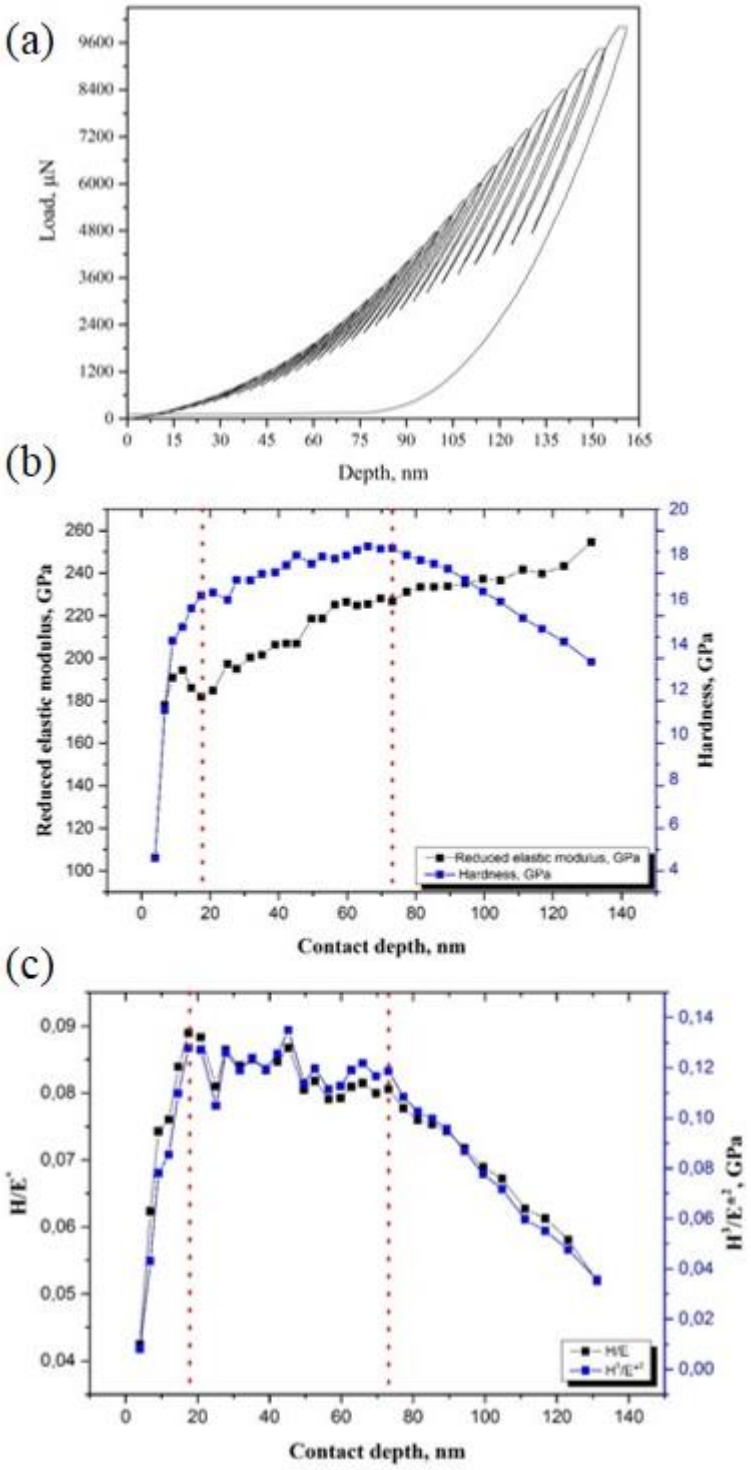

Figure 3.23. Typical sequential nanoindentation load-displacement (depth) curves of TiAlBSiN coating (a) and corresponding hardness and reduced elastic modulus as function of the contact depth (b) and variation of the ratio H/E^* and H^3/E^{*2} as function of contact depth (c).

The randomly oriented nanograins of the coating are separated by the relatively thick amorphous phase which prevents interaction of atomic planes in the adjusted

nanocrystalline grains and facilitate grain boundary sliding. The grain boundary sliding of the nanograins of the L1 combined with their misorientations can induce a significant effect on crack behaviour due lower normal stresses in critical locations **[350]**. Therefore, the achieved toughening in the coating is assumed mainly due to strain release via a certain degree of nanocrystal sliding in the amorphous matrix and relaxation of stress via plastic deformation of the amorphous phase. The suitable toughness of the TiAlBSiN coating due to enhanced resistance to the crack initiation and propagation and elasticity make them a promising candidate for use as a flexible hard protective coating.

3.2.8 Nanowear tests

For further investigation of tribological properties of the TiAlBSiN coating, nano-wear test was made using the nanoindenter. The advantage of nano-wear test is that wear properties are mainly determined by the intrinsic properties of the coating materials due to the small loads and scale that allows to exclude the influence of the substrate. Comparative study of nanowear for stainless steel and monocrystalline silicon (100) has been carried out and presented in Table 3.5. Fig. 3.24a shows typical surface topography of the TiAlBSiN coating after 1 cycle of wear test under a load of 1000 μN load in an area of 5 μm×5μm. The nanowear volume was 352.22×10^{-3} μm^3.

The study indicates small material loss and better wear resistance for the TiAlBSiN coating compared to the steel and silicon. Surface height profile in Fig. 3.24b shows that both the wear scar depth in the range ~10 to 15 nm and the pile- up height in the range ~15 nm to 25 nm are present at the wear square. The pile-up around the edges of the wear track is probably due to indentation in the film normal direction, which often leads to severe plastic deformation indentation in the film normal direction.

Table 3.5. Results of tribo-mechanical tests for TiAlBSiN coating, monocrystalline silicon (100) and stainless steel at 1000 μN peak load.

Sample	Wear depth, nm	Wear volume, $\times 10^{-3}$ μm^3	H, GPa	E^*, GPa	H/E^*	H^3/E^{*2}, GPa
TiAlBSiN	~15	352.22	17.55	202.7	0.087	0.1316
Si (100)	~25	502.3	12.4	189.67	0.091	0.1449
Stainless steel	~40	2226.72	10.30	194.38	0.053	0.0289

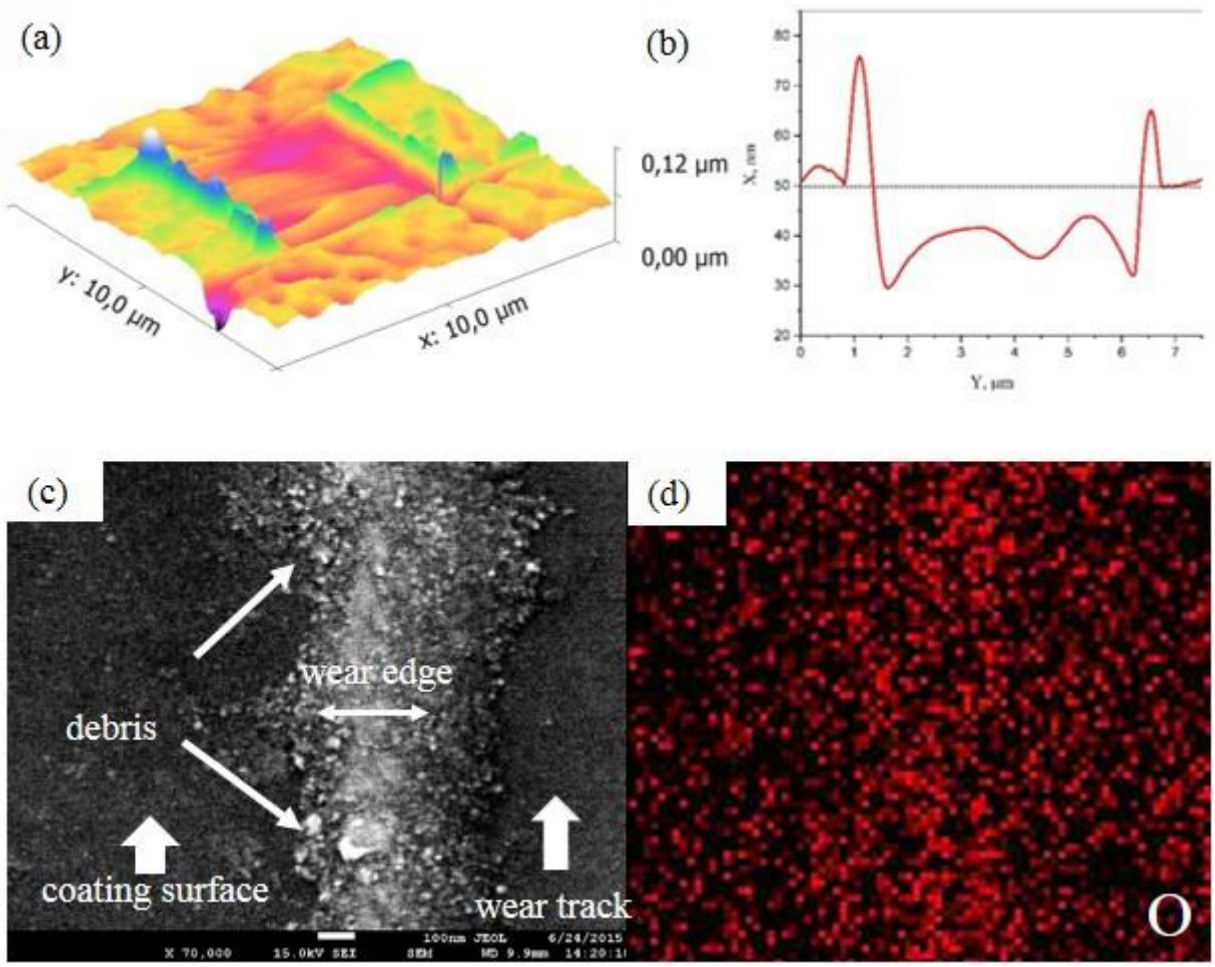

Figure 3.24. 3D topographical in-situ SPM image of the TiAlBSiN coating after 1 cycle of wear with 1000 µN normal load (a) and corresponding surface height profile (b). SEM image of the wear edge with debris (c) and corresponding EDS map of oxygen (d).

Further investigation of the wear track using SEM-EDS (Fig. 3.24c and d) clearly shows that the material loss take palace and wear debris were generated during wear process around the edges of the wear track. Plastic deformation occurs during scratch wear because of the indentation in the film normal direction, while translation along the sliding direction leads to material removal due to abrasive wear and generation of wear debris. For a large wear track, the translation motion dominates and material loss is mainly due to abrasive wear. It is important to note that non-uniform wear of the coating is observed.

It is well known that most metals oxidize in air to some extent and form a number of oxides in form of thin film typically between 1 and 10 nm thickness. The formation of such oxide film based mainly on (Ti, Al, Si)O_x on the surface of TiAlBSiN coating is confirmed by means of XPS studies. The oxide film acts as a low shear-strength film during wear and additionally leads to low friction because of low ductility. However, during sliding, these thin oxide films may be penetrated. Furthermore, the film is penetrated at higher loads, and

transition occurs to high values of friction. MeO_x wear debris around the edges of the wear track of TiAlBSiN coating is due to abrasive wear of thin oxide film, but addition oxidation stimulated by the complex chemical and thermal interactions within the sliding contact zone could not be excluded.

3.3 Amorphous nanocomposite coating based on TiAlBSiN

The following section focuses on the characterization and analysis of strucrure and physical properties of the amorphous nanocomposite coating based on TiAlBSiN. The influence of the high-temperature annealing on the structural features of the coating will be addressed first. Then the characterization of the mechanical and tribological properties of the coating before and after annealing will be presented.

3.3.1 AFM studies

Figure 3.25 shows a 3D image reflecting the surface morphology of the TiAlBSiN coating before and after annealing at 900 °C. In label represent the root-mean-square value, associated to the surface roughness (R_{rms}) of the TiAlSiBN coatings as deposited (Fig. 3.25a) and after annealing at 900 °C (Fig. 3.25b). The coating had a very smooth surface after deposition, with R_{rms} equal to 0.38 nm (measured over the area of 1×1 μm) and R_a equal to 0.47 nm (measured acros 1.2 μm).

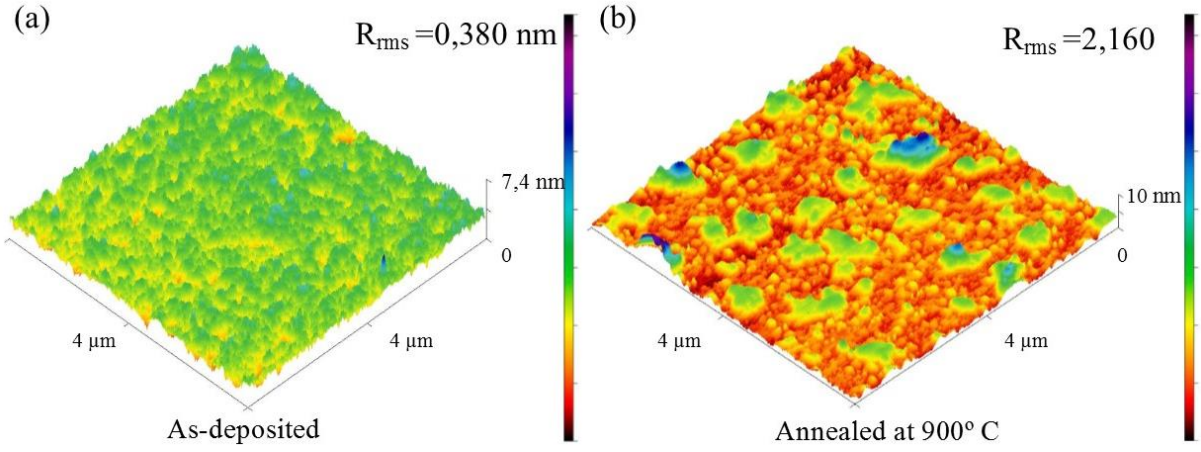

Figure 3.25. Three-dimensional AFM surface morphologies and their surface roughness of as-deposited (a) and annealed at 900 °C (b) TiAlBSiN coating on silicon wafer substrate.

Such nanoroughness develops as a consequence of influence of several factors during coating growth which were described in details above, Sec.3.2.1. Therefore, such

nanoroughness is a strong indication of amorphous structure of the TiAlSiBN coating after deposition. Me-Met-O_x (Me- metal, Met-metalloid) oxides formation during thermal annealing at 900 ºC, island growth and densification of the material, affecting the surface roughness were observed. Due to the growth of islands perpendicular to the substrate surface, the roughness slightly increased to R_{rms} = 2.16 nm and R_a = 1.76 nm after annealing. Nevertheless, although the high temperature of annealing used, not significantly affect were observed in the coating roughness, which is an important characteristic for coatings facing both, different friction condition during dry machining and high temperature impact.

3.3.2 SEM studies

Fig. 3.26a and b shows the top-view and cross-section images of the TiAlBSiN coatings as-deposited and after annealed at 900 ºC in air, respectively.

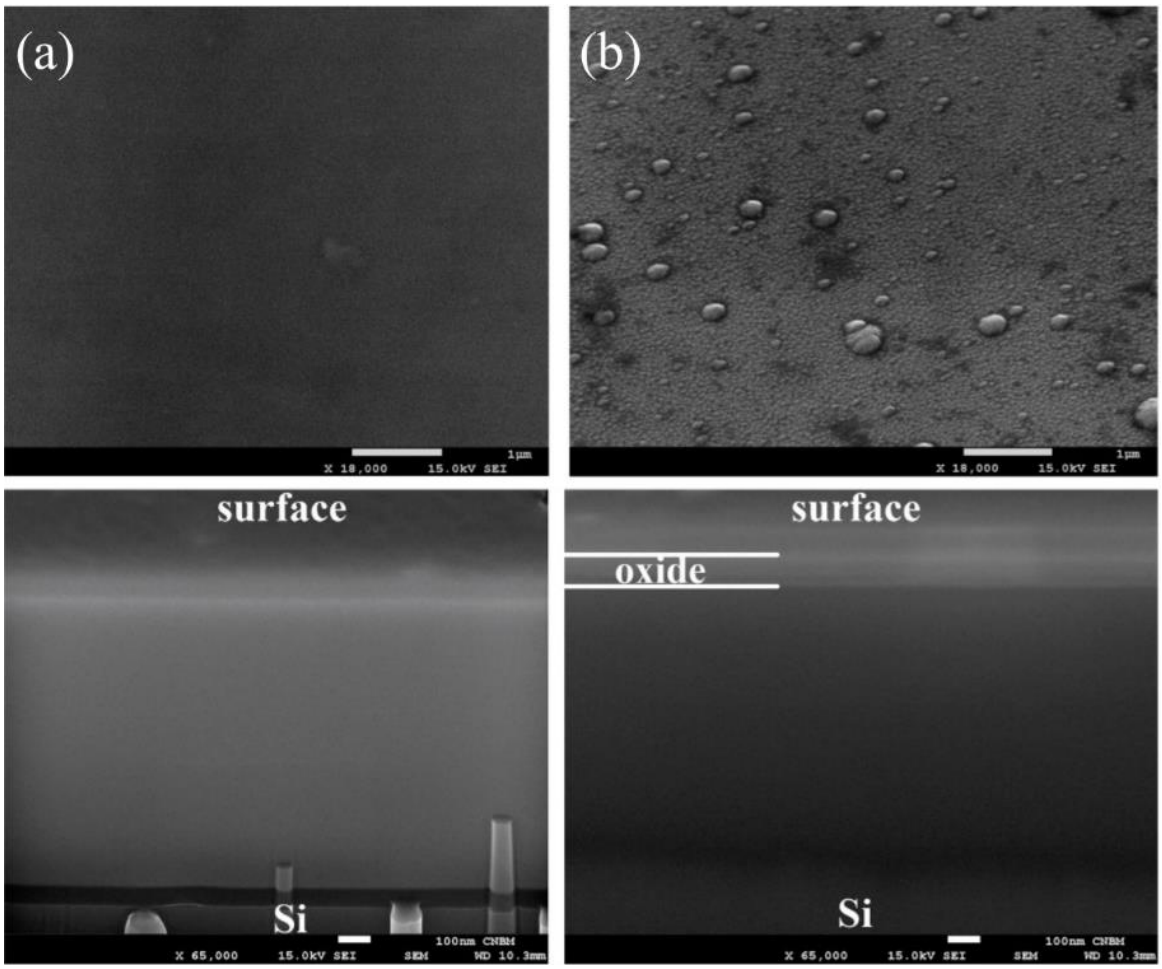

Figure 3.26. SEM images of TiAlBSiN coating's surface after deposition on silicon wafer substrate (a) and after annealing at 900 °C (b) in air (upper), and corresponding cross-section views (lower).

The observation of the surface of the as deposited coating revealed (Fig. 3.26a), the fine homogenous and uniform surface characteristics. The cross-section image shows the dense and featureless structure of the as-deposited coating with a sharp coating/substrate interface. As a consequence of the high temperature annealing, superficial globular oxide nodules and the macro grains of 400 nm are formed at the surface of the coating. The structure of the coating appears to be preserved, but the formation of the surface oxide layer and diffuse interface with the substrate are observed.

3.3.3 TEM-EDS studies

Fig. 3.27a shows the extracted EDS profile of the as-deposited TiAlBSiN coating with the corresponding bright-field TEM (BF-TEM) image (b), and HR-TEM images of top (c), middle (d) and barrier layer (e).

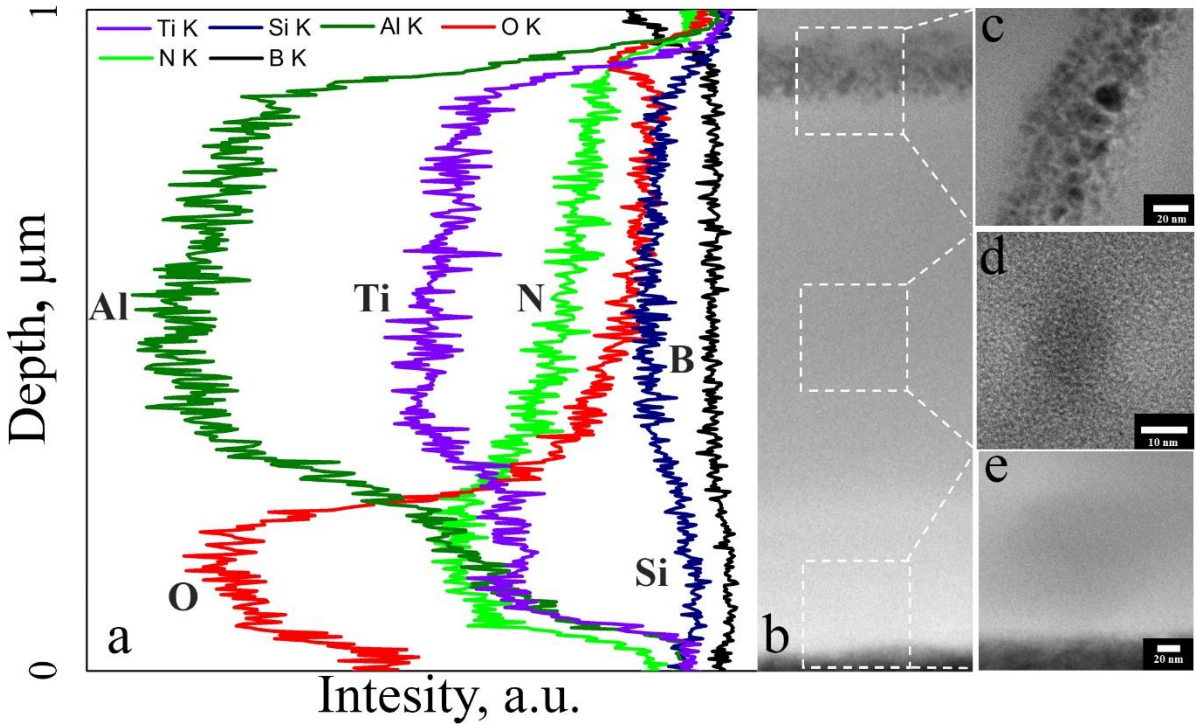

Figure 3.27. TEM-EDS line scan of the as deposited TiAlSiBN on silicon wafer substrate with corresponding cross section BF-TEM image (b), and HR-TEM images of top (c),middle (d) and barrier layer (e).

The as deposited coating shows fully amorphous structure as shown in the close magnification HR-TEM images. The coating microstructure is dense and void-free after the deposition. The formation of such microstructure is first of all a result of sufficiently high energy delivered to the growing coating due to relatively low deposition rate in

combination with optimal values of the substrate bias and the substrate ion current density **[113]**. Secondly, as follows from "confusion principle" **[351]**, the mixture of 5 elements which additionally have large difference in atomic size leads to a dense packing during deposition that favours amorphous phase formation over crystallization in the coating. Moreover, the nucleation of grains additionally constrained by the ion flux due to highly negative bias voltage applied to the substrate. Indeed, the deposition conditions used for growth of the nanocomposite coating described in Sec.3.2 and for the amorphous coating are the same, except the significantly higher bias voltage (–200 V) used in the latter case. Therefore, the high ion flux and high energy of the ions result in generation of higher density of growth defects in the nucleation layer thereby increasing the number of preferential nucleation sites and thus restricting grain growth. When the concentration of the growth defects reaches an amorphization threshold level, the amorphization dominates during the growth. At the same time, the high energy ions may also increase the mobility of adatoms which in turn can promote an annihilation of defects. The annihilation can be promoted by light atoms, which are the most mobile species at such conditions. Since Si and B are known to be effective in promoting amorphization, the coating tends to grow in an amorphous state. Moreover, during the atomic scale heating of the growing coating the kinetic energy of bombarding ions is transferred into very small areas of the coating and therefore its growth accompanied by an extrimelly fast cooling (typically 10^{14} K/s **[352]**) that additionally facilitates the formation of an amorphous state **[353]**. It is worth noting that the high substrate bias voltage can be responsible for the lower concentration of light elements (N, O and B) in the coating than in the target, due to the re-sputtering of these elements and thus causing a lower adatom mobility.

It is clearly seen on the EDS lines and BF-TEM image that the TiAlBSiN coating has a three-layer structure (Fig. 3.27, Table 3.6). The air exposure of the coating just after the deposition give rise to the oxidation of the surface starting from the room temperature with the formation of amorphous Me-Met-O at the outermost layer (~10 nm), therefore the top layer of the coating is characterized by a relatively high oxygen concentration ~13.23 at.% (see Table 3.6) in comparison to the bulk of the coating. The region beneath the Me-Met-O surface layer is a ~800 nm thick layer composed of Al, Ti and N with relatively lower concentration of other target elements such as B and Si. Finally, the barrier layer is depleted of Al and Ti, which could be explained by the characteristics of the sputtering process of a multiphase target during the reactive DC magnetron sputtering which was described previously in Sec.3.2.4. The O-rich barrier layer with amorphous structure serves as a "trap" for diffusive element from the both sides of the barrier. It limits elements of

both, the coating and the substrate, due to the high electronegativity of O and amorphous structure. Moreover, the amorphous state of the coating after deposition is the main reason of the observed nanoroughness of the coating surface.

Table 3.6. EDS quantitation results for the TiAlBSiN coatings on silicon wafer substrate ("–" means that the element was not quantified by the software but its characteristic peak was depicted on the EDS spectrum)

		Thickness, nm	Ti, at. %	Al, at. %	Si, at. %	O, at. %	N, at. %	B, at. %
As-deposited	**top oxide**	~10	12.66	24.05	3.96	13.23	10.04	36.05
	coating	~800	13.28	23.59	4.20	9.51	12.01	37.41
	barrier layer	~200	11.00	11.40	4.20	49.82	–	23.58
Annealed at 900 ºC	**top oxide**	~35	12.52	14.54	6.64	66.30	–	–
	coating	~800	22.21	28.97	7.50	29.10	12.22	–
	barrier layer	~200	11.34	12.16	10.79	65.71	–	–

Fig. 3.28 shows the analytical results of the structure transformation of TiAlBSiN coating after high temperature annealing in oxidative ambient at 900 °C. The EDS lines scan (Fig. 3.28a) and EDS quantitative analysis indicates that Al, Ti and N diffuses outwards, toward the free surface of the coating, which causes N depletion of the surface layer and non-uniform distribution of Ti and Al through the depth of the coating. The depletion of N in the surface oxide layer might be due to its escape to the gas phase that is commonly observed in TiAlN based coating starting from 600 °C **[181]**. The layering becomes more evident and the growth of the surface oxide layer up to ~35 nm is observed, with a relatively small amount of Al and Ti. The main driving force for the outward diffusion of Al to the surface of the coating is its oxidation, which is accompanies with a substantial decrease of free energy, as compared with formation of titanium, boron or silicon oxides (see Table 3.4.). The oxide layer protects the underneath layer from degradation and oxidation as shown by the low oxygen content on the O concentration profile, which remains relatively unchanged after annealing at the coating/barrier layer, whereas a slight increase of Al, Ti, Si and O concentration in the barrier layer is observed. This increment is due to the exchange of diffusion elements between the sacrificial barrier,

the coating and the Si substrate. The Si content in the coating increases to 3.3 at.% after annealing, while the Si concentration in the barrier layer increases to 6.59 at.% in comparison with the barrier layer just after the deposition. This is an indication of the suppression of the Si diffusion to the coating by the barrier layer. However, the barrier layer does not fully stop it, showing the effectiveness and stability of TiAlBSiN(O) sacrificial barrier layer at 900 °C with presence of interdiffusion between coating/barrier/ substrate.

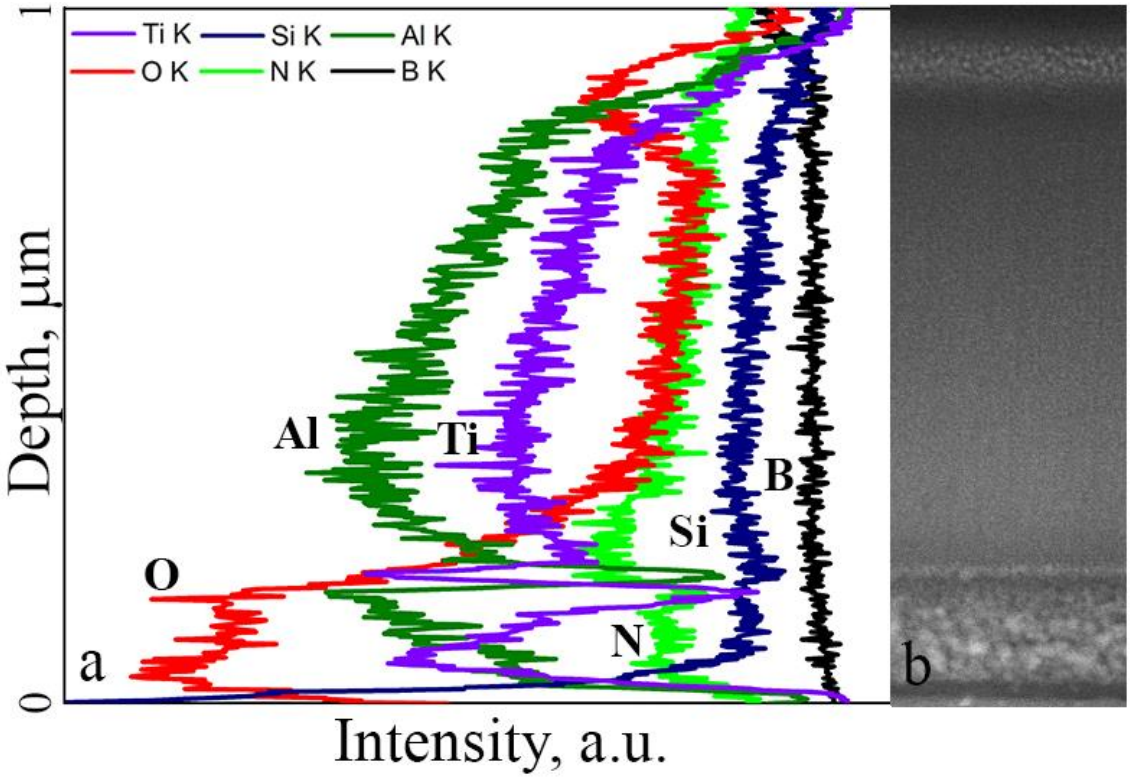

Figure 3.28. TEM-EDS line scan of TiAlSiBN on silicon wafer substrate after oxidation in ambient air at 900 °C (a) with corresponding cross section dark-field TEM image (b).

It is important to note that a significant redistribution of elements in the barrier layer volume take place after annealing. The outermost layer at the coating/barrier interface is mainly based on Ti. Considering the intensity difference of Al and Ti signals, it is assumed that this layer is probably formed at the top of the neighbour Al-O-based region (Ti-enriched area). The barrier/substrate interface is based on Ti and a depleted Al area. This mixing behaviour is kinetically driven by temperature initiated diffusion of the elements of the barrier layer and, probably, inward diffusion of the elements from the coating and the substrate.

More detailed analysis of TiAlBSiN coating's structure transformations after the high temperature annealing at 900 °C was carried out by means of HR-TEM. Fig. 3.29a shows

that the surface oxide layer remains in pure amorphous state after oxidation in ambient air at 900 °C and the FFT inset do not show any signs of crystallization of the surface oxide layer of the TiAlBSiN. The coating microstructure remains dense and void-free after the annealing. The cross-sectional view of the barrier layer reveals its crystallization after the annealing and the formation of a dense amorphous interface with the substrate, due to the Si diffusion from the substrate (Fig. 3.29b). The barrier/coating interface does not show a well-pronounced boundary that confirms interdiffusion between these two parts of the coating.

The selected area electron diffraction (SAED) pattern of the barrier layer (inset Fig. 3.29b) shows the diffraction spots that are attributed to SiO_2, Al_2O_3 and TiO_2. The size of these nanocrystals were estimated to be 8–15 nm range. This is in agreement with redistribution of the elements in the barrier layer observed by means of EDS. Therefore, the layered formation of the oxide layers in the barrier volume can be explained by the difference in the standard enthalpy of formation, the activation energy for diffusion and the diffusion coefficients of the participating elements. Thus, at the initial stages of the annealing, due to higher affinity of O to Al than to Ti, the thermodynamically more favourable Al_2O_3 (see enthalpy of formation, Table 3.4) starts to form first. The diffusivity of Ti in alumina is very low, even can be negligible at 350–700 °C, and therefore TiO_2 (see enthalpy of formation, Table 3.4) then forms at both sides of the Al_2O_3 based layer. Moreover, due to much higher activation energy for diffusion of O in Al_2O_3 than that in TiO_2, O will tend to concentrate at both sides of the Al_2O_3 layer, and subsequently oxidizes the available Ti. Due to the Ti out-diffusion from the coating toward the barrier and the diffusion inside the barrier, the concentration gradients of Ti and O at this temperature are high enough for the TiO_2 nucleation and growth. Moreover, the increment of Si concentration due the outward diffusion from the substrate and presence of reactive O in this layer result in growth of SiO_2. Thus, Si remain trapped in the barrier layer that prevents its further penetration into the coating. This additionally demonstrates the effectiveness of the barrier layer in question of suppressing the diffusion from the substrate.

The presented HRTEM image of the TiAlBSiN coating clearly shows a small crystal surrounded by the disordered regions (Fig. 3.29c). The fast Fourier transform (FFT) pattern taken from image Fig. 3.29c (Fig. 3.29c inset) displays the broad diffuse halo ring, corresponding to the disordered phase and two characteristic spots corresponding to a crystalline region. Among the possible products of solid phase reaction at 900 ºC between

the participating elements of the coating, the spots could be assigned to (200) planes of $TiAl_3$ phase.

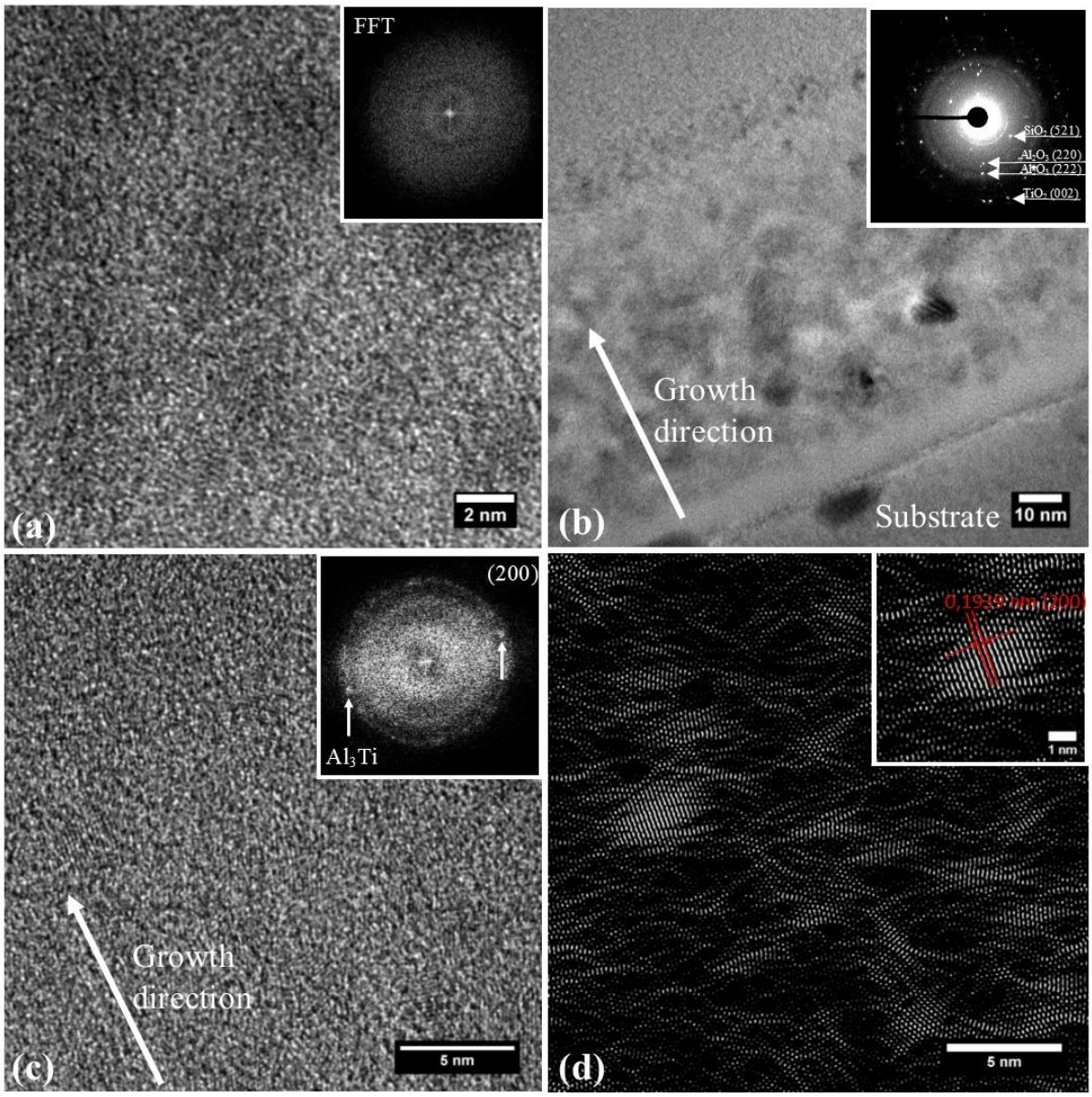

Figure 3.29. TEM analysis of structure transformations of TiAlBSiN coating on silicon wafer substrate after the annealing: (a) HRTEM image of the surface oxide layer with corresponding FFT image inset; (b) TEM overview image of the barrier layer with corresponding SAED inset; (c) HRTEM image of the coating with the corresponding FFT image inset, and (d) inverse fast Fourier transform(IFFT) image of (c) with zoomed image of the Al_3Ti nanograin.

The corresponding IFFT image confirms the presence of Al_3Ti nanograins (bright areas) with size ranging from 2 to 3 nm surrounded by SiBN(O) amorphous tissue phase (dark areas). The volume fractions of the crystalline and the amorphous phases in the coating are estimated based on IFFT of HRTEM image analysis to be ~30% and ~70%, respectively. The observed regions of bright disordered areas (non-crystalline) and dark areas arise due to

different scattering vector of these areas, which indicates different short-range order. Consequently, the SiBN(O) amorphous matrix is composed of different types of nanoclusters which are locally ordered and separated by the intercluster boundaries composed of irregularly ordered atoms. The former structure organization can be defined as the next-level structural organization, i.e. medium-range order, beyond the latter structure organization, i.e. short-range order, of the amorphous phase. Thus, as a result of the amorphous phase transformation, a phase separation takes place during the heat treatment, forming two amorphous phases with different degree of the short range topological order and the nanocrystalline phase. The central part of the $TiAl_3$ nanograin (zoomed image in the inset Fig. 3.29d) has the ideal crystalline structure which changes to amorphous at the periphery of the grain. The amorphous phase has no distinct interface boundaries with nanocrystalline phase. It is important to note that bright elongated areas on the inversed fast Fourier transform (IFFT) image (Fig. 3.29d) indicate that the process of ordering of the amorphous material into the nanoclusters with subsequent grain growth took place during the thermal treatment as a result of the diffusion processes leading to the formation of regions with different elemental compositions and different short-range orders.

It is commonly accepted that the main driving force for phase separation of amorphous phase during heat treatment in ambient air is the oxidation of constituent elements. This accompanied by crystallization of the coating because crystalline phase is more thermodynamically favourable than metastable amorphous phase formed in the as-deposited condition. However, the formation of intermetallic phase but not oxide phase is observed after the annealing of the TiAlBSiN coating. The formation of nitrides is not observed owing to low N content in the as-deposited coating and its release from the coating during annealing. It is well known **[354,355]**, that a large negative mixing enthalpy promotes stabilization of the amorphous phase by the formation of short-range order atomic clusters that is observed after annealing. However, a large negative mixing enthalpy favours also the formation of long-range-ordered intermetallic compounds and oxides. Therefore, there is a competitive growth between short-range order atomic clusters and intermetallic compound, both driven by negative mixing enthalpy. Apparently, under the annealing, the intermetallic phase is an intermediate product, which most probably precede the formation of more thermodynamically favourable oxide phase. Despite the increase of O content in the coating after annealing, a crystalline oxide phase is not observed in the coating while barrier layer demonstrate pronounced precipitation of the oxide phases. This difference mainly arise due to lower O content in the coating than in the barrier layer after deposition. In addition, although the O concentration increases in the surface layer, the O concentration profile

remain unchanged in the coating, meaning that the surface oxide layer suppress inward diffusion of O, and therefore significantly postpone oxidation of the coating. Once the amount of O will increase to above certain threshold, the crystalline oxide phase will start to form in the coating.

3.3.4 XPS studies

In order to better understand the formation of chemical bounding, quantitative elemental composition and chemical binding states of the TiAlBSiN coatings, pre and post annealing, were studied by XPS. Typical Al 2s and Ti 2p, Si 2s and B1s, O1s and N1s core-level XPS spectra of the amorphous surface layer of the as-deposited TiAlBSiN coating (upper) and the coating after annealing at 900 °C (lower) are presented in Fig. 3.30, Fig.3.31 and Fig. 3.32, respectively. The bulk composition of the as-prepared coating was determined to be non-stoichiometric $Ti_{0.07}Al_{0.24}B_{0.21}Si_{0.03}N_{0.28}O_{0.17}$. After annealing the elemental composition of the surface layer was stabilized at $Ti_{0.04}Al_{0.3}B_{0.04}Si_{0.02}N_{0.1}O_{0.5}$. The slight discrepancy in the composition of the top layer determined by means of EDS and XPS can be attributed to either the different characteristic depths of the methods or to the overlapping of the EDS signals from the light elements.

The Al 2s spectrum of the surface of the as-prepared TiAlBSiN coating (Fig. 3.30a, upper) shows the characteristic band at 118.9 eV, which could be attributed to the non-stoichiometric oxidized AlO_x phase **[356]**, whereas the high temperature oxidation at 900 °C caused the shift of the peak toward the higher binding energy 120.29 eV, that is attributed to the stoichiometric Al_2O_3 phase **[300]**. The Ti 2p spectrum of the surface of the as-prepared coating (Fig. 3.30b, upper) presents the asymmetrical Ti $2p_{3/2}$ and Ti $2p_{1/2}$ doublets (458.6 eV and 464.35, respectively) which can be unambiguously assigned to the TiO_2 phase **[357]**. The annealing of the coating caused a significant broadening of the asymmetrical Ti $2p_{3/2}$ and $2p_{1/2}$ doublets of the Ti 2p spectra. Therefore, the Ti 2p spectrum of the annealed coating was fitted with 4 spin-orbit doublets which could be attributed to Ti-Si-O (459.25 eV **[358]**), TiO_2 (458.1 eV **[357]**), Ti_2O_3 (456.85 eV **[357]**), Ti-N(455.54 eV **[288]**) bonds.

The Si 2s spectrum of the as-deposited coating can be fitted with one component which can be assigned to non-stoichiohe surface (152.7 eV **[359]**). After annealing, the broadening of the spectrum is observed, which could be fitted using three peaks located at 152.7 eV, 154.0 eV and 155.65 eV. The first peak was attributed to SiO_x bonds while the second peak originates from Si-N-O bonds **[300]**. The peak at 155.65 eV is typical for SiO_2 **[300]**.

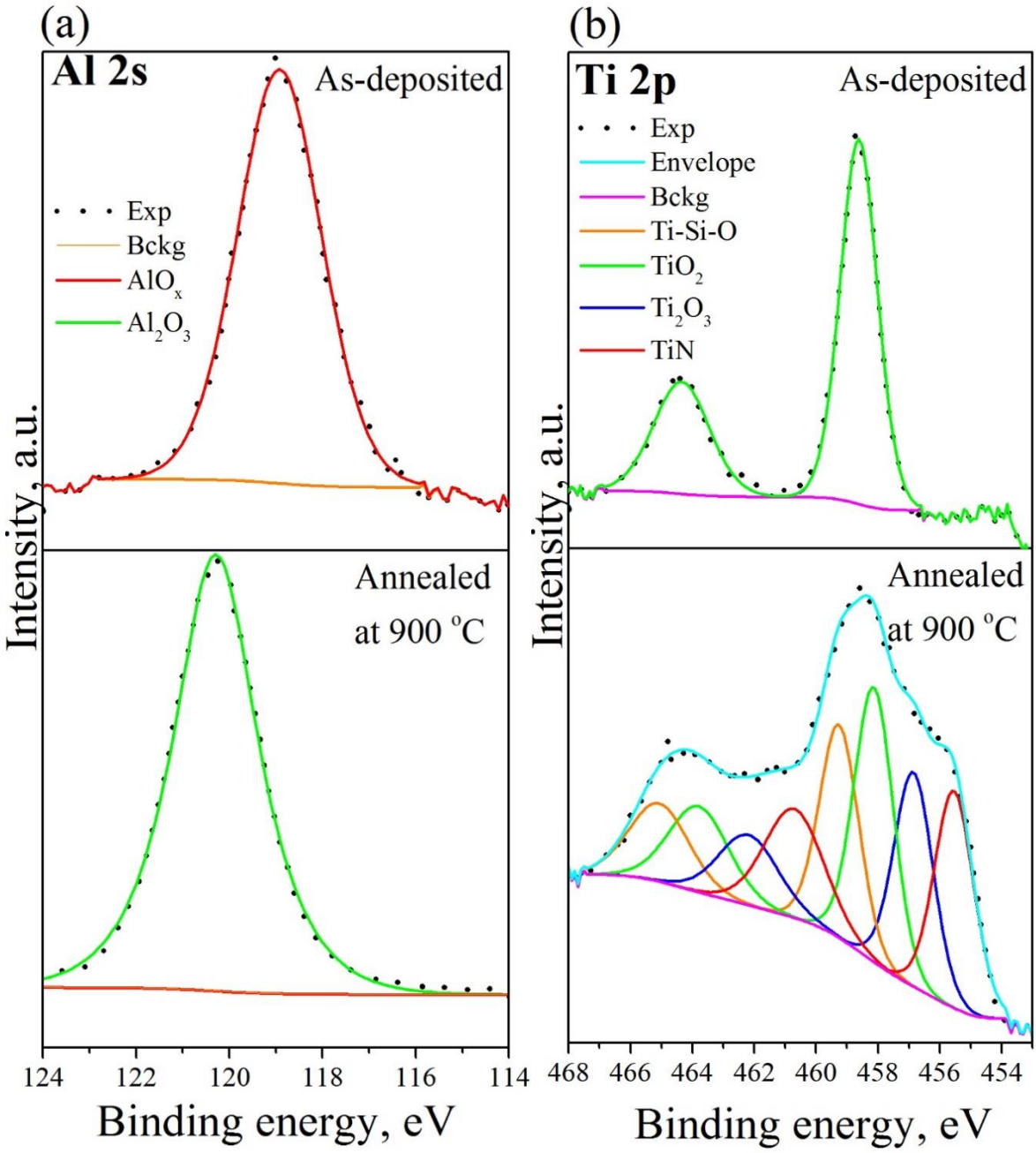

Figure 3.30. High-resolution XPS spectra of the Al 2s (a) and B 1s (b) core level signals obtained from the TiAlBSiN coating surface. Upper spectrum – as-deposited coating, lower spectra – after annealing at 900 °C.

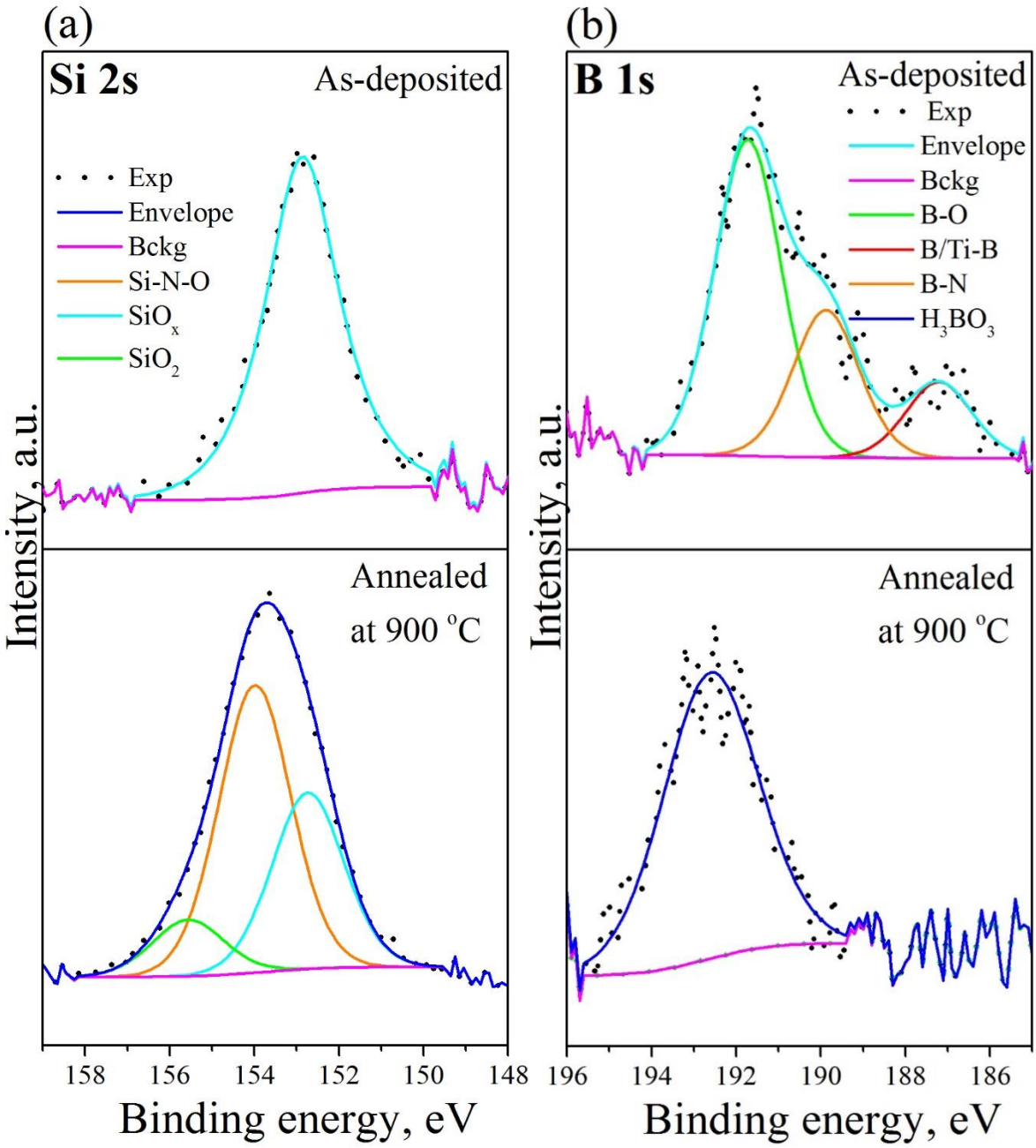

Figure 3.31. High-resolution XPS spectra of the Si 2s (a) and B 1s (b) core level signals obtained from the TiAlBSiN coating surface. Upper spectrum – as-deposited coating, lower spectra – after annealing at 900 °C.

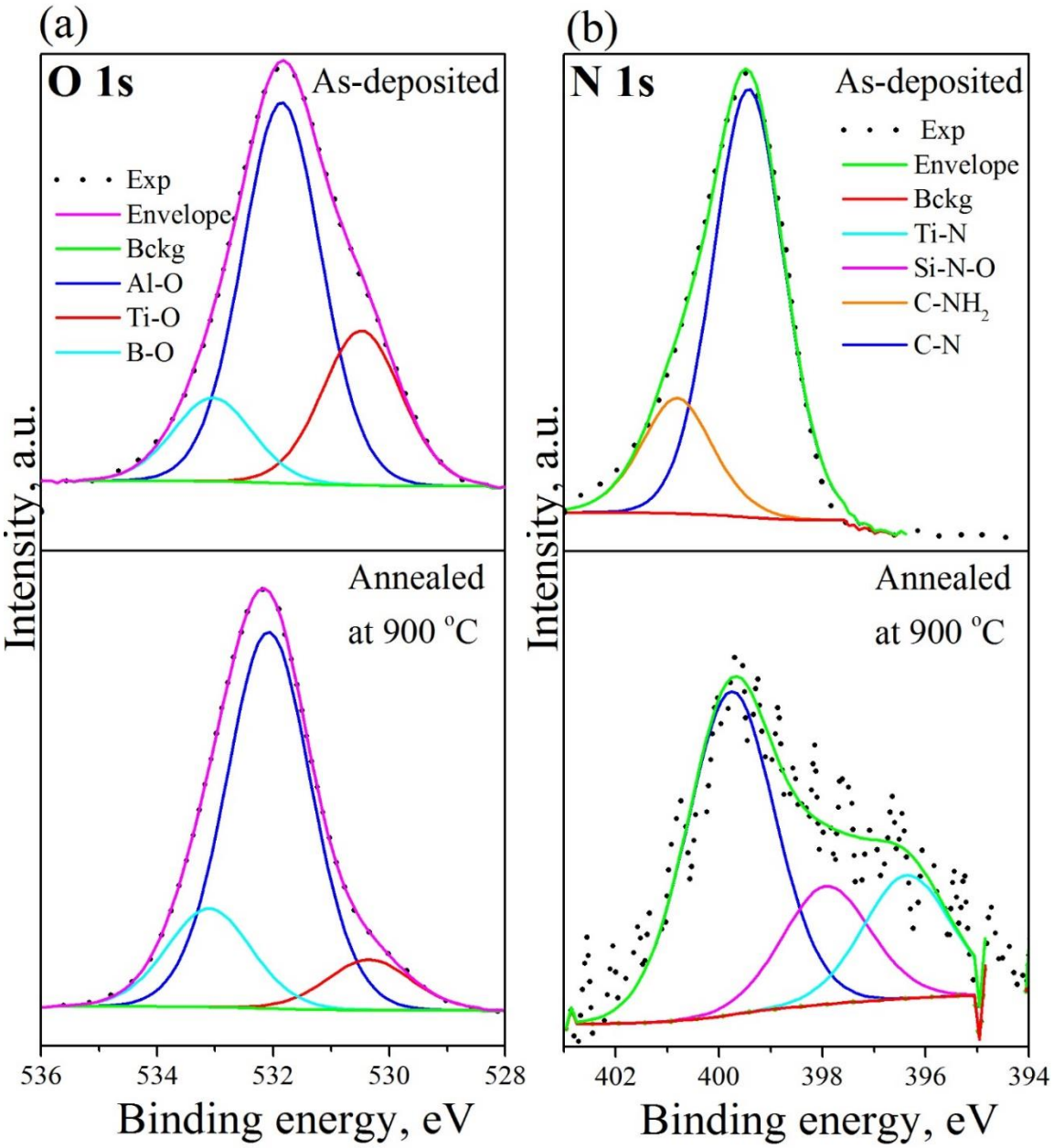

Figure 3.32. High-resolution XPS spectra of the O 1s (a) and N 1s (b) core level signals obtained from the TiAlBSiN coating surface. Upper spectrum – as-deposited coating, lower spectra – after annealing at 900 °C.

The B 1s spectra of the surface of the as-deposited TiAlBSiN coating was deconvoluted using three peaks at 187.11 eV, 189.88 eV and 191.7 eV , which were assigned to B or Ti-B **[157]**, B-N and B-O in B_2O_3 (or in B-N-O) **[300]**, respectively (Fig.6d, upper) **[51]**. After the heat treatment, a significant decrease of B 1s intensity was observed, with a shifting to higher binding energies, 192.58 eV. This can be assigned to the formation of boric acid H_3BO_3 at the surface of the coating **[360,361]**.

The O 1s spectrum of the as-deposited coating can be fitted with three components, Fig. 3.32a. The main component at around 531.8 eV can be associated with Al_2O_3 **[300]**.

Other minor components at around 530.47eVand 533.0 eV can be associated to TiO_2 and B_2O_3 bonds, respectively **[362]**. The spectrum of the surface after annealing did not change significantly, except the peak at 533 eV, which was slightly shifted to 533.2 eV that can be attributed to the formation of H_3BO_3 **[45]**. Moreover, the intensity of the O 1s spectrum has increased significantly after the annealing.

The N 1s spectrum of the coating's surface after deposition is fitted with two peaks (Fig. 3.32b, upper). The most intense peak at 399.43 eV can be attributed to C-N bonds **[363]** contamination, whereas the low intense peak at 400.86 to $C\text{-}NH_2$. The annealing of the coating caused the decrease of the N 1 s component intensity with arising of peaks at 397.9 eV and 396.3 eV, which could be due to Si-N-O and Ti-N bonds, respectively **[300]**.

A common trend among the XPS spectra of the coating after annealing is the broadening of Ti, Si, N and O spectra and decreasing of Ti, B, Si, and N intensity. The former is considered to be due to the solid-state reactions at the surface between the constituent elements as a result of their diffusion toward the surface. Moreover, during the high temperature oxidation, the surface layer serves as the interface between the coating and ambient atmosphere where the mixing process of O and the coating's elements occurs. On the other hand, it is well known, that Al diffusion rate in Al_2O_3 at 900 °C is higher than that of O **[364]**, so it is likely that Al diffuses through the Al_2O_3 as well and oxidizes near the free surface, whereas diffusivity of Ti in alumina is very low. Thus, due to the Al_2O_3 overgrowth, Ti, B, and N containing bonds give low contribution to the intensity of the photoelectron signals. Besides, N was reported to be released from the coatings during annealing **[181]**. Moreover, the B loss could be attributed to the reaction with the residual O to form a surface B_2O_3 layer which transforms, in the presence of residual moisture, to volatile boric acid H_3BO_3 (Fig. 3.31b, lower) which subsequently evaporates **[161]**. The release of H_3BO_3 from the surface, in addition to the Al_2O_3 overgrowth, explains the evolution of the surface roughness after the annealing (Fig. 3.25b). As revealed by HRTEM, the surface layer tends to grow remaining in the amorphous state during the high temperature annealing in ambient air. This process, in our case, is due to the synergetic effect of the kinetic factors and thermodynamic factors. The former given by the continuous interdiffusion of the constituting elements with the large difference in atomic size and variety of possible bonds coordination. The difference in diffusion rate of the constituent elements and the lack of time for a reorganization of the atomic orbital among the reactive atoms to form a particle of critical size (nucleus) and subsequent reorganization of elements along the lattice of the crystalline phase led to growth of the

amorphous phase. The thermodynamic driving force of the amorphous layer growth in this case can be based on the large negative heat of mixing and hence the low free energy of the amorphous phase **[365]**. The formation of amorphous surface oxide layer on the TiAlN coatings exposed to high temperature annealing in oxidative environment was frequently reported. Moreover, a doping with Si or B generally leads to thickening of this layer. The tendency of amorphous oxide overgrowth, according to recent thermodynamic modelling of L. Jeurgens **[366]**, is thermodynamically preferred in comparison to crystalline one due to the overcompensation of the high bulk Gibbs energy of the amorphous oxide phase by its lower sum of surface and interface energy as compared to the corresponding crystalline oxide configuration. Due to the small bulk energy difference between amorphous phase and crystalline phase of the Al_2O_3, TiO_2, SiO_2 and B_2O_3 phases, they tend to overgrow in the amorphous phase during annealing. However, if the thickness of the amorphous oxide layer will overcome a critical value, it will transform into the crystalline oxide layer. Among this oxides, the lowest difference of bulk Gibbs energy between amorphous and crystalline state in combination with the considerably lower surface energy of amorphous state has SiO_2 that promote the strikingly high stability of the amorphous SiO_2 overgrowth. The critical thickness of SiO_2 amorphous to crystalline transition is much higher than that of Al_2O_3, TiO_2 and B_2O_3. Therefore, exactly doping with Si is the main reason of the observed stability of the surface oxide layer of the TiAlBSiN coatings. Considering that the onset of crystallization temperature of Al_2O_3 and SiO_2 typically much higher than 900 ºC **[367,368]**, there is a high activation energy barrier for the amorphous to crystalline transition of this surface oxide, that can maintain amorphous oxide overgrowth beyond critical thickness.

Hence, the formation of the surface oxide layer on the coating's surface took place as a result of high-temperature oxidation in ambient air. The oxide layer is mainly based on a mixture of amorphous TiO_2, Al_2O_3, B_2O_3, and SiO_2 phases. The thickness of the oxide layer of ~35 nm is less than a critical value for its transformation to the crystalline state. It is proposed that the layer can maintain its barrier properties against inward diffusion of O at high temperature primarily due to such behaviour, and therefore is responsible for keeping the coating stable at high temperature in the oxidative environment.

3.3.5 Raman studies

The structural transformations of the TiAlSiBN coatings were additionally characterized using Raman spectroscopy. Raman is a powerful tool to study transitions where changes on a short length scale take place and hence crystallization-induced short-

range structural order changes during the high temperature treatment can be elucidated. The Raman spectra of the as-deposited TiAlSiBN coating and those annealed at 900 °C are shown in Fig. 3.32.

The spectrum of the as- deposited coating displays broad peaks caused by transitions in the acoustic frequency region and another set of lines resulting from the optical modes. The obtained Raman spectrum of the amorphous TiAlBSiN coating can be interpreted if consider that the local unit (such as nearest neighbours) in amorphous alloy has the same type of structure as their crystalline compounds with similar composition but lacks of long range order. An fcc/hcp cluster packing are the most favoured atomic clusters of an amorphous phase because they fill space most efficiently **[354,355]**. Spatial order in the positioning of atoms in a material with amorphous structure has topological nature while the ordering of different types of atoms in the multicomponent systems has chemical or compositional nature **[44]**.

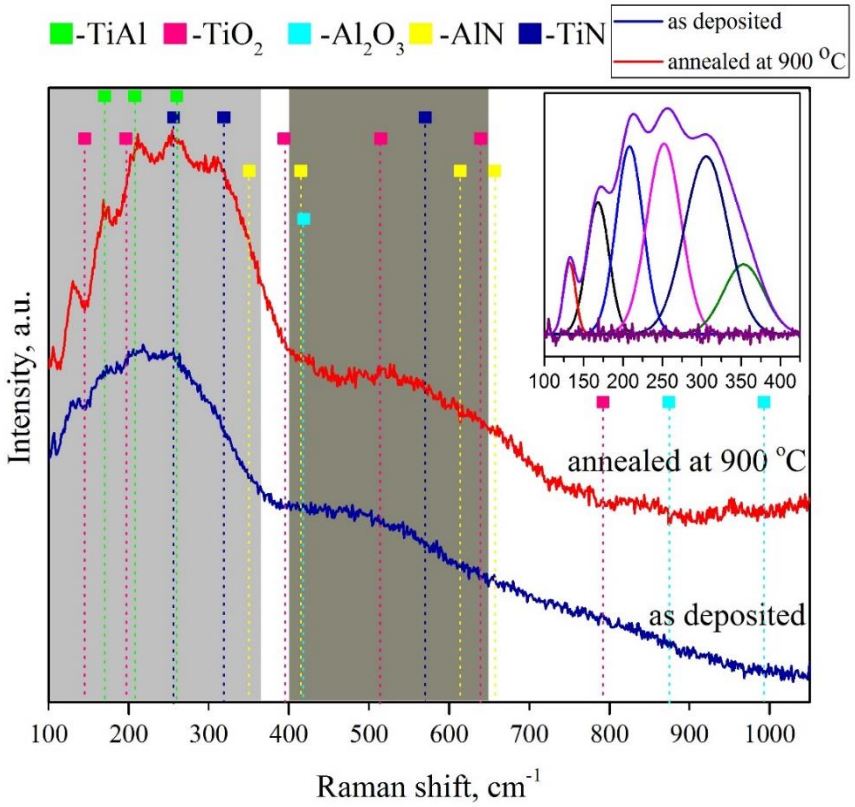

Figure 3.32. Raman spectra of the as-deposited TiAlBSiN coating (blue) and the coating after annealing (red) on the silicon wafer substrate. The fitting of the low-frequency spectrum part of the annealed coating is shown in the insert.

Moreover, presence of the imperfections in the amorphous structure, such as imperfect atom coordination, fluctuations of free volume, regions of large shear stresses,

vacancies and pseudo-vacancies, n-, p- and τ-defects **[369]**, forced us to adopt the conclusion that the richness of the possible defects and multiplicity of chemical bonds envisaged in the topological and chemical short-range order of the amorphous multi-element TiAlBSiN coating, is probably reflected in the multiplicity of the vibrational lines illustrated in the acoustic and optical range (red spectrum in Fig. 3.32). In compliance with the Hooke's law (Sec. 2.2.5, the lighter the atoms, the higher their vibration frequency will be) the first-ordered acoustic lines are related to the vibrations of Ti and Al atoms near N, B and O vacancies, while the broad first-ordered optical band arises from vibration of the light atoms adjacent to Ti and Al vacancies. Importantly, since the local structural elements of the amorphous phase are similar to that of the crystalline phase, the broad peaks are situated in the range of wave numbers of the corresponding crystalline phase with the same composition. This result is in the good agreement with the Raman spectra reported before for the amorphous TiAlN/TiAlSiN/Si_3N_4 and Ti/AlTiN/AlTiON/AlTiO coatings **[370,371]**.

The Raman spectrum of the coating after the annealing (Fig. 3.32, red line) showed that the drastic changes in the peak intensities of the first-order acoustic lines take place, implying the interplay between the species of the coating (structural units). The individual vibrational modes in the acoustical range were separated by applying a peak fitting procedure in order to proceed to the quantitative determination of the temperature dependence of the Raman spectra as well as the amorphous to nanocrystalline transition (see inset in Fig. 3.32). The sharp modes in acoustic frequency region are related to changes in the parameters of the chemical short-range order of the amorphous phase after the annealing. The signal in the low wave number range at around 120±4 cm^{-1} is assigned to the vibration of Ti-Ti bonding present in the octahedral chains of TiO_2 **[372]**. The strongest peaks located at 170 ± 4, 210 ± 4, 255 ± 4 cm^{-1} can be attributed to Ti-Al vibrations which agrees with **[373]**. In addition, the band at 255±4 could be the combination of two individual peaks due to Ti-Al vibration and non-stoichiometric TiN_x whose characteristic peak is positioned at 308±4 cm^{-1} as well **[374]**. The low intense peak at 350±4 cm^{-1} could be attributed to the Ti-B vibrations **[302]**. The characteristic peak of Al_2O_3 at 423 cm^{-1} **[375]** gives the evidence of the oxidation of the coating's surface.

Taking into account that the Raman intensity of a vibrational mode depends on the relative fraction of the species, it is evident that the phase segregation of the different components arises due to structural transformation of the amorphous phase. Besides, short-range ordered species (nanoclusters) of the amorphous phase react with neighboring irregularly ordered atoms and clusters with subsequent coalescence and grow, that leads to

the increase of the Raman intensity of the corresponding components **[376]**. Thus, the peak sharpening of the acoustic lines could be attributed to the formation of the nano-crystalline structure with the high concentration of grain boundaries which, due to their specific surface and interface at grain boundaries, strongly contribute to the vibrational modes. Correspondingly, the measured positions of the most intense lines in the acoustic region could be attributed to the vibration of metallic atoms at the nanograin boundaries adjusted to the lighter atoms of the amorphous tissue. Whereas the less intensive vibration lines in this region could be related to the vibration of the short-range ordered metallic components (clusters) of the amorphous phase adjusted to the light irregularly ordered atoms. The broad band in the optical region could be attributed to the vibration of the light atoms of the amorphous tissue at the interface with grain boundaries **[377]**.

3.3.6 Outcomes of structural characterization

It is important to note that the structure of an amorphous phase is not in the equilibrium state. Being in initial metastable state, the amorphous phase tends to the transformation to stable state upon heating with a local minimum of free energy. The structural transformation of the amorphous phase includes decrease in the free volume and changes in the parameters of the topological and chemical short-range order **[44]**. The structural transformations of the amorphous phases after the heat treatment due to the irreversible relaxation that related the changes in topological short-range order have been revealed by means of HRTEM, whereas the reversible relaxation is revealed by means of Raman spectroscopy.

The Raman results coupled with the HRTEM investigation allows us to conclude that the base part of the amorphous TiAlBSiN coating undergoes the phase separation with formation of the three dimensional nc-$TiAl_3$/a-SiBN(O) nanocomposite structure after post-deposition annealing at 900 °C in air. The observed separation into two amorphous phases with different short range order (Fig. 3.29) is due to the complex composition of the coating and the presence of several phases in this concentration range in the equilibrium phase diagram of Ti-Al-N **[378]** and Ti-Al-O **[379]** system, which are basic for TiAlBSiN coating. Furthermore, the stability of the amorphous phase of the TiAlSiBN coating could be associated with the content of Si and B atomic species, which due to the reduced diffusion mobility, were suggested to inhibit growth of oxide grains and to decrease the mass change of the coatings during oxidation **[255,380]**. Moreover, the oxidation resistance and thermal stability of the coating at 900 °C in ambient air additionally determined by the overgrowth of amorphous oxide surface layer, which has no fast paths

for O diffusion due to the efficient local packing of atoms, absence of grain boundaries or atomic vacancies. Moreover, according to XPS studies, this oxide layer is based on Al_2O_3 and SiO_2 which are known as good oxygen diffusion barriers and therefore hinder inward O diffusion.

The results on oxidation resistance of amorphous TiAlSiBN coatings reported previously **[104]** demonstrate the full oxidation after air annealing at 900 °C for 4 h, with the formation of several oxide layers of mixed rutile-TiO_2 +Al_2O_3 and TiN phases with average grain size of 100– 200 nm and 10–45 nm, respectively. Their lower oxidation resistance in comparison to the TiAlBSiN coatings reported in this thesis, could be associated with the higher concentration of Ti and Al (B concentration was not reported in **[104]**) in combination with a longer oxidation time that promoted the growth of the corresponding oxides. The formation of TiO_2 was already observed after oxidation at 800 °C for 1 h of amorphous TiAlSiBN coatings with further nucleation of $TiBO_3$, TiN_xO_y and $Ti_xAl_ySiO_z$ at 900 °C with the inward diffusion of O up to the depth of 800 nm **[235]**. Higher ratio of Ti/Al (29 at.% of Ti and 6 at.% of Al) in their coating points at the formation of TiO_2 at the surface which has worse barrier characteristics against O in comparison to Al_2O_3. Thus, having relatively the same concentration of B and Si, the TiAlBSiN coatings reported in **[235]** had lower oxidation resistance at 900°C.

3.3.7 Nanoindentation tests

The nanoindentation hardness H and reduced elastic modulus E^* for the as-deposited and annealed coatings were measured under depth and load control mode at indentation depth of 80 nm (<10 % of coating thickness) at the load of 3 mN, Fig. 3.33. The hardness is the highest for the coating after annealing with H = 24.41 GPa, followed by H = 15.20 GPa for the as deposited coating. The reduced elastic modulus follows the same trend with the highest value, E^* = 212.46 GPa for the coating after annealing, whereas for the as-deposited coating, it is slightly lower E^* = 177.6 GPa. The elastic recovery, W_e, of the coatings estimated from the loading- unloading curves (Fig. 3.33) was 61% for as-deposited TiAlBSiN coating and 68% for the coating annealed at 900 °C.

The residual impressions after indentation were studied by means of AFM (Fig. 3.34). In order to compare mechanical behaviour of the coatings it is important to establish whether the deformation of the amorphous and nanocrystalline coating is the same or not. It is observed that there are no pile-ups around the edges of the indents, no shear bands or radial cracks that means the deformation is the same in both samples and hardness and elastic modulus values can be compared between the samples.

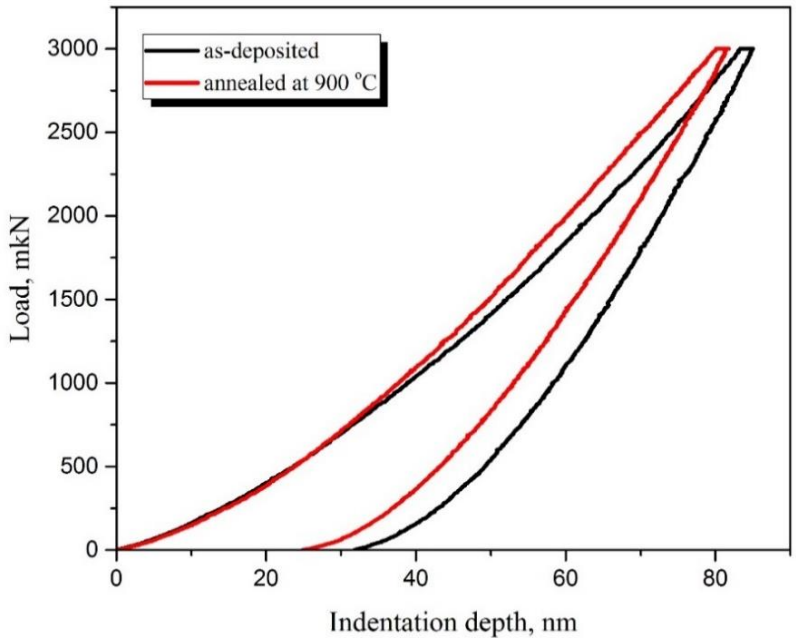

Figure 3.33. P–h plot for the as-deposited TiAlBSiN coating (black line) and the coating after annealing (red line) on the silicon wafer substrate at an indentation depth of 80 nm and maximum load of 3 mN.

The relatively low hardness of the amorphous coating could be associated with existence of the local areas with high ratio of free volume, which in turn promote the decrease of density of the amorphous phase. The high ratio of free volume in the amorphous phase was most probably caused by high ion bombardment of the coating during growth. The one more possible reason is a low density of the short range ordered species (bonds) with high strength. The higher density of low strength bonds may favour easier rearrangement of shear transformation zones under applied stress and thus promoting the plastic deformation. In earlier works, the hardness of the amorphous TiAlBSiN coatings was reported to be ~15 GPa **[235]**, 21 GPa **[104]** and 17.1±0.5GPa **[97]** and the growth of hardness was observed for coatings reported in **[97]** and **[104]** up to 21 GPa after annealing at 700 °C and up to ~20 GPa after annealing at 800 °C, respectively, but the hardness decreased for higher annealing temperatures **[104]** after the formation of crystalline oxide phase.

The transformation of the amorphous phase with formation of the nanocomposite structure dramatically changes the mechanical behaviour of the system **[381]**. The interaction between the grains hinders the generation of dislocations (grain size is smaller than the length of dislocation) and prevents cracks propagation due to the grain boundary enhancement and suppression of grain boundary sliding in nanocomposite coatings with small grain size. In our case the hardness increase could be attributed to the combined

effects of composite structure and free volume annihilation (defect annihilation) due to the structure transformation after the annealing.

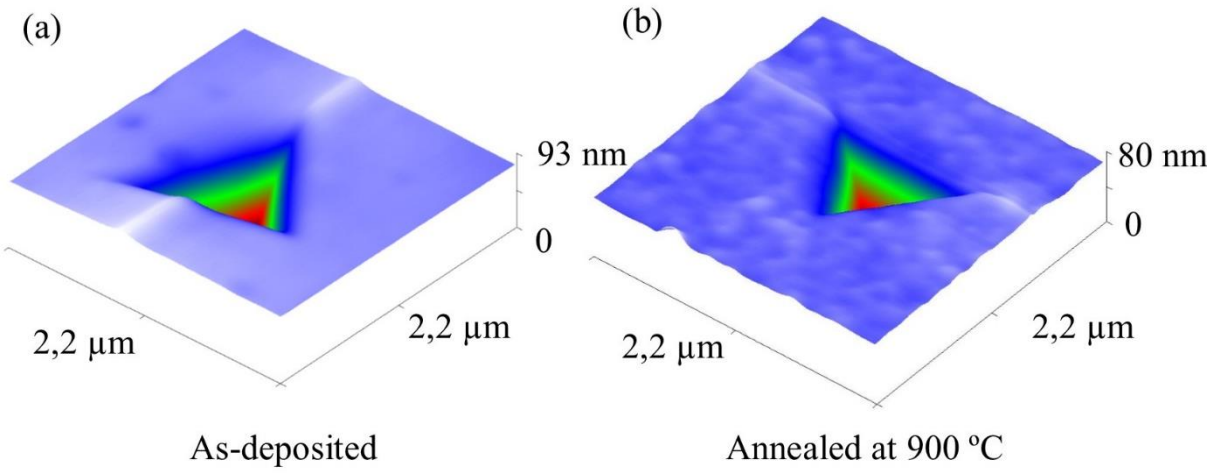

Figure 3.34. AFM 3D images showing the residual impressions following indentation in the as-deposited TiAlBSiN amorphous coating (a) and the coating after annealing (b) with a load of 3 mN.

The toughness (resistance to plastic deformation, H^3/E^{*2} ratio) and elastic strain prior to the plastic deformation (H/E^*) were calculated to be H^3/E^{*2} = 0.322 GPa and H/E^* = 0.115 for the annealed coating and H^3/E^{*2} = 0.111 GPa and H/E^* = 0.0856 for the as-deposited coating. The influence of elasticity in combination with hardness is a reliable indicator of the wear resistance. Thus, higher H^3/E^{*2} ratio of the coating after annealing is an indication of the coating's ability to resist mechanical degradation and failure in a tribo-contact events because the contact can remain elastic at higher stresses during the external impact. Relatively high value of the H/E^* ratio of the nanocomposite coating implies the increased ability of a material to absorb energy during deformation up to fracture. This in turn leads to the increase of the coating resistance to the formation of cracks and hence to lower brittleness. Moreover, the possible reason of the increase of the resistance to cracking of the TiAlSiBN coating after annealing could be associated with the generation of the compressive macro stresses due to the higher thermal expansion coefficient of the coating with respect to the silicon substrate **[39]**.

As have been already mentioned, surface properties have great influence on the tribological properties of coatings at initial stage of friction and wear and in consequence on behaviour of the whole system. In order to carry out an in-depth characterization of the mechanical properties of the coating surface layer, nanoindentation measurements were conducted using a multiple load function applied to a diamond Berkovich tip with maximum loads from 0.05 µN to 2mN. The hardness and reduced elastic modulus, H/E^* and H^3/E^{*2} ratio

values of each multi-cycle load plotted as a function of penetration depth for both TiAlBSiN as-deposited coating and those after annealing at 900 °C are displayed in Fig. 3.35.

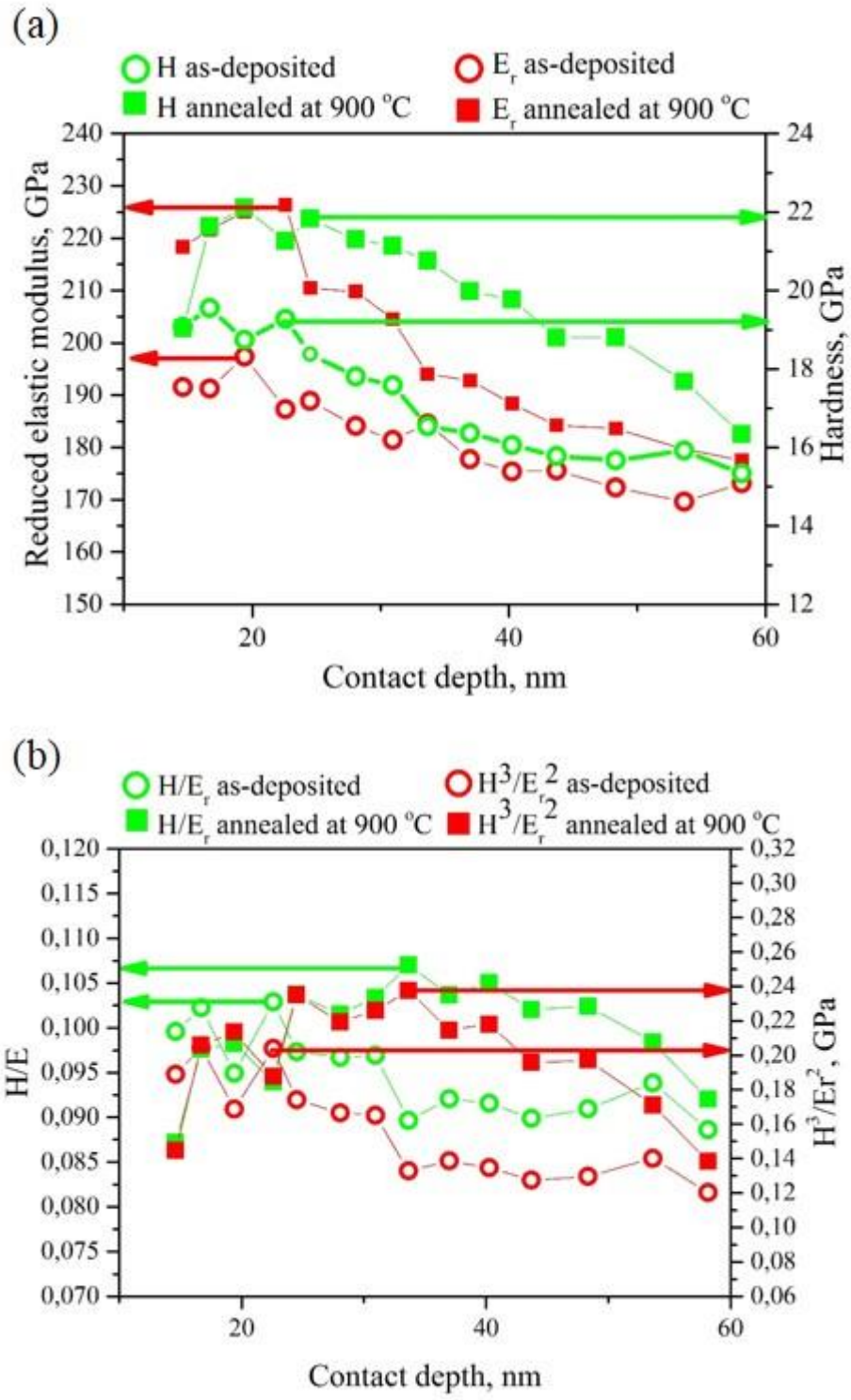

Figure 3.35. Hardness and reduced elastic modulus as the function of the contact depth (a) and variation of the ratio H/E^* and H^3/E^{*2} as the function of contact depth (b) of the as-deposited and annealed at 900 °C TiAlBSiN coatings on silicon wafer substrate

It is well visible in Fig. 3.35a, that the H and E^* of the amorphous layer of the coating after annealing are higher than those of as-deposited one. As was already shown, both layers are in the amorphous state. Thus, the increase of hardness after annealing could be associated with the change in the chemical short range order due to the interdiffusion in this part of the coating. The higher hardness of the surface of the annealed coating is due to its densification with high strength bonds that is in agreement with XPS results (the bond strength in kJ/mol are: Al-O ≈ 514, Si-O ≈ 800, Ti-O≈672, Ti-N≈476, B-O≈715 **[342]**).

The relatively high ratio $H/E^* \geq 0.1$, the high elastic recovery $W_e \geq 60$ % and the dense, void-free microstructure of TiAlBSiN coatings before and after annealing at 900 °C satisfy the needs for flexible hard nanocomposite coatings **[39]** and could therefore have a huge application potential. Moreover, due to its elastic properties,t he amorphous TiAlBSiN can be coated onto a brittle crystalline film for its protection against cracking during bending **[75]**.

3.3.8 Tribological tests

In order to optimize the tribological behaviour of the coating it is particularly useful to analyze the tribological changes at the nano- and micro scale and to study separately the mechanical and chemical changes as well as material transfer taking place in the contact.

3.3.8.1 Nanowear tests

A typical wear mark on the coating's surface, is of the size 5 μm×5μm, which is generated at a normal load of 1000 μN for one scan cycle is shown in Fig. 3.36 (a, d). The indentation depth in the film normal direction during the wear test did not exceed 25 nm that corresponds to the depth of the amorphous oxide layer. The analysis of the wear volume after the nanowear tests has revealed the higher wear volume 0.3818 μm^3 of the annealed coating than 0.046 μm^3 of the as-prepared coating. Fig. 3.36 (b, e) show wear edge of the corresponding wear tracks of the coatings where wear debris is clearly observed. The translation of the indenter along the sliding direction leads to the material removal due to the abrasive wear and generation of the wear debris. The morphology of the debris is different for the as-deposited and annealed coating. Many round-shaped <50 nm size wear debris was observed at the edge of the wear track of the as-deposited coating. The formation of the nanosized wear debris could be attributed to the high concentration of the local areas with free volume, which separates the areas with high density. A biased accumulation of the local strains incurred through an inelastic shear distortion of local areas with high density and the redistribution of the free volume promotes the plastic deformation of the surface with the generation of local areas with high density as wear debris **[382]**. Further densification and annihilation of free volume of the surface layer after annealing at 900 °C led to the formation

of the cutting type debris with flake-like morphology <500 nm size. The delamination of the wear debris (crack propagation) occurs at the boundary regions of the high density areas. The boundary regions could be composed of free volume or/and low shear strength phase.

Fig. 3.36 c, f shows EDS mapping of O at the wear edges of the as-deposited (c) and annealed coating (f). Due to the well visible contrast it is evident that the wear debris of both coatings is based on Me-Met-O phase. According to XPS analysis of the as-deposited coating surface, the base O containing phases are non-stoichiometric AlO_x and B_2O_3. B_2O_3 has high ionic potential and due to the pronounced screening of the cation by the surrounding anions, the cations interact very little with other cations which allows for easy shearing **[383]**. Further annealing of the coating promotes Al_2O_3 overgrowth, which has low ionic potential because its cations constantly interact with each other and form strong covalent or ionic bonds that make them very strong and hard to shear, and simultaneous release of B (volatile boric acid H_3BO_3) have caused higher wear of the coating. The amount of lubricious H_3BO_3 **[384]** is too low to separate asperities of the contacting surfaces and hence H_3BO_3 did not strongly effect the wear behaviour of the surface layer. This facts coupled with the EDS mapping indicate that the wear debris more probably based on Al_2O_3.

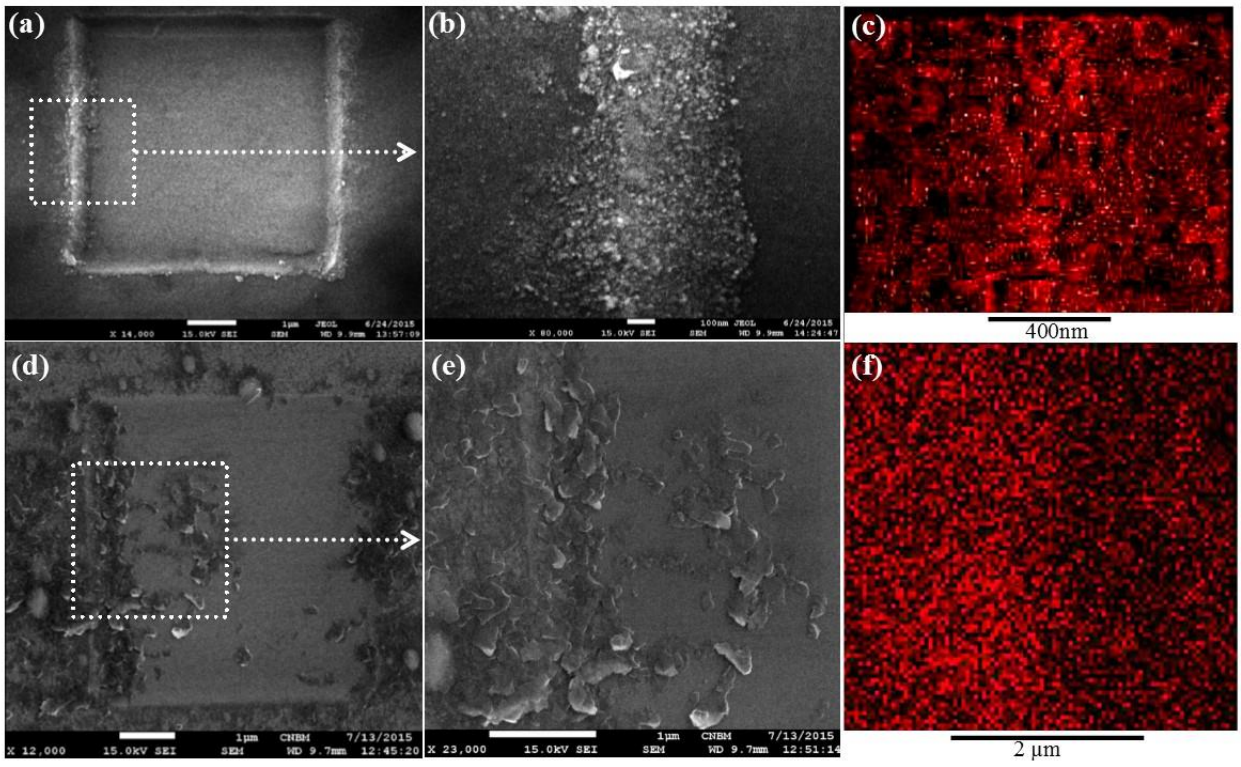

Figure 3.36. SEM images of the wear track of the as-deposited TiAlBSiN coating (a) and the coating after annealing at 900 °C (d) on silicon wafer substrate after 1 cycle of wear with 1000 µN normal load, and corresponding SEM images (b, e) of wear edge with results of EDS mapping of O (c, f).

Due to more pronounced relationship and higher values of the H/E^* and H^3/E^{*2} ration at depth >25 nm, the annealed coating could demonstrate much better wear resistance at this depth due to the relatively higher elastic strain-to-fracture and higher resistance to crack propagation, hence the contact can remain elastic at higher stresses during wear.

3.3.8.2 Micro-tribology measurements

Friction and wear tests at the micro-scale were performed on the reciprocating ball-on-block tribometer. Fig. 3.37 depicts the variations in friction coefficient, oven temperature, sample temperature, friction force and penetration depth of the amorphous TiAlBSiN coating with sliding time, sliding distance and laps.

The mean value of the friction coefficient was calculated to be 0.871 while wear rate was 0.2946 $\mu m^3/Nm$. The friction coefficient starts at relatively low values fluctuating for 66 min and suddenly rises to a high value after 500 m of sliding. The obtained value of the friction coefficient correlates well with values reported previously for the amorphous TiAlBSiN **[235]**. However, in the work **[235]** the 100Cr6 counter body was used which is known to generate a large amount of transfer material in form of Fe_3O_4 at the interface between coating and counterpart during the wear which influence the friction and wear. At the same time, the coefficient of friction of the amorphous TiAlBSiN is significantly smaller in comparison to that of high temperature stable amorphous SiBCNO coatings (0.96 at room temperature), which demonstrated self-adaptation to the friction conditions at high temperature **[46]**.

In order to obtain information on the wear mechanisms, observations of the wear track was carried out by means of SEM-EDS. Fig. 3.38a shows wear track of the TiAlBSiN coating after wear test at room temperature after 500 m of sliding. No wear debris was observed at the wear edge of the track. However, the narrow and sharp scars are observed in the wear track. This can be explained by wear debris of high hardness but low ductility which trapped in the contact area and act as an abrasive third body and thus increase wear and cause abrasion scars in the wear track after 500 m of sliding and increasing of the coefficient of friction as well. According to the results of EDS inspection of the wear track after 200, 300 and 1200 m of sliding distance (Fig. 3.38b), a significant increase of O concentration and decrease of B at the initial stage of sliding was detected. Moreover, the sample temperature increases after 200 m of sliding. The abrasive wear obviously leads to high flash temperatures in the contact zone. Thus, it is evident that the tribo-oxidation stimulated by the complex chemical and thermal interactions occurs within the sliding contact zone during sliding.

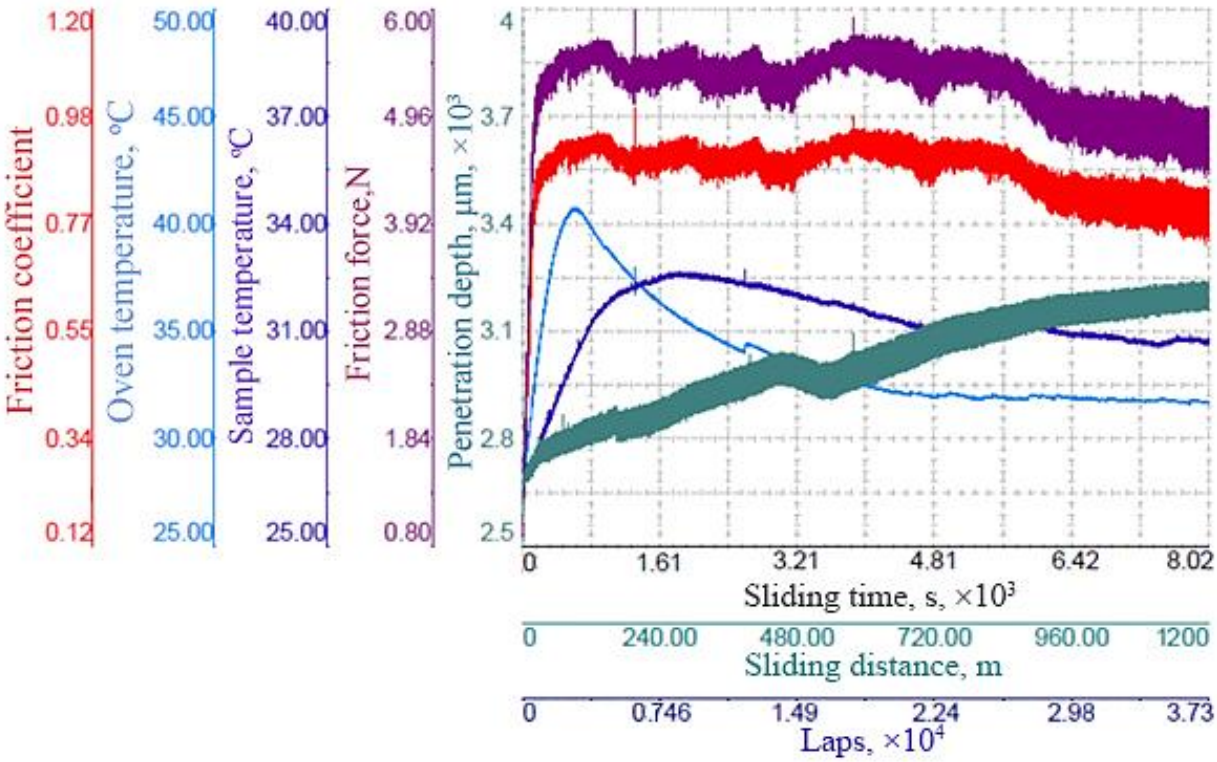

Figure 3.37. Dependencies of friction coefficient, sample temperature, oven temperature, friction force and penetration depth with sliding time, sliding distance and laps for TiAlBSiN coating on steel substrate against Al_2O_3 ball at room temperature.

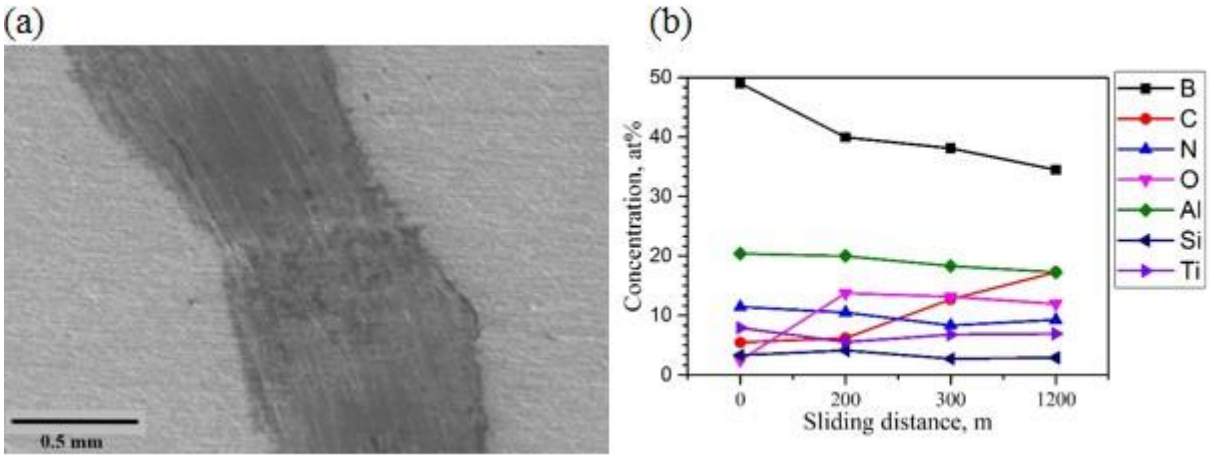

Figure 3.38. Surface morphology of the wear tracks on TiAlBSiN coating on steel substrate sliding against Al_2O_3 (a) and EDS results at different stages of the wear test (b).

The reported fluctuation of the friction coefficient is related to the surface status of tribo-contact region. The high temperature in tribo-contact promotes the oxidation of B and Al with formation of the corresponding oxides. The high friction coefficient at the initial stage of friction could be attributed to the generation of hard shear Al_2O_3 third body wear debris. Further temperature increase after longer sliding distance stimulates B oxidation to

low shear B_2O_3 thus slightly decreasing the friction coefficient **[385]**. The loss of B could be associated with the formation of H_3BO_3 and its decomposition after increase of temperature in tribo-contact **[386]**. This assumptions are in agreement with the standard enthalpy of formation for the mentioned substances (ΔH_{H3BO3}=−1072 kJ/mol **[387]** and Table 3.4). Moreover, due to presence of SiO_2 on the surface of the coating and tribo-chemical reaction with formation of $Si(OH)_2$ tribo-layer can not be excluded. Both SiO_2 and $Si(OH)_2$ are known as self-lubricating materials **[164]** which can contribute to the reduction of the friction and wear. Considering the existence of at least two elements which tend to form self-lubricating compounds, it is expected that the TiAlBSiN will potentially demonstrate self-lubricant behaviour in the ambient environment under high temperature impact. At the same time, the demonstrated elastic properties of the TiAlBSiN coating and their improvement after the annealing will allow to resist friction and wear by changing its microstructure in response to environment and loading changes.

Conclusions

Nanocomposite TiAlSiBN based coating with gradient microstructure was deposited by means of combined reactive/non-reactive DC magnetron sputtering of composite target AlN–TiB_2–$TiSi_2$. For the first time, the Al-rich TiAlN coating with high amount of B and Si was synthesized and characterized. The gradient microstructure was formed by the injection of N_2 during the reactive stage of the growth that resulted in a two-layer structure. The layers were composed of different phases and elemental composition. As a consequence of thermodynamic and kinetic constrains during the growth of the coating, the three dimensional nanocomposite structure has been formed in both layers. The obtained nanocomposite was composed of fcc-structured solid-solution of (Ti,Al)(N,O,B) and hcp-structured solid-solution of (Al,Ti)(N,O) nanocrystalline phases which are encapsulated into mixed a-TiB_2/a-BN(O)/a-SiB/a-AlO_x/a-TiO_x/a-Si_3N_4 amorphous phase. Moreover, the injection of N during the growth of the top layer accompanied by the preferential formation of a-BN in the mixture of the amorphous phase and slight increment of average grain size in the top layer. The higher content of hcp-AlN based phase than that of fcc-TiN based phase is observed in the coating. B and Si preferably form amorphous phase which suppresses the growth of TiN crystalline phase that is in agreement with previous results. The qualitative estimation revealed that the volume fraction of the amorphous phase is higher than that of the crystalline one. The coexistence of both hcp-AlN-based phase and fcc-TiN-based phase observed in this study is in agreement with the theoretical prediction of other authors. However, a slightly higher amount of AlN phase than of TiN was observed that assumed to be due the kinetic and thermodynamic constrains during the growth of the coating such as too high B and Si content in the coating and unsuitable growth conditions for promotion the growth of fcc-TiN-based phase. The measured combination of high hardness 17.55 GPa, elastic modulus 216.71 GPa, elastic recovery 60 %, elastic strain prior to failure ~ 0.08 and resistance to plastic deformation ~ 0.12 GPa of the gradient TiAlBSiN coating satisfy conditions for flexible protective coatings which due to their toughness are resistant to cracking. Additionally, the coating demonstrated relatively high wear resistance at nano-scale.

Amorphous nanocomposite coating TiAlBSiN was deposited by non-reactive magnetron sputtering of composite target AlN–TiB_2–$TiSi_2$. The as-deposited coating shown dense, void-free and featureless microstructure after deposition. The sacrificial amorphous barrier layer was grown by the reactive magnetron sputtering of the target. The amorphous phase of the coating underwent structural transformation after high temperature

annealing at 900 °C in ambient air. It was showed that the changes in topological and chemical short-range order took place during the amorphous phase transformation. It is showed that the transformation lead to the phase separation of the amorphous TiAlBSiN coating and the formation of a three dimensional nc-$TiAl_3$/a-SiBN(O) nanocomposite structure after the annealing. As a consequence of the annealing, the mixed amorphous surface layer mainly based on Al_2O_3 and SiO_2 was formed on the surface of the coating which assumed to be responsible for oxidation resistance and thermal stability of the coating. The studied Al-rich amorphous TiAlBSiN coating showed relatively better thermal stability in oxidative environment in comparison to the TiAlBSiN-based coatings reported in the literature previously. The barrier layer showed slight suppression of Si diffusion from the substrate to the coating. The hardness of the amorphous coating, elastic modulus, elastic recovery, elastic strain prior to failure and resistance to plastic deformation were significantly increased from 15.20 GPa, 177.6 GPa, 0.0856 and 0.111 GPa to 24.41 GPa, 212.46 GPa, 0.115 and 0.322 GPa, respectively, after the formation of the nanocomposite structure. This indicates that the coating became more flexible and resistant to cracking in response to high temperature impact, thus, could be suitable for a high temperature operation. This feature can considerably expand the possible applicability and reliability of this coating material in wide range of high temperature applications. Additionally, the revealed good tribological behaviour of the coating at nano- and micro- makes them potential candidates for application as protective coating for extreme tribological applications.

The obtained results may serve as a promising background for the design and manufacture of new multifunctional nanocomposite coatings. Due to its good barrier properties, amorphous TiAlBSiN coatings can be used for producing of new thermally stable protective coatings, e.g. they can be used as layers in nano-scale multilayer coatings. Moreover, the investigation of the structure-property relationship of amorphous TiAlBSiN coatings in wide composition range is still needed for disclosing their full potential.

The reported adjustment of the phase composition and structure of the gradient TiAlBSiN coating during the growth represents a novel and promising way for producing gradient nanocomposite protective coatings with high hardness and resistance to cracking. However, the studies on their behavior at high temperatures will have to be conducted in order to evaluate the stability of their functional properties, and thus to define a range of possible applications.

Hence, the reported in this thesis results on the characterization of the gradient TiAlBSiN coating and the amorphous TiAlBSiN coating may strongly contribute to

deepen present knowledge in the field of advanced protective nanocomposite coatings and will have far-reaching influence on the development of new multielement nanocomposite coatings.

References

[1] B.D. Beake, L. Ning, C. Gey, S.C. Veldhuis, A. Komarov, A. Weaver, et al., Wear performance of different PVD coatings during hard wet end milling of H13 tool steel, Surf. Coatings Technol. 279 (2015) 118–125. doi:10.1016/j.surfcoat.2015.08.038.

[2] H. Çalışkan, C. Kurbanoğlu, P. Panjan, M. Čekada, D. Kramar, Wear behavior and cutting performance of nanostructured hard coatings on cemented carbide cutting tools in hard milling, Tribol. Int. 62 (2013) 215–222. doi:10.1016/j.triboint.2013.02.035.

[3] A. Leyland, A. Matthews, Design criteria for wear-resistant nanostructured and glassy-metal coatings, Surf. Coatings Technol. 177–178 (2004) 317–324. doi:10.1016/j.surfcoat.2003.09.011.

[4] S. Veprek, M.J.G. Veprek-Heijman, Industrial applications of superhard nanocomposite coatings, Surf. Coatings Technol. 202 (2008) 5063–5073. doi:10.1016/j.surfcoat.2008.05.038.

[5] P.H. Mayrhofer, F. Kunc, J. Musil, C. Mitterer, A comparative study on reactive and non-reactive unbalanced magnetron sputter deposition of TiN coatings, Thin Solid Films. 415 (2002) 151–159. doi:10.1016/S0040-6090(02)00511-4.

[6] J.Sundgren, Structure and properties of TiN coatings, Thin Solid Films. 128 (1985) 21–44. doi:10.1016/0040-6090(85)90333-5.

[7] S.T. Oyama, ed., The Chemistry of Transition Metal Carbides and Nitrides, Blackie Academic & Professional, Glasgow, 1996.

[8] W.-D. Münz, Titanium aluminum nitride films: A new alternative to TiN coatings, J. Vac. Sci. Technol. A Vacuum, Surfaces, Film. 4 (1986) 2717. doi:10.1116/1.573713.

[9] T. Akhadejdamrong, A. Mitsuo, C. Iwamoto, T. Yamamoto, Y. Ikuhara, T. Aizawa, Formation of Protection Layer during Oxidation of Al-Implanted TiN Coating, Mater. Trans. 43 (2002) 1291–1297. doi:10.2320/matertrans.43.1291.

[10] S. PalDey, S. Deevi, Single layer and multilayer wear resistant coatings of (Ti, Al) N: a review, Mater. Sci. Eng. A. 342 (2003) 58–79. doi:10.1016/S0921-5093(03)00473-8.

[11] K. Yamamoto, S. Kujime, G. Fox-Rabinovich, Effect of alloying element (Si,Y) on properties of AIP deposited (Ti,Cr,Al)N coating, Surf. Coatings Technol. 203 (2008) 579–583. doi:10.1016/j.surfcoat.2008.05.046.

[12] V.V. Uglov, V.M. Anishchik, S.V. Zlotski, G. Abadias, The phase composition and stress development in ternary Ti–Zr–N coatings grown by vacuum arc with combining of plasma flows, Surf. Coatings Technol. 200 (2006) 6389–6394. doi:10.1016/j.surfcoat.2005.11.063.

[13] P. Yan, J. Deng, Z. Wu, S. Li, Y. Xing, J. Zhao, Friction and wear behavior of the PVD (Zr,Ti)N coated cemented carbide against 40Cr hardened steel, Int. J. Refract. Met. Hard Mater. 35 (2012) 213–220. doi:10.1016/j.ijrmhm.2012.06.003.

[14] M. Ertas, A. Can, G. Ekinci, B. Toydemir, S. Durdu, M. Usta, et al., Investigation of (Ti , V) N and TiN / VN coatings on AZ91D Mg alloys, Surf. Coat. Technol. 284

(2015) 252–257. doi:10.1016/j.surfcoat.2015.08.066.

[15] A. Niederhofer, P. Nesládek, H.-D. Männling, K. Moto, S. Veprêk, M. Jílek, Structural properties , internal stress and thermal stability of nc-TiN / a-Si3 N4 , nc-TiN / TiSix and nc- (Ti1-y Aly Six) N superhard nanocomposite coatings reaching the hardness of diamond, Surf. Coatings Technol. 121 (1999) 173–178. doi:Doi: 10.1016/s0257-8972(99)00451-x.

[16] S. Veprek, Recent search for new superhard materials: Go nano!, J. Vac. Sci. Technol. A Vacuum, Surfaces, Film. 31 (2013) 50822. doi:10.1116/1.4818590.

[17] H.A. Jehn, Multicomponent and multiphase hard coatings for tribological applications, Surf. Coatings Technol. 131 (2000) 433–440. doi:10.1016/S0257-8972(00)00783-0.

[18] H. Lind, R. Forsén, B. Alling, N. Ghafoor, F. Tasnádi, M.P. Johansson, et al., Improving thermal stability of hard coating films via a concept of multicomponent alloying, Appl. Phys. Lett. 99 (2011) 91903. doi:10.1063/1.3631672.

[19] L.A. Dobrzański, L. Wosińska, K. Gołombek, J. Mikuła, Structure of multicomponent and gradient PVD coatings deposited on sintered tool materials, J. Achiev. Mater. Manuf. Eng. 20 (2007) 99–102.

[20] D. V. Shtansky, P. V. Kiryukhantsev-Korneev, I.A. Bashkova, A.N. Sheveiko, E.A. Levashov, Multicomponent nanostructured films for various tribological applications, Int. J. Refract. Met. Hard Mater. 28 (2010) 32–39. doi:10.1016/j.ijrmhm.2009.07.014.

[21] P. Holubar, M. Jilek, M. Sima, Present and possible future applications of superhard nanocomposite coatings, Surf. Coatings Technol. 133–134 (2000) 145–151. doi:10.1016/S0257-8972(00)00956-7.

[22] L. Rebouta, F. Vaz, M. Andritschky, M.F. da Silva, Oxidation resistance of (Ti,Al,Zr,Si)N coatings in air, Surf. Coatings Technol. 76–77 (1995) 70–74. doi:10.1016/0257-8972(95)02501-4.

[23] A.D. Pogrebnjak, A. V. Pshyk, V.M. Beresnev, B.R. Zhollybekov, Protection of specimens against friction and wear using titanium-based multicomponent nanocomposite coatings: A review, J. Frict. Wear. 35 (2014) 55–66. doi:10.3103/S1068366614010073.

[24] A.D. Pogrebnjak, A.A. Bagdasaryan, I.V. Yakushchenko, V.M. Beresnev, The structure and properties of high-entropy alloys and nitride coatings based on them, Russ. Chem. Rev. 83 (2014) 1027–1061. doi:10.1070/RCR4407.

[25] C. Donnet, A. Erdemir, Historical developments and new trends in tribological and solid lubricant coatings, Surf. Coatings Technol. 180–181 (2004) 76–84. doi:10.1016/j.surfcoat.2003.10.022.

[26] P.H. Mayrhofer, C. Mitterer, H. Clemens, Self-organized Nanostructures in Hard Ceramic Coatings, Adv. Eng. Mater. 7 (2005) 1071–1082. doi:10.1002/adem.200500154.

[27] J. Musil, Hard nanocomposite coatings: Thermal stability, oxidation resistance and toughness, Surf. Coatings Technol. 207 (2012) 50–65. doi:10.1016/j.surfcoat.2012.05.073.

[28] P.H. Mayrhofer, C. Mitterer, J. Musil, Structure – property relationships in single-

and dual-phase nanocrystalline hard coatings, Surf. Coatings Technol. 175 (2003) 725–731. doi:10.1016/S0257-8972(03)00576-0.

[29] P.H. Mayrhofer, C. Mitterer, L. Hultman, H. Clemens, Microstructural design of hard coatings, Prog. Mater. Sci. 51 (2006) 1032–1114. doi:10.1016/j.pmatsci.2006.02.002.

[30] R.A. Andrievskii, G. V. Kalinnikov, Structure and properties of nanostructured films based on refractory compounds, Russ. Chem. Bull. 60 (2011) 1025–1031. doi:10.1007/s11172-011-0162-3.

[31] M. Aliofkhazraei, Nanocoatings: Size Effect in Nanostructured Films, Springer-Verlag, 2011. doi:10.1007/978-3-642-17966-2.

[32] V. Murashov, J. Howard, eds., Nanotechnology Standards, Springer, 2011. doi:10.1007/978-1-4614-4605-7.

[33] J. Musil, Physical and Mechanical Properties of Hard Nanocomposite Films Prepared by Reactive Magnetron Sputtering, in: A. Cavaleiro, J.T.M. De Hosson (Eds.), Nanostructured Coatings, Springer, 2006: pp. 407–463.

[34] F. Ebrahimi, ed., Nanocomposites - New Trends and Developments, InTech, 2012. doi:10.5772/3389.

[35] B. Bhushan, ed., Encyclopedia of Nanotechnology, 53 (2012) 2919. doi:10.1017/CBO9781107415324.004.

[36] S.C. Tjong, H. Chen, Nanocrystalline materials and coatings, Mater. Sci. Eng. R Reports. 45 (2004) 1–88. doi:10.1016/j.mser.2004.07.001.

[37] J. Musil, Properties of hard nanocomposite thin films, in: S. Zhang, N. Ali (Eds.), Nanocomposite Thin Film. Coatings, 2007: pp. 281–328.

[38] A.D. Pogrebnyak, A.P. Shpak, N.A. Azarenkov, V.M. Beresnev, Structures and properties of hard and superhard nanocomposite coatings, Physics-Uspekhi. 52 (2009) 29–54. doi:10.3367/UFNe.0179.200901b.0035.

[39] J. Musil, Flexible hard nanocomposite coatings, RSC Adv. 5 (2015) 60482–60495. doi:10.1039/C5RA09586G.

[40] S. Veprek, M.G.J. Veprek-Heijman, P. Karvankova, J. Prochazka, Different approaches to superhard coatings and nanocomposites, Thin Solid Films. 476 (2005) 1–29. doi:10.1016/j.tsf.2004.10.053.

[41] J. Musil, Hard and superhard nanocomposite coatings, Surf. Coatings Technol. 125 (2000) 322–330. doi:10.1016/S0257-8972(99)00586-1.

[42] S. Neuville, A. Matthews, A perspective on the optimisation of hard carbon and related coatings for engineering applications, Thin Solid Films. 515 (2007) 6619–6653. doi:10.1016/j.tsf.2007.02.011.

[43] A. Chauhan, R. Vaish, Hard coating material selection using multi-criteria decision making, Mater. Des. 44 (2013) 240–245. doi:10.1016/j.matdes.2012.08.003.

[44] G.E. Abrosimova, Evolution of the structure of amorphous alloys, Physics-Uspekhi. 54 (2011) 1227–1242. doi:10.3367/UFNe.0181.201112b.1265.

[45] J. Musil, J. Vlček, P. Zeman, Hard amorphous nanocomposite coatings with oxidation resistance above 1000°C, Adv. Appl. Ceram. 107 (2008) 148–154.

doi:10.1179/174367508X306460.

[46] H.A. Samra, A. Kumar, J. Xia, T. Staedler, X. Jiang, Development of a new generation of amorphous hard coatings based on the Si – B – C – N – O system for applications in extreme conditions, Surf. Coat. Technol. 223 (2013) 52–67. doi:10.1016/j.surfcoat.2013.02.028.

[47] J.J. Díaz, M.P. Garrett, J. Zhang, N.P. Kobayashi, Deposition of amorphous , transparent , corrosion-resistant films by pulsed DC reactive magnetron sputtering with RF substrate bias, Mater. Sci. Semicond. Process. Alum. Titan. Oxide Alloy. . 36 (2015) 96–102. doi:10.1016/j.mssp.2015.03.039.

[48] C. Koch, I. Ovid'ko, S. Seal, S. Veprek, Structural nanocrystalline materials, Cambridge University Press, 2007. doi:10.1007/s13398-014-0173-7.2.

[49] M. Kathrein, C. Michotte, M. Penoy, P. Polcik, C. Mitterer, Multifunctional multi-component PVD coatings for cutting tools, Surf. Coatings Technol. 200 (2005) 1867–1871. doi:10.1016/j.surfcoat.2005.08.105.

[50] A. Inspektor, P.A. Salvador, Architecture of PVD coatings for metalcutting applications: A review, Surf. Coatings Technol. 257 (2014) 138–153. doi:10.1016/j.surfcoat.2014.08.068.

[51] L. Bacakova, L. Grausova, J. Vacik, A. Kromka, H. Biederman, A. Choukourov, et al., Advances in Diverse Industrial Applications of Nanocomposites, InTech, 2011. doi:10.5772/1931.

[52] A.A. Voevodin, J.S. Zabinski, Smart nanocomposite coatings with chameleon surface adaptation in tribological applications, in: A.A. Voevodin (Ed.), Nanostructured Thin Film. Nanodispersion Strengthened Coatings, Kluwer Academic Publishers, 2004: pp. 1–8.

[53] A.A. Voevodin, T.A. Fitz, J.J. Hu, J.S. Zabinski, Nanocomposite tribological coatings with "chameleon" surface adaptation, J. Vac. Sci. Technol. A Vacuum, Surfaces, Film. 20 (2002) 1434. doi:10.1116/1.1487875.

[54] P.A. Corning, The Re-emergence of " Emergence ": A Venerable Concept in Search of a Theory, Complexity. 7 (2002) 18–30. doi:10.1002/cplx.10043.

[55] G.S. Fox-Rabinovich, K. Yamamoto, B. D Beake, I. S Gershman, A. I Kovalev, S. C Veldhuis, et al., Hierarchical adaptive nanostructured PVD coatings for extreme tribological applications: the quest for nonequilibrium states and emergent behavior, Sci. Technol. Adv. Mater. 13 (2012) 43001. doi:10.1088/1468-6996/13/4/043001.

[56] A.A. Voevodin, C. Muratore, S.M. Aouadi, Hard coatings with high temperature adaptive lubrication and contact thermal management: review, Surf. Coatings Technol. 257 (2014) 247–265. doi:10.1016/j.surfcoat.2014.04.046.

[57] A.D. Pogrebnjak, A.A. Bagdasaryan, A. Pshyk, K. Dyadyura, Adaptive multicomponent nanocomposite coatings in surface engineering, Physics-Uspekhi. 60 (2017). doi:10.3367/UFNe.2016.12.038018.

[58] J.J. Moore, I. Park, J. Lin, B. Mishra, K.H. Kim, Nanostructured, multifunctional tribological coatings, in: S. Zhang, N. Ali (Eds.), Nanocomposite Thin Film. Coatings, Imperial College Press, 2007: pp. 329–379.

[59] H. Gleiter, Nanostructured materials: basic concepts and microstructure, Acta Mater. 48 (2000) 1–29. doi:10.1016/S1359-6454(99)00285-2.

[60] A. Cavaleiro, Nanostructured coatings, Springer Science+Business Media, 2012. doi:10.1073/pnas.0703993104.

[61] E.A. Levashov, D. V Shtansky, Multifunctional nanostructured films, Russ. Chem. Rev. 76 (2007) 463–470. doi:10.1070/RC2007v076n05ABEH003679.

[62] S. Veprek, M.G.J. Veprek-Heijman, Limits to the preparation of superhard nanocomposites: Impurities, deposition and annealing temperature, Thin Solid Films. 522 (2012) 274–282. doi:10.1016/j.tsf.2012.08.048.

[63] R. Daniel, J. Musil, Novel Nanocomposite Coatings, Pan Stanford Publishing, 2013.

[64] M. Dao, Toward a quantitative understanding of mechanical behavior of nanocrystalline metals, Acta Mater. 55 (2007) 4041–4065. doi:10.1016/j.actamat.2007.01.038.

[65] S.-H. Jhi, J. Ihm, S.G. Louie, M.L. Cohen, Electronic mechanism of hardness enhancement in transition-metal carbonitrides, Nature. 399 (1999) 132–134. doi:10.1038/20148.

[66] D. Li, R.B. Kaner, Designing Superhard Materials, Science (80-.). 320 (2008) 1170–1171. doi:10.1126/science.1158180.

[67] J. Schiotz, F.D. Di Tolla, K.W. Jacobsen, Softening of nanocrystalline metals at very small grain sizes, Nature. 391 (1998) 561–563. doi:10.1038/35328.

[68] R. Kassing, P. Petkov, W. Kulisch, C. Popov, eds., Functional Properties of Nanostructured Materials, Springer, 2005.

[69] K.S. Kumar, H. Van Swygenhoven, S. Suresh, Mechanical behavior of nanocrystalline metals and alloys, Acta Mater. 51 (2003) 5743–5774. doi:10.1016/j.actamat.2003.08.032.

[70] K. Holmberg, A. Matthews, Coatings Tribology, Elsevier, 2009.

[71] S. Zhang, D. Sun, Y. Fu, H. Du, Toughness measurement of thin films: A critical review, Surf. Coatings Technol. 198 (2005) 74–84. doi:10.1016/j.surfcoat.2004.10.021.

[72] A. Leyland, A. Matthews, On the significance of the H / E ratio in wear control : a nanocomposite coating approach to optimised tribological behaviour, Wear. 246 (2000) 1–11.

[73] J. Musil, F. Kunc, H. Zeman, H. Polakova, Relationships between hardness , Young ' s modulus and elastic recovery in hard nanocomposite coatings, Surf. Coat. Technol. 154 (2002) 304–313. doi:10.1016/S0257-8972(01)01714-5.

[74] J. Musil, M. Jirout, Toughness of hard nanostructured ceramic thin films, Surf. Coatings Technol. 201 (2007) 5148–5152. doi:10.1016/j.surfcoat.2006.07.020.

[75] J. Musil, J. Sklenka, R. Cerstv, Protection of brittle film against cracking, Appl. Surf. Sci. 370 (2016) 306–311. doi:10.1016/j.apsusc.2016.02.132.

[76] T.Y. Tsui, G.M. Pharr, W.C. Oliver, C.S. Bhatia, R.L. White, S. Anders, et al., Nanoindetation and nanoscratching of hard carbon coatings for magnetic disks, Mater. Res. Soc. Symp. Proc. 383 (1995) 447–452.

[77] B. Bhushan, Nanotribology and nanomechanics, Wear. 259 (2005) 1507–1531. doi:10.1016/j.wear.2005.01.010.

[78] S. Veprek, P. Holubar, M. Veprek-Heijman, Industrial Applications of Hard and Superhard Nanocomposite Coatings on Tools for Machining , Forming , Stamping and Injection Molding, Adv. Mater. Res. 1135 (2016) 218–233. doi:10.4028/www.scientific.net/AMR.1135.218.

[79] F.P. Bowden, D. Tabor, The friction and lubrication of solids, Clarendon, UK, 1950.

[80] P.L. Menezes, S.P. Ingole, M. Nosonovsky, S. V. Kailas, M.R. Lovell, eds., Tribology for Scientists and Engineers: From Basics to Advanced Concepts, Springer, 2013. doi:10.1007/978-1-4614-1945-7.

[81] B. Bhushan, Principles and applications of tribology, John Wiley & Sons, 2013.

[82] M. Roy, Nanocomposite Films for Wear Resistance Applications, in: Surf. Eng. Enhanc. Perform. against Wear, Springer-Verlag, 2013: p. 324. doi:10.1007/978-3-7091-0101-8.

[83] J.F. Archard, Contact and rubbing of flat surfaces, J. Appl. Phys. 24 (1953) 981–988. doi:10.1063/1.1721448.

[84] A. Matthews, S. Franklin, K. Holmberg, Tribological coatings: contact mechanisms and selection, J. Phys. D. Appl. Phys. 40 (2007) 5463–5475. doi:10.1088/0022-3727/40/18/S07.

[85] G.S. Fox-Rabinovich, K. Yamamoto, B.D. Beake, a. I. Kovalev, M.H. Aguirre, S.C. Veldhuis, et al., Emergent behavior of nano-multilayered coatings during dry high-speed machining of hardened tool steels, Surf. Coatings Technol. 204 (2010) 3425–3435. doi:10.1016/j.surfcoat.2010.04.002.

[86] C. Muratore, A.A. Voevodin, J.J. Hu, J.G. Jones, J.S. Zabinski, Growth and characterization of nanocomposite yttria-stabilized zirconia with Ag and Mo, Surf. Coat. Technol. 200 (2005) 1549–1554. doi:10.1016/j.surfcoat.2005.08.032.

[87] J.R. Rice, J.S. Wang, Embrittlement of interfaces by solute segregation, Mater. Sci. Eng. A. 107 (1989) 23–40. doi:10.1016/0921-5093(89)90372-9.

[88] L. Hultman, Thermal stability of nitride thin films, Vacuum. 57 (2000) 1–30. doi:10.1016/S0042-207X(00)00143-3.

[89] J. Musil, P. Zeman, Hard a-Si 3N 4/MeN x Nanocomposite Coatings with High Thermal Stability and High Oxidation Resistance, Solid State Phenom. 127 (2007) 31–36. doi:10.4028/www.scientific.net/SSP.127.31.

[90] A. Raveh, I. Zukerman, R. Shneck, R. Avni, I. Fried, Thermal stability of nanostructured superhard coatings : A review, Surf. Coat. Technol. 201 (2007) 6136–6142. doi:10.1016/j.surfcoat.2006.08.131.

[91] H. Lind, F. Tasnádi, I.A. Abrikosov, Systematic theoretical search for alloys with increased thermal stability for advanced hard coatings applications, New J. Phys. 15 (2013) 95010. doi:10.1088/1367-2630/15/9/095010.

[92] E. Pflu, P. Voumard, L. Donohue, Influence of incorporation of Cr and Y on the wear performance of TiAlN coatings at elevated temperatures, Surf. Coat. Technol. 115 (2007) 17–23. doi:10.1016/S0257-8972(99)00059-6.

[93] M. Li, R. Wang, Y. Fan, L. Wang, Oxidation-resistance of (TiAlSiY) N coatings at 850 ° C, Mater. Res. Innov. 19 (2015) 190–194. doi:10.1179/1432891715Z.0000000001653.

[94] T. Chen, Z. Xie, F. Gong, Z. Luo, Z. Yang, Correlation between microstructure evolution and high temperature properties of TiAlSiN hard coatings with different Si and Al content, Appl. Surf. Sci. 314 (2014) 735–745. doi:10.1016/j.apsusc.2014.06.057.

[95] P. Zeman, J. Musil, R. Daniel, High-temperature oxidation resistance of Ta-Si-N films with a high Si content, Surf. Coatings Technol. 200 (2006) 4091–4096. doi:10.1016/j.surfcoat.2005.02.097.

[96] J. Musil, P. Zeman, P. Dohnal, Ti-Si-N Films with a High Content of Si, Plasma Process. Polym. 4 (2007) 574–578. doi:10.1002/ppap.200731408.

[97] H. Fager, J.M. Andersson, J. Jensen, J. Lu, L. Hultman, Thermal stability and mechanical properties of amorphous coatings in the Ti-B-Si-Al-N system grown by cathodic arc evaporation from TiB2, Ti33Al67, and Ti85Si15 cathodes, J. Vac. Sci. Technol. A Vacuum, Surfaces, Film. 32 (2014) 61508. doi:10.1116/1.4897170.

[98] H. Fager, J.M. Andersson, J. Lu, M.P.J. Jöesaar, M. Odén, L. Hultman, Growth of hard amorphous Ti \ Al \ Si \ N thin fi lms by cathodic arc evaporation, 235 (2013) 376–382. doi:10.1016/j.surfcoat.2013.07.014.

[99] J. Kohout, J. Vlček, J. Houška, P. Mareš, R. Čerstvý, P. Zeman, et al., Hard multifunctional Hf–B–Si–C films prepared by pulsed magnetron sputtering, Surf. Coatings Technol. 257 (2014) 301–307. doi:10.1016/j.surfcoat.2013.12.007.

[100] J. Houška, J. Vlček, Š. Potocký, V. Peřina, Influence of substrate bias voltage on structure and properties of hard Si–B–C–N films prepared by reactive magnetron sputtering, Diam. Relat. Mater. 16 (2007) 29–36. doi:10.1016/j.diamond.2006.03.012.

[101] P. Zeman, J. Musil, Difference in high-temperature oxidation resistance of amorphous Zr – Si – N and W – Si – N films with a high Si content, Appl. Surf. Sci. 252 (2006) 8319–8325. doi:10.1016/j.apsusc.2005.11.038.

[102] J. He, M. Zhang, J. Jiang, J. Vl, P. Zeman, P. Steidl, et al., Microstructure characterization of high-temperature , oxidation-resistant Si-B-C-N fi lms, Thin Solid Films. 542 (2013) 167–173. doi:10.1016/j.tsf.2013.07.013.

[103] H. Abu Samra, A. Kumar, J. Xia, T. Staedler, X. Jiang, Development of a new generation of amorphous hard coatings based on the Si–B–C–N–O system for applications in extreme conditions, Surf. Coatings Technol. 223 (2013) 52–67. doi:10.1016/j.surfcoat.2013.02.028.

[104] C. Paternoster, A. Fabrizi, R. Cecchini, S. Spigarelli, P.V. Kiryukhantsev-Korneev, A. Sheveyko, Thermal evolution and mechanical properties of hard Ti–Cr–B–N and Ti–Al–Si–B–N coatings, Surf. Coatings Technol. 203 (2008) 736–740. doi:10.1016/j.surfcoat.2008.08.013.

[105] M. Mikula, B. Grančič, M. Drienovský, L. Satrapinskyy, T. Roch, Z. Hájovská, et al., Thermal stability and high-temperature oxidation behavior of Si–Cr–N coatings with high content of silicon, Surf. Coatings Technol. 232 (2013) 349–356. doi:10.1016/j.surfcoat.2013.05.034.

[106] P. Martin, Handbook of deposition technologies for films and coatings: science, applications and technology, 2009. doi:10.1016/B978-0-8155-2031-3.00018-1.

[107] C. Mitterer, PVD and CVD Hard Coatings, Elsevier Ltd, 2014. doi:10.1016/B978-0-08-096527-7.00035-0.

[108] M. Henini, Handbook of Thin-Film Deposition Processes and Techniques, 2000. doi:10.1016/S0026-2692(99)00122-6.

[109] R.S. Pessoa, M.A. Fraga, L.V. Santos, N.K.A.M. Galvão, H.S. Maciel, M. Massi, Plasma-assisted techniques for growing hard nanostructured coatings, in: Anti-Abrasive Nanocoatings, Elsevier, 2015: pp. 455–479. doi:10.1016/B978-0-85709-211-3.00018-2.

[110] K. Reichelt, X. Jiang, The preparation of thin films by physical vapour deposition methods, Thin Solid Films. 191 (1990) 91–126. doi:10.1016/0040-6090(90)90277-K.

[111] A. Mubarak, E. Hamzah, M.R.M. Toff, Review of physical vapour deposition (PVD) techniques for hard coating, J. Mek. 20 (2005) 42–51.

[112] D. Manova, J.W. Gerlach, S. Mändl, Thin film deposition using energetic ions, Materials (Basel). 3 (2010) 4109–4141. doi:10.3390/ma3084109.

[113] J. Musil, J. Šůna, The Role of Energy in Formation of Sputtered Nanocomposite Films, Mater. Sci. Forum. 502 (2005) 291–296. doi:10.4028/www.scientific.net/MSF.502.291.

[114] D. Levchuk, Plasma assisted techniques for deposition of superhard nanocomposite coatings, Surf. Coatings Technol. 201 (2007) 6071–6077. doi:10.1016/j.surfcoat.2006.08.113.

[115] G. Bräuer, B. Szyszka, M. Vergöhl, R. Bandorf, Magnetron sputtering – Milestones of 30 years, Vacuum. 84 (2010) 1354–1359. doi:10.1016/j.vacuum.2009.12.014.

[116] J. Musil, J. Šícha, D. Heřman, R. Čerstvý, Role of energy in low-temperature high-rate formation of hydrophilic TiO2 thin films using pulsed magnetron sputtering, J. Vac. Sci. Technol. A Vacuum, Surfaces, Film. 25 (2007) 666. doi:10.1116/1.2736680.

[117] J. Musil, J. Vlcek, P. Baroch, Magnetron Discharges for Thin Films Plasma Processing, Mater. Surf. Process. by Dir. Energy Tech. (2006) 67–110. doi:10.1016/B978-008044496-3/50004-6.

[118] P.J. Kelly, R.D. Arnell, Magnetron sputtering: a review of recent developments and applications, Vacuum. 56 (2000) 159–172. doi:10.1016/S0042-207X(99)00189-X.

[119] J. Musil, P. Baroch, J. Vlček, K.H. Nam, J.G. Han, Reactive magnetron sputtering of thin films: present status and trends, Thin Solid Films. 475 (2005) 208–218. doi:10.1016/j.tsf.2004.07.041.

[120] R. Mientus, K. Ellmer, Reactive DC magnetron sputtering of elemental targets in Ar/N2 mixtures: relation between the discharge characteristics and the heat of formation of the corresponding nitrides, Surf. Coatings Technol. 116–119 (1999) 1093–1101. doi:10.1016/S0257-8972(99)00124-3.

[121] J. Musil, J. Vlček, Magnetron sputtering of hard nanocomposite coatings and their properties, Surf. Coatings Technol. 142–144 (2001) 557–566. doi:10.1016/S0257-8972(01)01139-2.

[122] J. Böhlmark, Fundamentals of High Power Impulse Magnetron Sputtering, Linköping University, 2012. doi:10.1063/1.3700242.

[123] J. Musil, S. Kadlec, Reactive to target sputtering distances, Vacuum. 40 (1990) 435–444. doi:10.1016/0042-207X(90)90241-P.

[124] T. Michely, J. Krug, Islands, Mounds and Atoms. Patterns and Processes in Crystal Growth Far from Equilibrium, Springer, 2004. doi:10.1017/CBO9781107415324.004.

[125] D. Magnfält, Fundamental processes in thin film growth: The origin of compressive stress and the dynamics of the early growth stages, Linköping University, 2014. doi:19.3384/diss.diva-105791.

[126] G.H. Gilmer, M.H. Grabow, Models of Thin Film Growth Modes, JOM. 39 (1987) 19–23. doi:10.1007/BF03258055.

[127] H. Holleck, Metastable coatings - Prediction of composition and structure, Surf. Coatings Technol. 36 (1988) 151–159. doi:10.1016/0257-8972(88)90145-4.

[128] J.A. Thornton, High Rate Thick Film Growth, Annu. Rev. Mater. Sci. 7 (1977) 239–260. doi:10.1146/annurev.ms.07.080177.001323.

[129] I. Petrov, P.B. Barna, L. Hultman, J.E. Greene, Microstructural evolution during film growth, J. Vac. Sci. Technol. A Vacuum, Surfaces, Film. 21 (2003) S117. doi:10.1116/1.1601610.

[130] R. Messier, Revised structure zone model for thin film physical structure, J. Vac. Sci. Technol. A Vacuum, Surfaces, Film. 2 (1984) 500. doi:10.1116/1.572604.

[131] A. Anders, A structure zone diagram including plasma-based deposition and ion etching, Thin Solid Films. 518 (2010) 4087–4090. doi:10.1016/j.tsf.2009.10.145.

[132] H. Fager, Growth and Characterization of Amorphous TiAlSiN and HfAlSiN Thin Films, Linköping University, 2012. doi:10.3384/diss.diva-106576.

[133] A. Inoue, Stabilization of metallic supercooled liquid and bulk amorphous alloys, Acta Mater. 48 (2000) 279–306. doi:10.1016/S1359-6454(99)00300-6.

[134] S. Stolen, T. Grande, N. Allan, Chemical Thermodynamics of Materials, John Wiley& Sons, Ltd, 2004. doi:10.1002/0470092688.

[135] J.W. Cahn, On spinodal decomposition, Acta Metall. 9 (1961) 795–801. doi:10.1016/0001-6160(61)90182-1.

[136] R.F. Zhang, S. Veprek, On the spinodal nature of the phase segregation and formation of stable nanostructure in the Ti-Si-N system, Mater. Sci. Eng. A. 424 (2006) 128–137. doi:10.1016/j.msea.2006.03.017.

[137] M. Katot, T. Moris, L.H. Schwartz, Hardening by spinodal modulated structure, Acta Metall. 28 (1980) 285–290.

[138] S. Veprek, A.S. Argon, Towards the understanding of mechanical properties of super- and ultrahard nanocomposites, J. Vac. Sci. Technol. B Microelectron. Nanom. Struct. 20 (2002) 650. doi:10.1116/1.1459722.

[139] K. Lu, Nanocrystalline metals crystallized from amorphous solids: Nanocrystallization, structure, and properties, Mater. Sci. Eng. R Reports. 16 (1996) 161–221. doi:10.1016/0927-796X(95)00187-5.

[140] Z. Zheng, Z. Yu, Characteristics and machining applications of Ti(Y)N coatings, Surf. Coatings Technol. 204 (2010) 4107–4113. doi:10.1016/j.surfcoat.2010.05.041.

[141] J. Musil, H. Hrubý, Superhard nanocomposite Ti1-xAlxN films prepared by magnetron sputtering, Thin Solid Films. 365 (2000) 104–109. doi:10.1016/S0040-

6090(00)00653-2.

[142] O. Knotek, M. Atzor, A. Barimani, F. Jungblut, Development of low temperature ternary coatings for high wear resistance, Surf. Coat. Technol. 42 (1990) 21–28. doi:10.1016/0257-8972(90)90111-O.

[143] G. Abadias, L.E. Koutsokeras, A. Siozios, P. Patsalas, Stress, phase stability and oxidation resistance of ternary Ti–Me–N (Me=Zr, Ta) hard coatings, Thin Solid Films. 538 (2013) 56–70. doi:10.1016/j.tsf.2012.10.119.

[144] J.R. Roos, J.P. Celis, E. Vancoille, H. Veltrop, S. Boelens, F. Jungblut, et al., Interrelationship between processing, coating properties and functional properties of steered arc physically vapour deposited (Ti,AI)N and (Ti,Nb)N coatings, Thin Solid Films. 193–194 (1990) 547–556. doi:10.1016/S0040-6090(05)80064-1.

[145] H. Hasegawa, A. Kimura, T. Suzuki, Microhardness and structural analysis of (Ti,Al)N, (Ti,Cr)N, (Ti,Zr)N and (Ti,V)N films, J. Vac. Sci. Technol. A Vacuum, Surfaces, Film. 18 (2000) 1038. doi:10.1116/1.582296.

[146] F. Regent, J. Musil, Magnetron sputtered Cr-Ni-N and Ti-Mo-N films: Comparison of mechanical properties, Surf. Coatings Technol. 142–144 (2001) 146–151. doi:10.1016/S0257-8972(01)01250-6.

[147] J.C. Caicedo, L. Yate, G. Cabrera, W. Aperador, G. Zambrano, P. Prieto, Effect of negative bias voltage on mechanical and electrochemical nature in Ti-W-N coatings, J. Mater. Sci. 46 (2011) 1244–1252. doi:10.1007/s10853-010-4904-7.

[148] S. Oktay, Z. Kahraman, M. Urgen, K. Kazmanli, XPS investigations of tribolayers formed on TiN and (Ti,Re)N coatings, Appl. Surf. Sci. 328 (2015) 255–261. doi:10.1016/j.apsusc.2014.12.023.

[149] R. Wiedemann, V. Weihnacht, H. Oettel, Structure and mechanical properties of amorphous Ti – B – N coatings, Surf. Coatings Technol. 116–119 (1999) 302–309. doi:10.1016/S0257-8972(99)00130-9.

[150] L. Zhang, G. Ma, H. Ma, G. Lin, Effect of pulsed bias voltage on the structure and mechanical properties of Ti–C–N composite films by pulsed bias arc ion plating, Nucl. Instruments Methods Phys. Res. Sect. B Beam Interact. with Mater. Atoms. 333 (2014) 1–5. doi:10.1016/j.nimb.2014.04.010.

[151] X. Zhou, A. Wu, W. Qu, X. Jiang, Fabrication and its characteristics of hard coating Ti-Al-N system prepared by DC magnetron sputtering, Rare Met. 31 (2012) 178–182. doi:10.1007/s12598-012-0487-6.

[152] J. Wagner, C. Mitterer, M. Penoy, C. Michotte, W. Wallgram, M. Kathrein, The effect of deposition temperature on microstructure and properties of thermal CVD TiN coatings, Int. J. Refract. Met. Hard Mater. 26 (2008) 120–126. doi:10.1016/j.ijrmhm.2007.01.010.

[153] P.. Mayrhofer, F. Kunc, J. Musil, C. Mitterer, A comparative study on reactive and non-reactive unbalanced magnetron sputter deposition of TiN coatings, Thin Solid Films. 415 (2002) 151–159. doi:10.1016/S0040-6090(02)00511-4.

[154] L. Chen, J. Paulitsch, Y. Du, P.H. Mayrhofer, Thermal stability and oxidation resistance of Ti–Al–N coatings, Surf. Coatings Technol. 206 (2012) 2954–2960. doi:10.1016/j.surfcoat.2011.12.028.

[155] J.C. Oliveira, A. Manaia, A. Cavaleiro, Hard amorphous Ti-Al-N coatings deposited

by sputtering, Thin Solid Films. 516 (2008) 5032–5038. doi:10.1016/j.tsf.2008.02.006.

[156] S. Vepřek, S. Reiprich, L. Shizhi, Superhard nanocrystalline composite materials: The TiN/Si3N4 system, Appl. Phys. Lett. 66 (1995) 2640. doi:10.1063/1.113110.

[157] M.A. Baker, C. Rebholz, A. Leyland, A. Matthews, Electron spectroscopic studies of nanocomposite PVD TiAlBN coatings, Vaccum. 67 (2002) 471–476. doi:10.1016/S0042-207X(02)00233-6.

[158] M.A. Baker, S. Klose, C. Rebholz, A. Leyland, A. Matthews, Evaluating the microstructure and performance of nanocomposite PVD TiAlBN coatings, Surf. Coat. Technol. 152 (2002) 338–343. doi:10.1016/S0257-8972(01)01657-7.

[159] P. Karvankova, M.G.J. Veprek-Heijman, O. Zindulka, A. Bergmaier, S. Veprek, Superhard nc-TiN/a-BN and nc-TiN/a-TiBx/a-BN coatings prepared by plasma CVD and PVD: A comparative study of their properties, Surf. Coatings Technol. 163–164 (2003) 149–156. doi:10.1016/S0257-8972(02)00492-9.

[160] P. Karvankova, M.G.J. Veprek-Heijman, D. Azinovic, S. Veprek, Properties of superhard nc-TiN/a-BN and nc-TiN/a-BN/a-TiB2 nanocomposite coatings prepared by plasma induced chemical vapor deposition, Surf. Coatings Technol. 200 (2006) 2978–2989. doi:10.1016/j.surfcoat.2005.01.003.

[161] P.H. Mayrhofer, C. Mitterer, J.G. Wen, I. Petrov, J.E. Greene, Thermally induced self-hardening of nanocrystalline Ti – B – N thin films Thermally induced self-hardening of nanocrystalline Ti – B – N thin films, 44301 (2006). doi:10.1063/1.2222406.

[162] S.Q. Wang, L. Chen, B. Yang, K.K. Chang, Y. Du, J. Li, et al., Effect of Si addition on microstructure and mechanical properties of Ti-Al-N coating, Int. J. Refract. Met. Hard Mater. 28 (2010) 593–596. doi:10.1016/j.ijrmhm.2010.05.001.

[163] M. Jilek, T. Cselle, P. Holubar, M. Morstein, M.G.J. Veprek-Heijman, S. Veprek, Development of novel coating technology by vacuum arc with rotating cathodes for industrial production of nc-(Al1-xTix)N/a-Si3N4 superhard nanocomposite coatings for dry, hard machining, Plasma Chem. Plasma Process. 24 (2004) 493–510. doi:10.1007/s11090-004-7929-3.

[164] I.-W. Park, S.R. Choi, J.H. Suh, C.-G. Park, K.H. Kim, Deposition and mechanical evaluation of superhard Ti–Al–Si–N nanocomposite films by a hybrid coating system, Thin Solid Films. 447–448 (2004) 443–448. doi:10.1016/S0040-6090(03)01122-2.

[165] Y. Tanaka, N. Ichimiya, Y. Onishi, Y. Yamada, Structure and properties of Al–Ti–Si–N coatings prepared by the cathodic arc ion plating method for high speed cutting applications, Surf. Coatings Technol. 146–147 (2001) 215–221. doi:10.1016/S0257-8972(01)01391-3.

[166] X. Ding, X.T. Zeng, Y.C. Liu, Structure and properties of CrAlSiN Nanocomposite coatings deposited by lateral rotating cathod arc, Thin Solid Films. 519 (2011) 1894–1900. doi:10.1016/j.tsf.2010.10.022.

[167] A. Niederhofer, T. Bolom, P. Nesladek, K. Moto, C. Eggs, D.S. Patil, et al., The role of percolation threshold for the control of the hardness and thermal stability of super- and ultrahard nanocomposites, Surf. Coatings Technol. 146–147 (2001) 183–188. doi:10.1016/S0257-8972(01)01469-4.

[168] K. Moto, T. Bolom, S. Veprek, The Role of nc-TiN Surface Coverage by a-Si_3N_4 for the Control of Room Temperature and In-Dry-Air Oxidation Resistance of nc-TiN/a-Si_3N_4/a- and nc-$TiSi_2$ Nanocomposites, Mater. Sci. Forum. 437–438 (2003) 403–406. doi:10.4028/www.scientific.net/MSF.437-438.403.

[169] S. Veprek, A. Niederhofer, K. Moto, T. Bolom, H.D. Männling, P. Nesladek, et al., Composition, nanostructure and origin of the ultrahardness in nc-TiN/a-Si3N4/a- and nc-TiSi2 nanocomposites with Hv = 80 to ≥105 GPa, Surf. Coatings Technol. 133–134 (2000) 152–159. doi:10.1016/S0257-8972(00)00957-9.

[170] S. Veprek, M. Haussmann, S. Reiprich, Superhard nanocrystalline W2N/amorphous Si3N4 composite materials, J. Vac. Sci. Technol. A-Vacuum Surfaces Film. 14 (1996) 46–51. doi:10.1116/1.579878.

[171] F. Huang, F. Ge, P. Zhu, H. Wang, F. Meng, S. Li, Superhard V-Si-N coatings (>50GPa) with the cell-like nanostructure prepared by magnetron sputtering, Surf. Coatings Technol. 232 (2013) 600–605. doi:10.1016/j.surfcoat.2013.06.035.

[172] M. Zhou, Y. Makino, M. Nose, K. Nogi, Phase transition and properties of Ti–Al–N thin films prepared by r.f.-plasma assisted magnetron sputtering, Thin Solid Films. 339 (1999) 203–208. doi:10.1016/S0040-6090(98)01364-9.

[173] A. Hörling, L. Hultman, M. Odén, J. Sjölén, L. Karlsson, Mechanical properties and machining performance of Ti1-xAlxN-coated cutting tools, Surf. Coatings Technol. 191 (2005) 384–392. doi:10.1016/j.surfcoat.2004.04.056.

[174] K. Kutschej, P.H. Mayrhofer, M. Kathrein, P. Polcik, R. Tessadri, C. Mitterer, Structure, mechanical and tribological properties of sputtered Ti1-xAlxN coatings with $0.5<x<0.75$, Surf. Coatings Technol. 200 (2005) 2358–2365. doi:10.1016/j.surfcoat.2004.12.008.

[175] Z.J. Liu, P.W. Shum, Y.G. Shen, Hardening mechanisms of nanocrystalline Ti-Al-N solid solution films, Thin Solid Films. 468 (2004) 161–166. doi:10.1016/j.tsf.2004.05.087.

[176] Y. Pinot, M.-H. Tuilier, M.-J. Pac, C. Rousselot, D. Thiaudière, The competitive growth of cubic domains in $Ti_{1-x}Al_xN$ films studied by diffraction anomalous near-edge structure spectroscopy, J. Synchrotron Radiat. 22 (2015) 1–10. doi:10.1107/S160057751501632X.

[177] M.J. Pac, S. Giljean, C. Rousselot, F. Richard, P. Delobelle, Microstructural and elasto-plastic material parameters identification by inverse finite elements method of Ti(1 − x)AlxN(0 < x < 1) sputtered thin films fromBerkovich nano-indentation experiments, Thin Solid Films. 569 (2014) 81–92. doi:10.1016/j.tsf.2014.07.037.

[178] B.-J. Kim, Y.-C. Kim, J.-W. Nah, J.-J. Lee, High temperature oxidation of (Ti[sub 1-X]Al[sub X])N coatings made by plasma enhanced chemical vapor deposition, J. Vac. Sci. Technol. A Vacuum, Surfaces, Film. 17 (1999) 133. doi:10.1116/1.581562.

[179] F. Esaka, K. Furuya, H. Shimada, M. Imamura, N. Matsubayashi, T. Kikuchi, et al., Composition Dependence of the Initial Oxidation Films Studied by XAS and XPS, Surf. Interface Anal. 1106 (1999) 1098–1106. doi:10.1002/(SICI)1096-9918(199912)27:12<1098::AID-SIA684>3.0.CO;2-I.

[180] D. McIntyre, J.E. Greene, G. Håkansson, J.E. Sundgren, W.D. Münz, Oxidation of metastable single-phase polycrystalline Ti 0.5Al0.5N films: Kinetics and

mechanisms, J. Appl. Phys. 67 (1990) 1542–1553. doi:10.1063/1.345664.

[181] F. Vaz, L. Rebouta, M. Andritschky, M.F. da Silva, J.C. Soares, Thermal oxidation of Ti1 − xAlxN coatings in air, J. Eur. Ceram. Soc. 17 (1997) 1971–1977. doi:10.1016/S0955-2219(97)00050-2.

[182] M.H. Tuilier, M.J. Pac, M. Ġrleanu, G. Covarel, G. Arnold, P. Louis, et al., Electronic and atomic structures of Ti1-x Alx N thin films related to their damage behavior, J. Appl. Phys. 103 (2008). doi:10.1063/1.2907415.

[183] P.H. Mayrhofer, A. Hörling, L. Karlsson, J. Sjölén, T. Larsson, C. Mitterer, et al., Self-organized nanostructures in the Ti-Al-N system, Appl. Phys. Lett. 83 (2003) 2049–2051. doi:10.1063/1.1608464.

[184] R. Rachbauer, S. Massl, E. Stergar, D. Holec, D. Kiener, J. Keckes, et al., Decomposition pathways in age hardening of Ti-Al-N films, J. Appl. Phys. 110 (2011) 0235151–02351510. doi:10.1063/1.3610451.

[185] R. Rachbauer, E. Stergar, S. Massl, M. Moser, P.H. Mayrhofer, Three-dimensional atom probe investigations of Ti-Al-N thin films, Scr. Mater. 61 (2009) 725–728. doi:10.1016/j.scriptamat.2009.06.015.

[186] B. Alling, A. V. Ruban, A. Karimi, O.E. Peil, S.I. Simak, L. Hultman, et al., Mixing and decomposition thermodynamics of c- Ti1-x Alx N from first-principles calculations, Phys. Rev. B - Condens. Matter Mater. Phys. 75 (2007) 1–13. doi:10.1103/PhysRevB.75.045123.

[187] F. Tasnádi, I.A. Abrikosov, L. Rogström, J. Almer, M.P. Johansson, M. Oḑn, Significant elastic anisotropy in Ti1-x Alx N alloys, Appl. Phys. Lett. 97 (2010) 23–26. doi:10.1063/1.3524502.

[188] P. Henry, M. Pac, C. Rousselot, M. Tuilier, Wear mechanisms of titanium and aluminium nitride coatings : A microtribological approach, Surf. Coat. Technol. 223 (2013) 79–86. doi:10.1016/j.surfcoat.2013.02.033.

[189] Y. Pinot, M.J. Pac, P. Henry, C. Rousselot, Y.I. Odarchenko, D.A. Ivanov, et al., Friction behaviour of TiAlN films around cubic/hexagonal transition: A 2D grazing incidence X-ray diffraction and electron energy loss spectroscopy study, Thin Solid Films. 577 (2015) 74–81. doi:10.1016/j.tsf.2015.01.044.

[190] S. Veprek, H.D. Männling, M. Jilek, P. Holubar, Avoiding the high-temperature decomposition and softening of (Al1-xTix)N coatings by the formation of stable superhard nc-(Al1-xTix)N/a-Si3 N4 nanocomposite, Mater. Sci. Eng. A. 366 (2004) 202–205. doi:10.1016/j.msea.2003.08.052.

[191] R.F. Zhang, A.S. Argon, S. Veprek, Understanding why the thinnest SiNx interface in transition-metal nitrides is stronger than the ideal bulk crystal, Phys. Rev. B. 81 (2010) 245418. doi:10.1103/PhysRevB.81.245418.

[192] C. Feng, S. Zhu, M. Li, L. Xin, F. Wang, Effects of incorporation of Si or Hf on the microstructure and mechanical properties of Ti – Al – N films prepared by arc ion plating (AIP), Surf. Coat. Technol. 202 (2008) 3257–3262. doi:10.1016/j.surfcoat.2007.11.036.

[193] C. Feng, M. Li, L. Xin, S. Zhu, Z. Shao, Q. Zhao, et al., Oxidation behavior of the compound Ti–Al–Si–N/1Cr11Ni2W2MoV at 800°C for 1000h in air, Surf. Coatings Technol. 232 (2013) 88–95. doi:10.1016/j.surfcoat.2013.04.057.

[194] S. Yang, Y. Chang, D. Lin, D. Wang, W. Wu, Thermal Stability of TiAlN and Nanocomposite TiAlSiN Thin Films, J. Nanosci. Nanotechnol. 9 (2009) 1108–1112. doi:10.1166/jnn.2009.C098.

[195] W. Xin, X.U. Jianhua, M.A. Shengli, X.U. Kewei, Effects of annealing temperature on the microstructure and hardness of TiAlSiN hard coatings, Chinese Phys. B. 56 (2011) 1727–1731. doi:10.1007/s11434-010-4237-6.

[196] L. Chen, B. Yang, Y. Xu, F. Pei, L. Zhou, Y. Du, Improved thermal stability and oxidation resistance of Al–Ti–N coating by Si addition, Thin Solid Films. 556 (2014) 369–375. doi:10.1016/j.tsf.2014.01.072.

[197] L. Chen, Y. Du, A.J. Wang, S.Q. Wang, S.Z. Zhou, Effect of Al content on microstructure and mechanical properties of Ti–Al–Si–N nanocomposite coatings, Int. J. Refract. Met. Hard Mater. 27 (2009) 718–721. doi:10.1016/j.ijrmhm.2008.12.002.

[198] H.C. Barshilia, M. Ghosh, Shashidhara, R. Ramakrishna, K.S. Rajam, Deposition and characterization of TiAlSiN nanocomposite coatings prepared by reactive pulsed direct current unbalanced magnetron sputtering, Appl. Surf. Sci. 256 (2010) 6420–6426. doi:10.1016/j.apsusc.2010.04.028.

[199] Q. Ma, L. Li, Y. Xu, X. Ma, Y. Xu, H. Liu, Effect of Ti content on the microstructure and mechanical properties of TiAlSiN nanocomposite coatings, Int. J. Refract. Met. Hard Mater. 59 (2016) 114–120. doi:10.1016/j.ijrmhm.2016.06.005.

[200] J. Suk Kim, G. Joong Kim, M. Chang Kang, J. Wook Kim, K. Ho Kim, Cutting performance of Ti–Al–Si–N-coated tool by a hybrid-coating system for high-hardened materials, Surf. Coatings Technol. 193 (2005) 249–254. doi:10.1016/j.surfcoat.2004.07.019.

[201] M. Pfeiler, J. Zechner, M. Penoy, C. Michotte, C. Mitterer, M. Kathrein, Improved oxidation resistance of TiAlN coatings by doping with Si or B, Surf. Coatings Technol. 203 (2009) 3104–3110. doi:10.1016/j.surfcoat.2009.03.036.

[202] S. Carvalho, L. Rebouta, E. Ribeiro, F. Vaz, C.J. Tavares, E. Alves, et al., Structural evolution of Ti – Al – Si – N nanocomposite coatings, Vaccum. 83 (2009) 1206–1212. doi:10.1016/j.vacuum.2009.03.009.

[203] J. Wu, N. He, H. Li, X. Liu, L. Ji, Deposition and characterization of TiAlSiN coatings prepared by hybrid PVD coating system, Surf. Interface Anal. 47 (2015) 184–191. doi:10.1002/sia.5680.

[204] S. Carvalho, L. Rebouta, A. Cavaleiro, L.. Rocha, J. Gomes, E. Alves, Microstructure and mechanical properties of nanocomposite (Ti,Si,Al)N coatings, Thin Solid Films. 398–399 (2001) 391–396. doi:10.1016/S0040-6090(01)01348-7.

[205] N. He, H. Li, L. Ji, X. Liu, H. Zhou, J. Chen, High temperature tribological properties of TiAlSiN coatings produced by hybrid PVD technology, Tribiology Int. 98 (2016) 133–143. doi:10.1016/j.triboint.2016.02.034.

[206] J. Wu, N. He, H. Li, X. Liu, L. Ji, Deposition and characterization of TiAlSiN coatings prepared by hybrid PVD coating system, Surf. Interface Anal. (2014). doi:10.1002/sia.5680.

[207] I.-W. Park, S.R. Choi, M.-H. Lee, K.H. Kim, Effects of Si addition on the microstructural evolution and hardness of Ti–Al–Si–N films prepared by the hybrid system of arc ion plating and sputtering techniques, J. Vac. Sci. Technol. A

Vacuum, Surfaces, Film. 21 (2003) 895. doi:10.1116/1.1576765.

[208] Y.S. Li, S. Shimada, H. Kiyono, A. Hirose, Synthesis of Ti – Al – Si – N nanocomposite films using liquid injection PECVD from alkoxide precursors, Acta Mater. 54 (2006) 2041–2048. doi:10.1016/j.actamat.2005.12.034.

[209] Y.-Y. Chang, S.-M. Yang, High temperature oxidation behavior of multicomponent TiAlSiN coatings, Thin Solid Films. 518 (2010) S34–S37. doi:10.1016/j.tsf.2010.03.020.

[210] D. Philippon, V. Godinho, P.M. Nagy, M.P. Delplancke-Ogletree, a. Fernández, Endurance of TiAlSiN coatings: Effect of Si and bias on wear and adhesion, Wear. 270 (2011) 541–549. doi:10.1016/j.wear.2011.01.009.

[211] E. Ribeiro, A. Malczyk, S. Carvalho, L. Rebouta, J. V. Fernandes, E. Alves, et al., Effects of ion bombardment on properties of d.c. sputtered superhard (Ti, Si, Al)N nanocomposite coatings, Surf. Coatings Technol. 151–152 (2002) 515–520. doi:10.1016/S0257-8972(01)01578-X.

[212] Z.L. Wu, Y.G. Li, B. Wu, M.K. Lei, Effect of microstructure on mechanical and tribological properties of TiAlSiN nanocomposite coatings deposited by modulated pulsed power magnetron sputtering, Thin Solid Films. 597 (2015) 197–205. doi:10.1016/j.tsf.2015.11.047.

[213] H. Fager, J.M. Andersson, J. Lu, M.P.J. Jöesaar, M. Odén, L. Hultman, Growth of hard amorphous TiAlSiN thin films by cathodic arc evaporation, Surf. Coatings Technol. 235 (2013) 376–382. doi:10.1016/j.surfcoat.2013.07.014.

[214] G.G. Fuentes, E. Almandoz, R. Pierrugues, R. Martínez, R.J. Rodríguez, J. Caro, et al., High temperature tribological characterisation of TiAlSiN coatings produced by cathodic arc evaporation, Surf. Coatings Technol. 205 (2010) 1368–1373. doi:10.1016/j.surfcoat.2010.09.004.

[215] Z.W. Xie, L.P. Wang, X.F. Wang, L. Huang, Y. Lu, J.C. Yan, Influence of oxidation on the structural and mechanical properties of TiAlSiN coatings synthesized by multi-plasma immersion ion implantation and deposition, Nucl. Instruments Methods Phys. Res. Sect. B Beam Interact. with Mater. Atoms. 271 (2012) 1–5. doi:10.1016/j.nimb.2011.10.011.

[216] D. Yu, C. Wang, X. Cheng, F. Zhang, Microstructure and properties of TiAlSiN coatings prepared by hybrid PVD technology, Thin Solid Films. 517 (2009) 4950–4955. doi:10.1016/j.tsf.2009.03.091.

[217] PLATIT AG, (2016). http://www.platit.com/.

[218] S. Heck, Tribological behaviour of Ti-Al-B-N-based PVD coatings, Surf. Coatings Technol. 86–87 (1996) 467–471. doi:10.1016/S0257-8972(96)02987-8.

[219] C. Mitterer, Radio-frequency sputter deposition of boron nitride based thin films, J. Vac. Sci. Technol. A Vacuum, Surfaces, Film. 7 (1989) 2646. doi:10.1116/1.575767.

[220] M.A. Baker, M.A. Monclus, C. Rebholz, P.N. Gibson, A. Leyland, A. Matthews, A study of the nanostructure and hardness of electron beam evaporated TiAlBN Coatings, Thin Solid Films. 518 (2010) 4273–4280. doi:10.1016/j.tsf.2009.12.109.

[221] D. V. Shtansky, K. Kaneko, Y. Ikuhara, E.A. Levashov, Characterization of nanostructured multiphase Ti-Al-B-N thin films with extremely small grain size,

Surf. Coatings Technol. 148 (2001) 206–215. doi:10.1016/S0257-8972(01)01341-X.

[222] V.H. Derflinger, a. Schütze, M. Ante, Mechanical and structural properties of various alloyed TiAlN-based hard coatings, Surf. Coatings Technol. 200 (2006) 4693–4700. doi:10.1016/j.surfcoat.2005.02.065.

[223] C. Rebholz, A. Leyland, A. Matthews, C. Charitidis, S. Logothetidis, D. Schneider, Correlation of elastic modulus, hardness and density for sputtered TiAlBN thin films, Thin Solid Films. 514 (2006) 81–86. doi:10.1016/j.tsf.2006.02.038.

[224] D.H. Jung, K. Il Moon, S.Y. Shin, C.S. Lee, Influence of ternary elements (X = Si, B, Cr) on TiAlN coating deposited by magnetron sputtering process with single alloying targets, Thin Solid Films. 546 (2013) 242–245. doi:10.1016/j.tsf.2013.05.046.

[225] C. Rebholz, Structure, mechanical and tribological properties of Ti–B–N and Ti–Al–B–N multiphase thin films produced by electron-beam evaporation, J. Vac. Sci. Technol. A Vacuum, Surfaces, Film. 16 (1998) 2851. doi:10.1116/1.581431.

[226] C. Rebholz, J.M. Schneider, A.A. Voevodin, J. Steinebrunner, C. Charitidis, S. Logothetidis, et al., Structure, mechanical and tribological properties of sputtered TiAlBN thin films, Surf. Coatings Technol. 113 (1999) 126–133. doi:10.1016/S0257-8972(98)00840-8.

[227] C. Rebholz, A. Leyland, A. Matthews, Deposition and characterisation of TiAlBN coatings produced by direct electron-beam evaporation of Ti and Ti-Al-B-N material from a twin crucible source, Thin Solid Films. 343–344 (1999) 242–245. doi:10.1016/S0040-6090(98)01635-6.

[228] C. Rebholz, M.A. Monclus, M.A. Baker, P.H. Mayrhofer, P.N. Gibson, A. Leyland, et al., Hard and superhard TiAlBN coatings deposited by twin electron-beam evaporation, Surf. Coatings Technol. 201 (2007) 6078–6083. doi:10.1016/j.surfcoat.2006.08.121.

[229] K. Kutschej, N. Fateh, P.H. Mayrhofer, M. Kathrein, P. Polcik, C. Mitterer, Comparative study of Ti 1 À x Al x N coatings alloyed with Hf , Nb , and B, Surf. Coat. Technol. 200 (2005) 113–117. doi:10.1016/j.surfcoat.2005.02.072.

[230] I. Zukerman, A. Raveh, Y. Shneor, R. Shneck, J.E. Klemberg-saphieha, L. Martinu, Internal stress in TiAlBN at high temperatures, Surf. Coat. Technol. 201 (2007) 6161–6166. doi:10.1016/j.surfcoat.2006.08.136.

[231] R.A. Andrievski, G. V Kalinnikov, Physical-mechanical and physical-chemical properties of thin nanostructured boride/nitride films, Surf. Coatings Technol. 142–144 (2001) 573–578. doi:10.1016/S0257-8972(01)01246-4.

[232] J. Morales-Hernández, L. García-González, J. Muñoz-Saldaña, F.J. Espinoza-Beltrán, Structure and mechanical properties of (Ti,Al)(B,N) coatings fabricated by reactive DC magnetron sputtering, Vacuum. 76 (2004) 161–164. doi:10.1016/j.vacuum.2004.07.059.

[233] P.V. Kiryukhantsev-Korneev, D.V. Shtansky, M.I. Petrzhik, E.A. Levashov, B.N. Mavrin, Thermal stability and oxidation resistance of Ti–B–N, Ti–Cr–B–N, Ti–Si–B–N and Ti–Al–Si–B–N films, Surf. Coatings Technol. 201 (2007) 6143–6147. doi:10.1016/j.surfcoat.2006.08.133.

[234] D.V. Shtansky, A.N. Sheveiko, M.I. Petrzhik, F.V. Kiryukhantsev-Korneev, E.A. Levashov, A. Leyland, et al., Hard tribological Ti–B–N, Ti–Cr–B–N, Ti–Si–B–N

and Ti–Al–Si–B–N coatings, Surf. Coatings Technol. 200 (2005) 208–212. doi:10.1016/j.surfcoat.2005.02.126.

[235] F. V. Kiryukhantsev-Korneev, M.I. Petrzhik, A.N. Sheveiko, E.A. Levashov, D. V. Shtanskii, Effect of Al, Si, and Cr on the thermal stability and high-temperature oxidation resistance of coatings based on titanium boronitride, Phys. Met. Metallogr. 104 (2007) 167–174. doi:10.1134/S0031918X07080091.

[236] C. Paternoster, A. Fabrizi, R. Cecchini, S. Spigarelli, P. V Kiryukhantsev-korneev, A. Sheveyko, Thermal evolution and mechanical properties of hard Ti – Cr – B – N and Ti – Al – Si – B – N coatings, Surf. Coat. Technol. 203 (2008) 736–740. doi:10.1016/j.surfcoat.2008.08.013.

[237] H.W. Hugosson, H. Högberg, M. Algren, M. Rodmar, T.I. Selinder, Theory of the effects of substitutions on the phase stabilities of Ti1-xAlxN, J. Appl. Phys. 93 (2003) 4505–4511. doi:10.1063/1.1557779.

[238] L.A. Dobrzański, L.W. Żukowska, Structure and properties of gradient PVD coatings deposited on the sintered tool materials, J. Achiev. Mater. Manuf. Eng. 44 (2011) 115–139.

[239] S. PalDey, S.C. Deevi, Properties of single layer and gradient (Ti,Al)N coatings, Mater. Sci. Eng. A. 361 (2003) 1–8. doi:10.1016/S0921-5093(03)00473-8.

[240] X.Q. U, Y. Hou, Y. Wu, J. Chen, Study on functionally gradient coatings of Ti - Al-N, Surf. Coatings Technol. (2000) 462–464.

[241] W. Lengauer, K. Dreyer, Functionally graded hardmetals, J. Alloys Compd. 338 (2002) 194–212. doi:10.1016/S0925-8388(02)00232-3.

[242] H.W. Sheng, G. Ren, L.M. Peng, Z.Q. Hu, K. Lu, Epitaxial dependence of the melting behavior of In nanoparticles embedded in Al matrices, J. Mater. Res. 12 (1997) 119–123. doi:10.1557/jmr.1997.0019.

[243] A.L. Greer, Diffusion and reactions in thin films, Appl. Surf. Sci. 86 (1995) 329–337. doi:10.1016/0169-4332(94)00399-8.

[244] Y.-Y. Chang, S.-J. Yang, W. Wu, Y.-C. Kuo, J.-W. Lee, C.-J. Wang, Mechanical properties of gradient and multilayered TiAlSiN hard coatings, Thin Solid Films. 517 (2009) 4934–4937. doi:10.1016/j.tsf.2009.03.036.

[245] L. Settineri, M.G. Faga, G. Gautier, M. Perucca, Evaluation of wear resistance of AlSiTiN and AlSiCrN nanocomposite coatings for cutting tools, CIRP Ann. - Manuf. Technol. 57 (2008) 575–578. doi:10.1016/j.cirp.2008.03.103.

[246] M.G. Faga, G. Gautier, R. Calzavarini, M. Perucca, E.A. Boot, F. Cartasegna, et al., AlSiTiN nanocomposite coatings developed via Arc Cathodic PVD: Evaluation of wear resistance via tribological analysis and high speed machining operations, Wear. 263 (2007) 1306–1314. doi:10.1016/j.wear.2007.01.109.

[247] M. Antonov, I. Hussainova, F. Sergejev, P. Kulu, A. Gregor, Assessment of gradient and nanogradient PVD coatings behaviour under erosive, abrasive and impact wear conditions, Wear. 267 (2009) 898–906. doi:10.1016/j.wear.2008.12.045.

[248] J. Zhang, H. Lv, G. Cui, Z. Jing, C. Wang, Effects of bias voltage on the microstructure and mechanical properties of (Ti,Al,Cr)N hard films with N-gradient distributions, Thin Solid Films. 519 (2011) 4818–4823. doi:10.1016/j.tsf.2011.01.036.

[249] J. Zhang, L. Yin, Microstructure and mechanical properties of (Ti,Al,Nb)N hard

films with N-gradient distributions, Thin Solid Films. 584 (2015) 141–145. doi:10.1016/j.tsf.2015.01.056.

[250] A. Abid, R. Bensalem, J.B. Sealy, The thermal stability of AIN, J. Mater. Res. 21 (1986) 8–11.

[251] C. Lin, F. Lu, Oxidation behavior of AlN films at high temperature under controlled atmosphere, 28 (2008) 691–698. doi:10.1016/j.jeurceramsoc.2007.07.015.

[252] P.H. Mayrhofer, C. Mitterer, J.G. Wen, J.E. Greene, I. Petrov, Self-organized nanocolumnar structure in superhard TiB2 thin films, Appl. Phys. Lett. 86 (2005) 1–3. doi:10.1063/1.1887824.

[253] W.Y. Yang, H. Iwakuro, H. Yagi, T. Kuroda, S. Nakamura, Study of Oxidation of TiSi2 Thin Film by XPS, Jpn. J. Appl. Phys. 23 (1984) 1560–1567.

[254] O.N. Grigor'ev, I.A. Podchernyaeva, A.D. Panasyuk, V. V. Varyukhno, Heat- and wear-resistant composite materials and coatings on AlN-TiB2, Refract. Ind. Ceram. 45 (2004) 373–378.

[255] J. Vlček, Š. Potocký, J. Čížek, J. Houška, M. Kormunda, P. Zeman, et al., Reactive magnetron sputtering of hard Si – B – C – N films with a high-temperature oxidation resistance, J. Vac. Sci. Technol. A-Vacuum Surfaces Film. 23 (2008) 1513–1522. doi:10.1116/1.2049298.

[256] A.D. Pogrebnjak, G. Abadias, O.V. Bondar, O.V. Sobol, V.M. Beresnev, A.V. Pshyk, et al., High Temperature Annealing of Ion-Plasma Nanostructured Coatings Based on AlN-TiB2(TiSi2), Acta Phys. Pol. A. 125 (2014) 1284–1287. doi:10.12693/APhysPolA.125.1284.

[257] B. Bhushan, ed., Scanning Probe Microscopy in Nanoscience and Nanotechnology, Springer, 2010. doi:10.1007/978-3-642-01495-6.

[258] Gwyddion, (2016). http://gwyddion.net/.

[259] W. Zhou, Z.L. Wang, eds., Scanning Microscopy for Nanotechnology, Springer, 2006. doi:10.1007/978-0-387-39620-0.

[260] D.B. Williams, C.B. Carter, Transmission Electron Microscopy, Springer, 2009. doi:10.1007/978-0-387-76501-3_1.

[261] B. Fultz, J. Howe, Transmission ElectronMicroscopy and Diffractometry of Materials, Springer, 2010. doi:10.1007/978-3-642-00710-1_2.

[262] S.-G. Lee, Y.-J. Kim, S.-J. Yoo, S.-H. Lee, J.-G. Kim, Application of FFT Data from HREM images to Electron crystallography, J. Anal. Sci. Technol. 3 (2012) 128–134. doi:10.5355/JAST.2012.128.

[263] N. Yao, Z.L. Wang, Handbook of Microscopy for Nanotechnology, Kluwer Academic Publishers, 2005. doi:10.1016/S1369-7021(05)71039-7.

[264] N. Yao, Focused ion beam systems: basics and applications, Cambridge University Press, 2007. doi:10.1017/CBO9780511600302.

[265] P.J. Larkin, IR and Raman Spectroscopy - Principles and Spectral Interpretation", Elsevier, 2011. doi:10.1016/b978-0-12-386984-5.10001-1.

[266] E. Smith, G. Dent, Modern Raman Spectroscopy – A Practical Approach, John Wiley& Sons, Ltd, 2005.

[267] H. Czichos, T. Saito, L. Smith, Handbook of Metrology and Testing, Springer, 2014. doi:10.1007/s13398-014-0173-7.2.

[268] S. Hofmann, Auger- and X-Ray Photoelectron Spectroscopy in Materials Science, 2013. doi:10.1007/978-3-642-27381-0.

[269] G. Moretti, Auger parameter and Wagner plot in the characterization of chemical states by X-ray photoelectron spectroscopy : a review, J. Electron Spectros. Relat. Phenomena. 95 (1998) 95–144.

[270] J. Rose, M. Auffan, O. Proux, V. Niviere, J.Y. Bottero, Encyclopedia of Nanotechnology, Encycl. Nanotechnol. (2012) 1576–1596. doi:10.1007/978-90-481-9751-4.

[271] J.J. Gilman, Chemistry and Physics of Mechanical Hardness, 2009. doi:10.1002/9780470446836.

[272] W.C. Oliver, G.M. Pharr, An improved technique for determining hardness and elastic modulus using load and displacement sensing indentation experiments, J. Mater. Res. 7 (1992) 1564–1583.

[273] C.A. Schuh, Nanoindentation studies of materials, Mater. Today. 9 (2006) 32–40. doi:10.1016/S1369-7021(06)71495-X.

[274] A.C. Fischer-Cripps, Nanoindentation, Springer, 2011. doi:10.1016/B978-0-12-387667-6.00013-0.

[275] C. Fischer-Cripps, Introduction to Contact Mechanics, Springer, 2013. doi:10.1017/CBO9781107415324.004.

[276] Y.W. Bao, W. Wang, Y.C. Zhou, Investigation of the relationship between elastic modulus and hardness based on depth-sensing indentation measurements, Acta Mater. 52 (2004) 5397–5404. doi:10.1016/j.actamat.2004.08.002.

[277] A.C. Lund, A.M. Hodge, C.A. Schuh, A.C. Lund, A.M. Hodge, Incipient plasticity during nanoindentation at elevated temperatures, Appl. Phys. Lett. 85 (2004) 1362. doi:10.1063/1.1784891.

[278] C.A. Schuh, T.G. Nieh, A nanoindentation study of serrated flow in bulk metallic glasses, Acta Mater. 51 (2003) 87–99. doi:10.1016/S.

[279] J. Jang, M.J. Lance, S. Wen, T.Y. Tsui, G.M. Pharr, Indentation-induced phase transformations in silicon : influences of load , rate and indenter angle on the transformation behavior, Acta Mater. 53 (2005) 1759–1770. doi:10.1016/j.actamat.2004.12.025.

[280] B. Bhushan, Nanotribology and Nanomechanics, Springer, 2008. doi:10.1007/s13398-014-0173-7.2.

[281] J.C. Slater, Atomic Radii in Crystals, J. Chem. Phys. 41 (1964) 3199. doi:10.1063/1.1725697.

[282] P.H. Mayrhofer, M. Stoiber, C. Mitterer, Age hardening of PACVD TiBN thin films, Scr. Mater. 53 (2005) 241–245. doi:10.1016/j.scriptamat.2005.03.031.

[283] B. Sartory, R. Tessadri, M.O. Sullivan, C. Mitterer, Nanocomposite Ti – B – N coatings synthesized by reactive arc evaporation, Acta Mater. 54 (2006) 4193–4200. doi:10.1016/j.actamat.2006.05.014.

[284] D. Depla, J. Haemers, R. De Gryse, Discharge voltage measurements during reactive sputtering of oxides, Thin Solid Films. 515 (2006) 468–471. doi:10.1016/j.tsf.2005.12.256.

[285] D.-C. Tsai, Z.-C. Chang, B.-H. Kuo, C.-T. Tsao, E.-C. Chen, F.-S. Shieu, Influence of discharge power on the structural, electro-optical, and mechanical properties of (TiZrHf)N coatings, J. Alloys Compd. 622 (2015) 446–457. doi:10.1016/j.jallcom.2014.10.073.

[286] U. Kroll, J. Meier, H. Keppner, A. Shah, S.D. Littlewood, I.E. Kelly, Origins of atmospheric contamination in amorphous silicon prepared by very high frequency (70 MHz) glow discharge, J. Vac. Sci. Technol. A-Vacuum Surfaces Film. 6 (2000) 2742–2746. doi:10.1116/1.579698.

[287] A.V. Pshyk, L.E. Coy, L. Yate, K. Załęski, G. Nowaczyk, A.D. Pogrebnjak, et al., Combined reactive/non-reactive DC magnetron sputtering of high temperature composite AlN–TiB2–TiSi2, Mater. Des. 94 (2016) 230–239. doi:10.1016/j.matdes.2015.12.174.

[288] G. Greczynski, L. Hultman, Self-consistent modelling of X-ray photoelectron spectra from air-exposed polycrystalline TiN thin films, Appl. Surf. Sci. 387 (2016) 294–300. doi:10.1016/j.apsusc.2016.06.012.

[289] L. Rosenberger, R. Baird, E. McCullen, G. Auner, G. Shreve, XPS analysis of aluminum nitride films deposited by plasma source molecular beam epitaxy, Surf. Interface Anal. 40 (2008) 1254–1261. doi:10.1002/sia.2874.

[290] J.H. Harris, R.A. Youngman, R.G. Teller, On the nature of the oxygen-related defect in aluminum nitride, J. Mater. Res. 5 (1990) 1763–1773.

[291] G. Greczynski, D. Primetzhofer, J. Lu, L. Hultman, Core-level spectra and binding energies of transition metal nitrides by non-destructive x-ray photoelectron spectroscopy through capping layers, Appl. Surf. Sci. 396 (2017) 347–358. doi:10.1016/j.apsusc.2016.10.152.

[292] I. Bertoti, M. Mohai, J.L. Sullivan, S.O. Saied, Surface characterisation of plasma-nitrided titanium: an XPS study, Appl. Surf. Sci. 84 (1995) 357–371.

[293] F. Esaka, K. Furuya, H. Shimada, M. Imamura, N. Matsubayashi, H. Sato, et al., Comparison of surface oxidation of titanium nitride and chromium nitride films studied by x-ray absorption and photoelectron spectroscopy, J. Vac. Sci. Technol. A-Vacuum Surfaces Film. 2521 (2014). doi:10.1116/1.580764.

[294] D. Jaeger, J. Patscheider, A complete and self-consistent evaluation of XPS spectra of TiN, J. Electron Spectros. Relat. Phenomena. 185 (2012) 523–534. doi:10.1016/j.elspec.2012.10.011.

[295] C. Guimon, D. Gonbeau, G. Pfister-Guillouzo, O. Dugne, A. Guette, R. Naslain, et al., XPS study of BN thin films deposited by CVD on SiC plane substrates, Surf. Interface Anal. 16 (1990) 440–445. doi:10.1002/sia.740160191.

[296] D. Schild, S. Ulrich, J. Ye, M. Stüber, XPS investigations of thick , oxygen-containing cubic boron nitride coatings, Solid State Sci. 12 (2010) 1903–1906. doi:10.1016/j.solidstatesciences.2010.05.029.

[297] J. Sjölén, L. Karlsson, S. Braun, R. Murdey, a. Hörling, L. Hultman, Structure and mechanical properties of arc evaporated Ti–Al–O–N thin films, Surf. Coatings Technol. 201 (2007) 6392–6403. doi:10.1016/j.surfcoat.2006.12.006.

[298] X. Zhang, Z. Lu, J. Lin, Y. Fan, L. Li, X. Xu, et al., Spectra Properties of BCNO Phosphor Prepared by a Two-Step Method at Low Sintering Temperature, ECS J. Solid State Sci. Technol. 2 (2012) R39–R43. doi:10.1149/2.012303jss.

[299] J.F. Marco, A.C. Agudelo, J.R. Gancedo, D. Hanz, Corrosion resistance of single TiN layers , Ti / TiN bilayers and Ti / TiN / Ti / TiN multilayers on iron under a salt fog spray (phohesion) test : an evaluation by XPS, Surf. Interface Anal. 27 (1999) 71–75. doi:10.1002/(SICI)1096-9918(199902)27:2<71::AID-SIA469>3.3.CO;2-7.

[300] A. V. Naumkin, A. Kraut-Vass, S.W. Gaarenstroom, C.J. Powell, NIST Standard Reference Database 20, (2012). http://srdata.nist.gov/xps/Default.aspx.

[301] I. Bertoti, Characterization of nitride coatings by XPS, Surf. Coat. Technol. 152 (2002) 194–203.

[302] I. Dreiling, C. Raisch, J. Glaser, D. Stiens, T. Chassé, Characterization and oxidation behavior of MTCVD Ti – B – N coatings, Surf. Coat. Technol. 206 (2011) 479–486. doi:10.1016/j.surfcoat.2011.07.067.

[303] P.W. Shum, Z.F. Zhou, K.Y. Li, Y.G. Shen, XPS, AFM and nanoindentation studies of Ti1-xAlxN films synthesized by reactive unbalanced magnetron sputtering, Mater. Sci. Eng. B Solid-State Mater. Adv. Technol. 100 (2003) 204–213. doi:10.1016/S0921-5107(03)00107-7.

[304] M. Braic, M. Balaceanu, A. Vladescu, A. Kiss, V. Braic, G. Epurescu, Preparation and characterization of titanium oxy-nitride thin films, Appl. Surf. Sci. 253 (2007) 8210–8214. doi:10.1016/j.apsusc.2007.02.179.

[305] J. Prokop, A. Kukunin, M. Pratzer, H. Elmers, Oxidation-driven changes of the in-plane magnetic surface anisotropies of the Fe (1 1 0)/ Al interface, J. Magn. Magn. Mater. 265 (2003) 60–68. doi:10.1016/S0304-8853(03)00225-7.

[306] R. Perrem, F. Henry, G. Peraudeau, B. Armas, R. Berjoan, E. Beche, An XPS and thermogravimetric study of oxidized AlN and AlN–Si3N4 layers deposited by liquid-phase chemical vapour deposition, J. Mater. Sci. 32 (1997) 1305–1312. doi:10.1023/A:1018556606993.

[307] a von Richthofen, R. Cremer, R. Domnick, D. Neuschütz, Use of Auger- and photoelectron lines in the identification of chemical states of novel ternary Ti–Al–O films prepared by reactive magnetron sputtering ion plating, Thin Solid Films. 315 (1998) 66–71. doi:10.1016/S0040-6090(97)00745-1.

[308] C.D. Wagner, D. A. Zatko, R.H. Raymond, Use of the oxygen KLL Auger lines in identification of surface chemical states by electron spectroscopy for chemical analysis, Anal. Chem. 52 (1980) 1445–1451. doi:10.1021/ac50059a017.

[309] C.M. Woodbridge, X.J. Gu, M.A. Langell, Extra-atomic relaxation energies and Auger parameters of titanium compounds, Surf. Interface Anal. 27 (1999) 816–824. doi:10.1002/(SICI)1096-9918(199909)27:9<816::AID-SIA637>3.0.CO;2-E.

[310] Q.Y. Zhang, Quantitative determination of titanium nitride films by high energy resolution Auger electron spectroscopy, J. Vac. Sci. Technol. A Vacuum, Surfaces, Film. 13 (1995) 2384–2389. doi:10.1116/1.579478.

[311] R. Cremer, M. Witthaut, D. Neuschütz, Electron spectroscopy applied to metastable ceramic solution phases, Fresenius J. Anal. Chem. 365 (1999) 28–37.

[312] P.W. Wang, S. Sui, W.G. Durrer, J.H. Craig, Auger peak shape analysis of AlN film

grown by ammonia plasma, Surf. Interface Anal. 35 (2003) 141–145. doi:10.1002/sia.1509.

[313] M. Witthaut, R. Cremer, D. Neusch, Electron spectroscopy of single-phase (Al , B) N films, Surf. Interface Anal. 30 (2000) 580–584.

[314] S. Hashmi, G.F. Batalha, C.J. Van Tyne, B. Yilbas, eds., Comprehensive Materials Processing, Elsevier, 2014. doi:10.1007/s13398-014-0173-7.2.

[315] G. Greczynski, J. Jensen, J.E. Greene, I. Petrov, L. Hultman, X-ray Photoelectron Spectroscopy Analyses of the Electronic Structure of Polycrystalline Ti $_{1-x}$ Al $_{x}$ N Thin Films with $0 \leq x \leq 0.96$, Surf. Sci. Spectra. 21 (2014) 35–49. doi:10.1116/11.20140506.

[316] A.S. Kamenetskih, A.I. Kukharenko, E.Z. Kurmaev, N.A. Skorikov, N.V. Gavrilov, S.O. Cholakh, et al., Characterization of TiAlSiON coatings deposited by plasma enhanced magnetron sputtering: XRD, XPS, and DFT studies, Surf. Coatings Technol. 278 (2015) 87–91. doi:10.1016/j.surfcoat.2015.08.007.

[317] L. Porte, L. Roux, J. Hanus, Vacancy effects in the x-ray photoelectron spectra of TiNx, Phys. Rev. B. 28 (1983) 3214–3224.

[318] A. Trenczek-zajac, M. Radecka, K. Zakrzewska, A. Brudnik, E. Kusior, S. Bourgeois, et al., Structural and electrical properties of magnetron sputtered Ti (ON) thin films : The case of TiN doped in situ with oxygen, J. Power Sources. 194 (2009) 93–103. doi:10.1016/j.jpowsour.2008.12.112.

[319] N. Schalk, J.F.T.S. Fotso, D. Holec, A. Fian, Microstructure , mechanical and optical properties of TiAlON coatings sputter-deposited with varying oxygen partial pressures, J. Phys. D. Appl. Phys. 49 (2016) 25307. doi:10.1088/0022-3727/49/2/025307.

[320] M. to Baben, L. Raumann, J.M. Schneider, Phase stability and elastic properties of titanium aluminum oxynitride studied by ab initio calculations, J. Phys. D. Appl. Phys. 46 (2013) 84002. doi:10.1088/0022-3727/46/8/084002.

[321] M. Radecka, E. Pamula, A. Trenczek-zajac, K. Zakrzewska, A. Brudnik, E. Kusior, Chemical composition , crystallographic structure and impedance spectroscopy of titanium oxynitride TiN x O y thin fi lms, Solid State Ionics. 192 (2011) 693–698. doi:10.1016/j.ssi.2010.07.021.

[322] F. Liu, J. Yu, X. Bai, Crystallinity improvement of hexagonal boron nitride films by molybdenum catalysts during microwave plasma chemical vapor deposition and post-annealing, Appl. Surf. Sci. 258 (2012) 10191–10194. doi:10.1016/j.apsusc.2012.06.108.

[323] M. Witthaut, R. Cremer, K. Reichert, D. Neuschutz, Characterization of ternary Al-B-N films, Thin Solid Films. 377 (2000) 478–483. doi:10.1016/S0040-6090(00)01435-8.

[324] S. Hofmann, Auger- and X-Ray Photoelectron Spectroscopy in Material Science, Springer, 2013. doi:10.1017/CBO9781107415324.004.

[325] Y.H. Lu, P. Sit, T.F. Hung, H. Chen, Z.F. Zhou, K.Y. Li, et al., Effects of B content on microstructure and mechanical properties of nanocomposite Ti–B[sub x]–N[sub y] thin films, J. Vac. Sci. Technol. B Microelectron. Nanom. Struct. 23 (2005) 449. doi:10.1116/1.1865117.

[326] M. Mizuno, I. Tanaka, H. Adachi, Chemical bonding in titanium-metalloid compounds, Phys. Rev. B. 59 (1999) 15033–15047. doi:10.1103/PhysRevB.59.15033.

[327] C.M.T. Sanchez, H.D. Fonseca-Filho, M.E.H. Maia da Costa, F.L. Freire, Nitrogen incorporation into titanium diboride films deposited by dc magnetron sputtering: Structural modifications, Thin Solid Films. 517 (2009) 5683–5688. doi:10.1016/j.tsf.2009.02.122.

[328] P.W. Shum, K.Y. Li, Z.F. Zhou, Y.G. Shen, Structural and mechanical properties of titanium – aluminium – nitride films deposited by reactive close-field unbalanced magnetron sputtering, 185 (2004) 245–253. doi:10.1016/j.surfcoat.2003.12.011.

[329] W. Spengler, R. Kaiser, First and second order Raman scattering in transition metal compounds, Solid State Commun. 18 (1976) 881–884. doi:10.1016/0038-1098(76)90228-3.

[330] W. Spengler, R. Kaiser, A.N. Christensen, G. Muller-Vogt, Raman scattering, superconductivity, and phonon density of states of stoichiometric and nonstoichiometric TiN, Phys. Rev. B. 17 (1978) 1095–1101. doi:10.1103/PhysRevB.17.1095.

[331] I. Dreiling, D. Stiens, T. Chassé, Raman spectroscopy investigations of TiB x C y N z coatings deposited by low pressure chemical vapor deposition, Surf. Coat. Technol. 205 (2010) 1339–1344. doi:10.1016/j.surfcoat.2010.09.022.

[332] H. Ju, J. Xu, Microstructure , oxidation resistance , mechanical and tribological properties of Ti – Y – N fi lms by reactive magnetron sputtering, Surf. Coat. Technol. 283 (2015) 311–317. doi:10.1016/j.surfcoat.2015.10.068.

[333] K.W. Nugent, S. Prawer, L.A. Bursill, J.L. Peng, Y.Z. Tong, P. Jewsbury, Micro-Raman scattering properties of highly oriented AlN films, Int. J. Mod. Phys. B. 12 (1998) 1963–1974.

[334] S.K. Mishra, S. Kumari, Development of hard and optically transparent Al-Si-N nanocomposite coatings, Surf. Interface Anal. (2016). doi:10.1002/sia.5954.

[335] F. Jose, R. Ramaseshan, S. Dash, S. Tripura Sundari, D. Jain, V. Ganesan, et al., Significance of Al on the morphological and optical properties of $Ti_{1-x}Al_xN$ thin films, Mater. Chem. Phys. 130 (2011) 1033–1037. doi:10.1016/j.matchemphys.2011.07.083.

[336] J. Wasyluk, T.S. Perova, S.A. Kukushkin, A. V Osipov, N.A. Feoktistov, S.A. Grudinkin, Raman investigation of different polytypes in SiC thin films grown by solid-gas phase epitaxy on Si (111) and 6H-SiC substrates, 648 (2010) 359–362. doi:10.4028/www.scientific.net/MSF.645-648.359.

[337] F.L. Riley, Silicon Nitride and Related Materials, J. Am. Ceram. Soc. 83 (2004) 245–265. doi:10.1111/j.1151-2916.2000.tb01182.x.

[338] R.F. Zhang, S. Veprek, Metastable phases and spinodal decomposition in Ti1-xAlxN system studied by ab initio and thermodynamic modeling, a comparison with the TiN-Si3N4 system, Mater. Sci. Eng. A. 448 (2007) 111–119. doi:10.1016/j.msea.2006.10.012.

[339] D. Holec, L. Zhou, R. Rachbauer, P.H. Mayrhofer, Alloying-related trends from first principles: An application to the Ti-Al-X-N system, J. Appl. Phys. 113 (2013). doi:10.1063/1.4795590.

[340] U. Mizutani, Hume-Rothery Rules for Structurally Complex Alloy Phases, CRC Press, 2011.

[341] S.H. Sheng, R.F. Zhang, S. Vepřek, Decomposition mechanism of Al1−xSixNy solid solution and possible mechanism of the formation of covalent nanocrystalline AlN/Si3N4 nanocomposites, Acta Mater. 61 (2013) 4226–4236. doi:10.1016/j.actamat.2013.03.048.

[342] M.W. Chase, C.A. Davies, J.R. Downey, D.J. Fruip, R.A. McDonald, A.N. Syverud, JANAF Thermochemical Tables, in: J. Phys. Chem. Ref. Data, 1985: p. 1856.

[343] Z. Liu, Y.H. Lu, Y.G. Shen, Grain growth in nanocomposite Ti – B – N films during deposition : The effect of amorphous phase precipitation, Jouranlal Mater. Res. 21 (2006) 82–87. doi:10.1557/JMR.2006.0038.

[344] K.A. Jackson, Diffusion in Amorphous Materials, in: Kinet. Process., WILEY-VCH Verlag GmbH & Co. KGaA, 2004: pp. 19–26.

[345] K. Kutschej, N. Fateh, P.H. Mayrhofer, M. Kathrein, P. Polcik, C. Mitterer, Comparative study of Ti1−xAlxN coatings alloyed with Hf, Nb, and B, Surf. Coatings Technol. 200 (2005) 113–117. doi:10.1016/j.surfcoat.2005.02.072.

[346] P. Losbichler, C. Mitterer, P.N. Gibson, W. Gissler, F. Hofer, P. Warbichler, Co-sputtered films within the quasi-binary system TiN-TiB2, Surf. Coatings Technol. 94–95 (1997) 297–302. doi:10.1016/S0257-8972(97)00440-4.

[347] D. Holec, R. Rachbauer, L. Chen, L. Wang, D. Luef, P.H. Mayrhofer, Phase stability and alloy-related trends in Ti – Al – N , Zr – Al – N and Hf – Al – N systems from fi rst principles, Surf. Coat. Technol. 206 (2011) 1698–1704. doi:10.1016/j.surfcoat.2011.09.019.

[348] K.L. Johnson, Contact Mechanics, J. Am. Chem. Soc. 37 (1985) 1–17. doi:10.1115/1.3261297.

[349] S. Hassani, M. Bielawski, W. Beres, L. Martinu, M. Balazinski, J.E. Klemberg-sapieha, Predictive tools for the design of erosion resistant coatings, Surf. Coat. Technol. 203 (2008) 204–210. doi:10.1016/j.surfcoat.2008.08.050.

[350] J. Shi, M.A. Zikry, Grain size, grain boundary sliding, and grain boundary interaction effects on nanocrystalline behavior, Mater. Sci. Eng. A. 520 (2009) 121–133. doi:10.1016/j.msea.2009.05.012.

[351] A.L. Greer, Confusion by design, Nature. 366 (1993) 303–304. doi:10.1038/366303a0.

[352] J. Musil, Physical and Mechanical Properties of Hard Nanocomposite Films Prepared by Reactive Magnetron Sputtering, in: A. Cavaleiro, J. Th. M. De Hosson (Eds.), Nanostructured Coatings, 2006: pp. 407–463.

[353] Z.H. Stachurski, On Structure and Properties of Amorphous Materials, Materials (Basel). 4 (2011) 1564–1598. doi:10.3390/ma4091564.

[354] H.W. Sheng, W.K. Luo, F.M. Alamgir, J.M. Bai, E. Ma, Atomic packing and short-to-medium-range order in metallic glasses., Nature. 439 (2006) 419–425. doi:10.1038/nature04421.

[355] D.B. Miracle, A structural model for metallic glasses, Nat. Mater. 3 (2004) 697–702. doi:10.1038/nmat1219.

[356] S.H. Whang, D.P. Pope, C.T. Liu, High temperature aluminides and intermetallics, Elsevier, 1992.

[357] R.L. Kurtz, Comparison of Ti 2p Core-Level Peaks from TiO 2 , Ti 2 O 3 , and Ti Metal , by XPS, Surf. Sci. Spectra. 5 (1998) 179–181.

[358] R. Methaapanon, S.F. Bent, Comparative Study of Titanium Dioxide Atomic Layer Deposition on Silicon Dioxide and Hydrogen-Terminated Silicon, J. Phys. Chem. C. 114 (2010) 10498–10504. doi:10.1021/jp1013303.

[359] Y. Murata, T. Higuchi, M. Morinaga, Oxidation Resistance of Ti5Si3 and (Ti,M)5Si3, (M:Nb,V) Intermetallic Compounds, in: S. Somiya (Ed.), Adv. Mater. '93. Ceram. Powders, Corros. Adv. Process., Elsevier, 1994: pp. 247–250.

[360] P.H. Mayrhofer, C. Mitterer, J.G. Wen, I. Petrov, J.E. Greene, Thermally induced self-hardening of nanocrystalline Ti – B – N thin films, 44301 (2006). doi:10.1063/1.2222406.

[361] C. Bindal, A. Erdemir, Ultralow friction behavior of borided steel surfaces after flash annealing, Appl. Phys. Lett. 923 (1995) 923. doi:10.1063/1.116232.

[362] V. Crist, Fundamental XPS Data from Pure Elements , Pure Oxides , and Chemical Compounds, Handb. Monochromatic XPS Spectra - Elem. Nativ. Oxides. (2000) 2.

[363] Thermo Fisher Scientific, Knowledgebase. (2013). http://xpssimplified.com/index.php.

[364] A. Joshi, H.S. Hu, Oxidation behavior of titanium-aluminium nitrides, Surf. Coatings Technol. 76–77 (1995) 499–507. doi:10.1016/0257-8972(95)02566-9.

[365] J.P. Chu, C.T. Liu, T. Mahalingam, S.F. Wang, M.J.O. Keefe, B. Johnson, et al., Annealing-induced full amorphization in a multicomponent metallic film, Phys. Rev. B. 69 (2008) 1–4. doi:10.1103/PhysRevB.69.113410.

[366] L.P.H. Jeurgens, Z. Wang, E.J. Mittemeijer, Thermodynamics of reactions and phase transformations at interfaces and surfaces, Int. J. Mater. Res. 100 (2009).

[367] X.Y. Chen, Y. Lu, Annealing and oxidation of silicon oxide films prepared by plasma-enhanced chemical vapor deposition, J. Appl. Phys. 97 (2004) 14913. doi:10.1063/1.1829789.

[368] L. Zhang, H.C. Jiang, C. Liu, J.W. Dong, P. Chow, Annealing of Al2O3 thin films prepared by atomic layer deposition, J. Phys. D. Appl. Phys. 40 (2007) 3707–3713. doi:10.1088/0022-3727/40/12/025.

[369] D. Srolovitz, K. Maeda, V. Vitek, T. Egami, Structural defects in amorphous solids Statistical analysis of a computer model, Philos. Mag. A. 44 (1981) 847–866.

[370] H.C. Barshilia, Growth , characterization and performance evaluation of Ti / AlTiN / AlTiON / AlTiO high temperature spectrally selective coatings for solar thermal power applications, Sol. Energy Mater. Sol. Cells. 130 (2014) 322–330. doi:10.1016/j.solmat.2014.07.037.

[371] J. Feng, S. Zhang, Y. Lu, H. Yu, L. Kang, The spectral selective absorbing characteristics and thermal stability of SS / TiAlN / TiAlSiN / Si 3 N 4 tandem absorber prepared by magnetron sputtering, Sol. Energy. 111 (2015) 350–356. doi:10.1016/j.solener.2014.11.005.

[372] J.M. Chem, F.D. Hardcastle, H. Ishihara, A.S. Biris, Photoelectroactivity and Raman

spectroscopy of anodized titania (TiO2) photoactive water-splitting catalysts as a function of oxygen-annealing temperature, J. Mater. Chem. 21 (2011) 6337–6345. doi:10.1039/c0jm03106b.

[373] M. Naguib, M. Kurtoglu, V. Presser, J. Lu, J. Niu, M. Heon, et al., Two-dimensional nanocrystals produced by exfoliation of Ti 3AlC 2, Adv. Mater. 23 (2011) 4248–4253. doi:10.1002/adma.201102306.

[374] M. Stoehr, C.S. Shin, I. Petrov, J.E. Greene, Raman scattering from TiNx (0.67 <x < 1.00) single crystals grown on MgO(001), J. Appl. Phys. 110 (2011) 0–4. doi:10.1063/1.3651381.

[375] P. V. Thomas, V. Ramakrishnan, V.K. Vaidyan, Oxidation studies of aluminum thin films by Raman spectroscopy, Thin Solid Films. 170 (1989) 35–40. doi:10.1016/0040-6090(89)90619-6.

[376] K.S. Andrikopoulos, S.N. Yannopoulos, G.A. Voyiatzis, A.V. Kolobov, M. Ribes, J. Tominaga, Raman scattering study of the a-GeTe structure and possible mechanism for the amorphous to crystal transition, J. Phys. Condens. Matter. 18 (2006) 965–979. doi:10.1088/0953-8984/18/3/014.

[377] G. Gouadec, P. Colomban, Raman Spectroscopy of nanomaterials: How spectra relate to disorder, particle size and mechanical properties, Prog. Cryst. Growth Charact. Mater. 53 (2007) 1–56. doi:10.1016/j.pcrysgrow.2007.01.001.

[378] V. Raghavan, Al-N-Ti (Aluminum-Nitrogen-Titanium), J. Phase Equilibria Diffus. 27 (2006) 159–162. doi:10.1361/154770306X97263.

[379] K. Das, P. Choudhury, S. Das, The Al-O-Ti (Aluminum-Oxygen-Titanium) System, J. Phase Equilibria. 23 (2002) 525–536. doi:10.1361/105497102770331271.

[380] P. Zeman, J. Musil, R. Daniel, High-temperature oxidation resistance of Ta-Si-N films with a high Si content, Surf. Coatings Technol. 200 (2006) 4091–4096. doi:10.1016/j.surfcoat.2005.02.097.

[381] C.A. Schuh, T.C. Hufnagel, U. Ramamurty, Mechanical behavior of amorphous alloys, Acta Mater. 55 (2007) 4067–4109. doi:10.1016/j.actamat.2007.01.052.

[382] A. Pshyk, E. Coy, A. Pogrebnjak, High temperature behavior of functional TiAlBSiN nanocomposite coatings, Surf. Coat. Technol. 305 (2016) 49–61. doi:10.1016/j.surfcoat.2016.07.075.

[383] R. Franz, C. Mitterer, Vanadium containing self-adaptive low-friction hard coatings for high-temperature applications: A review, Surf. Coatings Technol. 228 (2013) 1–13. doi:10.1016/j.surfcoat.2013.04.034.

[384] A. Erdemir, Modern tribology handbook, Boca Raton: CRC, 2001.

[385] S.M. Aouadi, H. Gao, A. Martini, T.W. Scharf, C. Muratore, Lubricious oxide coatings for extreme temperature applications: A review, Surf. Coatings Technol. 257 (2014) 266–277. doi:10.1016/j.surfcoat.2014.05.064.

[386] I. Dreiling, C. Raisch, J. Glaser, D. Stiens, T. Chassé, Temperature dependent tribooxidation of Ti – B – N coatings studied by Raman spectroscopy, Wear. 288 (2012) 62–71. doi:10.1016/j.wear.2012.02.011.

[387] D.R. Lide, CRC Handbook of Chemistry and Physics, CRC Press, Boca Raton, 2005.

List of figures

List of tables

List of abbreviations

2A – second-order longitudinal acoustic

3D – three dimensional

a – amorphous phase

AFM – atomic force microscope

BF – bright field

BSE – backscattered electrons

c – crystalline

CVD – chemical vapor deposition

DC – direct current

DF – dark field

EDS – energy-dispersive spectrometry

EELS – electron energy loses spectroscopy

fcc – face centered cubic

FFT – fast Fourier transform

FIB – focused ion beam

FWHF – full width at half maximum

HIPIMS – high-power impulse magnetron sputtering

HRTEM – high-resolution transmission electron microscopy

hcp – hexagonal close packed

IFFT – inverse fast Fourier transform

L1 – top layer

L2 – bottom layer

LA – longitudinal acoustic

LO – longitudinal optical

ML – monolayer

Me – metal

Met – metalloid

nACo G– TiN - AlTiN gradient coating

nACRo G– CrN – AlCrSiN gradient coating

nc – nanocrystalline phase

PDF – Powder Diffraction File

PVD – physical vapor deposition

RF – radio frequency

RG – reactive gas

RT – room temperature

SAED – selected area electron diffraction

SE – secondary electrons

SEM – scanning electron microscope

SPM – scanning probe microscopy

SZD – structure zone diagram

TA – transverse acoustic

TEM – transmission electron microscopy

TM – transition metal

TO – transverse optical

XPS – X-ray photoelectron spectroscopy

XRD – x-ray diffraction